Development of New Methods for Nonintrusive Induction Motor Energy Efficiency Estimation

By: Muhammad Aminu

A thesis presented for the Degree of DOCTOR OF PHILOSOPHY in the Department of Electrical Engineering, UNIVERSITY OF CAPE TOWN

February 2020

Declaration

This dissertation is submitted to the Department of Electrical Engineering, University of Cape Town, in complete fulfilment of the requirements for the degree of Doctor of Philosophy. It has not been submitted before for any degree or examination at this or any other university. I confirm that this thesis is based on my own work. Portions of this work have been published in peer-reviewed journals and at referred international conferences.

Signature: Signed by candidate Date: 6th February 2020

Student Name: Muhammad Aminu Student Number: AMNMUH003

I confirm that I have been granted permission by the University of Cape Town's Doctoral Degrees Board to include the following publication(s) in my PhD thesis, and where co-authorships are involved, my co-authors have agreed that I may include the publication(s):

1. **Muhammad Aminu**, Paul Barendse and Mohammed Azeem Khan "A Simplified Equivalent Circuit Method for Induction Machine Nonintrusive Field Efficiency Estimation" IEEE Transactions on Industrial Electronics, DOI 10.1109/TIE.2019.2945269,

2. **Muhammad Aminu**, John Mushenya, Paul Barendse, Mohammed Azeem Khan, "Converter-fed induction motor efficiency measurement under variable frequency/load points: An extension of the IEC/TS 60034-2-3" *IEEE energy conversion congress and expo (ECCE), September 2019, Baltimore, USA, pp. 3046 – 3052*

Signature: Signed by candidate Date: 6th February 2020

Student Name: Muhammad Aminu Student Number: AMNMUH003

Acknowledgments

In the name of Allah, the Most Gracious the Most Merciful, I am very grateful to Almighty Allah for His countless favours and immeasurable blessings that have made it possible for me to complete this PhD dissertation.

This thesis is dedicated to my dearest father, Justice Aminu Hamidu Modibbo, for his sacrifice, support, and encouragement. May the Almighty Allah forgive all his shortcomings and admit him to a very high place in paradise. I am equally indebted to my beloved mother, Haj. Khadijah Aliyu Modibbo, for her love, prayers, support and encouragement. May the Almighty Allah grant her long and healthy life and admit her to paradise. Ameen.

I wish to express my sincere thanks to my supervisor, Professor Paul Barendse for his invaluable mentorship and guidance throughout the course of this PhD research. He has indeed been a great mentor, and I am very happy to have pursued my PhD studies under his supervision. Also, my sincere gratitude goes to my co-supervisor Professor Azeem Khan for his mentorship and support, which made this work possible. I have learned a lot from his wealth of knowledge and experience.

My sincere gratitude and appreciation extend to my beloved wife, Maryam Bukhari Abubakar for her love, patience and support throughout the course of this work. I am equally thankful to my siblings, Ahmad, Hamidu, Musa, Abubakar, Fadimah and Hauwa'u for their, encouragement and support.

Special thanks and appreciation to Mr. Chris Wozniak for his invaluable technical guidance on the laboratory experiments. I am also grateful for the technical assistance from Mr. Maysam, Mr. Riyad and Mr. Hossain. Special thanks to the AMES research administrator Ms Shireen Sabodien and the departmental postgraduate adviser, Nicole

Moodley, for their support with regard to all the administrative tasks related to this study.

Finally, many thanks to my colleagues and friends in the Advanced Machines and Energy Systems (AMES) research group for their contributions toward the success of this work. These include: John, Olufemi, Akinola, Yusuf, Sampath, Akrama, Dolly, Mohammed and Hossain.

Abstract

Induction motors (IMs) are the most widely used motors in industries. They constitute about 70% of the total motors used in industries and are the largest energy consumers in industrial applications. As a result of the increasing need for energy savings and demand-side management, the development of methods for accurate energy efficiency estimation has become a crucial area of research. While several methods have been proposed for induction motor efficiency determination, majority of the methods cannot be easily applied in the field owing to the intrusive nature of the test procedures involved. This PhD work presents some novel methods for nonintrusive efficiency estimation of induction motors operating on-site using limited motor terminal measurements and nameplate data. The first method is developed for induction motors operating on sinusoidal supply source (line-fed). The method uses a modified inverse Γ-model equivalent circuit with series core loss arrangement to mitigate the inherent problems of higher computational burden and parameter redundancy associated with the conventional equivalent circuit method. Furthermore, a new method is presented for estimating the friction and windage loss using the airgap torque and motor nameplate data. The proposed Nonintrusive Field Efficiency Estimation (NFEE) technique was validated experimentally on four different induction motors for both balanced and unbalanced voltage supply conditions. The results demonstrate the accuracy of the proposed NFEE method and confirm its advantage over the conventional equivalent circuit method.

In addition to the problem of unbalanced voltage supply, the presence of harmonics significantly affects the operation of induction motors. The second novel approach for estimating efficiency proposed in this PhD work extends the NFEE method to cover for non-sinusoidal supply condition. The method considers the variation of core loss, rotor bar resistance and leakage inductance due to time harmonics and skin effects. Finally, the efficiency estimations are compared to the IEC/TS 60034-2-3 in the case of a

balanced non-sinusoidal supply condition. This allows not only the efficiency comparison but also the loss segregation analysis on the various components of the motor losses. In the case of an unbalanced supply, the efficiency results are compared to measured values obtained based on the direct input-output method. In both the first and second methods, a robust Chicken Swarm Optimization (CSO) algorithm has been used for the first time in conjunction with a simplified inverse Γ-model EC to correctly determine the induction motor parameters and hence its losses and efficiency while in-service.

As Variable Frequency Drives (VFDs) continue to dominate industrial process control, there is a need for stakeholders to quantify the converter-fed motor losses over a wide range of operating frequency and loading conditions. Although there is an increase in legislative activities, particularly in Europe, towards the classification and improvement of energy efficiency in electric drive systems, the handful of available standards for quantifying the harmonic losses are still undergoing validation. One of such standards is the IEC/TS 60034-2-3, which has been lauded as a step in the right direction. However, its limitation to rated motor frequency has been identified as one of its main weaknesses. Therefore, the third method proposed in this research demonstrates how the IEC/TS 60034-2-3 loss segregation methodology at nominal frequency can be extended over the constant-torque region of an induction motor (IM). The methodology has been validated by testing two motors using a 2-level voltage source inverter (VSI) in an open-loop V/F control mode. The results provide good feedback to the relevant IEC standards committee as well as guidance to stakeholders.

Contents

List of Figures

List of Tables

List of Abbreviations

ABC	– Artificial Bee Colony
AGT	– Airgap Torque
CSO	– Chicken Swarm Optimization
CVUF	– Complex Voltage Unbalance Factor
DAQ	– Data Acquisition
DE	– Differential Evolution
DF	– Distortion Factor
dq	– Direct and Quadrature (Axis)
EC	– Equivalent Circuit
FEA	– Finite Element Analysis
FFT	– Fast Fourier Transform
EMDS	–Electric Motor-Driven Systems
GA	– Genetic Algorithm
IE	International Efficiency
IEC	International Electrotechnical Commission
IEEE	– Institute of Electrical and Electronics Engineers
IM	– Induction Motor
MEC	–Motor Efficiency Classifications
MEPS	–Minimum Energy Performance Standard
MRAS	– Model Reference Adaptive System
NEMA	– Equipment Manufacturers Association
NFEE	– Nonintrusive Field Efficiency Estimation
OH	– Ontario Hydro
OP	– Operating Point
ORNL	– Oak Ridge National Laboratory
PSO	– Particle Swarm Optimization
PWM	– Pulse-Width Modulation
REE	– Realistic Error Estimation

SLLs – Stray-Load Losses

THD – Total Harmonic Distortion

THD_v – Total Voltage Harmonic Distortion

VFDs – Variable Frequency Drives

VU – Voltage Unbalance

VUF – Voltage Unbalance Factor

VSI – Voltage Source Inverter

WCEE – Worst-Case Error Estimation

List of Symbols

η – Efficiency

P_{output} – Output power

P_{input} – Input power

P_{scl} – Stator copper loss

P_{rcl} – Rotor copper loss

P_{fe} – Iron or core loss

P_{fw} – Friction and windage loss

P_{sll} – Stray-load loss

P_{ag} – Airgap power

R_s – Average stator winding line-to-line resistance

s – Slip

I_s – Stator line current

k_h – Steinmetz hysteresis coefficient

n – Steinmetz exponent

B_{max} – Maximum flux density of the material

f – Frequency of magnetic reversal (current)

P_e – Eddy current loss

k_e – Eddy current constant

P_k – Constant no-load losses

I_{s-nl} – No-load stator line current

R_{s-nl} – Stator resistance corrected to the no-load temperature

V_s – Average stator line-to-line voltage

$cos\varphi$ – Power factor

k_θ – Temperature correction coefficient factor

θ_w – Coolant inlet temperature

θ_{amb} – Ambient temperature

I_{nl} – No-load current

p – Number of poles

ω_r – Rotor angular speed

h – Harmonics order

I_{h-max} – Maximum amplitude of the harmonics order current

L_m – Magnetization inductance

R_r – Rotor resistance

L_{ls} – Stator leakage inductance

L_{lr} – Rotor leakage inductance

X_{ls} – Stator leakage reactance

X_{lr} – Rotor leakage reactance

X_m – Magnetization reactance

R_{fe} – Core loss resistance

ω_s – Stator angular speed

ω_{sl} – Slip angular speed

R_{sfe} – Stator series core loss resistance

R_{rfe} – Rotor series core loss resistance

R_c – Total core loss resistance

θ_w – Coolant inlet temperature

θ_{amb} – Ambient temperature

n_{syn} – Synchronous speed

I_{harm} – Harmonics current

I_{s-fund} – Fundamental component of the stator current

ω_e – Supply electrical frequency

$P_{k\,sin}$ – Constant no-load loss under sinusoidal supply

$P_{k\,PWM}$ – Constant no-load loss under PWM supply

P_{HL} – Total additional harmonic loss

Chapter one

Introduction

1.1 Background

One of the biggest challenges facing the world in the 21st century is the need for sufficient and sustainable energy supply to meet the ever-increasing energy demand and at the same time minimize the emissions of greenhouse gases, mainly carbon dioxide (CO_2) into the environment. Electric motor systems are the primary source of mechanical energy for various industrial operations. They constitute about two-thirds of industrial electricity consumption and nearly 40 percent of global electricity consumption [1]. Consequently, substantial energy savings can be realized from small improvements in the design and operation of these systems. Reducing the growing energy demand through minimizing energy losses in electric motor-driven systems (EMDS) and energy efficiency improvements have been identified as promising and cost-effective strategies of achieving simultaneously the dual goals of energy security as well as reductions in CO_2 emissions. According to a report by the International Energy Agency (IEA) [1], by 2030, the projected global energy consumption from EMDS without adapting an inclusive energy-efficiency strategy is expected to increase to 13,360 TWh per year and carbon dioxide emissions to 8,570 Mt per year (see Fig. 1.1). Conversely, if rigorous energy-efficiency measures are put in place, about 24,000 TWh in electricity demand will be saved and avoid some 16 Gt of CO_2 emissions [1].

To minimize energy losses in EMDS, and specifically the induction motors (due to their widespread application in industries), many countries around the world have introduced policies and regulations to minimize energy losses in electric motors and the loads they drive. Examples of such policies are the minimum energy performance standard (MEPS) and motor efficiency classifications (MEC). As a consequence of these policies, motors are now classified and appropriately labelled based on their energy efficiencies.

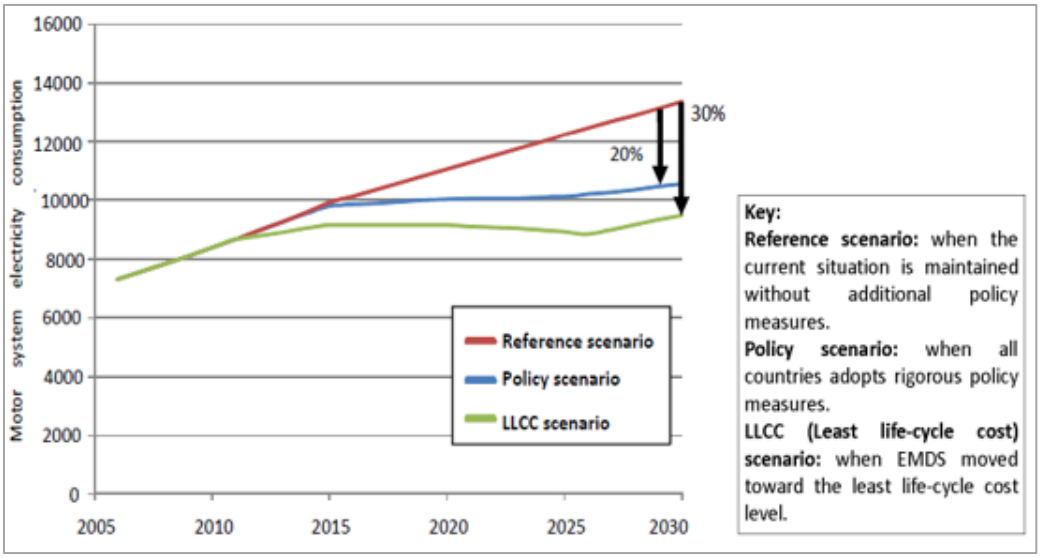

Fig. 1.1 Projected global electricity consumption of EMDS [1].

For instance, the International Electrotechnical Commission (IEC) in 2014 released the IEC 60034-30-1 technical standard on efficiency classifications for low voltage AC motors. Four different International Efficiency (IE) classes are defined in the standard for line-fed electric motors as shown in Table 1.1 [2].

TABLE 1.1

CLASSIFICATION OF INDUCTION MOTORS BASED ON EFFICIENCY

Super-premium efficiency	IE4
Premium efficiency	IE3
High efficiency	IE2
Standard efficiency	IE1

As a comparison, Fig. 1.2 shows the efficiency profiles of the four classes for different output power ratings. Based on these classifications, the EU's legislation which came

into effect on January 2015, stipulates that direct driven motors having rated power within the range of 7.5kW to 375kW must conform to the IE3 efficiency level or IE2 for converter-fed motors.

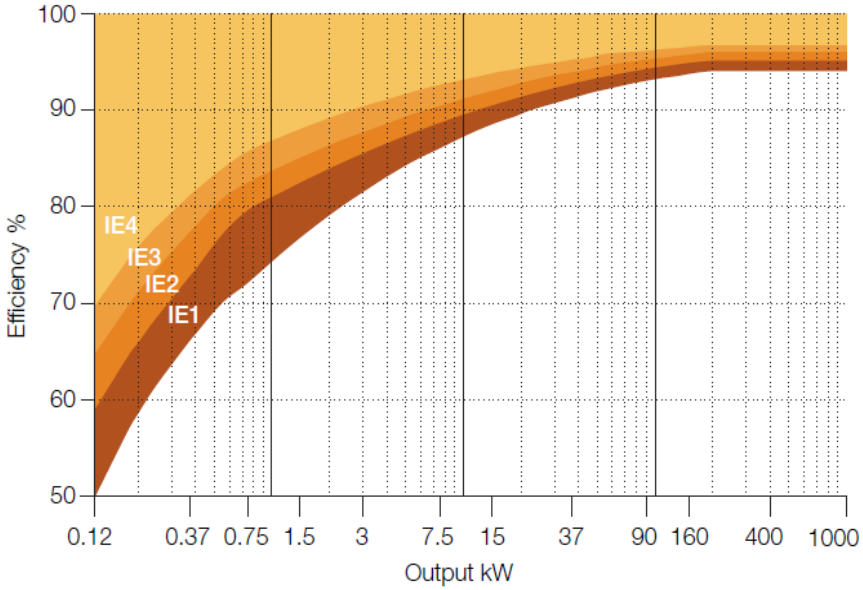

Fig.1.2. IE Efficiency profiles for 4 pole AC motors [2]

Aside the regulatory aspects, another area of interest for energy savings in industrial applications is the application of variable frequency drives (VFDs) for smooth process control and energy efficiency improvements. It has been argued that there could be substantial energy savings through the installation of VFDs in applications with variable flow rates such as pumps, fans and compressors [3], [4]. These types of loads are classified as centrifugal loads and are predictable by the so-called affinity laws, mathematically written as shown in (1.1) [5].

$$\frac{Q_1}{Q_2} = \frac{n_1}{n_2}; \frac{H_1}{H_2} = \frac{n_1^2}{n_2^2}; \frac{P_1}{P_2} = \frac{n_1^3}{n_2^3} \tag{1.1}$$

Where Q is the flow, n is the speed, H is the pressure head, and P is the power.

Based on (1.1), it is interesting to note that if the speed is reduced by half, there could be a reduction in the absorbed power by up to one-eighth of its original value.

One key step towards realizing energy efficiency improvements in EMDS is the accurate estimation of motor operating efficiency. This information is necessary in making informed decisions such as the replacement of less efficient motors with more efficient ones, identifying oversized installations or under/overload conditions. Furthermore, the accurate estimation of motor efficiency after repair could assist the machine repair industry to assess the quality of their work.

Thus, to provide the basic test procedures for assessing the performance of 3-phase induction motors, several international efficiency test standards have been developed. The most widely adopted amongst these standards are the IEEE Std. 112 [6] and the IEC 60034-2-1 standard [7]. Also, several other standards, such as the Canadian CAN/CSA C390-10 and NEMA MG-1 are in line with the IEEE and IEC standards. Although, detailed specifications, as well as procedures for efficiency measurements, are provided in these test standards, most of the test procedures can only be used in a standard laboratory environment. Certain specified tests such as the variable voltage no-load test and the variable load test cannot be easily applied under field operating conditions. This is because in the no-load, the test motor most be completely decoupled from its load, while the variable load test involves a dynamometer test which is expensive and may not be practical in the field.

Generally, the direct input-output method is the basic method used for testing IM efficiency. This test involves measurements of the input as well as the output power of the Motor Under Test (MUT). While the input power could be easily measured from the terminals of the MUT, the output power is deduced from measurements of torque and speed via transducers which could be difficult to install and too intrusive for in-service efficiency estimation.

For in-service efficiency estimation, measurement intrusions must be minimized as much as possible without compromising on accuracy. This constraint limits the adoption of the IEEE and IEC standards for in-service efficiency estimation. Besides, the standards only apply to motors operating on sinusoidal supply (fixed speed applications) in which measurement specifications are strict regarding the quality of the supply. Voltage unbalance (VU) and total harmonic distortion (THD), according to the

IEEE Std. 112 shall not exceed 0.5% and 5% respectively [6]. However, under field conditions, these strict conditions may hardly be realised as the presence of voltage unbalance and (or) harmonics may significantly affect the performance of the induction motor and hence the need to develop efficiency estimation methods that are capable of dealing with these challenges.

Despite the widespread application of VFDs in industrial applications, only a handful of draft standards have attempted to standardise the determination of the additional losses introduced by Pulse-Width Modulated (PWM) voltages and currents of an inverter [8]-[10]. One of such technical standards is the IEC/TS 60034-2-3 which specifies test methods, reference test converter parameters, and introduces the concept of *additional harmonic losses* for converter-fed motors. However, its limitation to motor-rated voltage and frequency has been identified as one of its main weaknesses [11]-[14]. This is because in certain applications, converter-fed motors are operated over a wide speed and torque range in service.

Thus, this dissertation responds to the above highlighted challenges by developing new methods for IM efficiency estimation considering the challenges prevalent in the field. In addition, a critical look at the IEC/TS 60034-2-3 and its application to conveter-fed motors to address its limitation to rated voltage and frequency is considered. The proposed method demonstrates the feasibility of extending the IEC/TS 60034-2-3 loss segregation methodology over a wide range of operating frequencies and loading conditions.

1.2 Research Objectives

Energy efficiency estimation for in-service induction motors has become a crucial area of research due to the increasing need for energy savings and demand-side management. As a result, several in-service efficiency estimation methods have been proposed. However, most of the methods are difficult to implement in the field due to the measurement intrusions involved. Thus, the first goal of this research is to develop new efficiency estimation methods for both direct mains-connected (sinusoidal) and converter-fed (non-sinusoidal) induction motors in the presence of balanced and

unbalanced voltage supply conditions. The proposed methods are developed based on a new equivalent circuit approach that can be regarded as nonintrusive, since it relies on only some few motor terminal measurements and nameplate data.

The second goal of this research is to demonstrate how the efficiency of converter-fed induction motors can be measured over a wide range operating points by extending the IEC/TS 60034-2-3 methodology at nominal frequency to other operating points within the constant-torque region. By using the measurements at some specific frequencies and load points, the efficiency estimates at any desired operating points within the achievable range of the motor can be obtained.

Based on the above highlighted goals, the specific objectives of the research are listed as follows:

1. To develop a modified equivalent circuit of an IM that can resolve some issues associated with the conventional T-model such as the parameter redundancy problems and the difficulties in estimating the core loss resistance.
2. To develop nonintrusive efficiency estimation methods that consider the problems of voltage unbalance and harmonics in the supply using the equivalent circuit approach.
3. To apply a robust CSO optimization algorithm for improved IM parameter identification and efficiency estimation.
4. To develop nonintrusive speed estimation method using only a single steady- state stator line current signal.
5. To identify the EC parameters of an IM through external measurements of the stator voltage and current signals at a single operating point.
6. To apply the form F2 of the IEEE Std.112 to estimate the IM efficiency using the identified EC parameters and speeds and to compare the results to the well-established loss segregation methods of the IEEE and IEC standards.

7. To determine the efficiency of IMs operating with unbalance power supply using modified negative and positive sequence EC models and compare the results to measured values.
8. To determine the efficiency of IMs operating with distorted supply signals using appropriate harmonic EC models and compare the results to measured values.
9. To demonstrate how the IEC/TS 60034-2-3 methodology for converter-fed motors at nominal frequency can be extended to other frequency/load points over the constant-torque region of an induction motor (IM).
10. To perform error analysis of the proposed efficiency estimation methods

1.3 Research Questions

In view of the above-listed objectives, the research questions answered in this research are as follows:

1. The equivalent circuit method can be used to calculate the efficiency of IMs based on the conventional steady-state motor EC model. What are the limitations of these methods for induction motors operating in the field?
2. How can the conventional motor EC model be modified to improve the accuracy of parameter identification and efficiency estimation?
3. What are the appropriate sequence and harmonic equivalent circuits for motors operating under unbalanced or distorted voltage supply? Which model and what approach is more relevant for field efficiency estimation?
4. What are the limitations of the IEC/TS 60034-2-3 efficiency determination method for variable speed/torque applications?
5. How can the IEC/TS 60034-2-3 efficiency loss segregation method at nominal frequency and voltage be extended over a wide operating range?

1.4 Dissertation Overview and Contributions

The research methods associated with this thesis are mainly based on experimental tests and simulations. The induction motors tested are modelled using MATLAB/ SIMULINK. Measured experimental data are used as inputs to the developed IM computer models for parameter identification. The estimated parameters are then used in the proposed algorithms to analyse the losses and efficiency of the different type/size induction motors.

The specific contributions of this PhD research include the following:

1. In Chapter four, a new method is developed for IM efficiency estimation without taking the motor out of service. The method uses the equivalent circuit approach in conjunction with a robust CSO optimization algorithm to overcome the challenges of field efficiency estimation such as, the presence of harmonic distortions and voltage unbalance scenarios. Most equivalent circuit methods reported in literature require test measurements at various loading conditions and therefore may not be suitable to field efficiency determination without causing disruptions to the motor and its operating processes. The novelty lies in the application of a simplified inverse Γ-model EC to correctly estimate the induction motor parameters and hence its losses and efficiency while in-service using limited measurements of motor terminal quantities. The proposed method has been accepted for publication in IEEE Transactions on Industrial Electronics. Details of the published paper are as follows:

   Muhammad Aminu, Paul Barendse and Mohammed Azeem Khan "A Simplified Equivalent Circuit Method for Induction Machine Nonintrusive Field Efficiency Estimation" DOI 10.1109/TIE.2019.2945269, IEEE Transactions on Industrial Electronics.

2. In Chapter five, a method is developed for IM efficiency determination in the presence of non-sinusoidal supply conditions - to take into account the presence of harmonics in the power supply. By using a modified equivalent circuit approach, the method considers the variations of the core loss resistance due to

time harmonics. Also, the changes in the rotor bar resistance and the leakage inductance due to skin effects at higher frequencies are considered. The results confirm the variations of the rotor and core loss resistances on the order of the harmonics and hence, the need to estimate these parameters separately using the harmonics equivalent circuit for each harmonic order.

3. In chapter six, a new approach is proposed to extend the methodology specified by the IEC/TS 60034-2-3 for converter-fed motors at nominal frequency to cover a much wider speed and torque range within the constant-torque region of an IM. The procedure to be followed as well as the technical considerations to be established for maintaining repeatable test conditions have been presented. Based on the findings from this chapter, the following paper has been presented at the 2019 IEEE energy conversion congress and expo (ECCE), Baltimore, USA:

   Muhammad Aminu, John Mushenya, Paul Barendse, Mohammed Azeem Khan, "Converter-fed induction motor efficiency measurement under variable frequency/load points: An extension of the IEC/TS 60034-2-3" IEEE energy conversion congress and expo (ECCE), September 2019, Baltimore, USA. pp. 3046 – 3042.

1.5 Dissertation Outline

The PhD thesis is structured as follows:

Chapter one presents a general introduction and highlight the aim and objectives of the research, the research questions as well as the specific contributions of the work.

Chapter two presents a review of relevant literature on in-service efficiency estimation techniques for induction motors. In addition, an overview of the impact of harmonics and voltage unbalance conditions on the efficiency of induction motors are presented. The chapter also reviews relevant studies on converter-fed motor losses and efficiency determination over a wide range of operating frequencies as opposed to the fixed speed operation.

Chapter three contains a critical review of the Chicken Swarm Optimization (CSO) optimization algorithm and justifies its choice in this PhD work for solving the IM parameter identification problem.

Chapters four presents the development of a simplified equivalent circuit method for in-service IM efficiency estimation. The chapter highlights the challenges of the conventional equivalent circuit method and proposes a new approach to solve these challenges using a modified inverse Γ-model EC. The method is validated by testing four different induction motors and the results demonstrate acceptable levels of accuracy. Detailed sensitivity and error analysis of the proposed method are also presented in the chapter.

Chapter five presents another novel approach using the equivalent circuit method with the CSO technique for induction motor efficiency estimation in the presence of non-sinusoidal supply. Two induction motors (a standard and a premium efficiency) are tested to validate the proposed method. The experimental tests are performed on a balanced supply for the first case and a combination of different levels of VU and THD levels for the second case.

Chapter six presents an overview of the IEC/TS 60034-2-3 loss segregation methodology (method 2-3-B) and proposes the methodology for determining the additional harmonic losses at diffrent frequencies and loading points. The chapter discusses some technical challenges that must be considered to ensure accurate determination of the additional harmonic losses.

Finally, chapter seven concludes the PhD work as a whole and also gives recommendations for further improvements.

Chapter two

Literature Review

2.1 Introduction

This chapter starts by defining efficiency and discussing the various components of losses in induction motors and how these losses are measured. The review of relevant literature on in-service efficiency estimation techniques for induction motors are also presented. This includes, the conditions under which the efficiency is to be determined, the measurements required, the accuracy and level of intrusion of the various methods and the considerations when choosing one technique over the other are discussed. In addition, the relevant literature review on induction motor efficiency determination in the presence of harmonics and voltage unbalance conditions are presented. Different IM equivalent circuit models are reviewed for in-service efficiency estimation. Finally, the relevant studies that have attempted to analyse the converter-fed motor losses and efficiency determination over a wide range of operating frequencies as opposed to the fixed speed operation are presented.

2.2 Definition of Efficiency and Losses in Induction Motors

In an electrical motor, efficiency can be defined as the ratio of the mechanical power output to the electrical power input. This can be expressed as:

$$\eta = \frac{P_{output}}{P_{input}} \times 100\% \tag{2.1}$$

It can also be defined in terms of the input power and the total losses in the motor, as shown in (2.2).

$$\eta = \frac{P_{input} - P_{losses}}{P_{input}} \times 100\% \tag{2.2}$$

For an induction motor, the total losses P_{losses} given in (2.2) is the summation of the five losses given by (2.3).

$$P_{losses} = P_{scl} + P_{rcl} + P_{core} + P_{fw} + P_{sll} \tag{2.3}$$

These losses are illustrated according to their locations by the power flow diagram shown in Fig. 2.1. The five losses can be classified as being load-dependent losses or load-independent (constant) losses and are discussed in the next four sections.

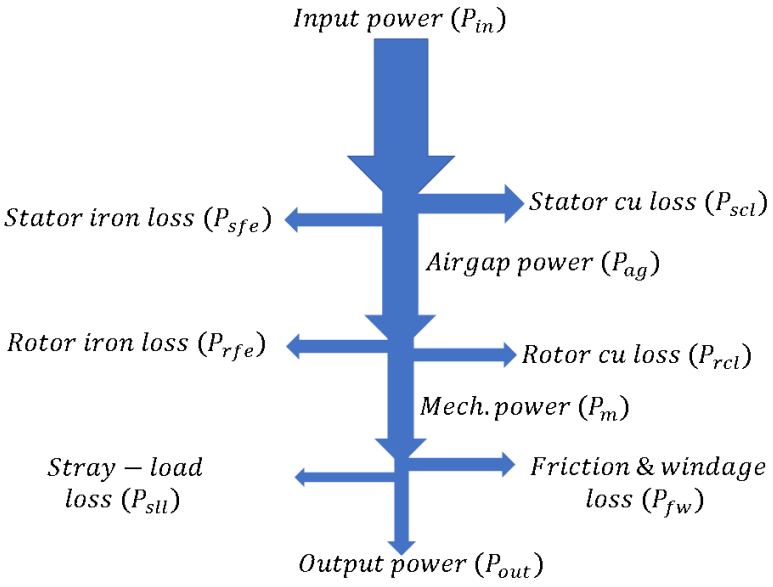

Fig. 2.1. Power flow diagram of an induction motor

2.2.1 Stator and Rotor Copper Losses

These losses are termed as winding losses or I^2R losses due to the currents in the stator and rotor windings of an induction motor. The stator and rotor copper losses are dissipated as heat and are proportional to the square of the load current. Since these losses are resistive, they are usually corrected to account for temperature changes. Typically, the stator copper losses are dominant and may account for up to 25 to 40% of the total losses in an IM [15], [16]. In a three-phase IM, the total stator copper loss is calculated according to (2.4).

$$P_{scl} = 1.5 I_s^2 R_s \tag{2.4}$$

Where: R_s is the dc resistance between any two terminals of the motor- corrected to the appropriate temperature. Note that the 1.5 term in (2.4) applies to both delta as well as star connected motors Alternatively, P_{scl} can be calculated in terms of the per phase dc resistance R_{s-ph} as follows:

$$P_{scl} = 3 I_s^2 R_{s-ph} \tag{2.5}$$

The rotor copper loss is determined from the slip using (2.6).

$$P_{rcl} = P_{ag} s \tag{2.6}$$

Where: $P_{ag} = \left(P_{input} - P_{scl} - P_{fe} \right)$ is the airgap power.

2.2.2 Core Losses

The core or iron losses occur in the magnetic materials that make up the stator and rotor cores. These losses can be categorised into the hysteresis and eddy current losses. Hysteresis losses are as a result of the magnetization and demagnetization of the core as current flows in the forward and reverse directions. Due to the ‘memory effect’ exhibited by the magnetic material, the flux density still retains a positive value when

the magnetic force is reduced to zero. The magnetization force (current) must be applied in the reverse direction to demagnetize the material as shown in Fig. 2.2 [17]. The hysteresis loop shows the energy required to traverse a complete cycle of magnetization and demagnetization and the area of the B-H curve represent the total energy required during this process.

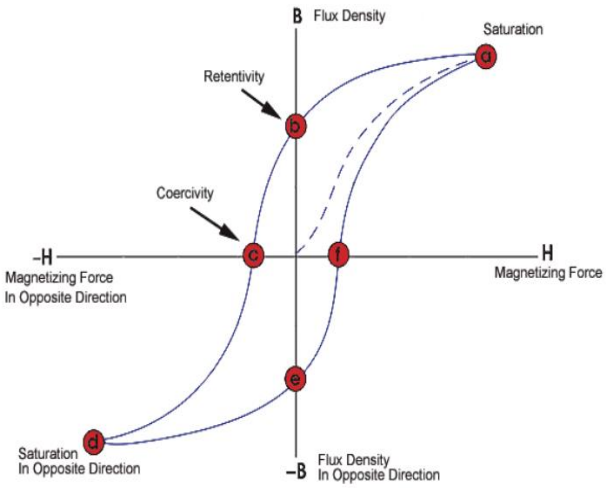

Fig. 2.2. B-H curve of a typical soft magnetic material [17]

The hysteresis loss can be expressed in terms of the frequency and magnetic flux density as given by (2.7).

$$P_h = k_h B_{max}^n f \tag{2.7}$$

Where: n is the Steinmetz exponent, (value ranges from 1.5 to 2.5 depending on magnetic material).

The eddy current component of the core loss is due to the variations of the magnetic field which causes a circulating current within the magnetic material. This current known as the eddy current can be minimized by increasing the effective resistance of the magnetic material through the use of thin pieces of laminations which are insulated from each other [18]. The eddy current is proportional to the square of the frequency and the flux density as given by (2.8).

$$P_e = k_e B_{max}^2 f^2 \tag{2.8}$$

Where: P_e is the eddy current loss, k_e is the eddy current constant.

Based on [19], a third component of the core loss apart from the hysteresis and eddy current losses is the anomalous loss which occur due to the movements of the magnetic domain walls. However, due to its complicated physical mechanism and how small its contributions are to the core loss, there is limited literature available on this component of the core loss [20].

2.2.3 Friction and Windage Losses

The friction and windage loss or mechanical losses consist of the frictional losses due to the movements of the bearings and the windage losses caused by the air friction experienced by the cooling fan attached to the shaft. Friction and windage losses account for about 5 to 15% of the total losses in an induction motor [15]. Generally, frictional losses can be minimized by lubricating the motor bearings, while windage losses can be reduced by enhancing the airflow through improved fan design [15].

2.2.4 Stray-load Losses

The stray-load losses (SLLs) or additional losses are losses that are not account for by the motor loss mechanisms. Although these losses are difficult to model or quantify, some portion of it can be attributed to the presence of magnetic field distortions in the load current. These distortions create additional iron loss that would not appear in the no-load test [19]. Therefore, although these are iron losses, they are typically grouped as stray-load loss, due to the way in which they appear in the testing sequence. The stray-load losses (SLLs) also depend on the stator current and not only are present in the core across the machine length but higher in core ends due to fringing flux. Additionally, the structural elements such as core compression plates, the frame etc. also have losses which are part of the SLL.

The largest part of the stray-load losses can be attributed to the harmonic energies generated when a motor is loaded [10]. These energies are dissipated due to harmonic

currents in the windings, harmonic flux components in the iron parts and as leakage in the laminated core. Motor vibration can also be seen as another source of SLLs [19].
In general, the most acceptable method for calculating the losses discussed above is the input-output method with loss segregation. This is because this method allows separate determination of the losses, hence, it has been widely accepted as a baseline for testing of induction motors. The loss segregation methods of the IEEE Std. 112 and IEC 60034-2-1 standards are discussed in the next section.

2.3 The Segregation of Loss Methods

Although the IEEE and IEC standards define several methods for calculating the losses and efficiency of induction motors, the methods that are widely accepted in industry are the loss segregation methods. While the loss segregation method by the IEEE and IEC standards are similar in terms of their test procedures as well as accuracy, they differ in some few aspects as can be seen in Table 2.1.

TABLE 2.1

COMPARISON OF OF THE IEEE STD 112 AND THE IEC 60034-2-1 LOSS SEGREGATION METHODS

Feature	**IEEE STD 112-2017 (Method B)**	**IEC 60034-2-1-2014 (Method 2-1-1B)**
Temperature sensor	Yes	No
Stator winding resistance correction	Yes	Yes
Slip correction	Yes	Yes
Input power correction	No	Yes
Output power correction	Yes	Yes
Voltage drop compensation for core loss	Yes	Yes
Torque meter correction	Yes	No
Dynamometer correction	Yes	Yes
Stray-load loss linear regression	Yes	Yes
Stray-load loss correlation coefficient	0.9	0.95
Ambient temperature	25 ℃	25 ℃

The loss segregation (or indirect) method involves the no-load and the load curve test to calculate the constant and load-dependent losses. As defined by (2.9), the constant losses are determined by subtracting the no-load stator winding loss from the no-load input power. The no-load input power P_{s-nl} is calculated using (2.10).

$$P_k = P_{in-nl} - P_{s-nl} = P_{fe} + P_{fw} \tag{2.9}$$

$$P_{s-nl} = 1.5 I_{s-nl}^2 R_{s-nl} \tag{2.10}$$

Where: P_k is the constant no-load losses, I_{s-nl} is the no-load stator current, R_{s-nl} is the stator resistance corrected to the no-load temperature at each test point.

The mechanical loss is obtained from the graph of the constant loss against the square of the no-load voltage as shown in Fig. 2.3. By using linear regression on the last four points of the no-load test, the intercept on the constant loss axis at zero voltage gives the friction and windage loss. Since the friction and windage loss is affected by speed, the corrected value is determined according to (2.11) [7]

$$p_{fw-c} = P_{fw}(1-s)^{2.5} \tag{2.11}$$

To determine the core loss at rated voltage and rated load, the curve of the core loss against the no-load voltage is used (see Fig. 2.4). The core loss value at rated load is interpolated from the curve at the inner voltage V_m to account for the resistive voltage drop of the stator. The inner voltage is calculated using (2.12).

$$V_m = \sqrt{\left(V_s - \frac{\sqrt{3}}{2} I_s R_s cos\varphi\right)^2 + \left(\frac{\sqrt{3}}{2} I_s R_s sin\varphi\right)^2} \tag{2.12}$$

Where: V_s is the average stator terminal line-to-line voltage, $cos\varphi$ is the power factor and $sin\varphi = \sqrt{1 - cos^2\varphi}$.

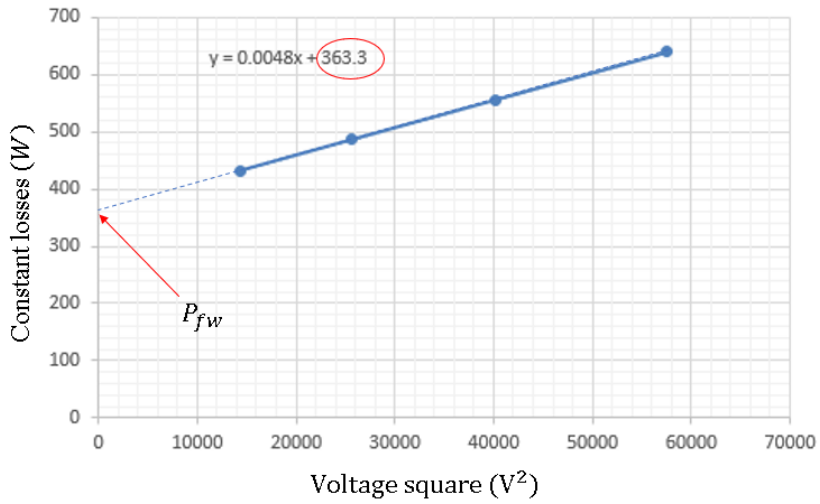

Fig. 2.3. Determination of the friction and windage loss from no-load test

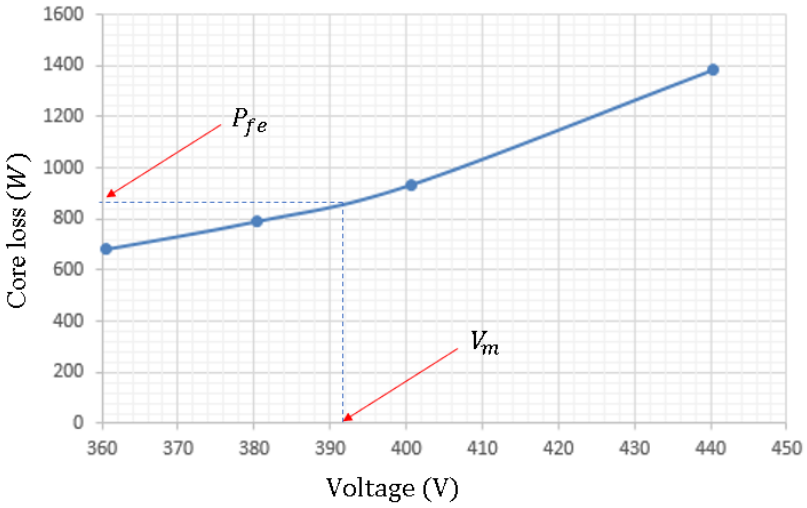

Fig. 2.4. Determination of the core loss from no-load test

From the load curve test, the stator and rotor winding losses are calculated using (2.13) and (2.14) respectively:

$$P_s = 1.5 I_s^2 R_s \tag{2.13}$$

$$P_r = \left(P_{in} - P_s - P_{fe} \right) s \tag{2.14}$$

Both P_{scl} and P_{rcl} are to be corrected to a reference coolant temperature of 25℃ as follows:

$$P_{scl\theta} = k_\theta P_{scl} \tag{2.15}$$

$$P_{rcl\theta} = \left(P_1 - P_{scl\theta} - P_{fe} \right) s_\theta \tag{2.16}$$

k_θ and s_θ are defined by (2.15) and (2.16) respectively [7]:

$$k_\theta = \frac{235 + \theta_w + 25 - \theta_{amb}}{235 + \theta_w} \tag{2.17}$$

$$s_\theta = s k_\theta \tag{2.18}$$

The stray-load loss for each load point is determined as the residual loss when all other losses are subtracted from the apparent loss (The difference between the input and output power) as expressed by (2.19).

$$P_{sll} = P_{input} - P_{output} - \left(P_{scl} + P_{rcl} + P_{fe} + P_{fw}\right) \tag{2.19}$$

Using linear regression as shown in Fig. 2.5 and 2.6, the stray-load loss is smoothened according to the relationship in (2.20). The test is only considered satisfactory if the correlation coefficient is greater or equal to 0.95 when using the IEC standard or 0.9 when using the IEEE Std. 112, otherwise, the worst point is deleted, and the linear regression repeated.

$$P_{sll} = AT^2 + B \tag{2.20}$$

The stray-load loss for each load point is calculated by setting the intercept B in (2.20) to zero.

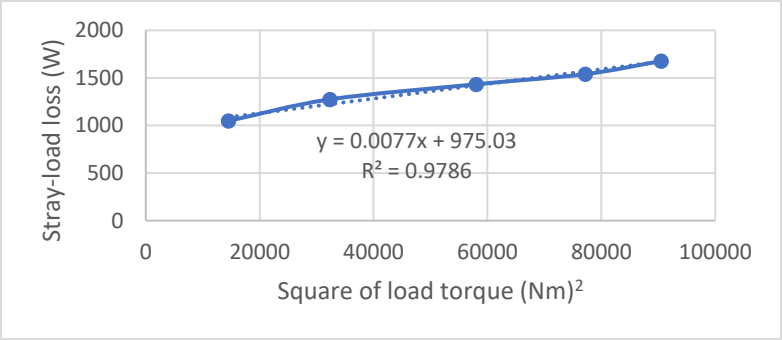

Fig. 2.5. Smoothing of the stray-load loss

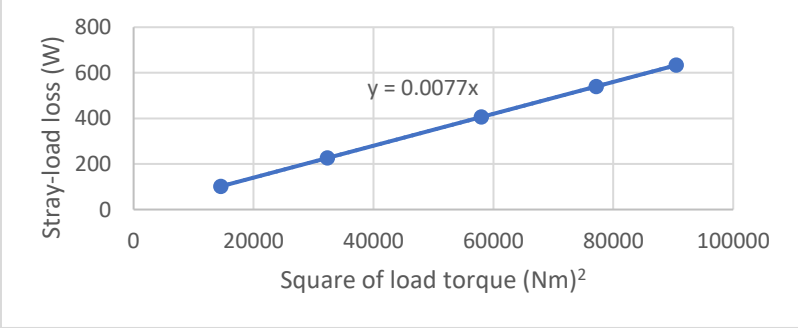

Fig. 2.6. Determination of the core loss from no-load test

2.4 Review of In-service IM Efficiency Estimation Methods

Unlike testing of motors using standard procedures in a laboratory environment, field efficiency determination comes with several challenges for which the standard methods cannot be applied. Therefore, several field efficiency determination methods have been proposed in literature. The first comprehensive literature survey was presented in 1998 by the Oak Ridge National Laboratory (ORNL), for the US Department of Energy (DOE) [21]. The study identified and compared several in-service efficiency estimation methods based on their physical nature, intrusiveness and accuracies. In a similar study by [22], the following six basic methods have been identified as suitable for field efficiency estimation:

1. Speed/Slip method
2. Current method
3. Nameplate method
4. Segregated loss method
5. Airgap torque (AGT) method
6. Equivalent circuit (EC) method

In another report [23], three out of the above six methods are suggested as the most potentially accurate methods for field efficiency determination. These methods are the airgap torque (AGT) method, the equivalent circuit method based on modified IEEE Method E1 and the equivalent circuit method based on nameplate data. In [24], a comprehensive literature review of methods for field efficiency evaluation was presented with particular interest in the condition monitoring of motors. The survey briefly described up to 20 methods and grouped them into six major categories. Based on the study, the following four methods were selected as the best candidates for field efficiency evaluation [24].

1. Equivalent circuit method based on nameplate data (ORMEL 96)
2. Rockwell Motor Efficiency Wizard (RMEW)
3. Modified IEEE Method F1 based on Ontario Hydro method
4. Airgap Torque (AGT) Method

In addition, the problems of stator resistance and rotor speed estimation in most field evaluation methods were identified in the paper using current signature analysis, and signal injection methods were proposed for solving these problems. Finally, the paper specified a general approach for field efficiency estimation, incorporating the proposed new strategies for speed and stator winding resistance estimation and the estimation of the no-load losses. In the following sections, brief descriptions of the methods for in-service efficiency estimation are presented. However, it is important to note that the major shortcoming of most of the methods is that they rely on design information which may not be accurate, especially when the test motor is rewound or suffers degradation due to aging.

2.4.1 Nameplate Method

The nameplate method is the least intrusive while also being the least accurate of the methods for field efficiency estimation. In this method, the motor efficiency is assumed to be equal to the nameplate efficiency value. However, the problems associated with this assumption are as follows: 1) the conditions under which the nameplate value is derived may be different from the field operating condition. 2) the nameplate data may differ from the real data and therefore not applicable if the motor is rewound or due to aging and 3) the efficiency on the nameplate may be obtained using a method other than the IEEE standard 112 making it difficult to compare the motor efficiency to the baseline values.

2.4.2 Slip Method

The slip method uses speed measurement to evaluate efficiency. In the standard slip method, the output power is assumed to be proportional to the slip ratio and thus the efficiency is expressed using (2.21) [24].

$$\eta = \frac{s}{s_{rated}}\left(\frac{P_{output-rated}}{P_{input}}\right) \tag{2.21}$$

Although this method is quite simple, its accuracy is poor because the slip ratio represents the percentage of load, not the efficiency [22]. In addition, the NEMA MG1 standard allows for up to 20% deviation from the nameplate rated speed value [25] and as a result, large error may be introduced in the efficiency estimation due to this deviation.

2.4.3 Current Method

Just like the slip method, this method assumes that the output power is proportional to the ratio of the input stator current and the rated motor current. Therefore, efficiency is calculated using the expression shown in (2.22).

$$\eta = \frac{I}{I_{rated}}\left(\frac{P_{output-rated}}{P_{input}}\right) \tag{2.22}$$

Based on (2.22), it is assumed that the load versus current curve is linear. However, at light loading conditions, the load-current curve is nonlinear and will be lower than the assumed curve. Thus, using (2.22) results in an overestimate. On the other hand, a modified expression for the efficiency as shown in (2.23) has been shown to give an underestimation [22].

$$\eta = \frac{I - I_{nl}}{I_{rated} - I_{nl}}\left(\frac{P_{output-rated}}{P_{input}}\right) \tag{2.23}$$

Thus, it is expected that the average of efficiencies determined by (2.22) and (2.23) will be more realistically accurate than using the methods in (2.22) or (2.23) separately. However, the no-load current introduced in (2.23) can only be accurately determined by performing a no-load test and as stated earlier, this may not be possible for motors operating in the field.

2.4.4 Loss Segregation Method

In this method, various components of the motor losses are separately determined and the difference between the input power and the sum of all the individual losses gives the output power. Although this method is considered quite accurate when testing motors using the standard methods, its accuracy when applied to field efficiency testing is poor due to the approximations in the estimation of the no-load and load-dependent losses. An example of this method is the simplified loss segregation version of the IEEE Std. 112 Method E1 referred to as the Ontario Hydro method [26]. In this method, the no-load test is avoided by assuming a value of 3.5% of the motor output power for the combined mechanical and core loss. However, it has been shown that this assumption may not be accurate for different motors [27], [28]. Furthermore, the error is expected to be more significant in the presence of voltage unbalance as the core loss varies based on the magnitude of the input voltage [28].

2.4.5 Airgap Method

The AGT method uses instantaneous measurements of the motor line voltages and currents to calculate the power crossing the airgap. The airgap torque is calculated using the well-known AGT equation shown in (2.24) [29].

$$T_{ag} = \frac{p}{2\sqrt{3}}\Big\{(I_A - I_B)\int [v_{CA} - R_s(i_C - i_A)]dt - (i_C - i_A)\int [v_{AB} - R_s(i_A - i_B)]dt\Big\} \quad (2.24)$$

Where: p is the number of poles, i_A, i_B and i_C are the line currents and v_{AB} and v_{CA} are the line-to-line voltages.

With the airgap torque determined using (2.24), the output power can be calculated by subtracting the mechanical and stray-load losses from the airgap power and the efficiency is estimated using (2.25).

$$\eta = \frac{T_{ag}\omega_r - P_{fw} - P_{sll}}{P_{input}} \tag{2.25}$$

Where: The input power P_{input} is expressed as the average of the instantaneous power summed over a period of time *T*.

$$P_{input} = \frac{\int_0^T (v_A i_A + v_B i_B + v_C i_C) dt}{T} \tag{2.26}$$

The AGT method has been recommended for field efficiency calculation due to its high accuracy (within $\pm 1\%$) and in addition, it can be used to account for the losses due to unbalance supply or distorted (harmonic) supply. However, as shown in (2.25), calculating the no-load losses will be impractical in the field since it requires an uncoupled no-load test. To avoid this problem, [30] considered the no-load losses to be load-independent and therefore used an empirical value of 3.5% of the rated output power. In [31], a new method for estimating the stator resistance using optimization method is presented. The method compares the rated torque (nameplate value) to the airgap torque estimated at the rated operating condition. The airgap torque calculated with the new resistance value is considered to be equal to the shaft. Although the use of nameplate data and the approximation involved in most proposed modifications to the convention AGT reduces the intrusion levels, the accuracy of such methods are however greatly compromised.

2.4.6 Equivalent Circuit Method

The efficiency and other performance characteristics of an induction motor can be determined from its equivalent circuit as depicted in Fig. 2.7.

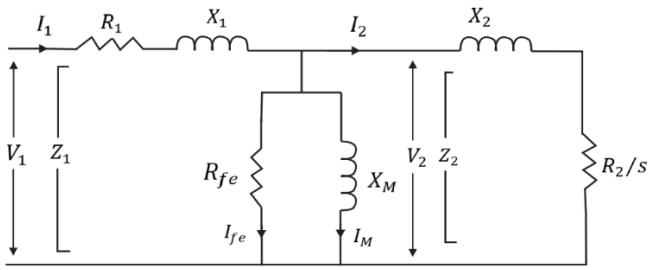

Fig. 2.7. Equivalent circuit of an induction motor

Where the parameters of the equivalent circuit are defined as follows:

R_1 and R_2:	are the stator and rotor resistance respectively
X_2 and X_2:	are the stator and rotor leakage reactance respectively
R_{fe} :	is the core loss resistance
X_M :	is the magnetizing reactance
V_1 and V_2:	are the stator and rotor phase voltages respectively
Z_1 and Z_1:	are the stator and rotor impedances respectively
I_1 and I_2:	are the stator winding and rotor bar currents respectively
I_{fe} and I_M:	are the core loss and magnetizing currents respectively

The advantage of the EC method is that it allows the calculation of efficiency at any desired operating condition in addition to the condition under which measurements are taken. Moreover, once the impedance of the equivalent circuit is correctly determined, the method can be applied for efficiency estimation in the absence of the load varying test. An example of the equivalent circuit method is the IEEE Std. 112, Method F1 [6]. This method involves an impedance test and a complete no-load test for calculating the equivalent circuit parameters and the no-load losses respectively. Although this method is expected to be quite accurate, it is still considered to be too intrusive for routine field use [22]. In the basic Method F1, four different impedance calculation methods are presented. Three out of the four methods require a locked rotor test while one method (method 3) requires a no-load low voltage test. These methods are not generally considered useful for field efficiency calculation due to the intrusiveness involved.

A simplified version of the F1 Method is the Ontario Hydro (OH) method [26] in which the variable-voltage no-load test is avoided by using measurements taken under no-load

and full-load condition at the rated voltage. In addition, the method uses a simplified equivalent circuit with a series magnetization branch to account for the core loss.

Another simplified EC method is the Oak Ridge (OR) method [23]. This method uses nameplate data, assumed friction and windage loss and locked rotor current to simplify the calculation of the equivalent circuit parameters. A resistor is added to the rotor side to account for the stray-load loss. However, since the equivalent circuit parameters are determined based on nameplate information, the error associated with the method could be quite substantial (up to $\pm 4\%$ inaccuracy [24]).

2.5 Parameter Identification Methods

Although the finite element analysis (FEA) method provides a useful modelling approach for estimating the per-phase equivalent circuit parameters, the complexity of electrical machines makes the correct choice for constructing detailed finite element models difficult. In addition, one must have a deep understanding of the physical behavior of the motor being modeled, including its geometry, saturation and eddy current effects. The FEA method is thus too intrusive to be used for field conditions.

The major challenge of the equivalent circuit method is the determination of the equivalent circuit parameters nonintrusively. These parameters are the stator and rotor resistances and reactances, the core loss resistance and the magnetization reactance. Once the speed and equivalent circuit parameters are determined, the motor efficiency can be calculated at any desired loading point. Since the stator resistance can be measured directly and the NEMA design value for the ratio of the stator and rotor reactance (X_1/X_2) can be used to calculate one of the reactance values, the number of parameters to be identified can be reduced to four. Usually, the following set of measurements may be required in estimating the motor parameters:

(i) Steady-state line voltages, line currents and input power
(ii) Rotor speed at different operating points
(iii) Stator winding temperature
(iv) Stator winding resistance

Several attempts have been made to solve the problems associated with motor parameter estimation using a variety of different methods. A review of the major techniques can be found in [32]. Depending on the motor application, the parameter identification method can be online or offline. The online methods are particularly useful for online parameter tracking in high-performance sensorless control schemes. However, the complexity of designing adaptive controllers and the added difficulty of online parameter identification due to temperature changes and motor saturation [33] makes the offline methods viable alternatives when dealing with non-adaptive applications. Generally, the parameter identification methods can be classified into the following three groups [34], namely: signal injection, model reference adaptive system (MRAS) and optimization methods. Signal injection methods are usually performed at standstill with the motor excited via a single-phase dc or ac signal and the motor parameters determined based on the resulting response from the system. Several studies using signal injection method are reported in [35]-[37]. But, the additional circuitry and problems of power dissipation and torque distortions are the main difficulties associated with this method.

The MRAS methods are implemented based on strategies that minimize the error between measured and estimated motor signals to identify the motor parameters. MRAS methods can be based on steady-state measurements [38]-[43] or transient measurements [34], [44]-[52]. Steady-state methods usually involve least square identification algorithms based on simplified (linearized) motor model to solve the parameter estimation problem. However, their disadvantage is the requirement for multiple test measurements under different loading scenarios. On the other hand, transient methods are based on dynamic models and use sinusoidal measurements of motor waveform signals [44]. These methods allow a better excitation at the expense of more sophistication in terms of the experimental and computational burden. The transient measurements could be taken under no-load condition during the motor start-up phase as reported in [34], [49]-[52], to minimize temperature variations and magnetic saturation problem.

Over the years, several optimization techniques for solving the motor parameter estimation problem have been proposed [53]-[68]. The method involves minimizing an

error between measured and estimated motor terminal quantities using artificial intelligence algorithms. Although the Genetic Algorithm (GA) has been widely used for IM parameter identification and efficiency estimation, recent optimization techniques including the Chicken Swarm Optimization (CSO) have demonstrated superior performance over the traditional GA method as clearly demonstrated in [69]-[70]. A detailed review of the CSO technique and its performance validation are presented in chapter 3.

2.6 Impact of Unbalance Voltage Supply on Induction Motor Efficiency

In theory, induction motors are designed to operate optimally on a balanced voltage supply. However, in practice, the supply voltages are hardly balanced. This problem is caused mainly due to unequal distribution of loads on the three phases of a power system. It can also be due to malfunction of equipment such as blown capacitor fuses, open-delta transformer connections and so on [71]. Usually, the motors are not adversely affected if the level of voltage unbalance is small, but excessive voltage unbalance can cause a disproportionate unbalance in current which can be up to 6 to 10 times the magnitude of the voltage unbalance [72] and consequently overheating of the induction motor. As shown in Fig 2.8, the motor temperature curve as a function of the voltage unbalance indicates that the temperature increases exponentially with respect to the voltage unbalance [73].

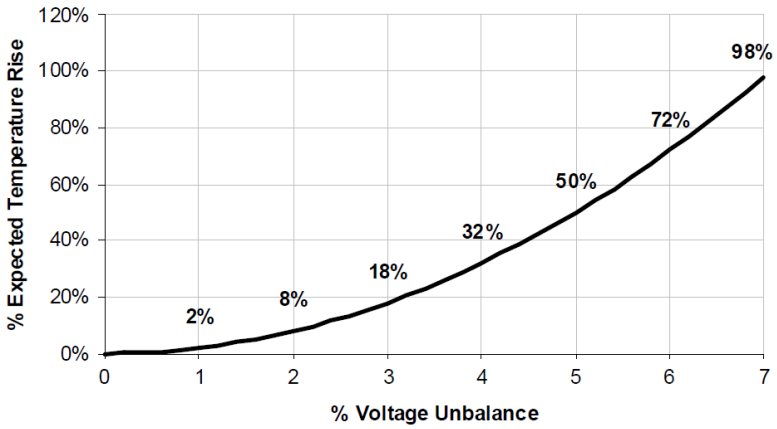

Fig. 2.8. Temperature rise due to voltage unbalance [73]

The voltage unbalance may differ depending on the definition or standard used. While the power community generally defines the percentage voltage unbalance as the ratio of the negative to the positive sequence voltage, the IEEE and NEMA used the definition given in (2.27).

$$\%VU = \frac{Maximum\ voltage\ deviation\ from\ the\ average\ voltage}{Average\ voltage} \quad (2.27)$$

In a similar way, there is no consensus regarding the appropriate voltage unbalance limit as the values specified by different standards differ. While the American National Standard for Electric Power Systems and Equipment, ANSI C84.1 recommends the maximum voltage unbalance limit to 3% under no-load condition [72], the National Equipment Manufacturers Association (NEMA) limits the voltage unbalance to 1% and recommends derating of motors when operating above this limit but should not exceed 5% [25]. This is because once the unbalance exceeds 5%, the temperature of the motor begins to rise so fast that protection from damage becomes impractical [74]. The derating curve as per the NEMA specifications [25] shown in Fig. 2.9 is to protect the motor by reducing its output power so that it can withstand the extra temperature rise imposed by the voltage unbalance.

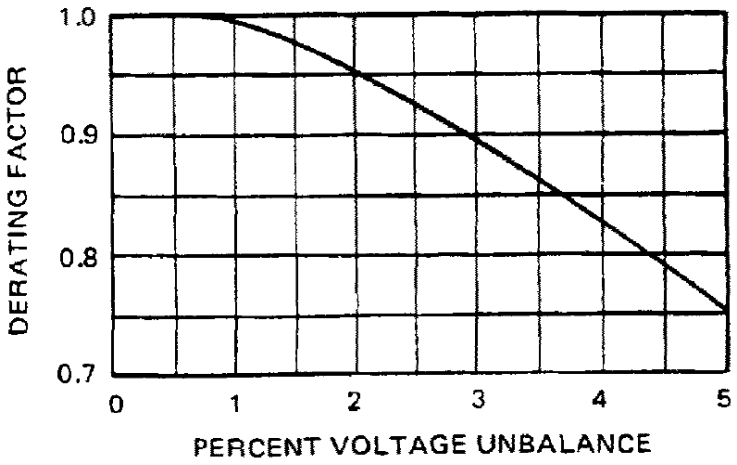

Fig. 2.9. NEMA derating curve of induction motors [25]

Several research articles have reported the impact of unbalanced voltage supply on the operation of induction motors. The study on this field dates back to the 1950s as the

earliest study by [75] examines the impact of voltage unbalance on induction motor losses using the symmetrical component method. The study shows that the additional losses caused by negative sequence components of an unbalance voltage are larger for motors having multiple cage rotors.

Further studies conducted by [76] also concluded that the temperature rise is primarily due to increase in copper loss and unbalanced spatial distribution of stator copper loss. It is demonstrated that negative-sequence current has more thermal effect than an equal positive-sequence current due to the greater negative-sequence rotor resistance and the unbalanced spatial distribution of losses.

In [77], the performance of IMs operating under different unbalance voltages but having the same voltage unbalance factor (VUF) were investigated. The paper shows based on eight different voltage unbalance conditions as shown in Fig. 2.10 that the higher positive sequence voltage gives higher motor efficiency. Thus, the authors suggested that the determination of temperature rise, derating curves and other related regulations should consider not only the VUF but also the magnitude of the positive sequence voltage.

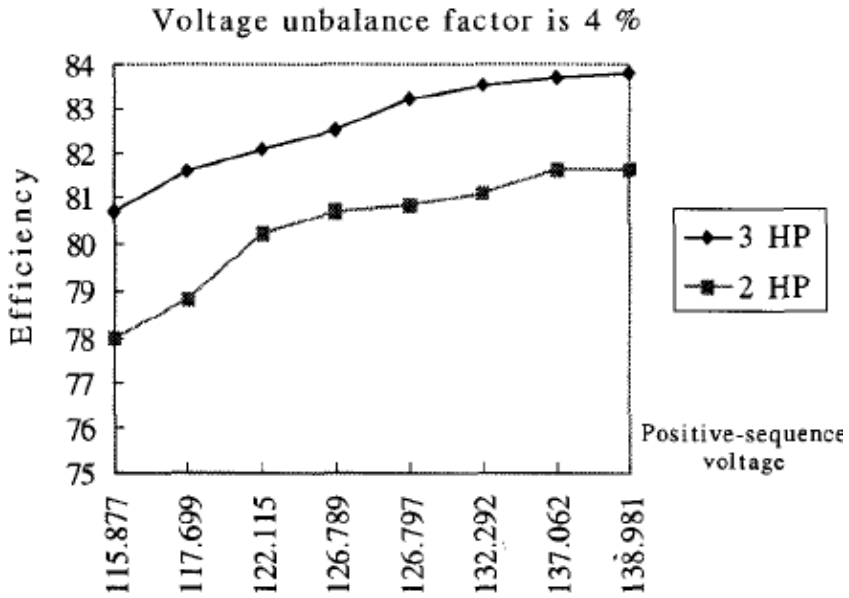

Fig. 2.10. Relationship between positive sequence voltage and motor efficiency at 4% VUF [77]

In a related work by [78], it was stated that; "*it is not sufficient to merely know the percent voltage unbalance, but it is equally important to know how they are unbalanced*". To demonstrate this observation, the authors applied two methods of voltage unbalancing to a 240V, 25hp induction motor. In the first method, (Case A) the average of the line voltage magnitudes is kept constant at 240V by holding the magnitude of V_{bc} constant and increasing the magnitude of V_{ab} while reducing the magnitude of V_{ca} at the same rate. In the second case (Case B), the average voltage is held constant at 240 V by allowing the magnitudes of V_{ab} and V_{ca} to increase while the magnitude of V_{bc} decreases. The derating factor for these two cases are shown in Fig. 2.11. For Case A, the derating factor for 5% voltage unbalance was 0.7018 while that of Case B was 0.7773 [78].

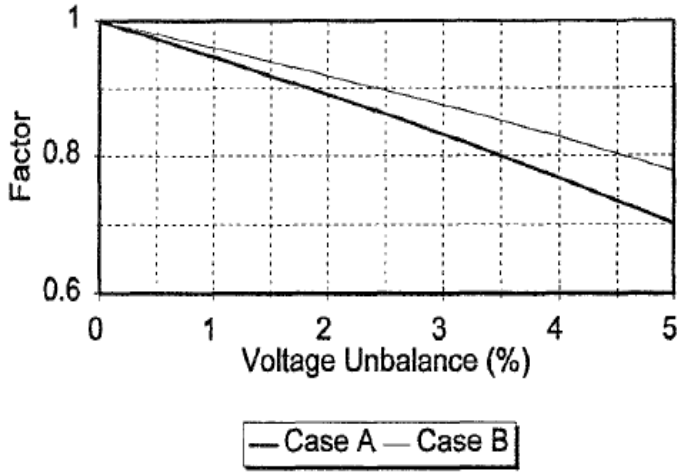

Fig. 2.11. Derating curve for two different unbalance cases [78]

In [79], it has been argued that the voltage unbalance factor (VUF) defined based on the ratio of the negative sequence to positive sequence represents only the unbalance percentage, whereas the heating effect due to unbalanced voltage is influenced by the angle of the complex voltage unbalance (CVUF). For line-to-neutral voltage, the CVUF is expressed by (2.28) [79]:

$$CVUF = \frac{V_n}{V_p} = k_v e^{-j\theta_v} \tag{2.28}$$

Where k_v and θ_v describe the magnitude and angle of the CVUF respectively.

The problem of derating of induction motors in the presence of a combination of unbalanced voltages and over/under-voltages has been studied in [74]. The authors render an extensive analysis of the different definitions of voltage unbalance and have observed an insignificant difference when the unbalance is in the 5% range.

In analysing the induction motor performance under voltage unbalance, the impact of the negative sequence current on the power output and torque can be clearly observed based on the expressions in (2.29) and (2.30). The negative sequence terms reduce the power and torque output of the motor and force it to operate at a higher slip.

$$P_m = 3I_{sp}^2 R_r' \left(\frac{1-s}{s}\right) - 3I_{sn}^2 R_r' \left(\frac{1-s}{2-s}\right) \tag{2.29}$$

$$T = 3R_r' \frac{\left(\left(\frac{I_{sp}^2}{s}\right) - \left(\frac{I_{sn}^2}{2-s}\right)\right)}{\omega_{syn}} \tag{2.30}$$

Where: I_{sp} and I_{sn} are derived as a function of the slip and the equivalent circuit parameters (see Fig. 2.12 and 2.13) as given by (2.31) and (2.32).

$$I_p = \frac{V_p}{\sqrt{\left(\left(R_s + \frac{R_r'}{s}\right)^2 + (X_s + X_r')^2\right)}} \tag{2.31}$$

$$I_n = \frac{V_n}{\sqrt{\left(\left(\frac{R_1 + R_r'}{2-s}\right)^2 + (X_s + X_r')^2\right)}} \tag{2.32}$$

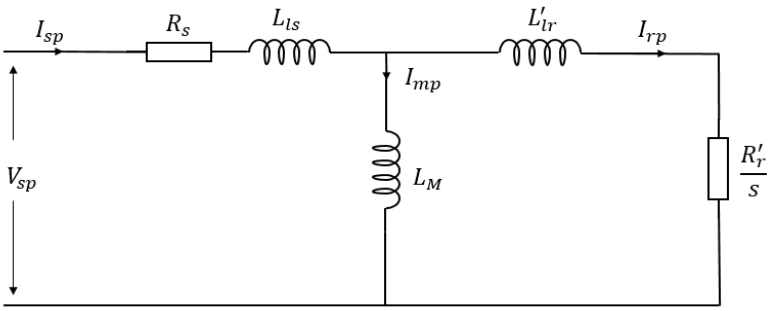

Fig. 2.12. Positive sequence equivalent circuit

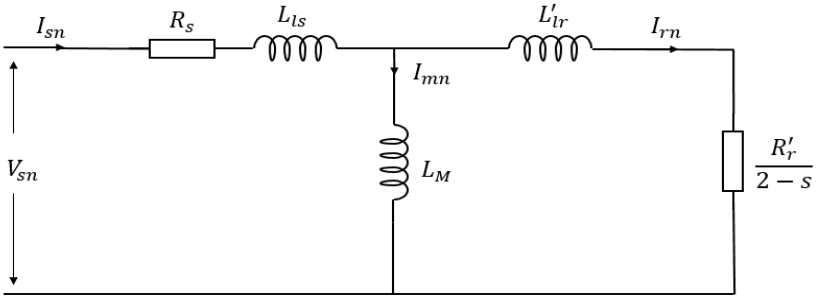

Fig. 2.13. Negative sequence equivalent circuit

In recent years, there has been significant interest in developing methods for in-service induction motor efficiency estimation [54], [59]-[66]. Since the supply voltages are not always balanced, it has become the norm to consider the unbalance supply conditions when developing these efficiency estimation methods.

In [53], a method was developed using the equivalent circuit approach for parameter estimation, losses and efficiency determination for induction motors operating in the field. The genetic algorithm was used to estimate the equivalent circuit parameters relying only on a few sets of data measurements. However, no validation was made to confirm the accuracy of the estimated motor parameters. Moreover, the methods still require multiple sets of measurements at different loading points.

A similar approach was used in [62]-[63] by employing different optimization methods, but the methods suffer the same problems identified in [53] as several steady-state rms measurements are needed to identify the motor parameters. In [64], only steady-state measurements at one load point was used, yet some motor parameters were held constant during optimization to reduce the number of unknown parameters. As a solution to this problem, direct start-up measurement of instantaneous stator voltage

and current waveforms have been used in [61] for full-load in-situ efficiency estimation. But the method has saturation and temperature adjustment issues since measurements are only taken during the start-up condition.

2.7 Nonintrusive IM Efficiency Estimation under Harmonics Supply

Additional losses are incurred by induction motors when operated with non-sinusoidal or distorted power supply due to the presence of harmonics in the voltage supply. With the rapid development in power electronics and the advances in motor control strategies, the application of variable frequency drives (VFDs) has become very popular in industrial applications in the past two decades. While there are several benefits that come with the use of VFDs, their outputs are not purely sinusoidal but rather a superposition of sinusoidal waves with frequencies that are multiples of the fundamental network frequency. These superimposed waveforms are termed as harmonics in the system. The harmonics generally exhibited by induction motors are of two types, namely: space harmonics and time harmonics. The space harmonics in a motor driven by a sinusoidal supply is caused by the non-sinusoidal distribution of the mmf produced in the air gap and the magnetic interaction of the different phase windings. Time harmonics are as a result of power supply distortions [80]. The harmonic currents produce rotating fields in the air gap that rotate at higher speeds than the rotating fundamental field [18]. The following mathematical expressions are given in this section to fully understand the impact of time harmonics on 3-phase induction motors.

Let the currents in an induction motor fed by a harmonic supply be given by:

$$i_a = \sum_{h=1}^{\infty} i_{h-max} \cos(h\omega t) \tag{2.33}$$

$$i_b = \sum_{h=1}^{\infty} i_{h-max} \cos\left(h\omega t - h\frac{2\pi}{3}\right) \tag{2.34}$$

$$i_c = \sum_{h=1}^{\infty} i_{h-max} \cos\left(h\omega t + h\frac{2\pi}{3}\right) \tag{2.35}$$

Assuming a sinusoidal distributed winding, the mmf generated along the angle θ due - to the current in the phase-A winding can be expressed as:

$$F_a = N i_a \cos(\theta) \tag{2.36}$$

Where N is the number of turns per phase. Substituting (2.33) into (2.36) gives:

$$F_a(t,\theta) = \sum_{h=1}^{\infty} N i_{h-max} \cos(h\omega t)\cos(\theta) \tag{2.37}$$

Similarly, for phases b and c, the mmfs are given by:

$$F_b(t,\theta) = \sum_{h=1}^{\infty} N i_{h-max} \cos\left(h\omega t - h\frac{2\pi}{3}\right)\cos\left(\theta - \frac{2\pi}{3}\right) \tag{2.38}$$

$$F_c(t,\theta) = \sum_{h=1}^{\infty} N i_{h-max} \cos\left(h\omega t + h\frac{2\pi}{3}\right)\cos\left(\theta + \frac{2\pi}{3}\right) \tag{2.39}$$

The resultant mmf $F(t,\theta)$ along the angle θ is the sum the mmfs $F_a(t,\theta)$, $F_b(t,\theta)$ and $F_c(t,\theta)$ expressed as:

$$\begin{aligned} F(t,\theta) = \sum_{h=1}^{\infty} N i_{h-max} \Big[& \cos(h\omega t)\cos(\theta) \\ & + \cos\left(h\omega t - h\frac{2\pi}{3}\right)\cos\left(\theta - \frac{2\pi}{3}\right) \\ & + \cos\left(h\omega t + h\frac{2\pi}{3}\right)\cos\left(h\theta - h\frac{2\pi}{3}\right)\Big] \end{aligned} \tag{2.40}$$

The supply may contain 3^{rd} 5^{th}, 7^{th}, 11^{th}, . . . harmonics. Note that even ordered harmonics do not exist in induction motors due to the symmetry of the waveform [79].

Thus, using (2.40), the fundamental mmf is given by:

$$F_1(t,\theta) = F_{1-max}\cos(\theta - \omega t) \tag{2.41}$$

Based on (2.41), $F_1(t,\theta)$ is rotating in the direction of θ (forward direction) with an angular speed of ω.

The 3^{rd}, 5^{th} and 7^{th} order harmonics are given by (2.42), (2.43) and (2.44) respectively.

$$F_3(t,\theta) = F_{3-max}\left\{\cos(3\omega t)\left[\cos(\theta) + \cos\left(\theta - \frac{2\pi}{3}\right) + \cos\left(\theta + \frac{2\pi}{3}\right)\right]\right\} = 0 \tag{2.42}$$

$$F_5(t,\theta) = F_{5-max}\cos(\theta + 5\omega t) \tag{2.43}$$

$$F_7(t,\theta) = F_{7-max}\cos(\theta - 7\omega t) \tag{2.44}$$

Equation (2.42) shows that the third order harmonic is absent. This is because all the three harmonic voltages are equal in magnitude and in phase (in space) but are phase shifted in time by 120 degrees. Hence, they cannot cause any current in a delta or star connection with an isolated neutral [81]. The fifth order harmonic rotates in an opposite direction to the rotating field at an angular speed of 5ω. The seventh order harmonic on the other hand rotates in the same direction as the fundamental rotating field at an angular speed of 7ω. By observing the trends in (2.42) – (2.44), it can be concluded that all odd harmonics of order $h = 6m \pm 1$ (where *m* is an integer) generate mmf wave that can be represented by:

$$F_h(t,\theta) = F_{h-max}\cos(\theta \pm h\omega t) \tag{2.45}$$

All harmonics of order $h = 6m + 1$ rotate in the same direction as the fundamental mmf, while harmonics of order $h = 6m - 1$ rotate in the opposite direction to the fundamental mmf.

The torque generated by the fundamental mmf, the fifth and seventh harmonics are shown in Fig. 2.14.

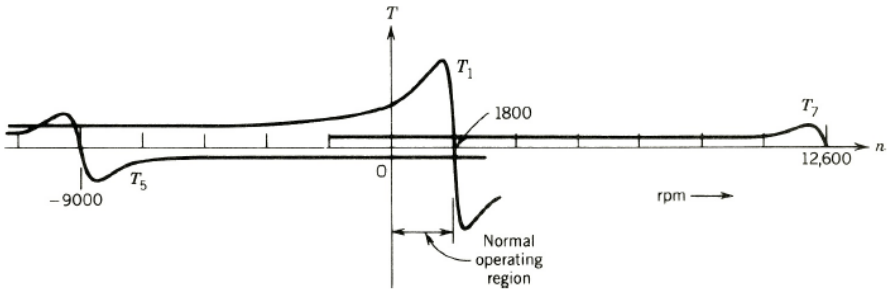

Fig. 2.14. Torque vs speed characteristics for different time harmonics currents [18]

The presence of time harmonics can cause excessive overheating which can increase the amount of losses and produce parasitic torques in the motor. It is estimated that the time harmonic losses account for about 18-20% of the fundamental losses under rated load condition [82].

To mitigate the problems of harmonics in industrial power systems, the IEEE Std. 519 [83] establishes a 5% voltage harmonic distortion limit on industrial power systems. The amount of voltage distortion is quantified by the distortion factor (DF) given by (2.46) [83]

$$DF = \sqrt{\frac{Sum\ of\ squares\ of\ amplitudes\ of\ all\ harmonic\ voltages}{Square\ of\ amplitude\ of\ fundamental\ voltage}} \tag{2.46}$$

On the other hand, ANSI-NEMA standard MG1-2009 [25] compute the harmonic voltage factor HVF as:

$$HVF = \sqrt{\sum_{h=5}^{h=\infty}\left(\frac{V_{hpu}^2}{h}\right)}, \qquad h = 5, 7, 11, 13, \ldots \tag{2.47}$$

Where V_{hpu} is the magnitude (in pu) of the harmonic voltage component of order h.

Generally, a common measure of the level of harmonics present in a power system is the Total Harmonic Distortion (THD) defined in terms of voltage as:

$$THD_v = \frac{\sqrt{\sum_{h=2}^{\infty} V_{h-rms}^2}}{V_{fund-rms}} \tag{2.48}$$

Where: V_{h-rms} is the RMS value of the n^{th} harmonic voltage, $V_{fund-rms}$ is the RMS value of the fundamental voltage

Although the determination of efficiency for direct mains supplied (sinusoidal) motors have attracted considerable attention as evidenced by the existence of several international efficiency measurement standards, on the contrary, converter-fed motors do not have final standards for efficiency determination. Only a handful of technical specifications covers the efficiency determination for converter-fed motors, while work on the standardization is still ongoing. One of such technical specification is the IEC/TS 60034-2-3 [10] in which three specific test methods for efficiency determination of converter-fed motors are presented. However, none of the test methods are applied for nonintrusive efficiency estimation.

In order to quantify the harmonic losses nonintrusively when operating with non-sinusoidal supply, alternative methods have been proposed. One of such methods is the equivalent circuit approach which has yielded promising results as reported in [84]-[85]. In the case of non-sinusoidal supply applications, it is not possible to use the well-known T-model equivalent circuit since it does not take into account the presence of time harmonics in the supply. Due to this limitation, several modifications have been proposed in literature. Reference [86] was the earliest to propose some modifications to the conventional T-Model equivalent circuit to account for time harmonics using the superposition principle as shown in Fig. 2.15. The simplification in Fig. 2.15(b) assumes that the harmonic slip s_k is close to unity under normal operating condition, therefore, the motor can be assumed to operate very close to the locked-rotor condition. Hence, the magnetization branch can be removed without resulting to large errors.

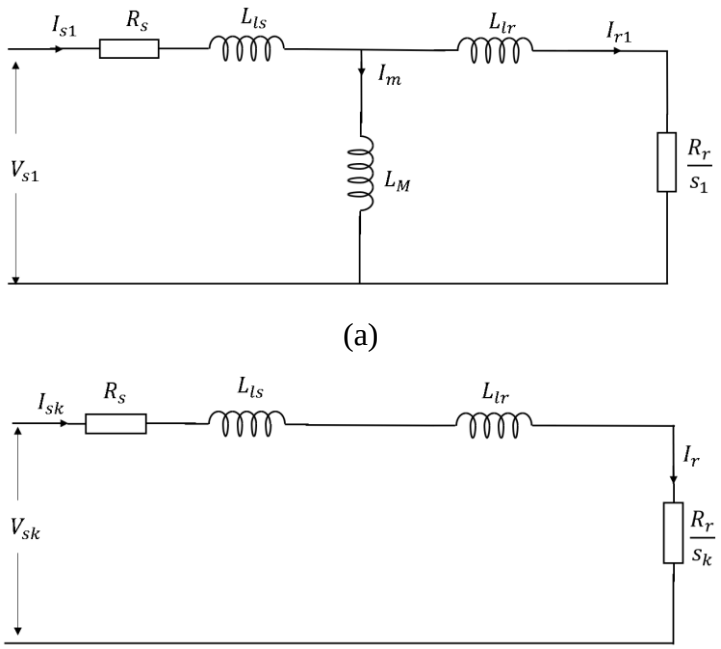

Fig. 2.15. Induction motor Equivalent Circuit (a) Fundamental equivalent circuit (b) Harmonic equivalent circuit

A similar assumption was also used in [87] for the purpose of derating induction motors due to waveform distortions. However, an additional resistance (R_{sllk}) was added to the rotor side for the motor stray-load loss component. The value of R_{sllh} is assumed to be proportional to the fundamental stray-load loss based on the expression given in (2.49) [88].

$$R_{sllk} = h^{0.8} R_{sll1} \tag{2.49}$$

Where R_{sll1} is the resistance representing the fundamental stray-load loss.

While the assumptions made in [86]-[88] greatly simplifies the harmonic equivalent circuit, neglecting the magnetization branch can lead to errors in calculating the motor slip and the rotor flux [89]. Besides, the simplified approach ignores the core loss component which is critical in motor efficiency estimation.

In another study [82], the fundamental EC is modified to accommodate the core loss associated with the leakage and mutual fluxes. The stator, rotor and magnetization

leakage fluxes are represented by the resistances R_{slh}, R_{rlh} and R_{mlh} respectively as shown in Fig. 2.16.

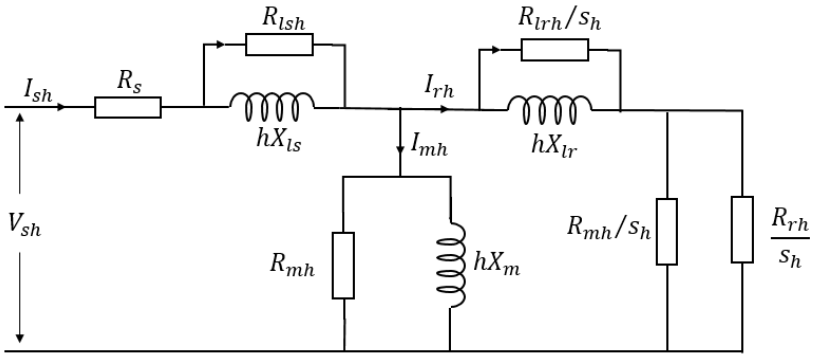

Fig. 2.16. Induction motor time harmonic equivalent circuit

The expressions for the leakage and mutual resistances are given by (2.50) – (2.53) [82]. As the core losses depend on frequency, the stator and rotor core loss resistances are at the fundamental and slip frequency respectively.

$$R_{lsh} = R_{lsb}\frac{hf_1(1+k_1f_b)}{f_b(1+k_1f_1)} \tag{2.50}$$

$$R_{lrh} = R_{lrb}\frac{s_hhf_1(1+k_1s_hf_b)}{s_hf_b(1+k_1s_hf_1)} \tag{2.51}$$

$$R_{msh} = R_{msb}\frac{hf_1(1+k_1f_b)}{f_b(1+k_1f_1)} \tag{2.52}$$

`

$$R_{mrh} = R_{mrb}\frac{s_hkf_1(1+k_1s_hf_b)}{s_hf_b(1+k_1s_hf_1)} \tag{2.53}$$

Where: R_{lsh} and R_{lrh} are the stray-load loss resistances due to the stator and rotor leakage fluxes respectively; $R_{msh}$and R_{mrh} are the stator and rotor core loss resistances respectively; R_{lsb} and R_{msb} are the stator leakage and core loss resistances at the base frequency respectively; R_{lrb} and R_{mrb} are the rotor leakage and core loss resistances at the base frequency respectively; f_1 and f_b are the fundamental and base frequencies

respectively; k_1 is the ratio of eddy current to hysteresis current and is assumed to be constant for a given motor [82].

The base values of the leakage and core loss resistances given in (2.50) – (2.53) are determined based on the following assumptions [82]:

(i) The leakage reactance of the stator and rotor are approximately equal. This means that at the based frequency, the standstill leakage resistances are equal.

(ii) Similarly, the standstill stator and rotor core loss resistance can be assumed to be equal.

(iii) For time harmonic frequencies, the rotor bar skin effect is considered for calculating the value of the rotor resistance.

(iv) The stator and rotor base leakage resistances are obtained from a full-load sinusoidal test at base (rated) voltage and frequency. Under this condition, the stray load loss is assumed to be within 1 – 5% of the motor full load losses.

The assumption in (i) may not be generalized for all motor types- this is only applicable for NEMA class A-type motors. Furthermore, the methods required for evaluating the equivalent circuit parameters such as the standstill test measurements and the application of motor design specifications are too intrusive and cannot be applied in case of nonintrusive efficiency determination.

While several studies have attacked the problem of nonintrusive efficiency determination for mains-fed motors, only some few published works dealing with the subject can be found for converter-fed motors [84]-[85]. In [84], a method for on-site efficiency estimation under variable frequency and load has been proposed. The method relies on the equivalent circuit approach using Genetic Algorithm (GA) to estimate the motor parameters. Similarly, [85] used population-based incremental learning (PBIL) algorithm to estimate motor parameters using RMS measurements of motor terminal quantities at different loading conditions. Despite the application of optimization algorithms to overcome the classical no-load and locked rotor test measurements, the methods in [84] and [85] require several load test measurements of motor rms quantities

for parameter determination which may not be convenient for on-site efficiency estimation. Furthermore, the results presented in the two papers lack proper validation in terms of the various loss components with respect to the well-established IEC 60034-2-3 loss segregation approach.

2.8 Converter-Fed IM Losses and Efficiency under Wide Range of Operating Frequencies and Loads

Through the application of VFD's, precise control of the induction motor can be achieved; allowing the motor to operate below or above the rated frequency and extending its torque/speed capabilities to match the load requirements. While most efficiency estimation studies are centred on operations at (or near) the rated condition, this approach is insufficient as converter-fed motors are required to operate over a much wider torque-speed range in-service. Hence, for a more complete approach, operations over different operating conditions must be considered to fully characterise the motor losses and its operating efficiencies.

In its attempt to establish repeatable test conditions for characterizing the converter-fed motor losses, the IEC/TS 60034-2-3 introduces the concept of *additional harmonic losses*. However, its limitation to the motor rated voltage and frequency condition has been identified as one of its main drawbacks. In addition, other technical issues as reported in [11]-[14] include challenges in the avoidance of overmodulation, lack of explicit guidance on no-load modulation technique and dead-time compensation.

Although a few studies have attempted to address the aforementioned challenges, only the direct (input-output) efficiency estimation method has been reported in [90]-[91]. The few studies that include loss segregation method [92]-[93] have barely reported on the harmonic losses, citing a lack of scientific methods for separating the no-load losses (core and mechanical losses). Therefore, the determination of converter-fed motor losses and operating efficiencies for variable frequency applications remains a challenging area for researchers to explore further.

Chapter 3

The Chicken Swarm Optimization (CSO) Technique

3.1 Overview

This chapter presents the theoretical background as well as the mathematical formulations of the chicken CSO algorithm. In addition, the chapter justifies the selection of the CSO method in this research over other optimization methods for solving the induction machine equivalent circuit parameter estimation problem. Validation of the CSO method compared to other methods is provided.

3.2 Introduction

The application of Swarm Intelligence (SI) in developing new optimization algorithms for solving several real-world optimization problems have continued to attract substantial research interest in recent times [94]-[95]. New algorithms that are inspired by the collective social behaviour of certain species of insects or animals in nature are still emerging. Examples are: Firefly Optimization Algorithm (FFA) [96], Cockroach

Swarm Optimization (CCS) [97], Cuckoo Search (CS) [98], Artificial Bee Colony (ABC) Optimization [99], Bat Algorithm (BA) [100], Chicken Swarm Optimization (CSO) [69] and many more.

3.3 The CSO Algorithm

The CSO technique is inspired by the intelligent foraging behaviour of chickens in a swarm. Through an extensive experimental study presented in [69], it has been shown that the CSO algorithm has demonstrated superior performance in terms of both accuracy and robustness of the optimization results when compared to other popular optimization methods. This can be attributed to the following reasons:

(i) The CSO algorithm inherits the most important advantages of several optimization algorithms. A clear demonstration of this is given in section 3.4 which conforms with what is presented in [69]-[70].

(ii) In the CSO, the motions of the chickens and the cooperation between multiple groups in the chicken swarm are governed by several distinct laws. Thus, the CSO can be viewed as a multi-swarm algorithm, hence the algorithms can more effectively explore the search space than single swarm algorithms.

(iii) While the CSO operates with groups in a swarm, the algorithm still maintains a team. Hence it can effectively strike a balance between exploration and exploitation of the search space.

Although the CSO algorithm is developed based on idealized chicken behavior, it is important to understand some basic biological characteristics that define the chickens' intelligent behavior.

3.3.1 Biological Characteristics of Chickens

Chickens are one of the most widely kept domestic animals, primarily to serve as a food source. They live together in swarms or flocks and communicate using distinct sounds. Over 30 different sounds including crackles, clucks and chirps have been identified for

information relating to nesting, food discovery, mating and warning of danger [69]. Generally, chickens are capable of learning by experience and through trial and error.

In a swarm, the chickens establish hierarchal order with the stout chickens dominating the weaker ones to remain close to the head rooster, while the more passive chickens stay near the border of the flock. Adding or removing chickens in a swarm will temporarily disturb the prevailing hierarchal order to a new one [70]. This is particularly useful to cover for situations where some chickens have died, or the chicks have grown up to become hens or roosters, some mother hens have hatched new chicks and so on.

The chickens in a group try to maintain their territory and prevent invasions by other chickens from a different group. While the hens can be gracious to their chicks by calling them whenever a food source is discovered, the roosters also share this gracious behavior towards the members of its group [69]. Although chickens generally work as a team when foraging, they do compete in a specific hierarchal order which depend on the attributes of a group such as the size, gender and age.

3.3.2 Assumptions for Developing the CSO Algorithm

The CSO algorithm is developed to mimic the intelligent features exhibited by chickens in nature as highlighted above. For the sake of simplicity, the following assumptions have been made in developing the CSO algorithm [69]:

(i) Each swarm group is headed by a dominant roaster and followed by some hens and chicks.

(ii) Grouping and the hierarchy (roosters, hens and chicks) in a swarm is determined by the individual chicken's fitness value. The chickens with the best fitness values are classified as roosters, each heading a specific group in the swarm while those chickens with the worst fitness values are classified as chicks. The remaining chickens in the group are regarded as the hens.

(iii) The hens randomly decide which group to follow and the mother-child relationship between the hens and chicks is also randomly decided.

(iv) The hierarchal order in a group will remain unaffected and is only updated after a specified number of trails defined by a constant number (G).

(v) Chickens follow their head rooster in search of food, while the chicks search for food around their mother (a hen). Chickens in a group prevent others from eating their food and also tries to snatch food from others. Dominant individuals have an advantage in competition for the food source.

3.3.3 Mathematical Formulation of the CSO Algorithm

Firstly, the CSO algorithm is formulated by defining the positions of each individual chicken in the swarm. If *RN*, *HN*, *CN* and *MN* represent the number of roosters, hens, chicks and mother hens respectively, then, all *N* virtual chickens are defined by their positions $x_{i,j}^{t}$ $(i \in [1,2,3,\dots,N], j \in [1,2,3,\dots,D])$ at time *t*. where *N* is the total population of chickens in the swarm and *D* is the dimension or boundary within which the chickens search for food.

The roosters with better fitness value can search for food in a wider range than those with the worst fitness values. This is defined by the position equation (3.1)-(3.2) [69].

$$x_{i,j}^{t+1} = x_{i,j}^{t} * \left(1 + Randn(0, \sigma^2)\right) \tag{3.1}$$

$$\sigma^2 = \begin{cases} 1, & if \quad f_i \leq f_k \\ exp\left(\dfrac{f_k - f_i}{|f_i| + \varepsilon}\right), & otherwise \end{cases} \tag{3.2}$$

Where $k \in [1, N], k \neq i$, $Randn(0, \sigma^2)$ is a Gaussian distribution with mean 0 and standard deviation σ^2, ε is the smallest constant used to avoid zero division, k is the rooster's index and f is the fitness value.

For the hens, the dominant would have more advantage in competing for food than the passive ones. This can be formulated as shown in (3.3)-(3.5) [69]:

$$x_{i,j}^{t+1} = x_{i,j}^{t} + S1 * Rand[0,1] * \left(x_{r1,j}^{t} - x_{i,j}^{t}\right) + S2 * Rand[0,1] * \left(x_{r2,j}^{t} - x_{i,j}^{t}\right) \quad (3.3)$$

$$S1 = exp\left(\frac{f_i - f_{r1}}{abs(f_i) + \varepsilon}\right) \quad (3.4)$$

$$S2 = exp(f_{r2} - f_i) \quad (3.5)$$

Where $r1 \in [1,2,3,\ldots,N]$ is the rooster's index in the i^{th} group, while $r2 \in [1,2,3,\ldots,N]$ is the index of chicken (rooster or hen) randomly chosen from the swarm, but $r1 \neq r2$.

The chicks forage for food around their mother. This feature is formulated by (3.6) [69].

$$x_{i,j}^{t+1} = x_{i,j}^{t} + FL * \left(x_{m,j}^{t} - x_{i,j}^{t}\right) \quad (3.6)$$

Where $x_{m,j}^{t}$ is the position of the i^{th} chick's mother ($m \in [1,N]$). The parameter $FL(FL \in [0,2])$ is randomly chosen to determine the distance of the chick from its mother.

The six parameters: *RN*, *HN*, *CN*, *MN*, *G and FL* must be correctly specified in the CSO algorithm. This process must be guided by the following assumptions:

(i) The value of *HN* is usually bigger than *RN*. This is because of the fact that the hens are more beneficial to keep than roosters.
(ii) *HN* is also greater than *MN* because hens do not lay eggs and hatch at the same time.
(iii) The number of adult chickens in a swarm is usually higher than the number of chicks.

As suggested in [69], $RN = 0.2N, HN = 0.6N, CN = N - RN - HN, MN = 0.1N$ generally work well for most optimization problems. However, the selection of the appropriate value for *G* is problem specific. If *G* is very large, the convergence rate of

the algorithm becomes slow while very small value may result in the algorithm converging to a local optimal solution. Generally, it is recommended that $G \in [2, 20]$ and $FL \in [0.4, 1]$ may give good results for most problems [69]. Fig. 3.1 shows the flow chart of the CSO algorithm.

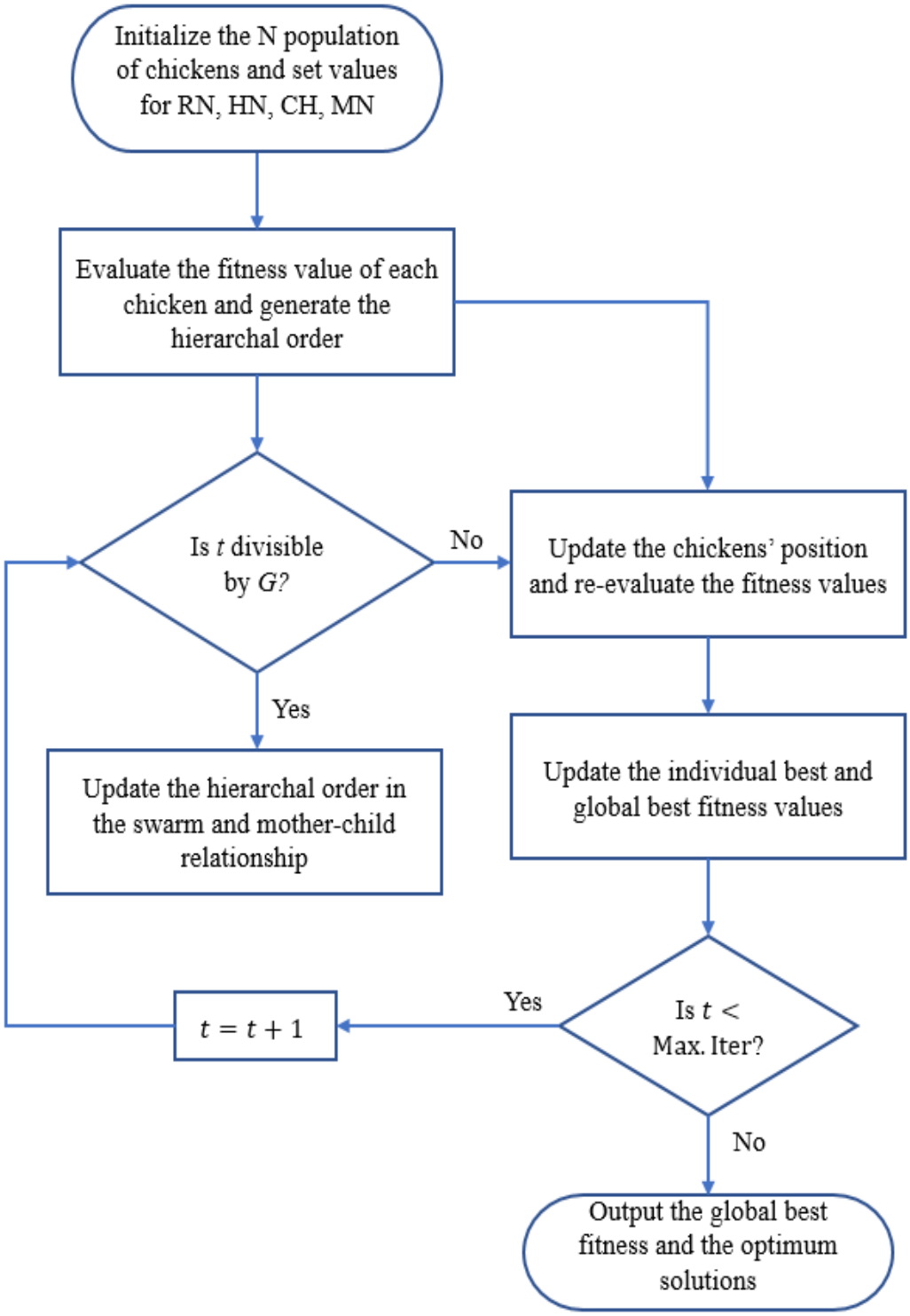

Fig. 3.1. Flow chart of the CSO algorithm

3.4 Validation and Comparison of the CSO to Other Algorithms

Although the superiority of the CSO algorithm over most popular optimization algorithms has been accented in literature [69], [70], nonetheless, it is important to validate this assertion by way of comparison to some selected algorithms using benchmark test functions. Five popular test functions are selected as shown in Table 3.1 [101]. Performance of the CSO is compared to that of Particle Swarm Optimization (PSO), Differential Evolution (DE), Artificial Bee Colony (ABC) optimization algorithm and Genetic Algorithm (GA).

TABLE 3.1

THE SELECTED BENCHMARK TEST FUNCTIONS

S/N	Function	Formula	Bounds	Global Optimum
1	Sphere	$f(x) = \sum_{i=1}^{d} x_i^2$	$x_i \epsilon [-5.12, 5.12]$	$f(x^*) = 0$ at $x^* = 0$
2	Rastrigin	$f(x) = 10d + \sum_{i=1}^{d} [x_i^2 - 10\cos(2\pi x_i]$	$x_i \epsilon [-5, 10]$	$f(x^*) = 0$ at $x^* = 0$
3	Ackley	$f(x) = -20exp\left(-0.2\sqrt{\frac{1}{d}\sum_{i=1}^{d} x_i^2}\right) - exp\left(\frac{1}{d}\sum_{i=1}^{d}\cos(2\pi) + 20 + \exp(1)\right)$	$x_i \epsilon [-32, 32]$	$f(x^*) = 0$ at $x^* = 0$
4	Rosenbrock	$f(x) = \sum_{i=1}^{d-1} [100(x_{i+1} - x_i^2)^2 + (x_i - 1)^2]$	$x_i \epsilon [-5, 10]$	$f(x^*) = 0$ at $x^* = 1$
5	Griewank	$f(x) = \sum_{i=1}^{d} \frac{x_i^2}{4000} - \prod_{i=1}^{d} cos\left(\frac{x_i}{\sqrt{i}}\right) + 1$	$x_i \epsilon [-600, 600]$	$f(x^*) = 0$ at $x^* = 0$

In order to guarantee a fair comparison, all commonly used parameters such as the problem dimensions, the population size and the maximum number of iterations are set

to be the same for all the tested algorithms. The common parameters for the five algorithms in testing all the benchmark test functions are set as follows:

Population size = 100

Maximum number of iterations = 100

Problem dimensions = 10

Other default settings for specific parameters of the different optimization algorithms are shown in Table 3.2

TABLE 3.2

PARAMETER SETTINGS FOR THE OPTIMIZATION ALGORITHMS

Algorithm	**Parameters**
CSO	$RN = 0.2N, HN = 0.6N, CN = N - RN - HN,$ $MN = 0.1N, G = 10, FL\epsilon[0.5,0.9]$
PSO	$C1 = C2 = 1.5, w = 0.7$
ABC	$CS = 100, L = 500$
DE	$CR = 0.9, F = 0.6$
GA	$Pc = 0.85, Pm = 0.01, Er = 0.05$

Performances and validations of the optimization algorithms are realized by comparing the convergence profiles of the benchmark test functions for each of the optimization algorithms. The results obtained are shown in Fig. 3.2 to 3.6.

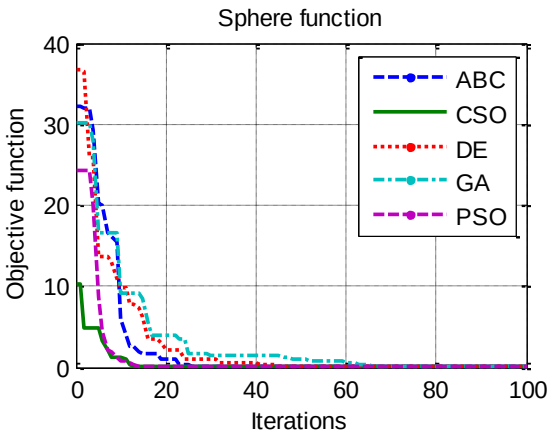

Fig. 3.2. Sphere function minimization

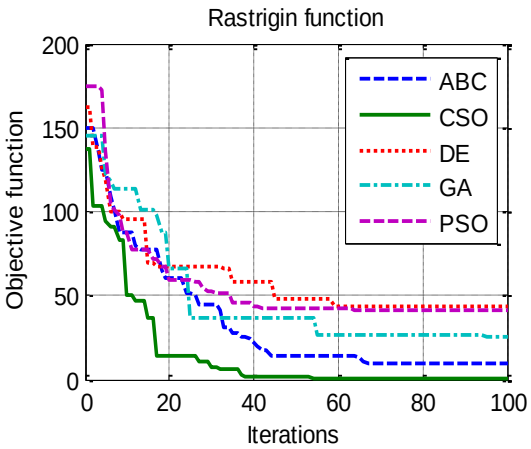

Fig. 3.3. Rastrigin function minimization

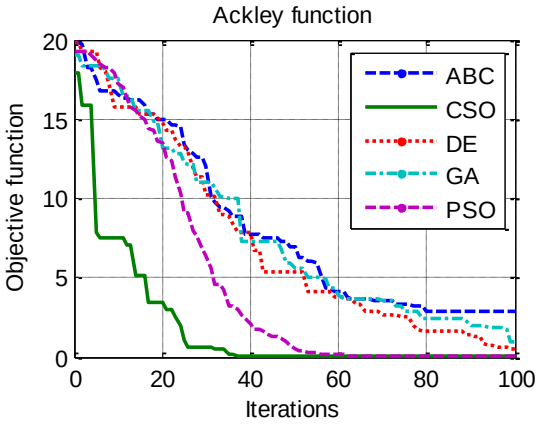

Fig. 3.4. Ackley function minimization

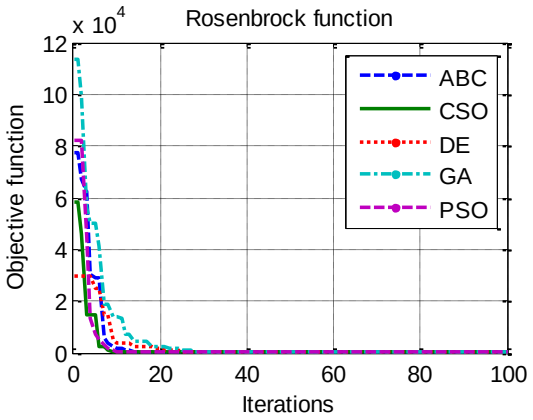

Fig. 3.5. Rosenbrock function minimization

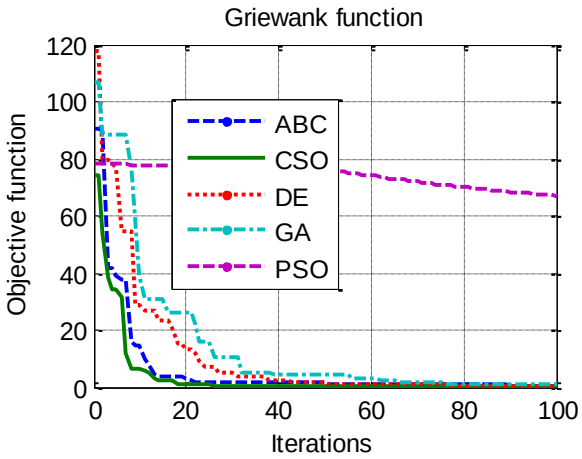

Fig. 3.6. Griewank function minimization

It can be observed that the CSO algorithm converges faster and gives more optimal search results for all the benchmark test functions when compared to the ABC, DE, PSO and GA algorithms. Furthermore, an in-depth statistical analysis on thirty independent test trials has been performed for each of the five optimization algorithms to assess the repeatability, robustness and accuracy of each algorithm. A summary of the statistical results is presented in Table 3.3. For the sake of clarity, these results are also represented in bar chart graphs as depicted in Fig. 3.7 to 3.11.

TABLE 3.3

STATISTICAL RESULTS OF DIFFERENT OPTIMIZATION ALGORITHMS

Benchmark Function	Algorithm	Best	Mean	Worst	Std.
Sphere	ABC	4.1E-06	3.33E-05	6.6E-05	2.25E-05
	CSO	**7.4E-15**	**7.85E-14**	**5.7E-13**	**1.64E-13**
	DE	0.00026	0.00055	0.001	0.00020
	GA	0.00258	0.00551	0.00954	0.00201
	PSO	2.2E-07	5.87E-06	2.2E-05	7.09E-06
Rastrigin	ABC	1.09422	1.83486	3.90603	0.81825
	CSO	**8.1E-13**	**5.01E-09**	**2E-08**	**7.22E-09**
	DE	31.4606	37.4876	43.5871	3.83790
	GA	16.5433	24.34897	30.0911	3.78228
	PSO	17.91	22.68926	28.8554	3.55366
Ackley	ABC	0.49923	0.81396	1.42109	0.29655
	CSO	**3.6E-08**	**2.06E-07**	**4.6E-07**	**1.19E-07**
	DE	0.25166	0.50545	0.7927	0.16443
	GA	0.46548	0.76694	1.95109	0.40523
	PSO	0.01124	0.25676	1.15535	0.44966
Rosenbrock	ABC	0.78467	4.55581	8.72835	2.75217
	CSO	**1.00135**	**1.18404**	**1.46916**	**0.12140**
	DE	7.10631	8.07292	8.91641	0.59306
	GA	6.04931	8.09573	9.40239	6.04931
	PSO	0.13319	4.46039	8.82567	2.78322
Griewank	ABC	0.06113	0.14688	0.24817	0.04820
	CSO	**2.8E-10**	**2.56E-07**	**2E-06**	**5.88E-07**
	DE	0.53174	0.68562	0.74312	0.05842
	GA	0.54211	0.77932	1.31805	0.21525
	PSO	75.1524	90.89927	116.416	11.54569

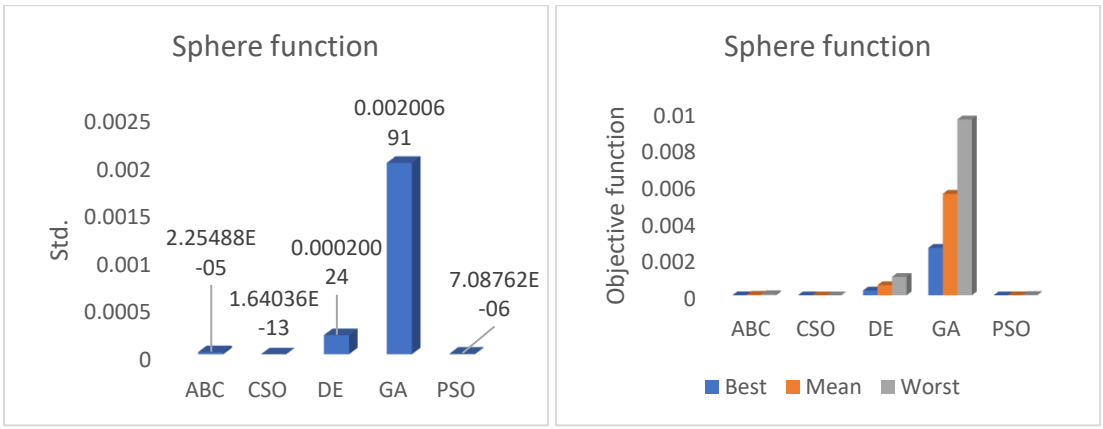

(a) (b)

Fig. 3.7. Sphere function statistical results (a) Standard deviation (b) Objective function convergence

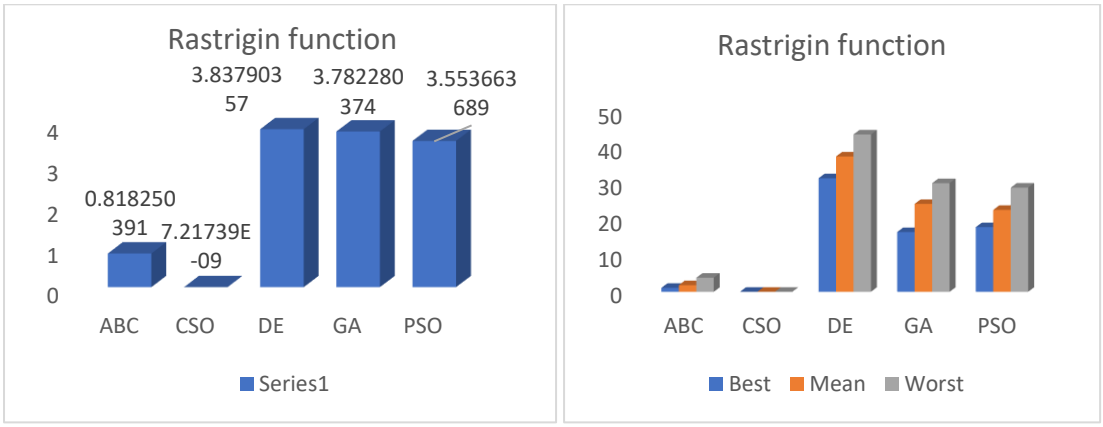

(a) (b)

Fig. 3.8. Rastrigin function statistical results (a) Standard deviation (b) Objective function convergence

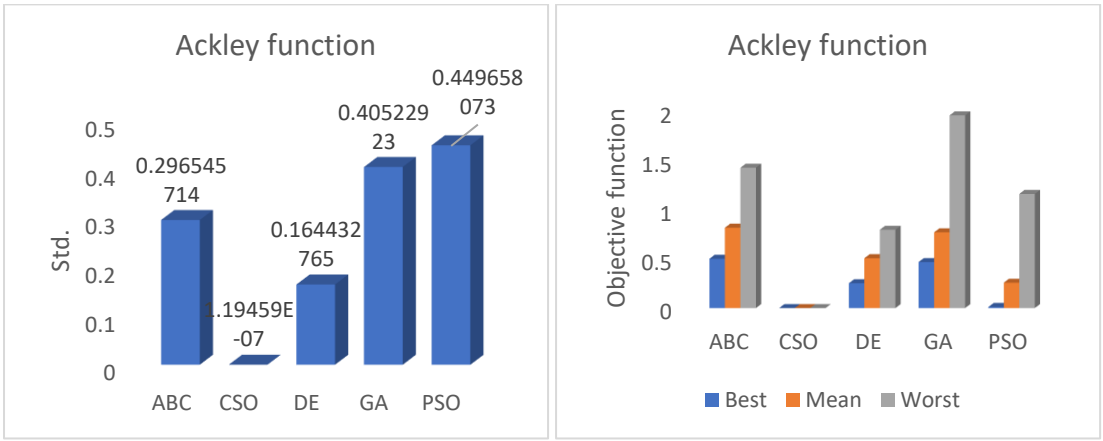

(a) (b)

Fig. 3.9. Ackley function statistical results (a) Standard deviation (b) Objective function convergence

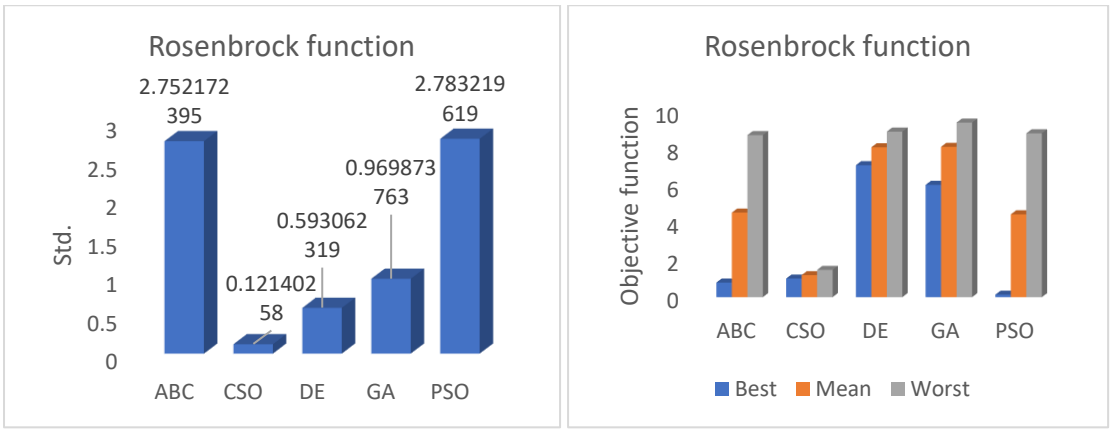

(a) (b)

Fig. 3.10. Rosenbrock function statistical results (a) Standard deviation (b) Objective function convergence

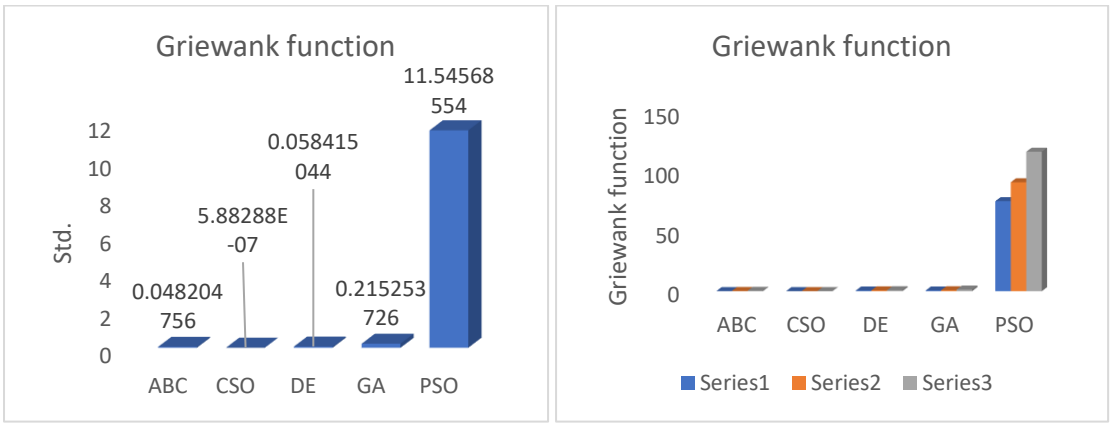

Fig. 3.11. Griewank function statistical results (a) Standard deviation (b) Objective function convergence

These results further strengthen the earlier observations and also provide more credence to the conclusions found in [69] and [70] that the CSO generally has some advantage in terms of accuracy, repeatability, robustness and faster convergence rate than most popular optimization algorithms. These conclusions should be the case since the following observations can be made with regards to the CSO algorithm [69]:

(i) If we consider the case in which $RN = CN = 0$ and assume $S1$ and $S2$ to be comparable to the $c1$ and $c2$ parameters in standard PSO algorithm. Then, the CSO inherits the advantages in the PSO algorithm.

(ii) If we consider the case in which $RN = MN = 0$, then CSO essentially performs like the basic mutation scheme of the DE algorithm.

(iii) If we set $RN = CN = 0$, then the CSO becomes similar to the basic ABC algorithm.

3.5 Conclusion

In this chapter, the performance of the CSO is compared to that of ABC, DE, GA and PSO optimization algorithms using five popular benchmark test functions. It has been shown that the CSO algorithm outperformed the ABC, DE, GA and PSO algorithms in terms of accuracy, robustness and convergence speed in all the test functions. The main reason for the outstanding performance of the CSO is that the chickens' diverse movements can be effectively utilized to strike a balance between exploration and exploitation of the search space. Moreover, the CSO can be regarded as a multi-swarm algorithm in which the individual chickens can work as a team by establishing a hierarchical order among the diverse chicken groups.

Although the CSO algorithm has not been used in literature for parameter estimation of induction motors, it is chosen in this research due to its impressive performance as clearly demonstrated in this chapter and in also, the conclusions drawn from other works in literature [69]-[70].

Chapter 4

Development of a Simplified Nonintrusive Induction Motor Field Efficiency Estimation Method

4.1 Overview

In this chapter, a new method is presented for induction motor field efficiency estimation. The method is based on the equivalent circuit approach in which a modified inverse Γ-model equivalent circuit with series core loss arrangement is used to mitigate the inherent problems of higher computational burden and parameter redundancy in the conventional method. Limited terminal measurements and motor nameplate data are required; hence the proposed method could serve as a suitable alternative for IM field efficiency determination.

In addition, a robust bio-inspired optimization algorithm known as Chicken Swarm Optimization (CSO) is used for the first time to accurately estimate the induction motor equivalent circuit parameters, as discussed previously. Due to the difficulty of estimating the core loss using the conventional equivalent circuit method, a new method is presented for specifying good initial boundary range for the core loss resistance. This will guarantee the convergence of the core loss resistance to a consistent value regardless of the initial value decided by the CSO. Furthermore, a new method is presented for estimating the friction and windage loss. The method relies on the well-known Airgap Torque (AGT) equation and some nameplate data to estimate the losses not accounted for by the motor equivalent circuit.

The main contribution of the proposed method is the use of a simplified inverse Γ-model EC to accurately determine the induction motor parameters and hence its losses and efficiency using only limited measurements of motor terminal quantities at a single load point. The proposed method referred to in this work as the "Nonintrusive Field Efficiency Estimation" (NFEE) technique is validated for the case of a balance voltage supply (CASE 1) and an unbalanced voltage supply condition (CASE 2). The validation for CASE 1 is accomplished through several experimental tests on four different induction motors by comparing the estimated efficiencies and the individual loss components to the IEEE Std. 112 and the IEC 60034-2-1 standard loss segregation methods. For CASE 2, the estimated efficiencies are compared to the direct (input-output) measurement method. Finally, repeatability analysis, sensitivity and error analysis are performed to assess the accuracy of the proposed NFEE method.

4.2 Introduction

Although several methods have been considered in literature for IM efficiency estimation, the equivalent circuit approach has been identified amongst the best methods for field efficiency estimation [28] owing to its advantages over other methods; some of which include:

(i) The ability to estimate the efficiency of an IM for any desired loading condition in addition to the condition under which measurements are taken.
(ii) Predicting IM efficiency in the absence of the load varying test. This is useful in the case of large induction motors where testing under full-load or locked rotor condition may not be attainable due to the high-power requirements.

An example of the equivalent circuit method is the Method F1 of the IEEE Std. 112. In this method, the motor parameters are estimated by performing a no-load test and an impedance test. While this method is quite accurate, it is still considered too intrusive for routine field efficiency test [23]. Several optimization approaches to predict the motor EC parameters and efficiency relying only on external measurements of motor terminal voltages, currents and shaft speed have been proposed [62]-[65]. However, some challenges may arise when using these methods for field efficiency estimation. These challenges include:

(i) Outputs of the conventional T-model equivalent circuit may fit to experimental data even if the motor parameters are incorrectly estimated. This leads to an infinite set of solutions for the same set of input/output measurements.
(ii) Large deviations in the estimation of the core loss resistance which may result in inconsistent core loss calculations.
(iii) The requirement for test measurements under several operating scenarios for motor parameter estimation. Taking these measurements to the field may be difficult without causing interruptions to the operations of the motor.

Specifically, on the parameter identification problem, it has been shown that some parameters of the conventional T-model EC are not uniquely identifiable using external measurements [42], [102]-[103]. This non-identifiability is related to the structure of the model itself and arises due to the presence of redundant elements (parameters) within the model. Hence, it is possible to obtain different sets of solutions representing the motor EC parameters regardless of the quality of measurements or optimization algorithms used [42]. While different methods have been proposed to tackle this

problem, these methods are mostly not suitable for field applications because of the substantial time required to take measurements under different loading conditions [62]-[63] or are less reliable because some parameters are held constant to limit the number of unknown variables [64].

Alternatively, models with different structures such as the Γ and inverse Γ-model have been proposed to address the non-identifiability issues [102]. These models are a simplified representation of the conventional T-model with no loss of information or accuracy [103].

4.3 The Induction Motor Steady-state Model

The voltage equations of an induction motor in the *dq* axis synchronous reference frame considering the core loss resistance, can be represented as shown in (4.1) – (4.3).

$$\vec{v}_{sdq} = \vec{\imath}_{sdq}R_s + L_{ls}\frac{d\vec{\imath}_{sdq}}{dt} + L_m\frac{d\vec{\imath}_{mdq}}{dt} + \mathrm{j}\omega_s L_{ls}\vec{\imath}_{sdq} + j\omega_s L_m\vec{\imath}_{mdq} \tag{4.1}$$

$$\vec{v}_{rdq} = \vec{\imath}_{rdq}R_r + L_{lr}\frac{d\vec{\imath}_{rdq}}{dt} + L_m\frac{d\vec{\imath}_{mdq}}{dt} + \mathrm{j}\omega_{sl} L_{lr}\vec{\imath}_{rdq} + \mathrm{j}\omega_{sl} L_m\vec{\imath}_{mdq} \tag{4.2}$$

$$\vec{\imath}_{sdq} + \vec{\imath}_{rdq} = \left(\frac{L_m}{R_{fe}}\right)\left(\frac{d\vec{\imath}_{mdq}}{dt} + \mathrm{j}\omega_s\vec{\imath}_{mdq}\right) + \quad \vec{\imath}_{mdq} \tag{4.3}$$

Where: $\vec{v}_{sdq}$ and $\vec{\imath}_{sdq}$, are the *dq* axis stator voltage and current space vectors respectively, R_s is the stator winding resistance, $\vec{v}_{rdq}$ and $\vec{\imath}_{rdq}$ are the rotor voltage and current space vectors respectively, $\vec{\imath}_{mdq}$ is the magnetization current space vector.

Based on (4.1) – (4.3), the dynamic equivalent circuit of an induction motor in the synchronous reference frame can be represented as shown in Fig. 4.1.

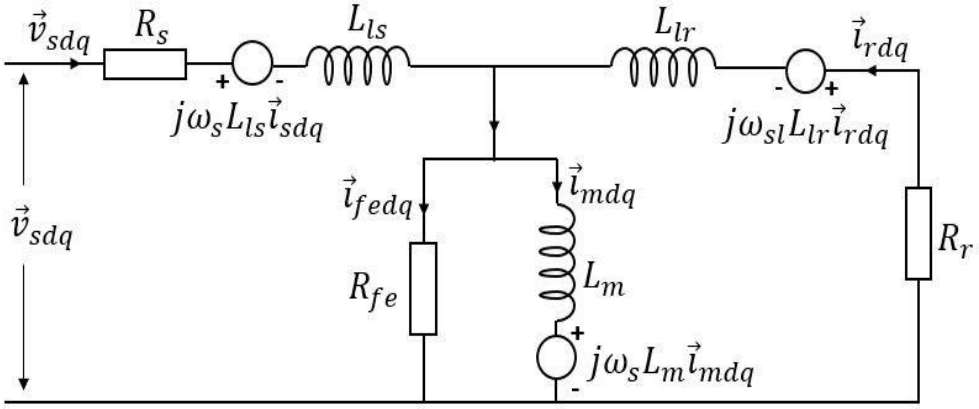

Fig. 4.1: *dq* equivalent circuit with parallel core loss resistance

The core loss resistance as represented in (4.3) introduces two extra state variables to the induction motor model. In order to simplify this model, it is possible to reduce the order by transforming the parallel magnetization branch into a series arrangement and treating R_{fe} and L_m as frequency dependent impedance phasors [89]. Considering that the magnetizing current $\vec{\imath}_{mdq}$ can be assumed constant for speeds not exceeding the rated value, (4.3) can be simplified to give:

$$\vec{\imath}_{mdq} = \frac{R_{fe}\left(\vec{\imath}_{sdq} + \vec{\imath}_{rdq}\right)}{R_{fe} + \mathrm{j}\omega_s L_m} \tag{4.4}$$

In a balanced sinusoidal steady-state condition, the voltage equations for the series equivalent circuit can be derived by substituting (4.4) into (4.1) and (4.2) and simplifying.

$$\vec{v}_{sdq} = \vec{\imath}_{sdq}R_s + \mathrm{j}\omega_s L_{ls}\vec{\imath}_{sdq} + \left(\mathrm{j}\omega_s L_M + R_{sfe}\right)\left(\vec{\imath}_{sdq} + \vec{\imath}_{rdq}\right) \tag{4.5}$$

$$0 = \vec{\imath}_{rdq}R_r + \mathrm{j}\omega_{sl} L_{lr}\vec{\imath}_{rdq} + \left(\mathrm{j}\omega_{sl} L_M + R_{rfe}\right)\left(\vec{\imath}_{sdq} + \vec{\imath}_{rdq}\right) \tag{4.6}$$

Equations (4.5) and (4.6) corresponds to the following phasor equations:

$$V_s = I_s R_s + \mathrm{j}\omega_s L_{ls} I_s + \left(\mathrm{j}\omega_s L_M + R_{sfe}\right)\left(I_s + I_r\right) \tag{4.7}$$

$$0 = I_r R_r + \mathrm{j}\omega_{sl} L_{lr} I_r + \left(\mathrm{j}\omega_{sl} L_M + R_{rfe}\right)\left(I_s + I_r\right) \tag{4.8}$$

Where:

$$L_M = \frac{L_m R_{fe}^2}{R_{fe}^2 + \omega_s^2 L_m^2} \approx L_m \tag{4.9}$$

R_{sfe} and R_{rfe} represents the stator and rotor series core loss resistances respectively and are dependent on ω_s and ω_{sl} as expressed in (4.10) and (4.11) [89].

$$R_{sfe} = \frac{L_m^2 \omega_s^2 R_{fe}}{R_{fe}^2 + \omega_s^2 L_m^2} \approx \frac{L_m^2 \omega_s^2}{R_{fe}} \tag{4.10}$$

$$R_{rfe} = \frac{L_m^2 \omega_{sl} \omega_s R_{fe}}{R_{fe}^2 + \omega_s^2 L_m^2} \approx \frac{L_m^2 \omega_{sl} \omega_s}{R_{fe}} \tag{4.11}$$

Equations (4.7) and (4.8) combined corresponds to the per-phase T-model equivalent circuit with series core loss representation. Because of its complexity, this model can be simplified further by selecting an arbitrary 'turns ratio' value between the stator and the rotor circuits of the d-q model with the motor being operated with no voltage applied to the rotor (cage rotor type). However, for convenience, the following four cases for the choice of the turns ratio (α) could be made [104];

1. $L_s = \alpha^2 L_r$ or $\alpha = \left(\frac{L_s}{Lr}\right)^{1/2}$. This selection gives equal self-inductances and results in a model with equal leakage inductances ($L_{ls} = L_{lr}$).
2. $\alpha L_m = \alpha^2 L_r$ or $\alpha = \frac{L_M}{L_r}$. This selection yields equal mutual and rotor self inductances and results in a circuit model with all leakage inductances located in the stator.
3. $L_s = \alpha L_M$ or $\alpha = \frac{L_s}{L_M}$. This gives equal mutual and stator self inductance and results in a circuit model with all leakage inductances located in the rotor.
4. $\alpha = \frac{N_s}{N_r}$. This choice is based on the actual computation of the leakage inductances based on design.

Although Case 1 is often used when machine parameters are determined from laboratory test, the assumption of equal leakage inductances may not be generalized for

all induction motors. Case 4 requires machine design details to compute the actual leakage inductances. The circuit models resulting from Case 2 and 3 are simplified representation of the T-equivalent circuit but with only two inductances. While both circuits are particularly well suited for vector control systems, these models can provide solution to the unwanted parameter dependence in the motor per-phase equivalent circuit model [103].

Based on Case 2, the transformation equations between the parameters of the per-phase T-model and the inverse Γ-model are as follows [42], [105]:

$$\alpha = \frac{L_M}{L_r} \tag{4.12}$$

$$L'_{ls} = L_s - \alpha L_m \tag{4.13}$$

$$L'_M = \alpha L_M \tag{4.14}$$

$$R'_r = \alpha^2 R_r \tag{4.15}$$

Where: $L_s = L_{ls} + L_m$ and $L_r = L_{lr} + L_m$

Finally, the resulting simplified inverse Γ-model with series core loss arrangement is shown in Fig. 4.2. Where R_c is the total core loss in the motor which is represented by the sum of R_{sfe} and R_{rfe} and R_{sll} represents the stray-load loss.

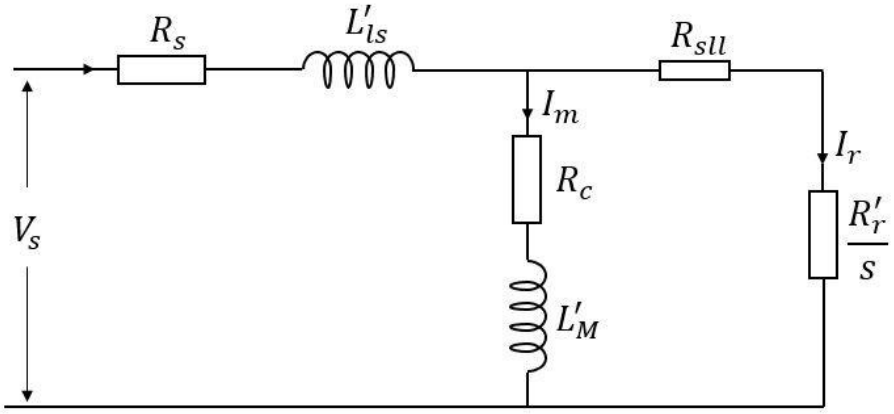

Fig. 4.2. Induction motor inverse Γ-model with series core loss resistance

For an induction motor fed by an unbalanced voltage supply, Fig. 4.2 can be decomposed into positive and negative sequence equivalent circuits as shown in Fig. 4.3.

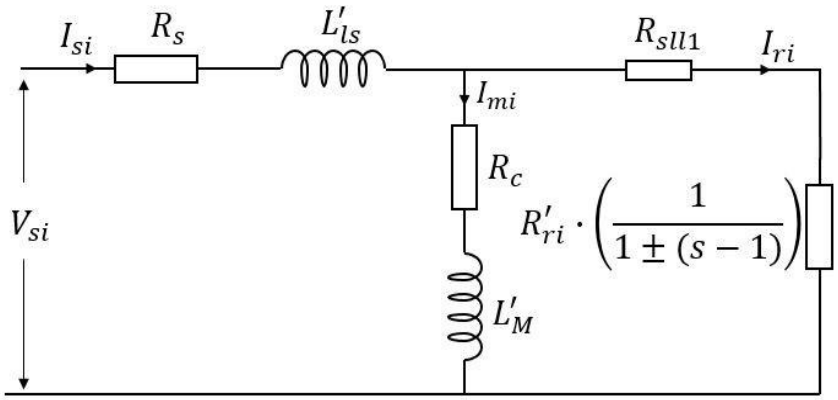

Fig. 4.3. Induction motor model fed with unbalanced supply voltages ($i = 1$ for positive sequence and $i = 2$ for negative sequence)

The stator and magnetization branch parameters are assumed to be constant for the positive and negative sequence equivalent circuits, while the rotor impedance is notably affected by skin effect due to the double frequency of the negative sequence field. Generally, skin effect causes an increase in the rotor bar resistance R'_r and a reduction in the rotor leakage inductance L_{lr} due to saturation of the leakage path [106]. Sine for the inverse Γ model, L_{lr} is transferred to the stator side, it is expected that the skin effect in this case, will cause a slight change in the stator leakage inductance L'_{ls}. However, considering that L_m is usually much larger than L_{lr} for induction motors, this impact can be ignored with marginal loss of accuracy. Moreover, in computing the efficiency, the sensitivity of L'_{ls} is quite small when compared to that of the rotor bar resistance R'_r. Therefore, in estimating the negative sequence EC parameters for the inverse Γ-model, it is assumed that only the rotor resistance is affected by skin effect due to unbalanced voltage supply. Since the stray-load loss is mainly produced by the positive sequence field, the stray-load resistance R_{sll} is only placed on the positive sequence equivalent circuit.

4.4 Identifiability Analysis

In literature, several mathematical models have been developed to represent the dynamic behaviour of the induction motor. For the parameter identification purpose, it is necessary to confirm if all the model parameters are identifiable. It has been shown that an infinite set of solutions may be obtained if a model is unidentifiable regardless of the quality of measurements and estimation algorithm utilized [42], [102]. This problem can be attributed to the presence of redundant elements in the model which not only contribute to the non-identifiability issues but also increases the computational burden [103]. Structural identifiability can be analysed experimentally or through simulations using the bond graph or the transfer function method [102].

The bond-graph method is a graphical approach to modelling in which components or elements of a model are connected by lines (bonds) to specify the transfer of energy [107]. The graphical nature of the bond graph method allows for visual characterization of a system to get an insight into its correctness [107]-[108]. For an electrical system, the bond graph can be constructed using the following concepts:

(i) Signals: are represented by the energy source (SE) (voltage) and the flow source (SF) (current).

(ii) Elements: are represented by the electrical components (R, L and C).

(iii) Bond: represents the connection between the component ports in a system and show the exchange of energy at a given junction.

(iv) Junction: indicates how component are connected in a system (model). 1-junction represents a series connection while 0-junction represents a parallel connection.

(v) Causality: this indicates the direction of energy or power flow in a system. In each bond, causality is represented by a stroke (bar). The rule for proper causal assignment is such that, only one bond imposes a flow on each 1-junction. Similarly, only one bond must impose an effort on each 0-junction [107].

The authors in [42] and [102] have analysed the structural identifiability of different induction motor models through experimental and bond graph approach respectively. However, none of the models analysed considers the core loss resistance in the analysis. As shown in Fig. 4.4, the constructed bond graph of the conventional T-model with parallel core loss arrangement indicates two causality conflicts due to the presence of redundant energy storage components associated with the leakage reactances and magnetization branch. Also, the bond graph for the T-model with series core loss arrangement as shown in Fig. 4.5 indicates one causality conflict due to the leakage reactances. Thus, these conflicts clearly indicate the difficulty in estimating the two leakage reactances separately.

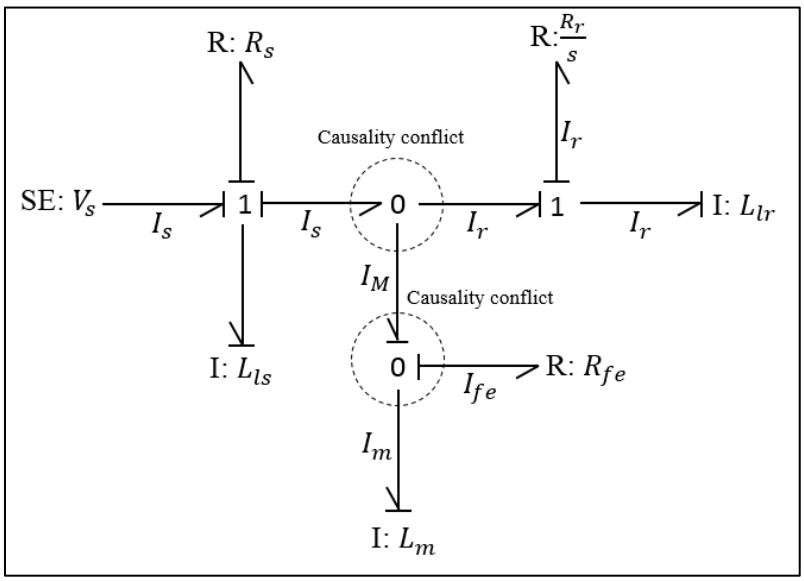

Fig. 4.4. T-Model bond graph with parallel core loss resistance

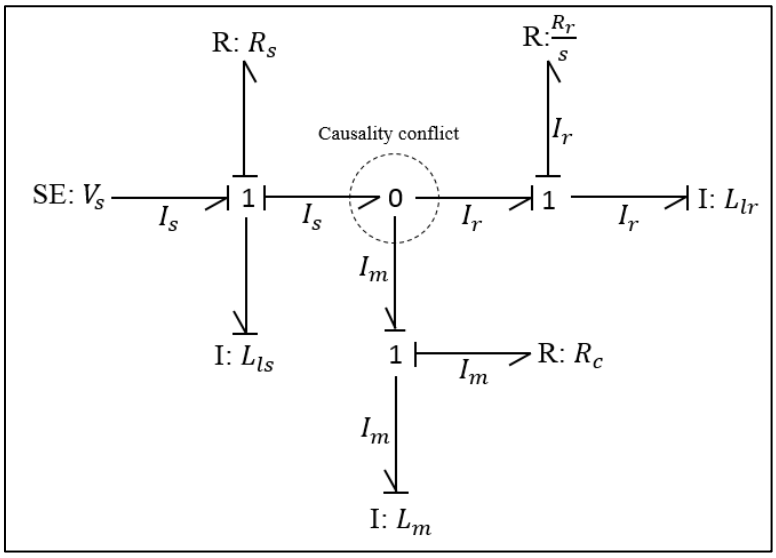

Fig. 4.5. T-Model bond graph with series core loss resistance

To resolve this problem, alternative models with different model structures such as the Γ and inverse Γ-model have been considered. In these models, the stator and rotor leakage reactances are combined into an equivalent leakage reactance. For the inverse Γ-model, the equivalent leakage reactance is placed on the stator side as reported in Fig. 4.2 and the corresponding bond graphs for this model along with that of the Γ-model are shown in Fig. 4.6 and 4.7 respectively. As can be observed, proper bond graphs are obtained with no causality conflicts. Therefore, it can be concluded that no redundant parameters are present in these models. All parameters can therefore, be accurately identified using external measurements.

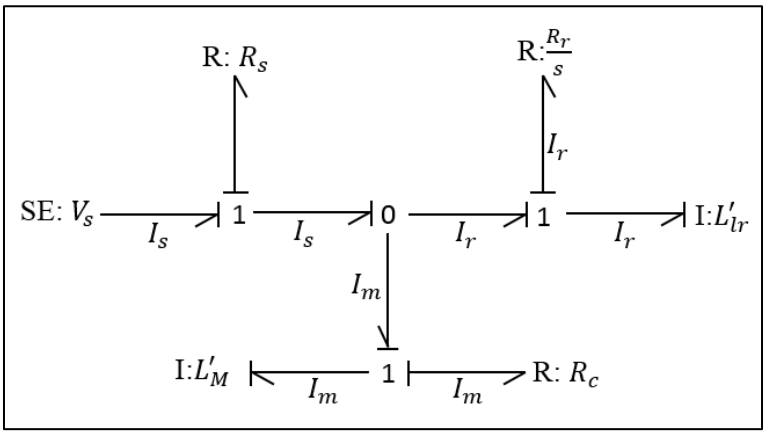

Fig. 4.6. Γ model bond graph with series core loss resistance

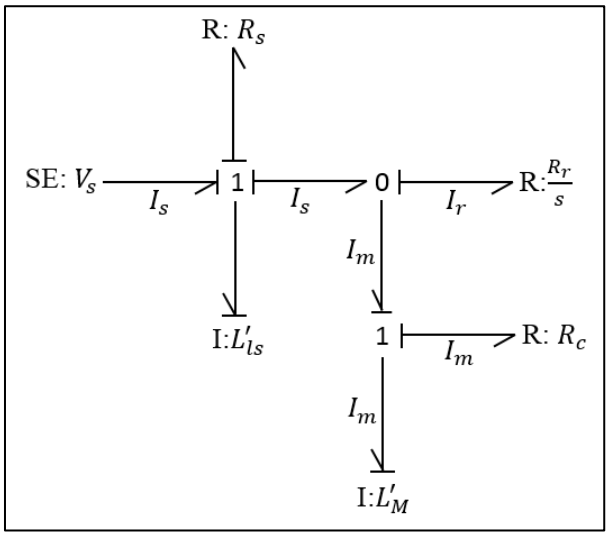

Fig. 4.7. Inverse Γ-model bond graph with series core loss resistance

4.5 The Proposed Nonintrusive Field Efficiency Estimation Method

The proposed NFEE method adopts the IEEE Std. 112 Method F1 for calculating motor efficiency. It is well-known that accurate motor parameter identification is key in all EC-based efficiency estimation methods. For field efficiency tests, these parameters must be determined non-intrusively without the need for the no-load and blocked rotor test. Fig. 4.8 shows a complete flow chart of the proposed NFEE method. The method has the advantage that the shaft speed, EC parameters and hence the motor efficiency can be determined using only one single load point measurement of the motor terminal quantities (voltages and currents).

For calculating the friction and windage loss P_{fw}, the method most widely used in literature is the no-load test. In the absence of this test, an estimated value is normally used which may lead to inaccurate results. On the other hand, a variable load test is required for the indirect estimation of the motor stray-load loss which is clearly not intended for field efficiency test. Thus, in this research, a new method is proposed for calculating the friction and windage loss at any desired loading condition. The method as detailed in section 4.5.3 relies on the well-established airgap torque equation and the motor nameplate data.

The rotor speed is estimated using the machine current signature analysis (MCSA) to detect the speed-dependent harmonics contained in the stator line current. Detailed descriptions of the steps involved in developing the NFEE method are presented in the following subsections.

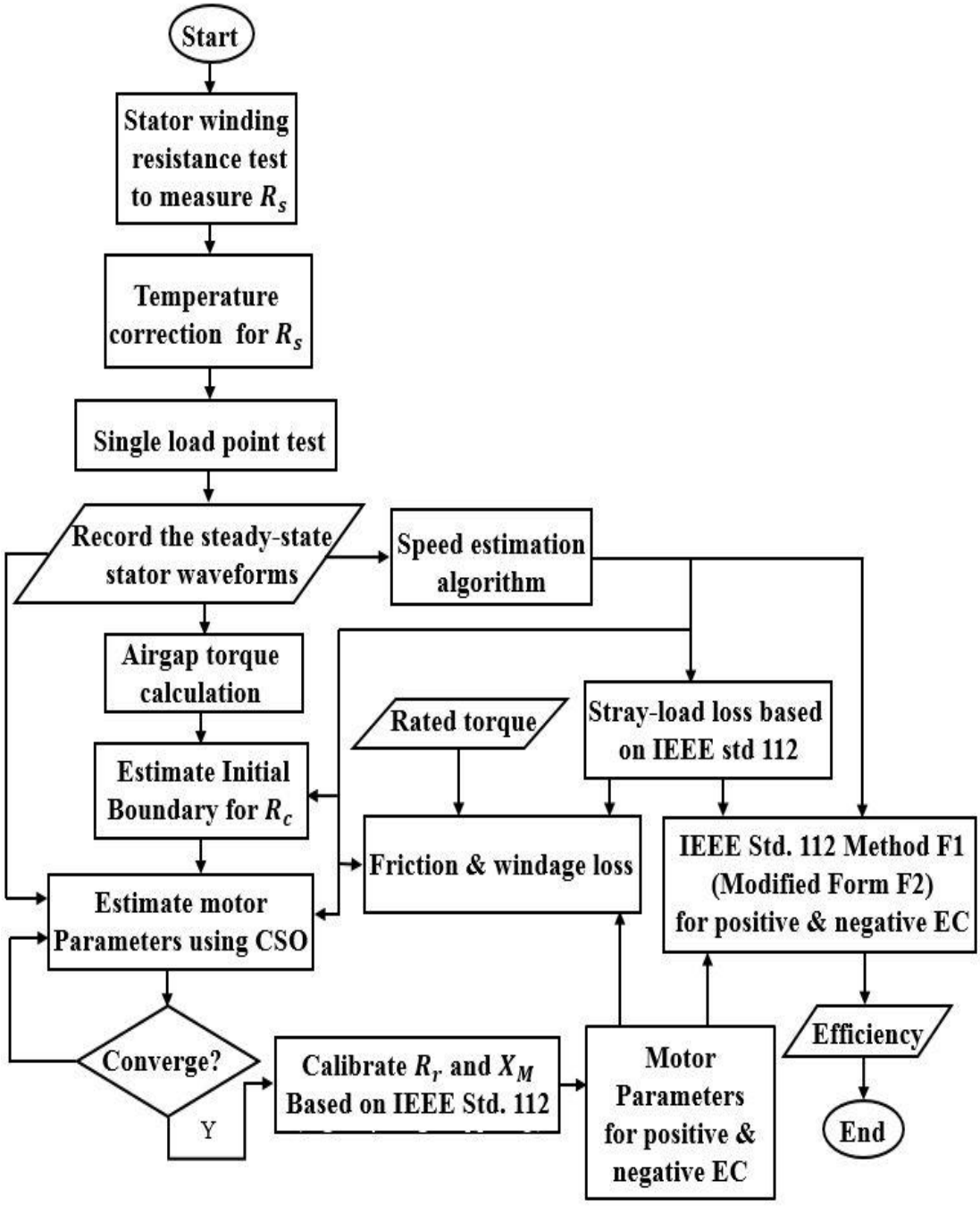

Fig. 4.8. Flow chart of the proposed NFEE method

4.5.1 Nonintrusive Speed Estimation

Majority of IM efficiency estimation methods require the rotor speed information. Although conventional speed measurements through direct shaft mounted sensors are quite accurate, the intrusion and cost involved are the major drawbacks. Conversely, sensorless speed estimation offers several advantages such as low cost, reduced hardware complexity and size, better noise immunity, increased reliability, and fewer maintenance requirements. Thus, several studies have focused on developing nonintrusive or sensorless speed estimation methods [109]-[120]. In general, the speed estimation methods can be classified into three, namely: rotor slot harmonics method, frequency signal injection method and machine model-based methods as shown in Fig. 4.9.

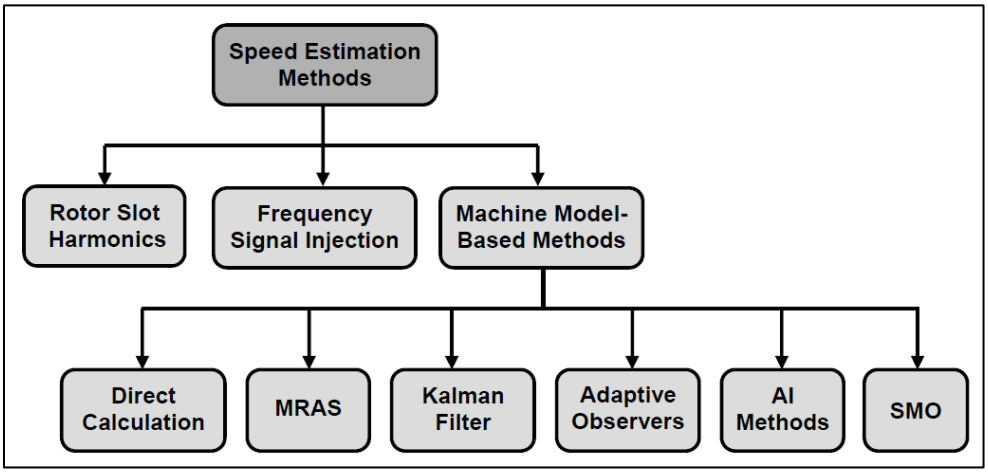

Fig. 4.9. Sensorless speed estimation methods [99]

In the frequency signal injection methods [115]-[117], a high frequency carrier signal is injected on the stator and the resulting dynamic response of the machine is analysed. Although these methods are generally independent of the motor parameters and allow speed estimation at low-speed operations, they, however, introduce in the machine significant torque and speed ripples [109].

In the machine model-based methods [109], [118]-[120], the rotor speed is expressed in terms of the machine's parameters and terminal variables. The machine model-based methods can be classified into the following three main groups depending on the

strategy used [109]: Direct calculation method (DCM), Model Reference Adaptive System (MRAS) and Kalman Filter Method (KFM). Although these methods are simple to implement, they do however depend on the detailed knowledge of the motor parameters and have poor performance in low-speed operation [109].

The rotor slot harmonics methods [63]-[64], [110] detects the speed-dependent rotor slotting and eccentricity harmonics in the stator current signal using digital signal processing (DSP) techniques. Fig. 4.10 shows an example of the line current spectrum of an inverter-fed motor [121].

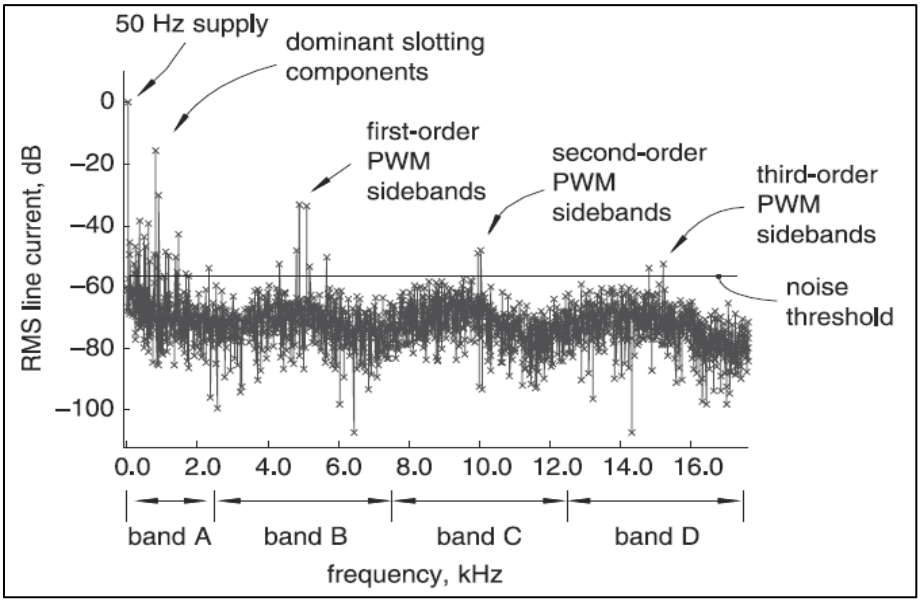

Fig. 4.10. Line current spectrum for an inverter-fed motor [121]

As shown in the figure, the rotor slotting components are the harmonics closest to the fundamental frequency. The frequency of the speed-dependent harmonics reflected in the stator current is given by (4.16) [110].

$$f_{sh} = f_1\left(1 \pm \frac{(1-s)}{p}\right) \tag{4.16}$$

Where f_1 is the fundamental frequency of the stator voltage, s is the slip and p is the number of pole pairs. As can be observed in (4.16), the speed-dependent harmonic

frequencies are independent of the machine structural parameters. Only the number of poles is needed to obtain the slip information. However, because the slot harmonic frequencies are very close to the fundamental harmonic component and have smaller amplitudes, these spectral components are very difficult to detect [112]. A nonlinear adaptive filter algorithm originally proposed in [122] is used to extract the main components (amplitude, frequency and phase angle) of the stator current signal. The residual current after the extraction is analysed using Fast Fourier Transform (FFT) to detect the speed-dependent frequency. The basic equations governing the nonlinear adaptive filter are expressed as follows [122].

Let $u(t)$ represent the stator current signal, and $y(t)$ given in (4.17) represents the sinusoidal component of $u(t)$.

$$y(t) = Asin(\omega t + \delta) \tag{4.17}$$

Where, $A, \omega \; and \; \delta$ are the amplitude, frequency and constant phase angle of $y(t)$ respectively.

Ideally, parameters $A, \omega \; and \; \delta$ are fixed quantities, however, in practice, this assumption does not hold true. $u(t)$ has a general form that can be represented by:

$$u(t) = \sum_{i=1}^{\infty} A_i sin(\omega_i t + \delta_i) + n(t) \tag{4.18}$$

Where $n(t)$ is the disturbance or noise signal.

Since the problem is to extract the main sinusoidal component in $u(t)$, then, it can be treated as a least-square optimization problem as expressed in (4.19)

$$(\hat{\theta}) = \underset{\theta(t) \in \phi}{arg\ min} \left[F_{obj}(\theta(t))\right] \tag{4.19}$$

Where $F_{obj}(\theta) = [u(t) - y(t, \theta(t))]^2$ is the error cost function, $\theta(t) = [A(t), \omega(t), \delta(t)]^T$ is the vector of parameters situated within the boundary space: $\phi = \{[A, \omega, \delta]^T |\ A \in [A_{min}, A_{max}], \omega \in [\omega_{min}, \omega_{max}], \delta \in [\delta_{min}, \delta_{max}]\}$

The parameter vector $\hat{\theta} = \left[\hat{A}(t), \hat{\omega}(t), \hat{\delta}(t)\right]^T$ is estimated using gradient descend method.

$$d\hat{\theta}(t) = -\mu \frac{\partial F_{obj}(\theta)}{\partial \theta(t)} \tag{4.20}$$

Where μ is a diagonal matrix of the algorithm's regulating constants as defined by (4.21). The values of μ control the convergence rate as well as the stability of the algorithm.

$$\mu = \begin{bmatrix} m_1 & 0 & 0 \\ 0 & m_2 & 0 \\ 0 & 0 & m_3 \end{bmatrix} \tag{4.21}$$

Thus, (4.20) can be represented as follows:

$$\begin{bmatrix} \frac{d\hat{A}(t)}{dt} \\ \frac{d\hat{\omega}(t)}{dt} \\ \frac{d\hat{\delta}(t)}{dt} \end{bmatrix} = \begin{bmatrix} m_1 & 0 & 0 \\ 0 & m_2 & 0 \\ 0 & 0 & m_3 \end{bmatrix} \begin{bmatrix} \frac{\partial}{\partial \hat{A}(t)} \left[u(t) - \hat{A}(t)\sin\left(\hat{\omega}(t)t + \hat{\delta}(t)\right)\right]^2 \\ \frac{\partial}{\partial \hat{\omega}(t)} \left[u(t) - \hat{A}(t)\sin\left(\hat{\omega}(t)t + \hat{\delta}(t)\right)\right]^2 \\ \frac{\partial}{\partial \hat{\delta}(t)} \left[u(t) - \hat{A}(t)\sin\left(\hat{\omega}(t)t + \hat{\delta}(t)\right)\right]^2 \end{bmatrix} \tag{4.22}$$

$$\frac{d\hat{A}(t)}{dt} = 2m_1 e(t) \sin\left(\hat{\omega}(t)t + \hat{\delta}(t)\right) \tag{4.23}$$

$$\frac{d\hat{\omega}(t)}{dt} = 2m_2 e(t)\, \hat{A}(t)\cos\left(\hat{\omega}(t)t + \hat{\delta}(t)\right) \tag{4.24}$$

$$\frac{d\hat{\delta}(t)}{dt} = 2m_3 e(t)\, \hat{A}(t)\cos\left(\hat{\omega}(t)t + \hat{\delta}(t)\right) \tag{4.25}$$

Where $e(t) = u(t) - \hat{A}(t) \sin\left(\hat{\omega}(t)t + \hat{\delta}(t)\right)$

A major trouble in (4.23) – (4.25) is the presence of the time variable t which implies that the response of the system to a given input signal varies depending on when the system is initialized [122]. To solve this problem, the time variable t is substituted by a constant number m_4. Hence, the resulting set of differential equation representing the nonlinear adaptive filter can then be represented as:

$$\frac{d\hat{A}(t)}{dt} = 2\mu_1 e(t) sin\hat{\varphi}(t) \tag{4.26}$$

$$\frac{d\hat{\omega}(t)}{dt} = 2\mu_2 e(t)\hat{A}(t) cos\hat{\varphi}(t) \tag{4.27}$$

$$\frac{d\hat{\varphi}(t)}{dt} = \hat{\omega}(t) + \mu_3 \frac{d\hat{\omega}(t)}{dt} \tag{4.28}$$

Where: $e(t) = u(t) - \hat{A}(t) sin\hat{\varphi}(t)$, $\hat{\varphi}(t) = \hat{\omega}(t)t + \hat{\delta}(t)$, $\mu_1, \mu_2 \; and \; \mu_3$ are constants values given by:

$$\mu_1 = m_1, \; \mu_2 = m_2 m_4, \mu_3 = m_4 + \frac{m_3}{m_2 m_4}$$

These values are chosen based on the following conditions:

$0 < \mu_1 < 2f_s$, $0 < \mu_2 < \left(\frac{2f_s}{A}\right)^2$, generally, μ_3 is chosen such that the product of $\mu_2\mu_3$ is of the same order of magnitude as μ_1 [122].

Fig. 4.11 shows the block diagram implementation of the filter. It can be observed that the upper branch represents the amplitude estimator, while the lower branch is for the frequency/phase estimator. However, these two branches are interdepended as shown by the cross-coupling lines.

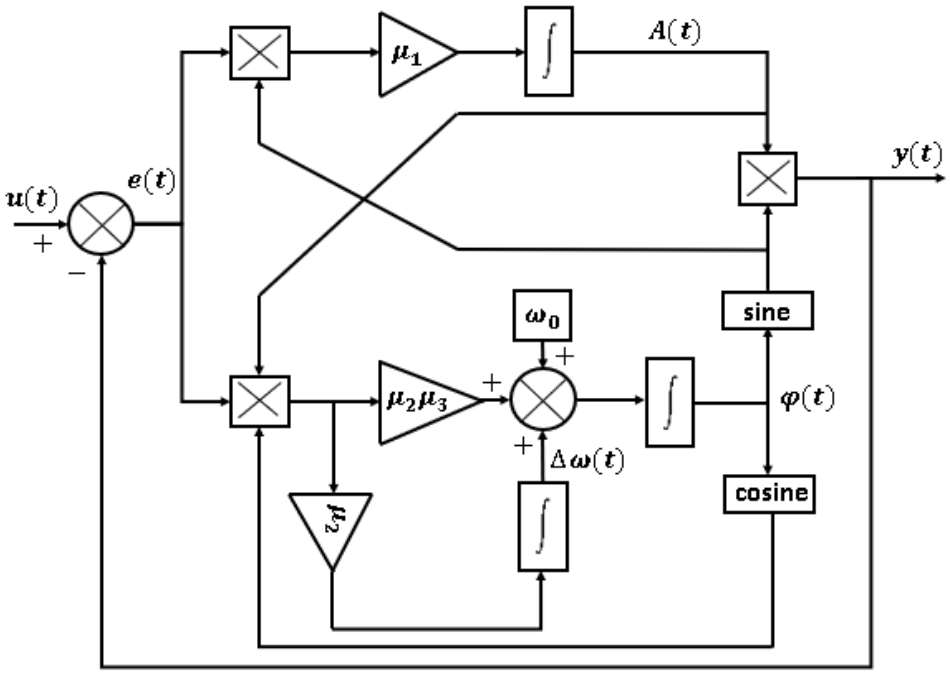

Fig. 4.11. Nonlinear Adaptive filter [122]

To demonstrate its performance, the algorithm was implemented with the Mtlab/Simulink software. A signal $u(t)$ with frequency of 50Hz and a unit magnitude (1 pu) was used for testing the algorithm. The initial conditions are chosen as $A_0 = 0$, $f_0 = 30Hz$ and $\varphi_0 = 0$. Given input signal frequency $f_0 = 50Hz$, the choice of the values for the μ-parameters are as follows: $\mu_1 = 2f_0 = 100$, $\mu_2 = (2f_0)^2 = 10000$ (for a unit-amplitude sinusoid), the choice of μ_3 is dependent on the choice of μ_2. Based on the general guideline specified in [122], the value of μ_3 is chosen such that the product of $\mu_2\mu_3$ become of the same order of magnitude as μ_1. Thus, $\mu_3 = 0.02$ is used.

Fig. 4.12 shows the performance of the algorithm in terms of its convergence. It can be observed that the algorithm converges to the periodic orbit associated with the input sinusoid in a few cycles. Also, the algorithm is insensitive to the initial conditions used. The extracted sinusoid signal, its frequency and amplitude are shown the Fig. 4.13 – 4.15 respectively.

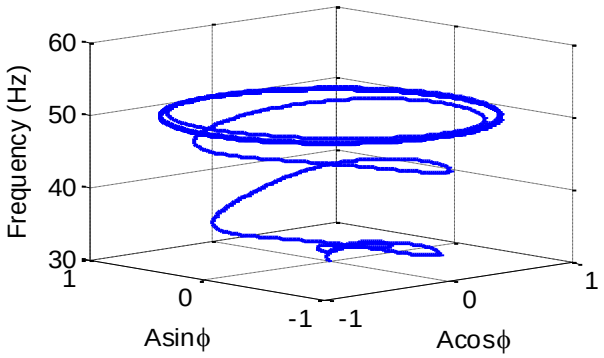

Fig. 4.12. Convergence of the algorithm to a periodic orbit

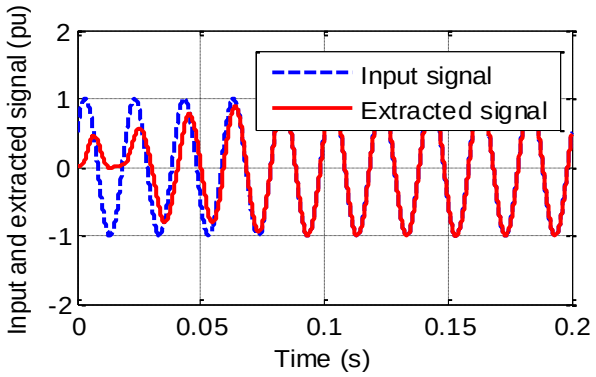

Fig. 4.13. Input and Extracted sinusoid signals

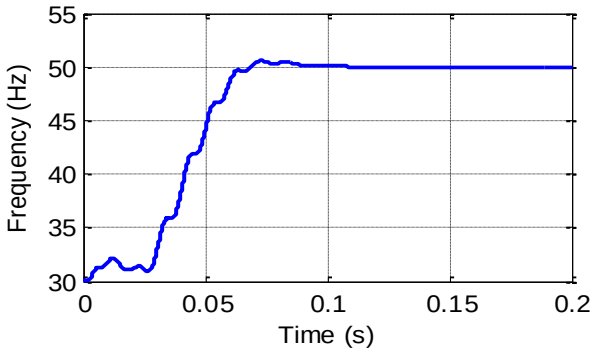

Fig. 4.14. Extracted frequency of the sinusoid signal

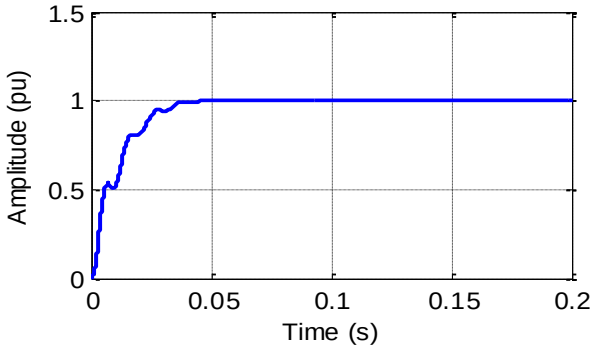

Fig. 4.15. Extracted amplitude of the sinusoid signal

The stability of the algorithm to time variations in amplitude as well as frequency is shown in Fig. 4.16 and 4.17 respectively. A 50% decrease in amplitude of the sinusoid and 30% decrease in frequency is used. The new value of the amplitude is tracked within a few cycles while the frequency oscillates for a few cycles before settling on the new value.

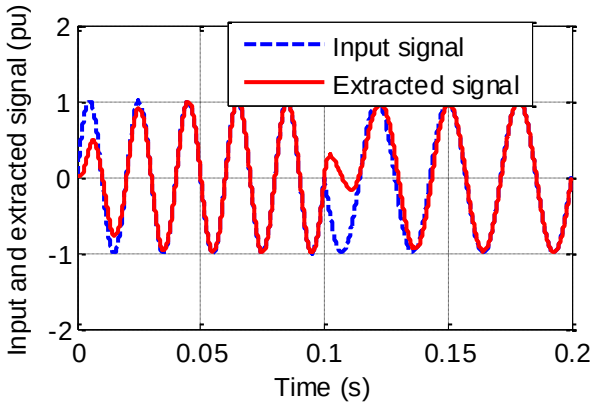

Fig. 4.16. Algorithm response to 30% change in frequency

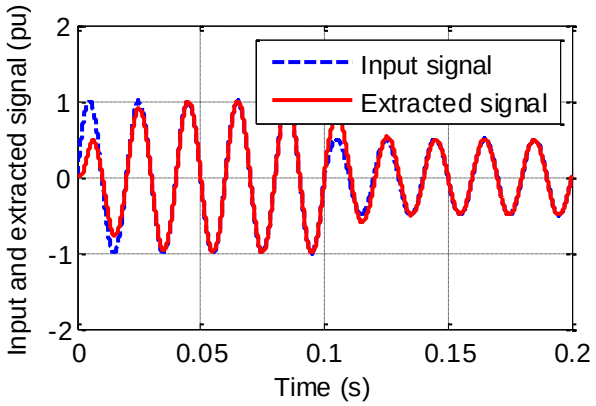

Fig. 4.17. Algorithm response to 50% change in amplitude

4.5.2 Equivalent Circuit Parameter Identification

Since the method proposed in this research is intended for in-service efficiency estimation, the challenges of accurate motor equivalent circuit predictions with limited nonintrusive measurements must be addressed. Given the conventional T-model equivalent circuit, six electrical parameters associated with the stator, rotor and magnetization branch are to be determined. The stator resistance R_s can be measured from a dc resistance test [6] and based on the NEMA motor classification, an assumed

value for one of the leakage reactances based on the ratio of stator and rotor leakage reactances X_{ls}/X_{lr} can also be determined. Although this assumption leads to a reduced number of variables to be estimated, it may not accurately represent the relationship between the two leakage reactances for all motor types [42]. Clearly, the inverse model offers an advantage in this aspect since only one leakage reactance is present. The remaining four parameters namely: the core loss resistance R_c, the stator leakage reactance X_{ls}, the rotor resistance R_r and the magnetization reactance X_m can be determined using a suitable optimization search algorithm.

For induction motors fed by an unbalanced voltage supply, the positive and negative sequence equivalent circuit reported in Fig. 4.3 is used. For this equivalent circuit, the stator and magnetization branch parameters are assumed to be constant for the positive and negative sequence equivalent circuits, while the rotor resistance is influenced by skin effect due to the double frequency of the negative sequence field. Since the stray-load loss is largely produced by the positive sequence field, the stray-load resistance R_{sll} is only placed on the positive sequence equivalent circuit.

For a nonlinear system like the IM model, one way to solve the parameter identification problem is to search for the motor parameter vector θ by minimizing an error fitness function $f_{err}(\theta)$ as follows:

$$\hat{\theta} = \underset{\theta \in [\theta_{min}, \theta_{max}]}{arg\ min} \quad f_{err}(\theta) \tag{4.29}$$

Where $f_{err}(\theta)$ is defined (based on Fig. 4.3) by:

$$f_{err}(\theta) = \sum_{j=1}^{n} \left(\sum_{i=1}^{2} \left(\tilde{I}_{si}(j) - \tilde{I}'_{si}(j) \right)^2 \right) \tag{4.30}$$

Where θ is a vector set of the motor parameters, $\theta = [R_r, R_c\ X_{ls}\ X_m]^T$ for a balanced supply and $\theta = [R_{r1}, R_{r2}, R_{\ c}\ X_{ls}, X_m,]^T$ for an unbalanced supply. θ_{min} and θ_{max} are the lower and upper boundaries of the constraints respectively. The current sets $\tilde{I}_{si}$ and

$\tilde{I}'_{si}$ are the measured and estimated symmetrical component currents in the stator respectively, *j* is the data sample index and *n* is the total number of data samples.

As shown in Fig. 4.18, the optimization algorithm continuously updates the motor parameters for each iteration by minimizing $f_{err}(\theta)$ until a close match is established between the measured and estimated instantaneous stator symmetrical component currents.

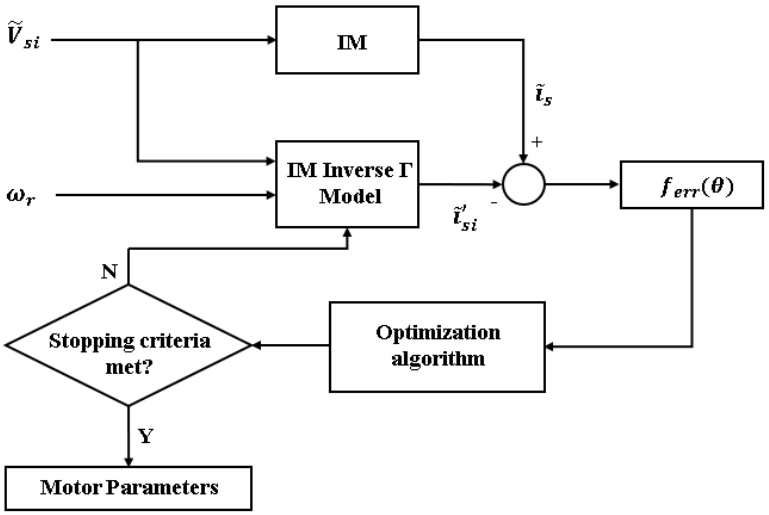

Fig. 4.18. The parameter estimation scheme

The symmetrical component voltages in Fig. 4.3 are calculated from the complex phase voltages using the power-invariant transformation.

$$\begin{bmatrix} \mathrm{V}_0 \\ \mathrm{V}_1 \\ \mathrm{V}_2 \end{bmatrix} = \frac{1}{\sqrt{3}} \begin{bmatrix} 1 & 1 & 1 \\ 1 & a & a^2 \\ 1 & a^2 & a \end{bmatrix} \begin{bmatrix} \mathrm{V}_\mathrm{a} \\ \mathrm{V}_\mathrm{b} \\ \mathrm{V}_\mathrm{c} \end{bmatrix} \tag{4.31}$$

Where $a = e^{\mathrm{j}\frac{2\pi}{3}}$, $\mathbf{V}_\mathrm{a} = V_a e^{\mathrm{j}\theta_a}$, $\mathbf{V}_\mathrm{b} = V_b e^{\mathrm{j}\theta_b}$, $\mathbf{V}_\mathrm{c} = V_c e^{\mathrm{j}\theta_c}$. The zero-sequence voltage V_0 can be neglected since induction motors are mostly connected without the neutral in industrial applications.

The phase voltages are calculated from the line-to-line voltages using the following sets of equations [61].

$$V_a = \frac{1}{3}\sqrt{2(V_{ca}^2 + V_{ab}^2) - V_{bc}^2} \tag{4.32}$$

$$V_b = \frac{1}{3}\sqrt{2(V_{bc}^2 + V_{ab}^2) - V_{ca}^2} \tag{4.33}$$

$$V_c = \frac{1}{3}\sqrt{2(V_{ca}^2 + V_{bc}^2) - V_{ab}^2} \tag{4.34}$$

$$\theta_a = 0 \tag{4.35}$$

$$\theta_b = -\arccos\left(\frac{V_{ab}^2 - V_a^2 - V_b^2}{-2V_aV_b}\right) \tag{4.36}$$

$$\theta_c = \arccos\left(\frac{V_{ca}^2 - V_c^2 - V_a^2}{-2V_cV_a}\right) \tag{4.37}$$

4.5.3 Range Specification for the Core Loss Resistance

Generally, the core loss in an induction motor is modelled by a simple resistance placed in parallel with the magnetization reactance. However, the core loss resistance with this arrangement will have minimal impact on the stator current due to the portion of the current in it relative to the input current. As a result, each optimization cycle converges to a different result and therefore resulting in inconsistent core loss estimates when using the IEEE Std. 112-2017 method F1.

In [68], an alternative solution based on Gauss-Seidel and empirical factors was mentioned. However, no further information was given on how the method was implemented. As reported in [54], specifying an appropriate range for constraints is necessary to avoid possible divergence in optimization but this may not contribute to the overall estimation accuracy. A modified equivalent circuit with a series arrangement of the magnetization branch as presented in [58] has been shown to give better results than the parallel connection. This is because the value of the series core loss resistance (R_c) is comparable to the other equivalent circuit parameters whereas the parallel core loss resistance (R_{fe}) is much larger. Since the expressions for R_c and X_m are dependent

on R_{fe} as given in (4.9) – (4.11), having prior information on the core loss is important to specify good boundary range for R_{fe}. This can be achieved using the following set of equations given by (4.38) – (4.38):

The total loss in an induction motor is given by:

$$P_L = P_{scl} + P_{rcl} + P_h + P_{fw} + P_{sll} \tag{4.38}$$

Where; P_{scl} and P_{rcl} are the stator and rotor copper losses respectively, P_h is the core loss, P_{fw} is the friction and windage loss and P_{sll} is the stray-load loss.

The total loss can also be represented by (4.39).

$$P_L = P_{rated} - P_{shaft} \tag{4.39}$$

Where P_{rated} is the rated input power and P_{shaft} the output shaft power.

By equating (4.38) and (4.39), an expression for the core loss can be derived as:

$$P_h = P_{rated} - P_{shaft} - P_{scl} - P_{rcl} - P_{fw} - P_{sll} \tag{4.40}$$

The shaft power and the rotor copper loss in (4.40) can be expressed in terms of the airgap power P_{ag} as follows:

$$P_{shaft} = P_{ag}(1 - s) - P_{fw} - P_{sll} \tag{4.41}$$

$$P_{rcl} = sP_{ag} \tag{4.42}$$

Where $P_{ag}(1 - s)$ in (4.41) is the mechanical power transferred to the shaft. $P_{ag} = T_{ag}\omega_{syn}$ is calculated using the well-known airgap toque equation [29]. Substituting (4.41) and (4.42) into (4.40) and simplifying gives:

$$P_h = P_{rated} - P_{ag} - P_{scl} \tag{4.43}$$

The value of P_h in (4.43) is substituted into (4.44) to calculate an approximate value for R_{fe}. However, to ensure the search algorithm converges to the actual value of Rfe, the search boundaries are narrowed to within $\pm 20\%$ of the approximate value of Rfe obtained in (4.44).

$$R_{fe} = 3\frac{v_m^2}{P_h} \tag{4.44}$$

Where v_m is the inner voltage across the magnetization branch and is determined based on the expression:

$$v_m = \sqrt{\left(v_s - \frac{\sqrt{3}}{2} i_s R_s cos\varphi\right)^2 + \left(\frac{\sqrt{3}}{2} i_s R_s sin\varphi\right)^2} \tag{4.45}$$

Where:

$$cos\varphi = \frac{P_{in}}{\sqrt{3} v_s i_s} \tag{4.46}$$

$$sin\varphi = \sqrt{1 - cos^2\varphi} \tag{4.47}$$

v_s, i_s and P_{in} are the measured voltage, current and input power at rated operating condition respectively.

4.5.4 Friction and Windage Loss and Stray-Load Loss Determination

In this research, a method that relies on the motor nameplate information (rated torque, speed and efficiency) and the airgap torque is proposed to estimate the total losses in an induction motor not accounted for by the motor equivalent circuit. These losses are

the stray-load loss and the friction and windage loss. The SLL mainly occurs in the stator as the rotor operates only at the slip frequency with negligible core losses. It also depends on the lamination thickness, material compression and heat treatment, manufacturing process, assembly (stress in the cores), temperature etc.

Based on the power flow of an induction motor, these two losses make up the difference between the generated mechanical power and the shaft power. However, since the friction and windage loss and the stray-load loss are by their nature different, it is important to determine them separately. Thus, according to the IEEE Std. 112 [6] the stray-load loss P'_{sll} at rated condition is considered as 1.8% of the rated output power. For other than the rated condition, the stray-load loss is assumed to be proportional to the rotor current and can be represented by a resistance R_{sll} estimated using (4.48).

$$R_{sll} = 0.018R'_2\left(\frac{1 - s_{rated}}{s_{rated}}\right) \tag{4.48}$$

Where s_{rated} is the slip corresponding to the rated condition.

The friction and windage loss P_{fw} at any desired load condition is estimated according to the airgap torque method using (4.49).

$$P_{fw} = \frac{2\pi n_r}{60}\left(\frac{s}{s_{rated}}\right)\left(T_{ag} - T_{rated}\right) - P_{sll} \tag{4.49}$$

Where P_{fw} and P_{sll} are the friction and windage loss and the stray-load loss at a rotor speed n_r and slip s, T_{rated} is the motor rated torque and n_{rated} is the rated speed.

Using the nameplate rated speed value to calculate s_{rated} in (4.48) and (4.49) could potentially introduce a large error in the loss estimation as the NEMA MG1 standard [25] allowed up to 20% variation of the nameplate rated speed value. To mitigate this problem, the method proposed in [123] is adapted in this research. The rated speed is determined using the corrected value expressed by (4.50) [123].

$$n_{rated}^{*} = n_{syn50} - \left(\frac{2\pi T_{rated}}{60}\right) \left(\frac{\left(n_2\left(n_{syn2} - n_2\right)\right) - \left(n_1\left(n_{syn1} - n_1\right)\right)}{\Delta P \eta_{rated}}\right) \quad (4.50)$$

Where: n_{rated}^{*} is the corrected rated speed, n_{syn50} is the motor synchronous speed at the mains frequency, n_1 and n_2 are the speeds at two different load situations corresponding to the two synchronous speeds n_{syn1} and n_{syn2} respectively, ΔP is the change in input power between the two operating points and η_{rated} is the motor rated efficiency.

To maintain nonintrusive measurements, it can be assumed that the second operating point corresponds to the synchronous speed condition, consequently; $n_2 = n_{syn2} = n_{syn50}$ and the corresponding power at this point is zero. Thus (4.50) is simplified to give:

$$n_{rated}^{*} = n_{syn50} - \left(\frac{2\pi T_{rated}}{60}\right)\left(\frac{\left(n_1\left(n_{syn1} - n_1\right)\right)}{P_1 \eta_{rated}}\right) \quad (4.51)$$

Where P_1 is the input power at operating point 1.

The new rated speed n_{rated}^{*} in (4.51) is used in (4.48) and (4.49) to estimate P_{sll} and P_{fw} at any desired rotor speed n_r. As an example, the measurements recorded at 75% load for a 37kW motor as shown in Table 4.1 is used to estimate the rated speed as follows:

$$n_{rated}^{*} = 1500 - \left(\frac{2 \cdot \pi \cdot 240}{60}\right) \cdot \left(\frac{1481.147 \cdot (1499.997 - 1481.147)}{31578.605 \cdot 0.916}\right)$$
$$= 1475.75 rpm$$

The percentage error in the rated speed estimation:

$$\Delta n_{rated}^{*} = \frac{1475.75 - 1475.00}{1475.00} = 0.0508\%$$

TABLE 4.1

DATA USED TO ESTIMATE THE RATED SPEED

Load point	Input power (W)	Frequency (Hz)	Estimated Speed (rpm)
75%	31578.605	50.000	1481.147

4.5.5 Temperature Estimation

Temperature measurement is needed in order to correct the values of the stator and rotor resistances to the machine's operating temperature. The windings' temperature can be measured using embedded detectors (thermocouples). However, since most motors do not have these detectors preinstalled, it is acceptable in such situations to use the specified insulation class temperature of the machine [6]. If resistance value R_a is known at a temperature t_a, then the corrected resistance value R_b at any other temperature t_b can be calculated by (4.52) [6]:

$$R_b = R_a \left(\frac{t_b + k_1}{t_a + k_1} \right) \tag{4.52}$$

Where k_1 is 234.5 (for copper conductors)

4.5.6 Modified IEEE Std. 112-2017 Form F2

Method F1of the IEEE Std. 112 is used to calculate the efficiency based on the proposed equivalent circuit. For this purpose, the set of equations on Form F2 [6] are modified to conform with the proposed positive and negative sequence equivalent circuits reported in Fig. 4.3. The superposition principle is applied to calculate the total input and output power, the total losses and finally the motor efficiency using the proposed equivalent circuit. The set of equations used for the calculation are as follows:

$$G_r = \frac{s}{R_r} \tag{4.53}$$

$$G_m = \frac{R_c}{Z_m^2} \tag{4.54}$$

$$G = G_r + G_m \tag{4.55}$$

$$B_m = -\left(\frac{X_m}{Z_m^2}\right) \tag{4.56}$$

$$B = B_m \tag{4.57}$$

$$Y_r^2 = G^2 + B^2 \tag{4.58}$$

$$R_g = \frac{G}{Y_r^2} \tag{4.59}$$

$$R = R_s + R_g \tag{4.60}$$

$$X_g = -\left(\frac{B}{Y_r^2}\right) \tag{4.61}$$

$$X = X_s + X_g \tag{4.62}$$

$$Z = \sqrt{R^2 + X^2} \tag{4.63}$$

$$I_s = \frac{V_{ph}}{Z} \tag{4.64}$$

$$I_r = \frac{I_s}{\sqrt{\left(\frac{R_r}{s}\right)^2 \times Y_r^2}} \tag{4.65}$$

$$P_s = 3I_s^2 R \tag{4.66}$$

$$P_r = 3I_r^2 \left(\frac{R_r}{s}\right) \tag{4.67}$$

$$P_{scl} = 3I_s^2 R_1 \tag{4.68}$$

$$P_{rcl} = sP_r \tag{4.69}$$

$$P_c = 3I_s^2 \left(\frac{G_m}{Y_r^2}\right) \tag{4.70}$$

$$P_t = P_{scl} + P_{rcl} + P_c + P_{fw+sll} \tag{4.71}$$

$$P_{shaft} = P_s - P_t \tag{4.72}$$

$$\eta = \left(\frac{P_{shaft}}{P_s}\right) \times 100 \tag{4.73}$$

4.6 Experimental Results and Discussion

In this research, the proposed NFEE method has been validated by testing the efficiency of four totally enclosed fan-cooled induction motors operating on a balanced as well as unbalanced voltage supply conditions. The nameplate data of these motors are shown in Table 4.2

TABLE 4.2

NAMEPLATE DATA OF THE INDUCTION MOTORS USED FOR VALIDATION

Motor	**7.5kW Motor**	**11kW Motor**	**37kW Motor**	**45kW Motor**
Efficiency class	Premium Eff.	Premium Eff.	Standard Eff.	Standard Eff.
Voltage (V)	380	380	400	400
Current (A)	14.4	21.5	67.4	81.6
Frequency (Hz)	50	50	50	50
Speed (rpm)	1460	1460	1475	1475
Power factor	0.88	0.85	0.86	0.86
Insulation class	F	F	F	F
Number of poles	4	4	4	4
Stator connection	Δ	Δ	Δ	Δ

4.6.1 Experimental Setup

Two different experimental test rigs were used in testing the motors. The 110kW test bench shown in Fig. 4.19 was used for testing the 37kW and 45kW standard efficiency motors while the 22kW test bench shown in Fig. 4.20 was used for the 7.5kW and 11kW premium efficiency motors. These two test rigs are part of the state-of-the-art motor testing facilities at the Machines laboratory unit of the University of Cape Town, South Africa.

Fig. 4.19. The complete 110kW laboratory test bench showing all the system components

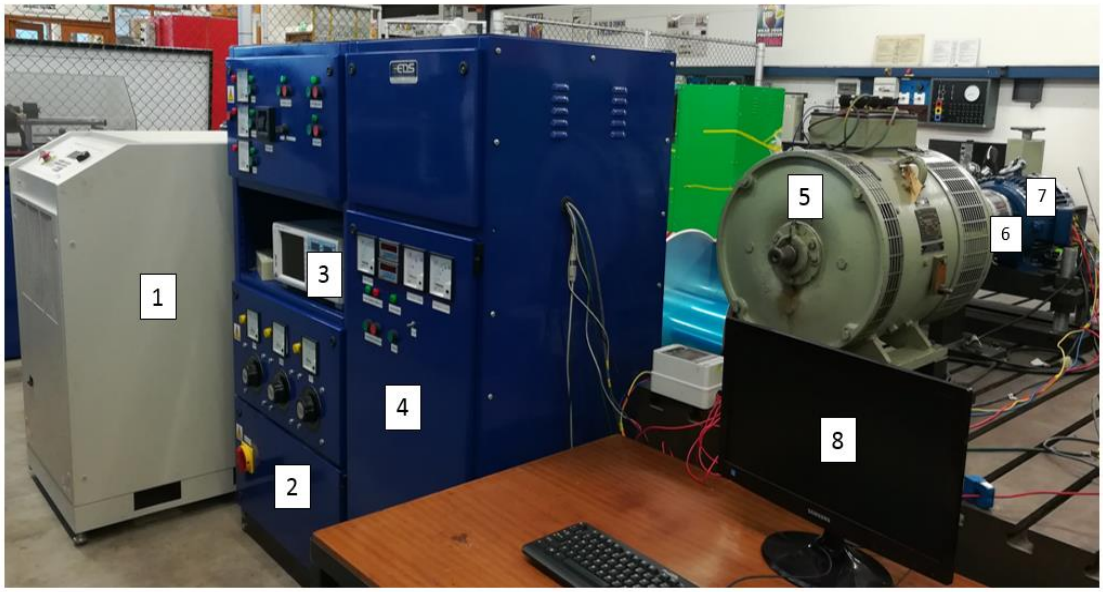

Fig. 4.20. The 22kW Experimental Test Rig: 1. Programmable power supply MX 30, 2. Power supply panel, 3. Yokogowa WT1800 Power Analyzer, 4. 4-Quadrant DC Drive Load Assembly, 5. 15kW DC Machine, 6. In-line torque transducer-Magtrol TM 300, 7. Induction motor, 8. Data acquisition pc.

The 110kW test rig consists of a 110kW AC dynamometer, an Active Front-End (AFE) bi-directional drive unit (Model SPMC 1402), an in-line torque/speed transducer and a high-performance Genesis 7i Data Acquisition (DAQ) system. The schematic diagram of this system is shown in Fig. 4.21. The system is powered either through the MX 60 programmable power supply unit or by the bi-directional Variable Speed Drive (VFD).

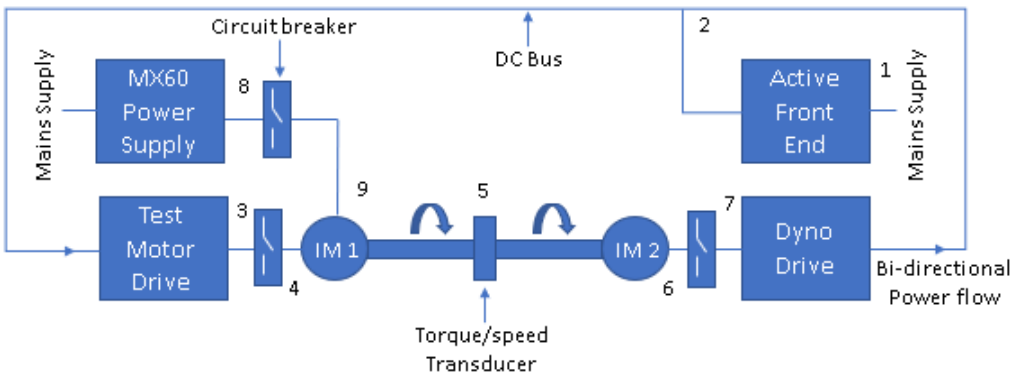

Fig. 4.21. Schematic diagram of the 110kW rig test

The individual components making up the 110kW test rig are briefly described as follows:

(i) 110kW AC Dynamometer

The 110kW AC dynamometer is operated in a closed-loop vector control mode and act as a load to the Motor Under Test (MUT). Different torque values can be programmed through the drive software to impose the required torque values on the MUT. Alternatively, the torque can be controlled using an analgue switch on the drive control panel.

(ii) Active Front-End (AFE)

The AFE consists of a thyristor controlled rectifier unit (SPMC1402 model) that supplies a DC voltage of 700V to the DC bus and a regenerative IGBT drive unit (SPMD1404 model) allowing the MUT to be tested in motoring or generating mode. A phase-locked-loop PLL ensures syncronised operation of the system to the mains supply in all operating modes.

(iii) Genesis 7i data acquisition system

At the heart of the system is the high-performance Gen. 7i DAQ that is used for data aquisition and data recording. The system has up to 24 distinct channels through which external sensor signals can be fed to the DAQ recorders. The input data are sampled at a very high sampling rate of 2MS/s. As reported in Fig. 4.21, measurements are taken at nine different locations using the Gen. 7i DAQ system. The type of signal measured at each of these locations are specified in Table 4.3. The Gen. 7i DAQ system has advanced signal processing capabilities such as Fast Fourier Transform (FFT), and filtering which allows the extraction of fundamental and harmonic components of a signal. This feature is quite useful when dealing with measurements of harmonic signal waveforms. Thus this feature has been used in this research for testing the efficiency of converter-fed motors as will be seen in chapter 6.

TABLE 4.3

LOCATION AND TYPE OF SIGNAL MEASURED ON 110KW TEST RIG

Location	Component	Measured signal type
1	Active Front End	Three-phase AC voltages and currents
2	Common DC bus	DC voltage and current of the DC bus
3	Test Motor drive output	Three-phase AC voltages and currents
4	MUT input from test drive	Three-phase AC voltages and currents
5	Torque transducer	Shaft torque and speed
6	Load motor drive output	Three-phase AC voltages and currents
7	Load motor input	Three-phase AC voltages and currents
8	MX60 power supply output	Three-phase AC voltages and currents
9	MUT input from MX60	Three-phase AC voltages and currents

(iv) In-line torque transducer

Torque and speed measurements were obtained using a Magtrol 314 torque transducer. The in-line torque transducer provides extremely accurate torque and speed measurements over a broad range. The model has an integrated electronic conditioning module that provides a 0 to $\pm$10V DC torque output and an open collector 5V pulse speed output. The transducer has a torque rating of 1000Nm with an overload capacity of 200% and a speed range of 1 to 7000rpm. Fig. 4.22 shows the basic configuration of the torque transducer.

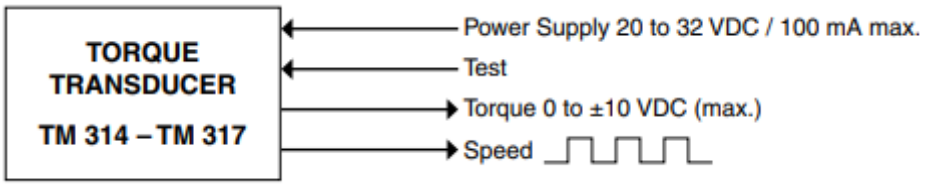

Fig. 4.22. Basic configuration of the Magtrol TM 314 torque transducer

(v) MX 1609 temperature measurement module

The stator winding temperature from three type-K thermocouples are fed into a QuantumX MX 1609 module which was then interfaced to the DAQ.

For the 22kW test rig, the MUT is connected to a 15kW DC machine through an in-line torque transducer. The DC machine is connected to a four-quadrant drive (Emerson Mentor MP27kW) which allows it to operate as a motor or a generator. In this research, the DC machine runs as a generator and acts as a load to the MUT. For measurements, the system uses a WT1800 power analyser and a National Instrument data acquisition module NI3245 interfaced to a computer. The MUT is powered through a California Instrument MX 30 programmable power supply unit.

4.6.2 Performance Validation of the Proposed NFEE Method

For validation purposes, the motors were tested for balanced (CASE 1) and unbalanced (CASE 2) voltage supply conditions. In case 1, the tests were performed in accordance with the loss segregation methods of the IEEE Std. 112-2017 and the IEC60034-2-1 standards and the results serve as a reference for comparison to the proposed NFEE method. For the unbalanced supply condition, the motors were tested with a voltage unbalance of up to 5% and the results obtained were compared to the direct measurement method.

4.6.3 CASE 1: Balanced Voltage Supply Condition

In this case, the machine-under-test (MUT) was powered by the California Instruments MX 60 programmable Power supply unit to avoid voltage and frequency fluctuations which are unavoidable on the mains supply. For the loss segregation methods, firstly a rated temperature test was performed to allow the temperature of the test motor to stabilize. To reduce the time needed to attain the steady-state temperature, the motors were slightly overloaded at the start of the test for about 2 hours and then allowed to stabilize at the rated condition. A complete variable load curve test was then performed and was immediately followed by a no-load test. The two tests were performed in conformity to the IEEE and IEC standards. At each test point, the voltage, current, power, speed, and temperature readings were recorded (as shown in Appendix B). In addition, instantaneous readings of the stator voltage and current signals at rated

condition were recorded at a sampling rate of 100μs using LABVIEW. The waveforms serve as inputs to the proposed NFEE method.

The methods presented in sections 4.5.1, and 4.5.3 for rotor speed estimation and range specification respectively were used to accurately determine the motor parameters. The ability of the speed estimation algorithm to track the motor speed was tested using the Matlab/Simulink software. A single stator line current signal was measured at a sampling rate of 100μs and serves as input to the speed estimation algorithm. The nonlinear adaptive filter was able to extract the fundamental and residual signal from the input signal as shown in Fig. 4.23 and Fig. 4.24. By performing Fast Fourier Transform (FFT) on the residual signal, the frequency of the dominant speed-dependent harmonics was obtained as shown in Fig. 4.25. Based on the frequency result, the calculated slip using (4.16) at the rated condition was found to be 0.0172 and using (4.74), the estimated speed is 1474.2rpm which gives 0.054% error when compared to the measured rated speed of 1475.0rpm for the tested motor.

$$n_r = (1 - s)n_{syn} \tag{4.74}$$

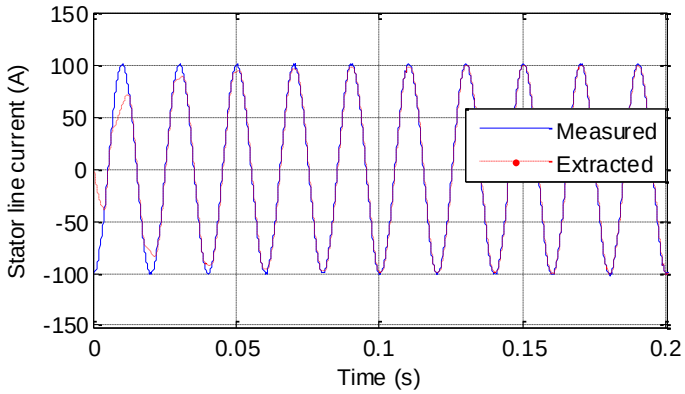

Fig. 4.23. Measured and extracted currents for the 7.5kW test motor

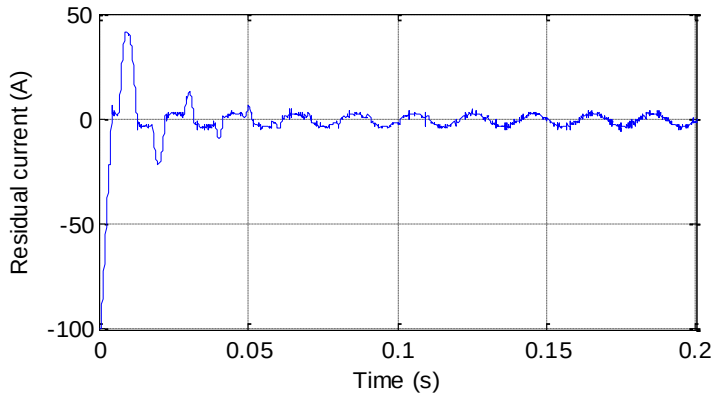

Fig. 4.24. Residual signal after extraction of the fundamental component

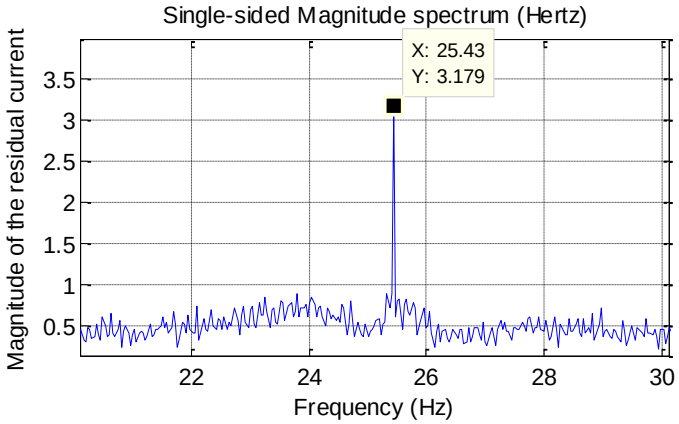

Fig. 4.25. FFT analysis on the residual signal

Table 4.4 shows the summary of the parameter identification results for the conventional T-model and the modified inverse Γ-model implementation for all the tested motors. The CSO algorithm was set to run for 10 cycles and the average value was taken for each parameter (see Appendix C). This is necessary to confirm the repeatability of the estimation algorithm. Based on the repeatability test, the summary of the recorded results for all the four motors is given in terms of the mean and standard deviation as reported in Table 4.4. As can be seen, the standard deviation values for the modified inverse Γ-model show very close agreement for all the estimated motor parameters. For the sake of brevity, only the 37kW test motor results are shown in graphical form.

TABLE 4.4

ESTIMATED PARAMETERS OF THE INDUCTION MOTORS

Model Type	$\mu, \sigma,$ & cv	$R_r(\Omega)$	$X_{ls}(\Omega)$	$X_{lr}(\Omega)$	$X_m(\Omega)$	$R_c(\Omega)$	$R_{fe}(\Omega)$
7.5kW premium efficiency motor							
T-model	μ	0.642	3.475	4.659	62.498	-	1718.22
	σ	0.017	0.704	0.805	2.154	-	140.500
	cv	2.686	20.255	17.279	3.446	-	8.177
Inverse Γ-Model	μ	0.640	3.257	-	63.291	2.344	-
	σ	0.001	0.002	-	0.270	0.028	-
	cv	0.093	0.061	-	0.427	1.190	-
11kW premium efficiency motor							
T-model	μ	0.630	3.676	4.438	64.993	-	1826.48
	σ	0.016	0.792	0.891	2.353	-	96.070
	cv	2.561	21.558	20.082	3.620	-	5.260
Inverse Γ-Model	μ	0.650	2.479	-	69.146	2.629	-
	σ	4.5E-05	0.0003	-	0.032	0.010	-
	cv	0.00697	0.013	-	0.046	0.364	-
37kW standard efficiency motor							
T-model	μ	0.134	1.198	0.761	30.247	-	1181.47
	σ	0.004	0.403	0.429	5.820	-	301.000
	cv	2.621	33.659	56.388	19.240	-	25.477
Inverse Γ-Model	μ	0.140	0.796	-	26.968	0.870	-
	σ	3.4E-05	0.0003	-	0.067	0.005	-
	cv	0.024	0.031	-	0.249	0.589	-
45kW standard efficiency motor							
T-model	μ	0.128	0.650	0.646	22.021	-	1044.64
	σ	0.004	0.280	0.295	2.155	-	184.664
	cv	2.852	43.037	45.643	9.785	-	17.677
Inverse Γ-Model	μ	0.130	0.519	-	21.1222	0.6029	-
	σ	4.4E-05	0.0001	-	0.04751	0.0071	-
	cv	0.034	0.021	-	0.22493	1.1808	-

μ : Mean; σ : Standard deviation, cv : Coefficient of variance

Fig. 4.26(a) and 4.26(b) show the convergence profiles of the fitness function f_{err} for the conventional T-model and the modified Inverse Γ-model implementation respectively.

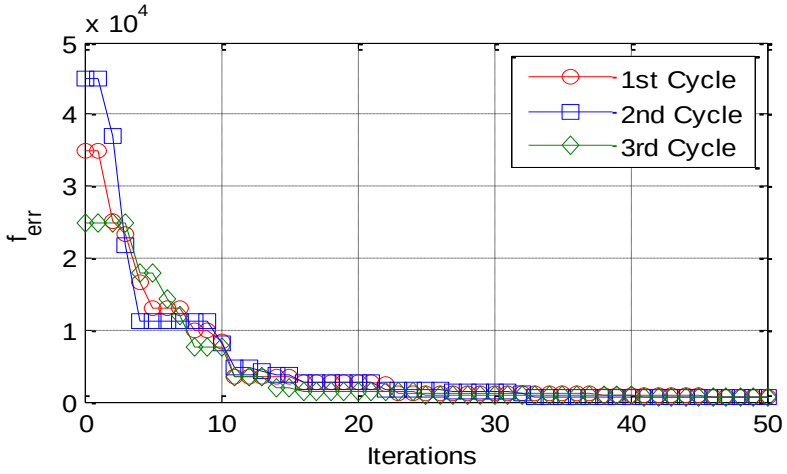

(a)

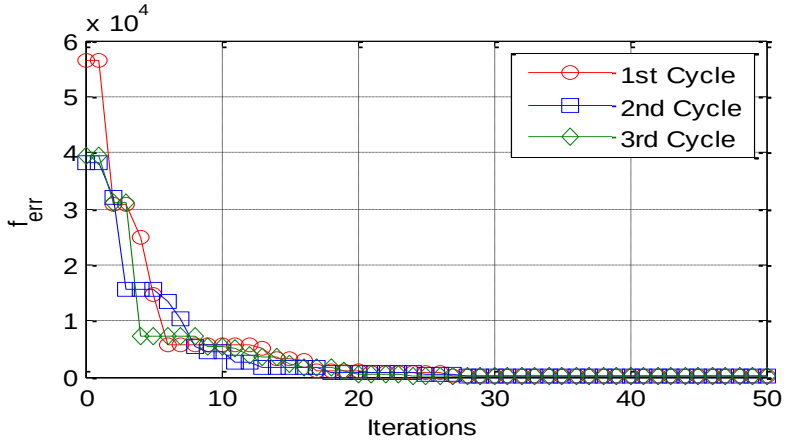

(b)

Fig. 4.26. Convergence profile of the error function f_{err} (a) Conventional T-model (b) Modified Inverse Γ-model

Similarly, the convergence of the motor parameters is shown in Fig. 4.27(a) to (e) and Fig 4.28(a) to (d). For clarity, only 3 optimization cycles are shown on the graphs. Although the error performance index for the standard T-model indicates very close agreement for all the optimization cycles, a different set of motor parameters are recorded for each cycle, as can be observed in Fig. 4.27(a) to (e). This problem can be more clearly seen for the core loss resistance R_{fe} as depicted in Fig. 4.27(e). This inconsistency can largely be attributed to the structural deficiencies of the T-model than

to the quality of the measurements used, because very promising results were obtained using same sets of measurements in the case of the modified inverse Γ-model.

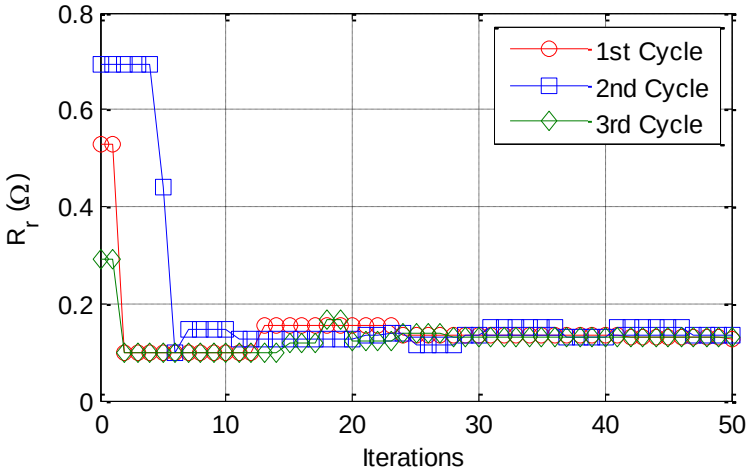

(a)

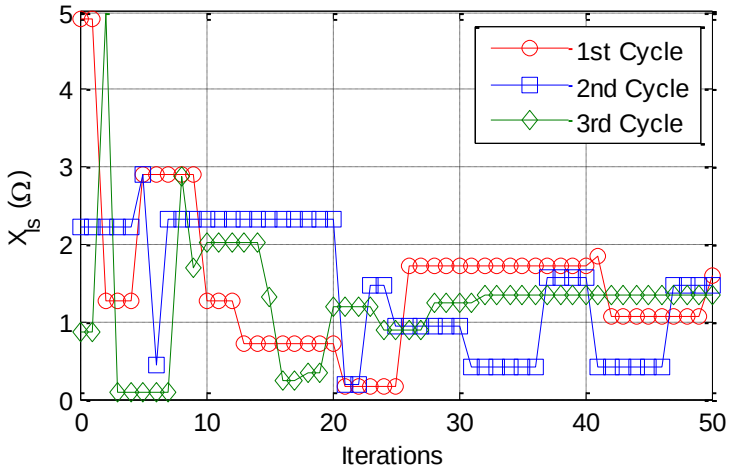

(b)

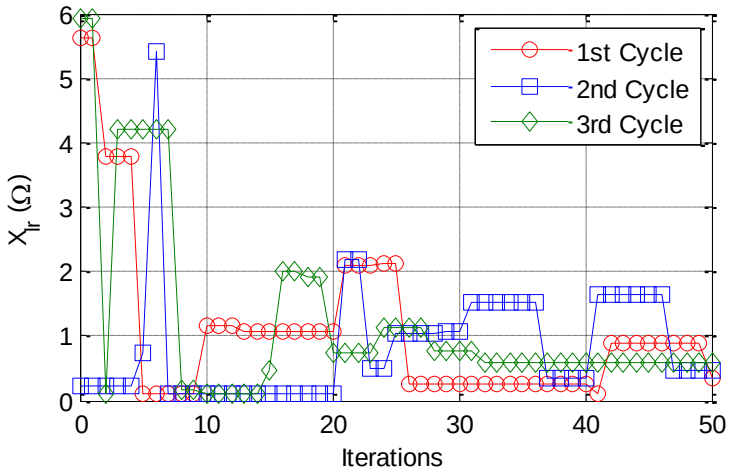

(c)

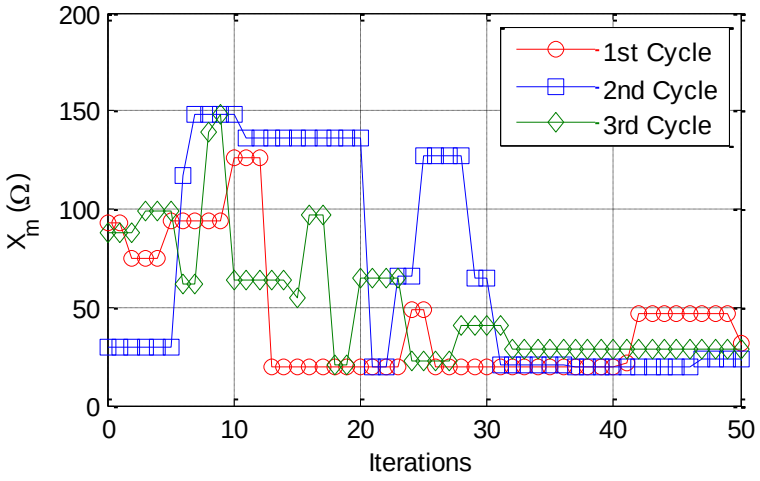

(d)

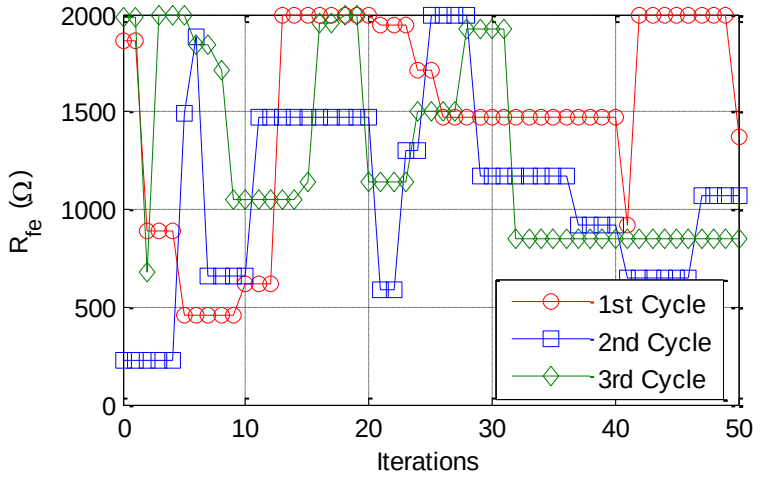

(e)

Fig. 4.27. 37kW test motor parameter estimation using the conventional T-model. (a) R_r (b) X_{ls} (c) X_{lr} (d) X_m (e) R_{fe}

On the other hand, a similar procedure was followed to estimate the motor parameters based on the modified inverse Γ-model. The results recorded in Fig. 4.28(a) - (d) show close agreements for all the estimated parameters including the core loss resistance R_c. As shown in Fig. 4.28(d), R_c is uniquely identifiable for all the optimization cycles. Similarly, as reported in Fig. 4.28(b) and (c), the leakage and magnetization reactances are also identifiable using the inverse Γ-Model. These results are clearly in conformity with the observations made in the identifiability analysis in section 4.4. In addition, the results confirm the repeatability of the CSO parameter estimation algorithm using the modified inverse Γ-model.

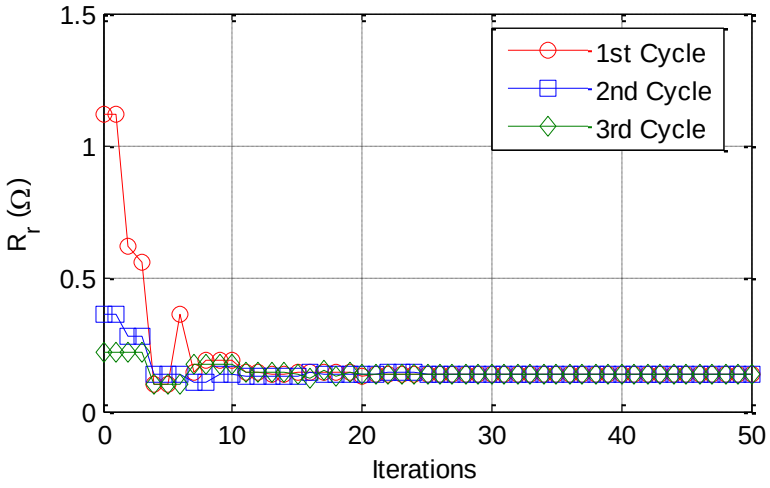
1.5
1
0.5
0
R_r (Ω)
0
10
20
30
40
50
Iterations
1st Cycle
2nd Cycle
3rd Cycle

(a)

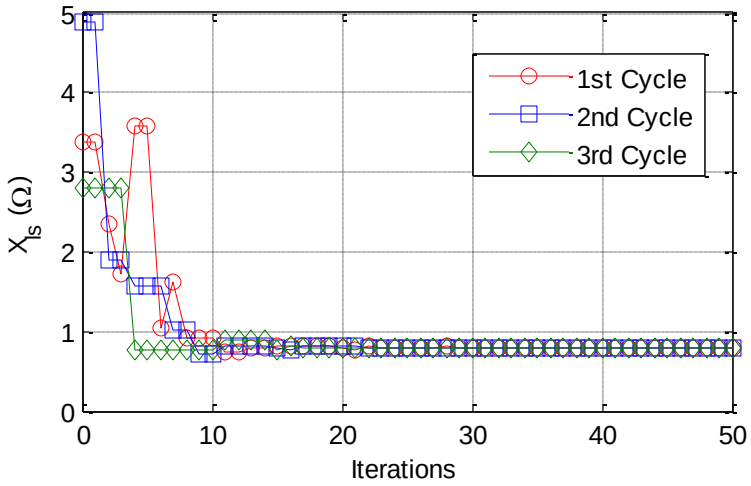
5
4
3
2
1
0
X_{ls} (Ω)
0
10
20
30
40
50
Iterations
1st Cycle
2nd Cycle
3rd Cycle

(b)

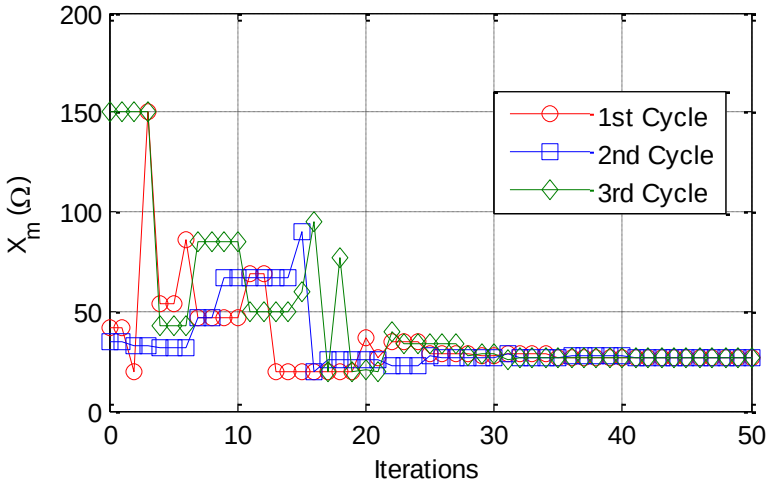
200
150
100
50
0
X_m (Ω)
0
10
20
30
40
50
Iterations
1st Cycle
2nd Cycle
3rd Cycle

(c)

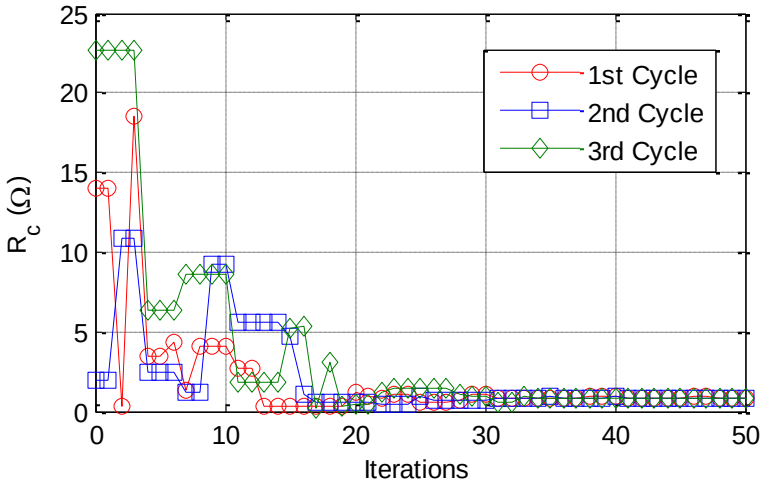

(d)

Fig. 4.28. 37kW Test Motor Parameter estimation using the modified Inverse Γ model. (a) R_r (b) X_{ls} (c) X_m (d) R_c

To validate the accuracy of the parameter estimation algorithm, the estimated motor parameters are compared to the actual parameters (obtained using the no-load/locked rotor test) shown in Table 4.5 for the 7.5kW test motor. Similar accuracies were obtained for the other tested motors.

TABLE 4.5

COMPARISON OF ACTUAL AND ESTIMATED MOTOR PARAMETERS – 7.5KW MOTOR

Parameter	**Actual**	**Inverse Γ-Model**	**Abs. Error**	**T-model**	**Abs. Error**
$\boldsymbol{R_r}(\Omega)$	0.642	0.653	0.011	0.570	0.071
$\boldsymbol{X_{ls}}(\Omega)$	3.257	3.262	0.005	4.103	0.846
$\boldsymbol{X_{lr}}(\Omega)$	4.862	-	-	4.281	0.582
$\boldsymbol{X_m}(\Omega)$	69.150	69.585	0.435	68.105	1.045
$\boldsymbol{R_c}(\Omega)$	2.634	2.543	0.091	-	-
$\boldsymbol{R_{fe}}(\Omega)$	1865.600	-	-	1522.590	343.010

The efficiency results for the four motors are shown in Fig. 4.29 to Fig. 4.32. The NFEE method and the conventional equivalent circuit method are compared to the IEEE and IEC loss segregation methods.

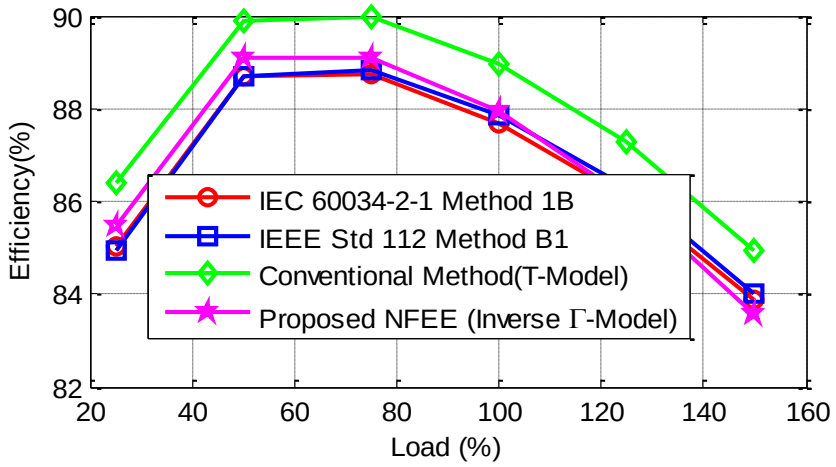

Fig. 4.29. Comparison of efficiency results for the 7.5kW motor

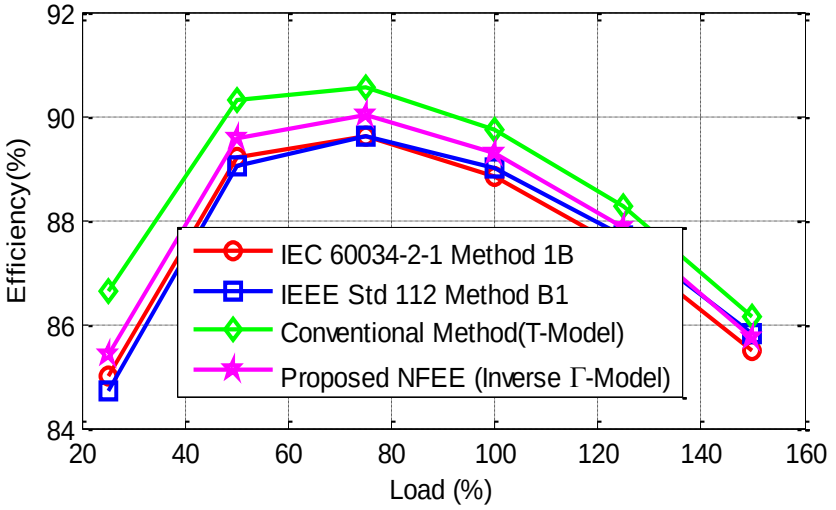

Fig. 4.30. Comparison of efficiency results for the 11kW motor

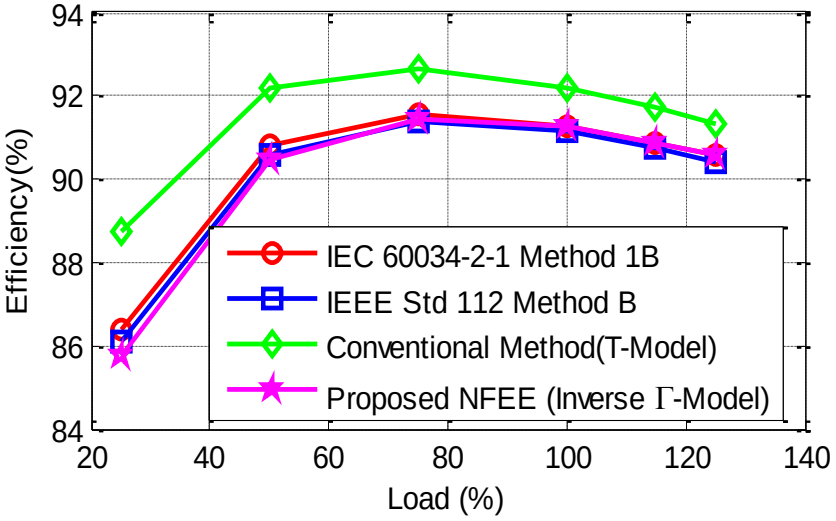

Fig. 4.31. Comparison of efficiency results for the 37kW test motor

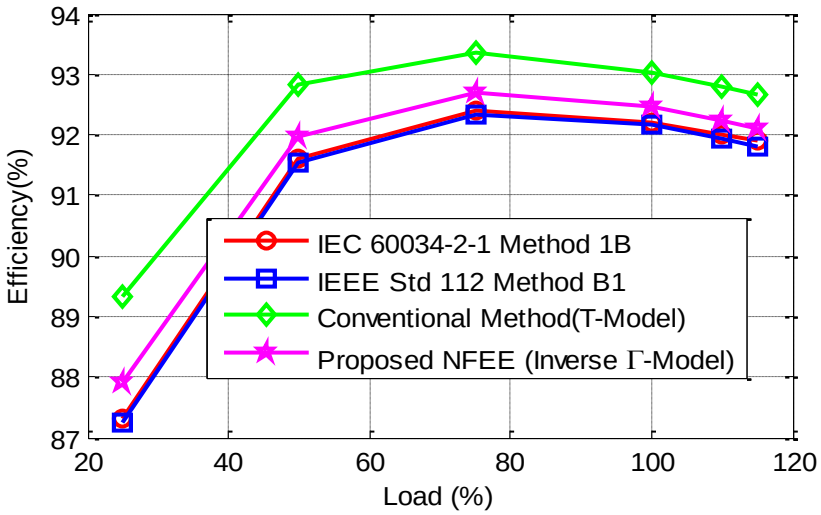

Fig. 4.32. Comparison of efficiency results for the 45kW test motor

Using linear regression analysis to smoothen the stray-load loss, the correlation coefficients R^2 results for the tested motors are shown in Fig's. 4.33 to 4.36. A value for R^2 close to 1 is required in the loss segregation method, as this is indicative of the level of correctness or accuracy of the instruments and the test readings. According to the IEEE Std. 112 and IEC60034-2-1, the value of R^2 should be greater than 0.90 and 0.95 respectively for a test to be considered satisfactory. Based on the obtained correlation coefficients values, it can be concluded that the test measurements are satisfactory and in conformity to the stipulated conditions of the IEEE and IEC standards.

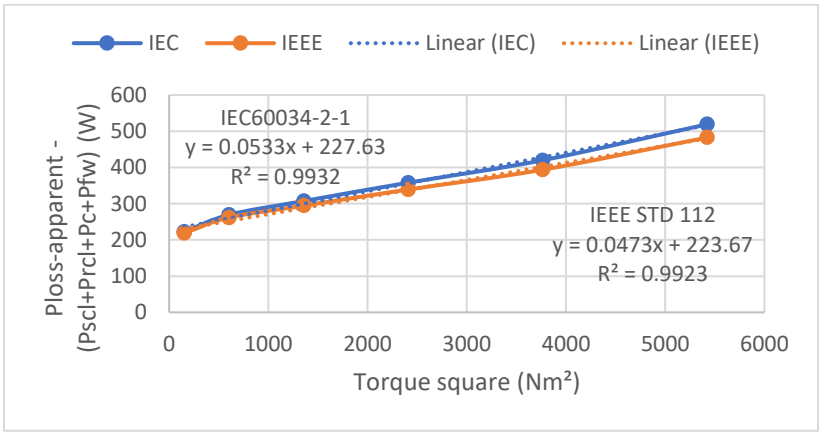

Fig. 4.33. Correlation coefficients of the IEEE and IEC methods for the 7.5kW test motor

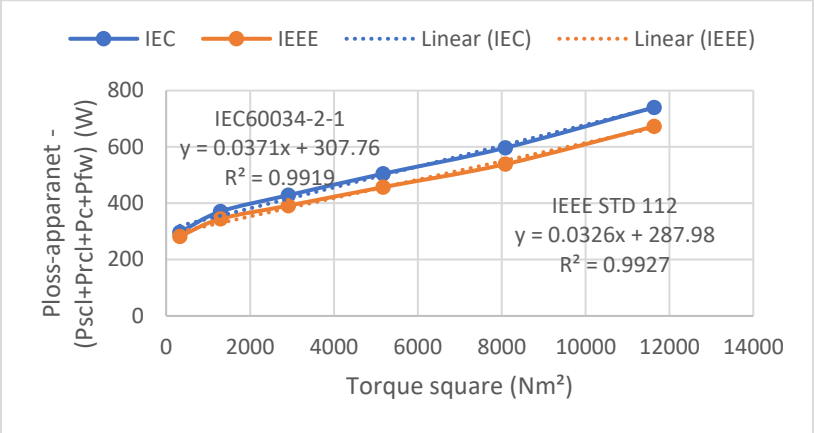

Fig. 4.34. Correlation coefficients of the IEEE and IEC methods for the 11kW test motor

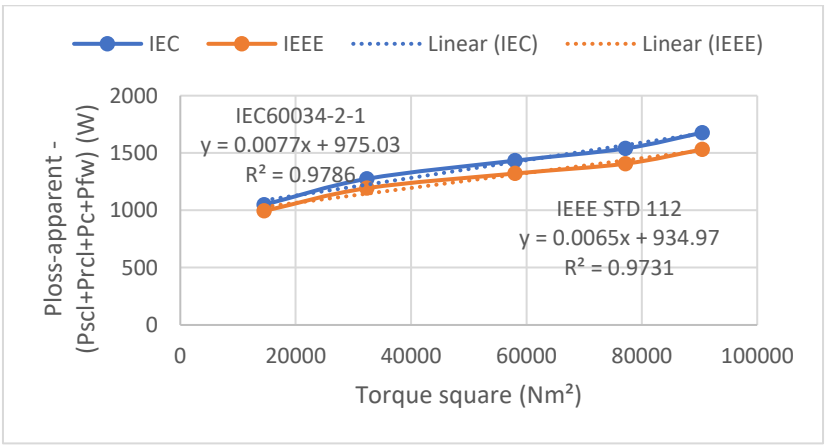

Fig. 4.35. Correlation coefficients of the IEEE and IEC methods for the 37kW test motor

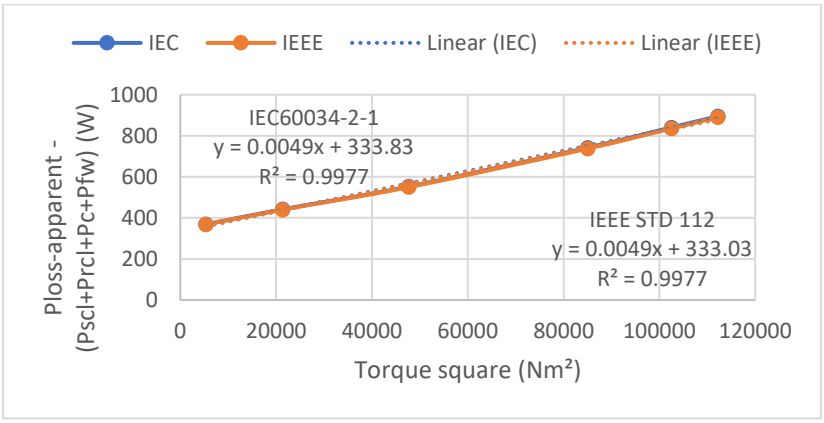

Fig. 4.36. Correlation coefficients of the IEEE and IEC methods for the 45kW test motor

The efficiency results based on the proposed NFEE method as reported in Fig's. 4.29 to 4.32 indicate close agreement when compared to the loss segregation methods for all the loading points. This can further be clearly seen in the summary of the results at key load points and the corresponding absolute errors with respect to the IEEE and IEC methods as presented in Table 4.6. Taking for instance, the results presented in Fig. 4.31 in respect to the 37kW test motor, the NFEE absolute efficiency errors at the rated operating condition when compared to the IEEE and IEC methods are 0.17606% and 0.32441% respectively. However, the conventional method presents efficiency errors of 0.73970% and 0.88805% when compared to the IEEE and IEC standards respectively. Again, referring to Table 4.6, the maximum absolute efficiency errors (considering all the tested motors) are 0.79243% and 2.4261% respectively for the NFEE and the convention method.

The relatively good results by the NFEE method with respect to all the tested motors can be attributed to the improvements in the parameter identification method as well as the friction and windage loss estimation using the proposed AGT method as opposed to using an assumed fixed value for all load points.

TABLE 4.6

ESTIMATED EFFICIENCIES OF THE MOTOR AT KEY LOAD POINTS

Motor	Load (%)	Measured		Estimated					
		IEEE	IEC	NFEE			T-Model		
		Eff. (%)	Eff. (%)	Eff. (%)	Abs. Error IEEE	Abs. Error IEC	Eff. (%)	Abs. Error IEEE	Abs. Error IEC
7.5kW	100	87.699	87.672	87.946	0.247	0.274	88.948	1.249	1.276
	75	88.703	88.757	89.104	0.402	0.347	89.978	1.275	1.221
	50	88.606	88.709	89.077	0.471	0.368	89.883	1.277	1.174
	25	84.898	85.030	85.474	0.576	0.443	86.386	1.488	1.356
11kW	100	88.857	88.984	89.109	0.252	0.125	89.799	0.942	0.815
	75	89.629	89.611	90.091	0.461	0.479	90.851	1.222	1.240
	50	89.192	89.038	89.831	0.639	**0.792**	90.796	1.604	1.758
	25	84.986	84.726	85.432	0.446	0.706	87.049	2.063	2.322
37kW	100	91.292	91.144	91.468	**0.176**	**0.324**	92.032	0.740	0.888
	75	91.576	91.387	91.650	0.074	0.263	92.485	0.909	1.098
	50	90.786	90.567	90.736	0.050	0.169	92.030	1.244	1.463
	25	86.369	86.116	86.155	0.214	0.038	88.542	2.174	**2.426**
45kW	100	92.156	92.216	92.470	0.314	0.254	93.040	0.884	0.824
	75	92.342	92.410	92.704	0.362	0.294	93.358	1.016	0.948
	50	91.527	91.599	91.974	0.447	0.376	92.823	1.296	1.225
	25	87.238	87.321	87.911	0.673	0.590	89.325	2.087	2.004

Various components of the motor losses can be analysed through the loss segregation methods of the IEEE and IEC standards. These respective losses can then be compared to the proposed NFEE and standard EC method. The results shown in Fig's. 4.37 to 4.41 are in respect to the 37kW (standard efficiency) and 11kW (premium efficiency) test motors. As expected, the copper losses for the IEEE and IEC methods are quite similar, with only slight differences at higher load points. This can be attributed to the difference in approach for temperature correction. An overestimation of the copper losses for both the NFEE and the conventional EC method can be explained by the difference in the measured and estimated stator currents from equivalent circuits.

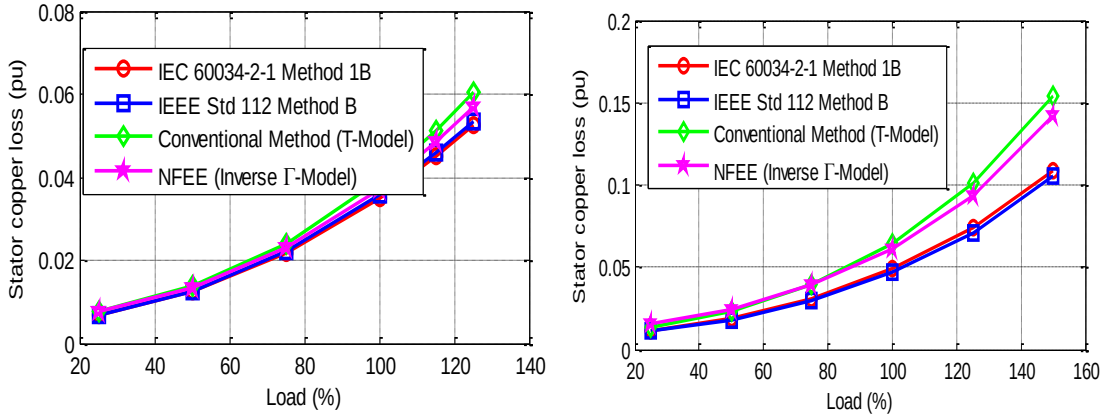

(a) (b)

Fig. 4.37. Measured and estimated P_{scl} losses. (a) 37kW test motor (b) 11kW test motor

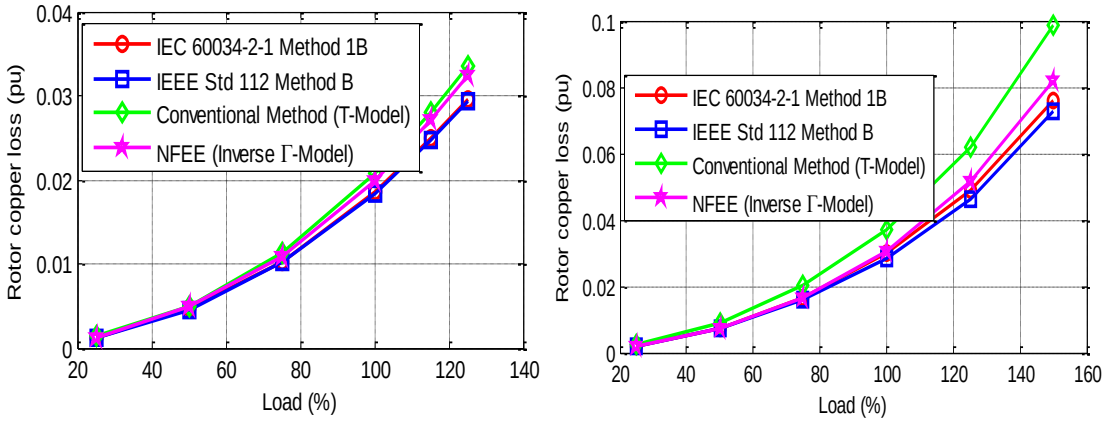

(a) (b)

Fig. 4.38. Measured and estimated P_{rcl} losses. (a) 37kW test motor (b) 11kW test motor

For the core loss, similar results are obtained for both the IEEE and IEC methods as reported in Fig. 4.39 (a) and (b). This is because both standards use the same voltage drop equation to account for the stator winding voltage drop for each load point. However, divergent results could be observed in the case of the proposed NFEE and the Conventional method. While the NFEE method slightly overestimates the core loss for the 37kW motor (Fig. 4.39(a)), the conventional EC method underestimates the core loss. However, as reported in Fig. 4.39(b) the conventional method overestimates the core loss for the 11kW motor. Thus, the conventional method cannot provide an acceptable estimation of the core loss due to the disparity in the core loss resistance estimation. Clearly, the disparity in the core loss has a greater impact on the efficiency

results than the other estimated losses that are seen to be closer to their respective measured values (from the IEEE and IEC loss segregation methods).

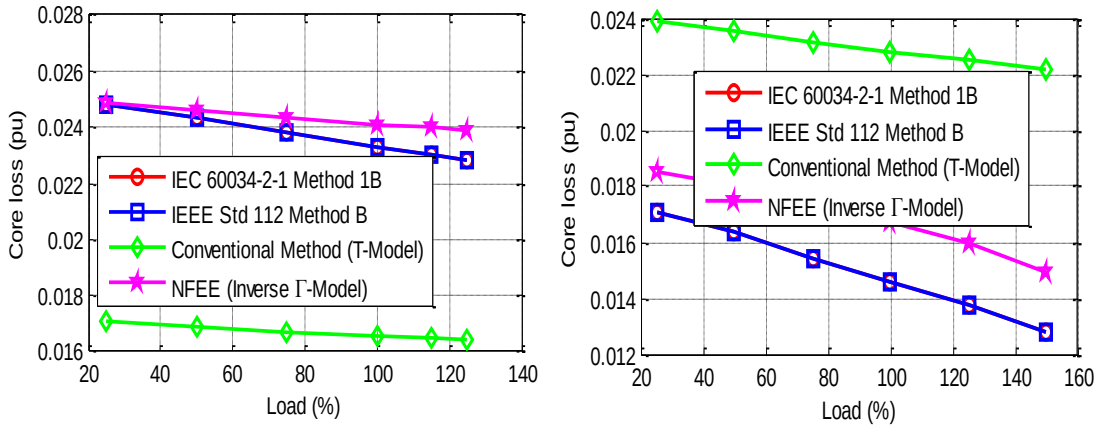

Fig. 4.39. Measured and estimated core loss P_{fe} losses (a) 37kW test motor (b) 11kW motor

With reference to the stray-load loss results shown in Fig. 4.40(a) and (b), both the NFEE and conventional method account for the stray-load loss in a similar manner by introducing a load dependent resistance on the rotor side. However, the NFEE method gives more acceptable estimation of the stray-load loss for the two tested motors when compared to the conventional method. This is because of the difference in the estimated rotor currents for the two EC implementations.

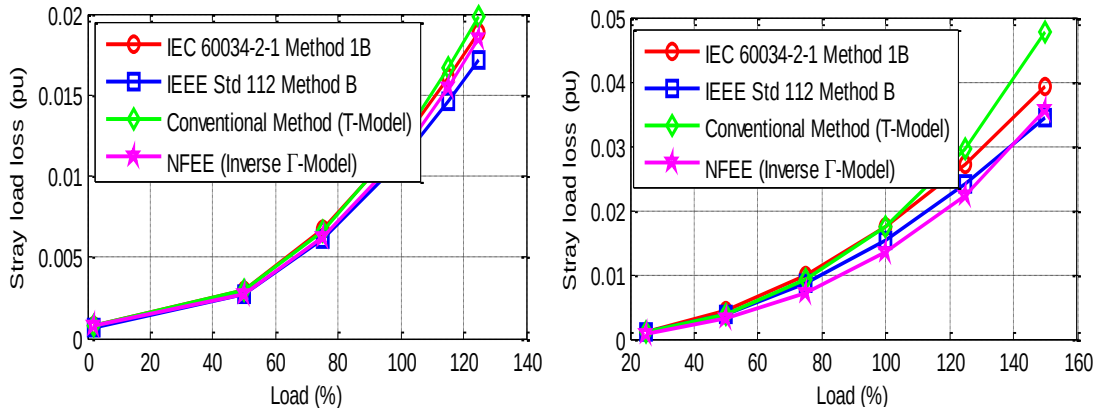

Fig. 4.40. Measured and estimated stray-load loss P_{sll} losses (a) 37kW motor (b) 11kW motor

For the friction and windage loss, the NFEE results as shown in Fig. 4.41(a) and (b) for all load points are closer to the loss segregation methods when compared to the conventional method which is based on an assumed value of 1.2% of the rated power as suggested in [7].

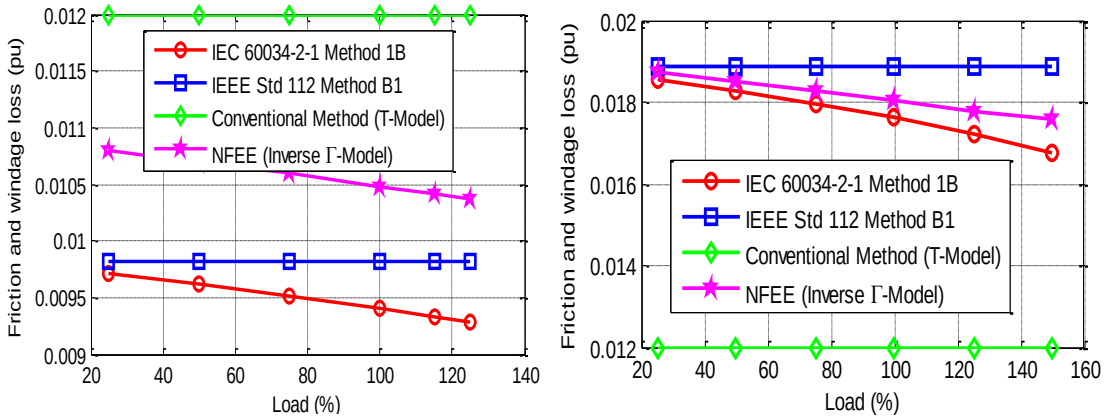

(a) (b)

Fig. 4.41. Measured and estimated friction and windage P_{fw} losses (a) 37kW motor (b) 11kW motor

4.6.4 CASE 2: Unbalanced Voltage Supply Condition

The motors were tested at different voltage unbalance (VU) values ranging from mild (1% VU) to severe (5% VU) condition. This was realized by adjusting the amplitudes of the line-to-line voltages using the programmable power supply unit. Throughout the VU test, the highest total voltage harmonic distortion (THD_v) value was kept below 0.36% in order to limit the impact of harmonics on the motors. The sequence component voltages and hence the VU defined as the ratio of the negative to positive sequence voltage are calculated from the line-to-line voltages using (4.31) to (4.37).

Since only the rotor parameters are largely influenced by skin effect due to the VU condition, only the negative sequence rotor parameters are set as unknown variables and are determined by the method proposed in section 4.5.2. The estimated parameters are presented in Table 4.7.

TABLE 4.7

ESTIMATED NEGATIVE SEQUENCE EC PARAMETERS OF THE TESTED MOTORS

Motor	Model	X_{lr2} (Ω)	R_{r2} (Ω)
7.5kW	T-Model	2.926	2.109
	Inverse Γ -Model	-	2.059
11kW	T-Model	2.627	1.898
	Inverse Γ -Model	-	1.831
37kW	T-Model	0.438	0.382
	Inverse Γ -Model	-	0.368
47kW	T-Model	0.332	0.308
	Inverse Γ -Model	-	0.285

With the parameters of the positive and negative sequence equivalent circuits determined, the full-load and partial loads efficiencies can be calculated as per the proposed NFEE method. The impact of VU on the efficiency of the 37kW motor is shown in Fig. 4.42 and 4.43. The results at rated load are summarized in Table 4.8 alongside the computed absolute efficiency errors for each VU when compared to the Measured efficiencies. As can be observed in Table 4.8 for the 37kW motor, the NFEE method was able to predict the efficiency more correctly with a maximum error of 0.48% at 2% VU when compared to the conventional method which gives a maximum error of 1.37%. Furthermore, these results suggest an improvement in terms of accuracy when compared to the results presented in similar studies [54], [64].

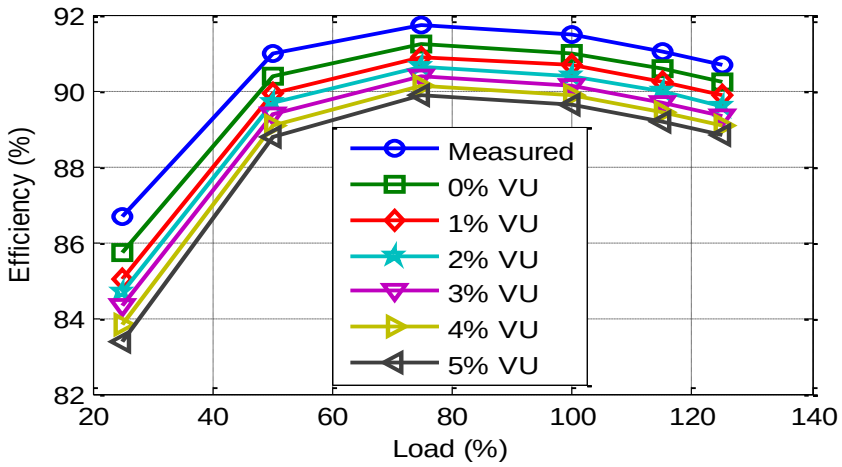

Fig. 4.42. Efficiency under VU on the 37kW motor (Inverse Γ-Model)

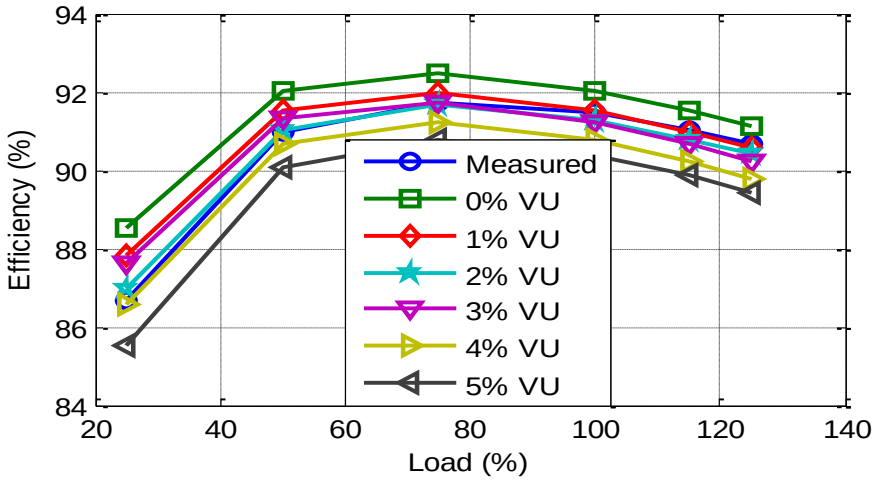

Fig. 4.43. Efficiency under VU on the 37kW motor (T-Model)

TABLE 4.8

MEASURED AND ESTIMATED EFFICIENCY FOR THE TESTED MOTORS

Motor	VU (%)	Measured Eff. (%)	Eff. (%) (NFEE)	Error (NFEE)	Eff. (%) (Conv.)	Error (Conv.)
7.5kW	0	87.70	87.95	0.25	88.95	1.25
	1	87.04	87.78	0.74	88.65	1.61
	2	86.82	87.69	0.87	88.4	1.58
	3	86.57	87.52	0.95	88.02	1.45
	4	86.39	87.4	1.01	87.92	1.53
	5	86.07	87.31	1.24	87.49	1.42
11kW	0	88.86	89.01	0.15	89.86	1.00
	1	88.51	88.89	0.38	89.58	1.07
	2	88.11	88.75	0.64	89.52	1.41
	3	87.83	88.64	0.81	89.12	1.29
	4	87.48	88.38	0.9	88.63	1.15
	5	87.22	88.2	0.98	88.21	0.99
37kW	0	91.51	91.00	0.51	92.03	0.52
	1	90.34	90.67	0.33	91.05	0.71
	2	**89.92**	**90.40**	**0.48**	**91.29**	**1.37**
	3	90.25	90.14	0.11	91.22	0.97
	4	90.15	89.89	0.26	90.76	0.61
	5	89.20	89.65	0.45	90.39	1.19
45kW	0	92.16	92.47	0.31	93.04	0.88
	1	91.86	92.28	0.42	92.76	0.9
	2	91.55	92.17	0.62	92.49	0.94
	3	91.07	92.03	0.96	92.21	1.14
	4	90.94	91.89	0.95	92.04	1.10
	5	90.71	91.74	1.03	91.82	1.11

4.6.5 Repeatability Analysis

The repeatability test has been performed in order to verify the consistency of results obtained using the proposed NFEE method. The NFEE algorithm is repeated ten times using the same set of measured input data and the results are statistically analysed. Fig. 4.44 and 4.45 show the efficiency profiles of the 7.5kW motor under balanced power supply for the conventional and NFEE method.

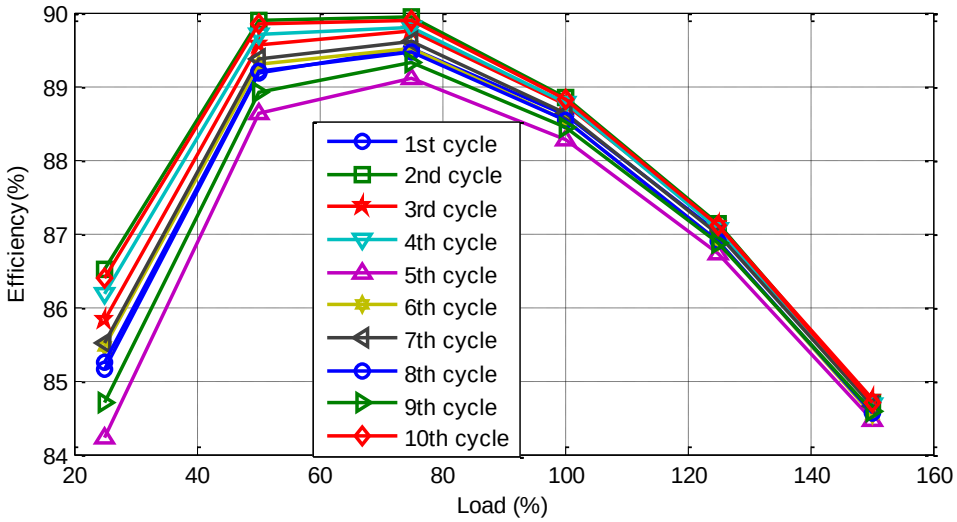

Fig. 4.44. Repeatability test on the 7.5kW motor using the conventional method

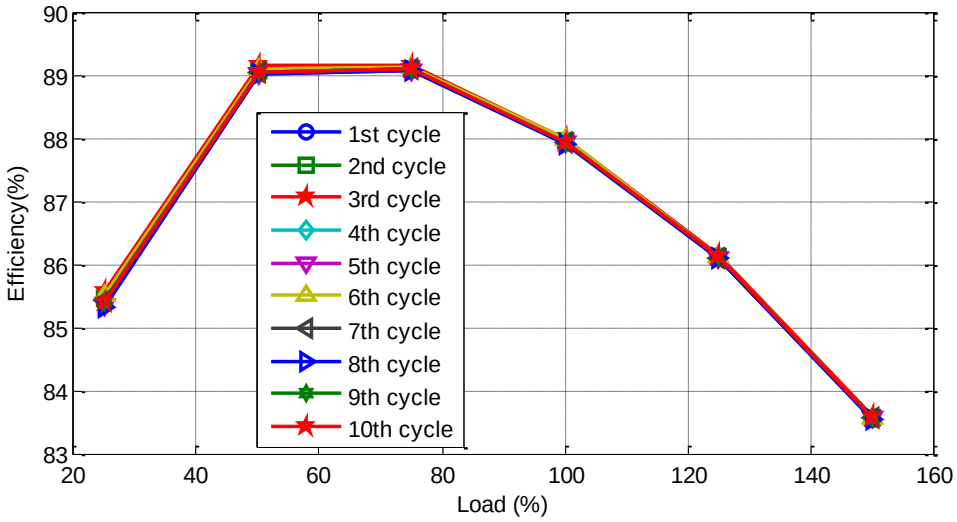

Fig. 4.45. Repeatability test on the 7.5kW motor using the proposed NFEE method

Referring to Fig. 4.44 and 4.45, it can be clearly seen that deviations in the efficiency results are much wider for the conventional method. Also, these deviations are wider on the low loading points which is expected as the motor generally experiences a slight rise in voltage at lower loadings and consequently an increase in the flux density. The statistical analysis of the results in terms of the mean, standard deviation and coefficient of variance of the results presented in Fig 4.44 and 4.45 are summarized in Tables 4.9.

TABLE 4.9

STATISTICAL ANALYSIS OF EFFICIENCY RESULTS FOR THE 7.5KW MOTOR

Method	**Load**	**Mean** $(\boldsymbol{\mu})$	**Std. Deviation** $(\boldsymbol{\sigma})$	**Coefficient of Variance** $(\boldsymbol{cv})$
Conventional Method	150%	84.636	0.095	0.112
	125%	86.978	0.127	0.146
	100%	88.621	0.179	0.202
	75%	89.589	0.259	0.289
	50%	89.358	0.404	0.452
	25%	85.523	0.730	0.853
NFEE Method	150%	83.563	0.013	0.015
	125%	86.115	0.015	0.018
	100%	87.949	0.019	0.022
	75%	89.102	0.026	0.030
	50%	89.064	0.040	0.044
	25%	85.437	0.070	0.082

At the rated condition, the coefficients of variance (which is a measure of the dispersion of data points relative to the mean) for the absolute error in full-load efficiency when compared to the measured value are calculated as 19.38% and 8.16% respectively for the conventional and NFEE method. These results as summarized in Table 4.10 and 4.11 confirm the consistency of the efficiency results obtained using the NFEE algorithm.

TABLE 4.10

STATISTICAL ANALYSIS OF EFFICIENCY RESULTS FOR 7.5KW MOTOR USING THE CONVENTIONAL METHOD

Cycle	Measured Eff. (IEEE) (%)	Estimated Eff. (%)	Absolute Error (%)
1	87.699	88.598	0.899
2	87.699	88.846	1.147
3	87.699	88.751	1.052
4	87.699	88.765	1.067
5	87.699	88.284	0.585
6	87.699	88.545	0.846
7	87.699	88.632	0.933
8	87.699	88.528	0.829
9	87.699	88.446	0.747
10	87.699	88.821	1.122
Mean	-	88.621	0.923
Std.	-	0.179	0.179
cv. (%)	-	0.202	**19.375**

TABLE 4.11

STATISTICAL ANALYSIS OF EFFICIENCY RESULTS FOR 7.5KW MOTOR USING THE NFEE METHOD

Cycle	Measured Eff. (IEEE) (%)	Estimated Eff. (%)	Absolute Error (%)
1	87.699	87.941	0.243
2	87.699	87.951	0.252
3	87.699	87.990	0.291
4	87.699	87.953	0.254
5	87.699	87.932	0.234
6	87.699	87.973	0.274
7	87.699	87.943	0.244
8	87.699	87.916	0.218
9	87.699	87.943	0.245
10	87.699	87.943	0.244
Mean	-	87.949	0.250
Std.	-	0.020	0.020
cv. (%)	-	0.023	**8.163**

4.6.6 Sensitivity Analysis

The impact of parameter changes on the performance of the efficiency estimation algorithms are analysed in this section. To investigate the sensitivity, the algorithms were tested at the rated condition for the balanced condition and a 5% VU condition according to the following scenarios:

- Case (A) to (F): A $\pm 10\%$ change in values of R_s, X_{ls}, X_{lr}, X_m, R_c and R_{fe} respectively considering the parameters reported in Table 4.4 as reference. One parameter is varied at a time while keeping all other parameters constant.
- Case (G): The magnetization branch in the negative sequence equivalent circuit due to unbalance operation is omitted.
- Case (H): The changes in rotor leakage reactance due to skin effect for the VU case is omitted. Hence only the change in rotor bar resistance is considered.
- Case (I): Both the change in rotor bar resistance and rotor leakage reactance due to skin effect for the VU case is omitted. This implies that same equivalent circuit parameters are used for the positive and negative sequence circuits. This condition is applied to both the T-model and the inverse Γ-model equivalent circuits implementations.

In all the cases considered, the highest error with reference to the measured value using the IEEE Method B1 is considered. These values are reported in Table 4.12 while the detail for other load points can be found in Appendix D. Based on the results of the sensitivity analysis, the following conclusions can be made:

1) The results for case (A) to (F) indicates that the parameters with most notable influence on the efficiency are the stator and rotor resistances. This is because their values directly affect the motor output power. Similar results have been observed for all other tested motors. It is therefore important to ensure accurate estimation or measurement of these parameters.

2) The results obtained for case (G) shows that neglecting the impact of the magnetization branch on the negative sequence equivalent circuit due to VU

condition is negligible. This is because of the high impedance along the magnetization branch when compared to the rotor circuit. By comparing the results reported in Tables 4.6 and 4.12, the relative change in the absolute errors were 0.3% and 0.17% for the conventional and NFEE method respectively.

3) The results for case (H), is applicable only to the conventional model since the inverse Γ-model has only the stator leakage reactance. The relative error in this case is about 0.49% which shows that the change in rotor leakage reactance has impact on the efficiency results.

4) The results for case (I) show notable changes in efficiency results owing to the impact of skin effect on the motor. Relative errors of 0.58% and 0.33% were obtained for the conventional and NFEE method respectively

TABLE 4.12

SENSITIVITY ANALYSIS OF EFFICIENCY RESULTS FOR 7.5KW MOTOR USING THE CONVENTIONAL METHOD

Voltage Supply	Case	Mea. Eff. (%)	Conventional Method		NFEE Method	
			Est. Eff. (%)	Abs. Error (%)	Est. Eff. (%)	Abs. Error (%)
Balanced	A	87.699	89.321	1.622	88.535	0.836
	B	87.699	88.830	1.131	87.949	0.250
	C	87.699	88.876	1.177	-	-
	D	87.699	88.950	1.251	88.109	0.410
	E	87.699	-	-	88.058	0.359
	F	87.699	88.981	1.282	-	-
Unbalanced (5% VU)	G	86.079	87.615	1.536	87.332	1.253
	H	86.079	87.808	1.729	-	-
	I	86.079	87.904	1.824	87.431	1.752

4.6.7 Error Analysis

Although various sources of errors are associated with the experimental efficiency testing process, an error analysis could be used to determine the level of accuracy of the measurements and the final efficiency results. Generally, the three sources of error typically associated with experimental measurements are the methodological, instrumental, and personnel errors, which can be expressed as:

$$\zeta = \zeta_m + \zeta_i + \zeta_h \tag{4.75}$$

Where: ζ is the absolute measured error, ζ_m is the methodological error and ζ_p is the human error.

In this study, the Worst-Case Error Estimation (WCEE) method and the Realistic Error Estimation (REE) method are used to quantify the errors associated with the proposed NFEE method. The WCEE represent the worst-case scenario in which it is assumed that maximum errors of all instruments are present simultaneously [124]. Each individual error source is treated separately by computing its impact on the output using the expression in (4.76).

$$\varepsilon_y = \frac{\zeta_y}{y} = \frac{1}{y}\frac{\partial f}{\partial x_p}\zeta_{x_p} = \frac{x_p}{y}\frac{\partial f}{\partial x_p}\varepsilon_{x_p} \tag{4.76}$$

Where: ε_y is the relative error on the output y due to the independent input variable $x_p (0 \leq p \leq n)$.

Based on (4.76), the sensitivity of the input variable x_p in relation to the output variable y can be written as:

$$I_{x_p} = \frac{\varepsilon_y}{\varepsilon_{x_p}} = \frac{x_p}{y}\frac{\partial f}{\partial x_p} \tag{4.77}$$

Thus, the WCEE in the output is determined using (4.78) [124].

$$WCEE = \sum_{i=1}^{n} I_{x_i}\varepsilon_{x_i} + \frac{1}{y}\sum_{i=1}^{n} W_{z_i}z_i \tag{4.78}$$

Where: z_i is the additive noise and W_{z_i} is its influence coefficient.

The derivative terms in (4.77) for a complex system such as the induction motor cannot be easily determined, hence the easiest alternative is to add small perturbations to the input variables in order to calculate the sensitivity or influence coefficient associated with each individual variable. In this research, a perturbation of ± 5 were added to the input variables and the corresponding influence on the efficiency were determined. As an example, Fig. 4.46(a) and (b) show the influence coefficients in terms of the variations in the input voltage obtained at rated load through linear regression for two of the tested motors (7.5kW and 37kW). All other graphs for computing the influence coefficient are shown in Appendix E.

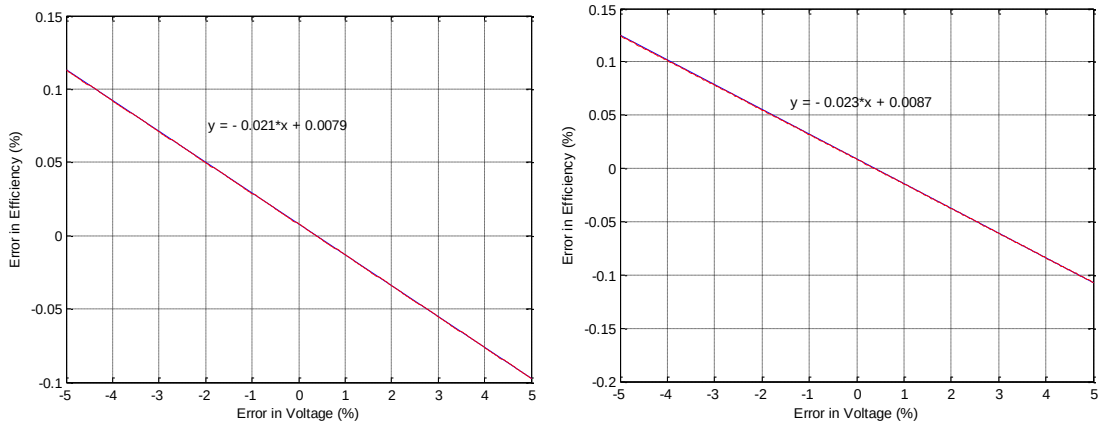

(a) (b)

Fig. 4.46. Influence coefficients for input voltage perturbations for the (a) 7.5kW test motor and (b) 37kW test motors

The REE method provides a more realistic estimation of the error when compared to the WCEE. This is because the REE accounts for the influence of individual errors separately. The method differentiates the errors based on their overall influence on the output, hence the overall estimation reflects the reality of errors that occur in

measurement systems [125]. For uniformly distributed errors, the expression for the REE is given by [124].

$$REE = \sqrt{\sum_{i=1}^{n}\left(I_{x_i}\varepsilon_{x_i}\right)^2 + \frac{1}{y^2}\sum_{i=1}^{n}\left(W_{z_i}z_i\right)^2} \tag{4.73}$$

By using the WCEE and the REE methods, the errors in efficiency estimation for the direct method and the NFEE method are obtained. Tables 4.13 to 4.16 show the computed error estimates at rated load. These results are summarized in Table 4.17 for the NFEE and the direct method.

TABLE 4.13

ERROR ANALYSIS OF EFFICIENCY RESULTS FOR 7.5KW MOTOR USING THE DIRECT METHOD

Error Source	Instrument Error (%)	Absolute Influence Coefficient	WCEE (%)	REE (%)	Rank
Input Voltage	±0.200	0.000	0.000	0.000	NA
Input Current	±0.200	0.000	0.000	0.000	NA
Input Power	±0.200	1.000	0.200	0.040	1.000
Shaft Torque	±0.200	1.000	0.250	0.063	1.000
Rotor Speed	±0.050	1.100	0.055	0.003	2.000
Temperature	±0.075	0.000	0.000	0.000	NA
Sum			**0.505**	**0.325**	

TABLE 4.14

ERROR ANALYSIS OF EFFICIENCY RESULTS FOR THE 37KW MOTOR USING THE DIRECT METHOD

Error Source	Instrument Error (%)	Absolute Influence Coefficient	WCEE (%)	REE (%)	Rank
Input Voltage	±0.200	0.000	0.000	0.000	NA
Input Current	±0.200	0.000	0.000	0.000	NA
Input Power	±0.200	1.000	0.200	0.040	1.000
Shaft Torque	±0.200	1.000	0.200	0.040	1.000
Rotor Speed	±0.050	1.000	0.050	0.003	2.000
Temperature	±0.075	0.000	0.000	0.000	NA
Sum			**0.450**	**0.287**	

TABLE 4.15

ERROR ANALYSIS OF EFFICIENCY RESULTS FOR 7.5KW MOTOR USING THE PROPOSED NFEE METHOD

Error Source	Instrument Error (%)	Absolute Influence Coefficient	WCEE (%)	REE (%)	Rank
Input Voltage	±0.200	0.021	0.004	0.000	2.000
Input Current	±0.200	0.021	0.004	0.000	2.000
Input Power	±0.200	0.000	0.000	0.000	NA
Shaft Torque	±0.200	0.000	0.000	0.000	NA
Rotor Speed	±0.050	4.300	0.215	0.046	1.000
Temperature	±0.075	0.012	0.009	0.000	3.000
Sum			**0.232**	**0.215**	

TABLE 4.16

ERROR ANALYSIS OF EFFICIENCY RESULTS FOR 37KW MOTOR USING THE PROPOSED NFEE METHOD

Error Source	Instrument Error (%)	Absolute Influence Coefficient	WCEE (%)	REE (%)	Rank
Input Voltage	±0.200	0.023	0.005	0.000	2.000
Input Current	±0.200	0.078	0.016	0.000	2.000
Input Power	±0.200	0.000	0.000	0.000	NA
Shaft Torque	±0.200	0.000	0.000	0.000	NA
Rotor Speed	±0.050	4.700	0.235	0.055	1.000
Temperature	±0.075	0.012	0.009	0.000	3.000
Sum			**0.264**	**0.236**	

TABLE 4.17

ERROR ANALYSIS RESULTS FOR THE DIRECT AND PROPOSED NFEE METHOD

Machine	Error in Efficiency Direct Method		Error in Efficiency Proposed NFEE Method	
	WCEE (±%)	REE (±%)	WCEE (±%)	REE (±%)
7.5kW motor	0.505	0.325	0.232	0.215
37kW motor	0.450	0.287	0.264	0.236

Based on the results obtained as shown in Table 4.17, the following conclusions can be made:

(i) The REE method using direct and NFEE method for the two tested motors gives lower error values than the WCEE method. This is expected since the WCEE considers all errors simultaneously whereas the REE only reflects on specific error associated with the measurement process. Thus, the REE gives a more realistic estimation of the errors.

(ii) For both motors, the error results show close agreement for the direct and NFEE method.

(iii) The REE results for the NFEE method for both motors show improvements when compared to the results of the equivalent circuit method presented in [62].

(iv) The results show that the average error to be expected when using the proposed NFEE method is about $\pm 0.22\%$.

4.6.8 Software Development

Using the Matlab's App designer toolbox, an interactive software tool is developed based on the proposed NFEE algorithm. The software which uses an interactive Graphic User Interface (GUI) allows the user to enter the motor test measurements and nameplate data on the front panel in order to estimate its efficiency. The two methods (i.e. Case 1 and Case 2) for balanced and unbalanced power supply condition are integrated into the software tool using a drop-down box as shown on the screen shoot of the front panel in Fig. 4.47.

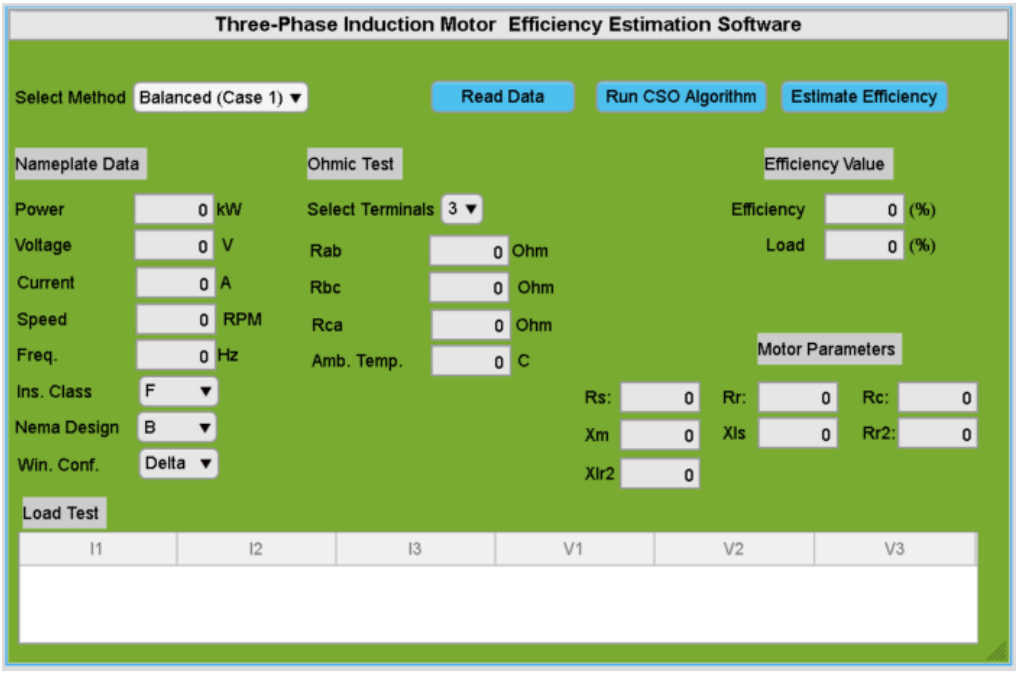

Fig. 4.47. Front panel of the developed software

The software was implemented in three stages using three separate push buttons (shown in blue) on the front panel. These push buttons link the call-back subroutines to the GUI for reading data and implementing the parameter identification and efficiency estimation algorithms. To run the software, the user needs to follow the following steps.

1. Selects the method of estimation and specify the nameplate data and stator resistance ohmic test measurements.
2. Click on the read data button. This will load the data points of the recorded steady state voltage and current signals and also display the results on the front panel (table). However, the user must ensure the recorded experimental waveform signal file is saved on the same Matlab's current directory prior to loading the data.
3. Click on the run CSO algorithm button. This will execute the CSO algorithm to estimate the motor equivalent circuit parameters. The estimated parameters at the end of the CSO iterations are displayed on the front panel.
4. Finally click on the estimate efficiency button to run the modified IEEE Form F2 for calculating the motor efficiency.

Fig. 4.48 shows the efficiency test results and the parameter estimates results on the front panel after running the software.

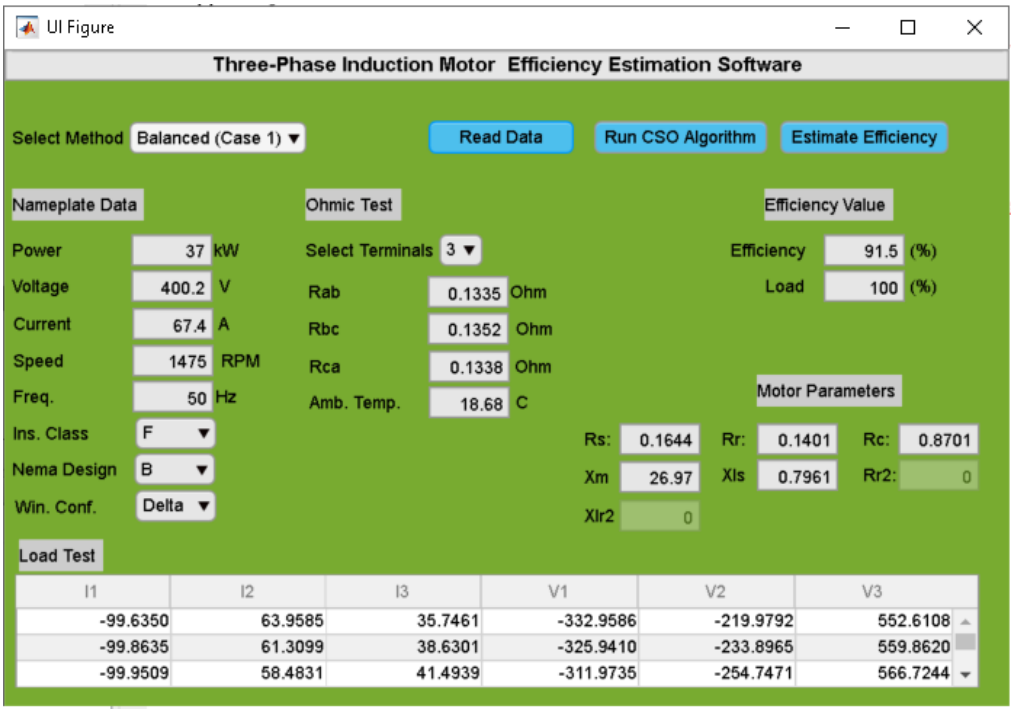

Fig. 4.48. 37kW motor efficiency test results for Case 1.

4.7 Conclusions

For in-field motor efficiency estimation, an acceptable level of accuracy is required while maintaining the lowest level of intrusion. This challenging task can only be realized using methods that rely on limited nonintrusive measurements at the motor terminals. The goal was to develop such a method for induction motor efficiency estimation. Firstly, the conventional T-model equivalent circuit has been modified into an inverse Γ-model with series core loss arrangement to improve motor parameter estimation accuracy. Furthermore, the airgap torque method was introduced to determine good initial boundary conditions for the core loss resistance. This is necessary to guarantee the convergence and accuracy of the core loss estimation. In addition, the airgap torque and motor nameplate data are applied to estimate the friction and windage loss. This loss component is not accounted for in the motor equivalent

circuit and is usually assigned a fixed percentage based on the motor power rating, which may significantly affect the accuracy of the overall efficiency results.

The proposed NFEE method is validated by experimental tests on four distinct induction motors. The accuracy of the conventional method in estimating the core-loss resistance seems compromised to a large extent with some levels of inconsistency as well in the estimation of the leakage and magnetization reactances. Conversely, the proposed NFEE method offers a more acceptable estimation of the core loss and other motor EC parameters. Consequently, the NFEE gave more acceptable efficiency errors of 0.32% and 0.13% for a balance voltage supply at rated load for the 37kW and 11kW motors respectively when compared the well-known IEEE Std. 112 Method B. Also, for unbalanced voltage supply, the proposed NFEE method was able to predict more correctly the efficiency with a maximum error of 0.48% at 2% VU when compared to the conventional method which gives a maximum error of 1.37%.

The error analysis results indicate that the proposed method has about $\pm 0.22\%$ uncertainty level which is an acceptable margin. Thus, the proposed NFEE can be used to estimate the efficiency of induction motors with acceptable accuracy and intrusion level.

Finally, an interactive software was developed to simplify the efficiency estimation process and accommodate both balanced and unbalanced supply conditions. This makes the proposed algorithm a handy tool that can be used in industry for three-phase induction motor efficiency estimation.

Chapter 5

Induction Motor Efficiency Estimation under Non-sinusoidal Supply Condition

5.1 Overview

Considering that the proposed method presented earlier in chapter four for IM efficiency estimation worked well under sinusoidal supply condition with acceptable levels of accuracies for both balance and unbalanced supply conditions, this chapter extends the method for non-sinusoidal supply conditions - to take into account the presence of harmonics in the power supply. By using a modified equivalent circuit approach, the method considers the variations of the core loss resistance due to time harmonics. Also, the changes in the rotor bar resistance and the leakage inductance due to skin effects at higher frequencies is considered in the harmonic equivalent circuit. Finally, the efficiency estimation via the proposed method is compared to the IEC60034-2-3 standards in the case of a balanced non-sinusoidal supply condition. This will allow not only the efficiency comparison but also the loss segregation analysis on the various components of the motor losses. In the case of an unbalanced supply, the

efficiency results are compared to measured values obtained via the direct input-output method.

5.2 Introduction

In addition to the problem of unbalanced voltage supply, the presence of harmonics significantly affects the operation of induction motors. More notably is the increase in copper and core losses. In terms of the copper losses, the additional losses come from the increase in the rms values of the stator currents and stator winding resistance due to the higher operating temperature of the inverter or distorted power supply [126]. The core loss, comprising of the hysteresis and eddy current losses (both of which are frequency dependant) are directly affected by the presence of low order harmonics in the power supply.

While there are several methods that allow for the estimation of induction motor efficiency, only a few of those methods can be considered for motors operating under distorted or non-sinusoidal supply condition. One of the methods is the airgap torque method in which the airgap power is estimated based on the voltage and current waveforms. However, in the AGT method, the mechanical and core loss are not accounted for, hence, an assumed fixed percentage value is used. This may have an impact on the accuracy of the method particularly for the non-sinusoidal supply since the presence of harmonics directly affect the core loss due to its dependence on frequency.

The equivalent circuit method in conjunction with optimization techniques can be used for solving the efficiency estimation problem in the presence of harmonics in the power supply as clearly demonstrated in [65], [84]-[85]. However, the impact of the non-sinusoidal supply on the rotor and core loss resistances has not been taken into consideration.

5.3 Additional Motor Losses due to Harmonic Voltage Supply

Induction motor equivalent circuit parameters may vary considerably with frequency due to harmonics associated with non-sinusoidal supply. The expression for the stator copper loss P_{scl-h} due to harmonic supply is given by:

$$P_{scl-h} = 3R_{sc}\left(I_{sf}^2 + \sum_{h=5}^{\infty} I_{sh}^2\right) \tag{5.1}$$

Where:

I_{sf} is the stator fundamental current.

I_{sh} is the h^{th} order harmonic current in the stator.

R_{sc} is the stator winding resistance corrected to account for the additional losses due to harmonics in the supply.

The harmonic copper loss in the rotor P_{rcl-h} is given by:

$$P_{rcl-h} = 3\left(\frac{R_{r-f}}{s_f} I_{rf}^2 + \left(\sum_{h=5}^{\infty} I_{rh}^2 \frac{R_{rh}}{s_h}\right)\right) \tag{5.2}$$

Where:

I_{rf} is the rotor fundamental current.

I_{rh} is the h^{th} order harmonic current in the rotor.

R_{rh} is the h^{th} harmonic rotor winding resistance.

s_f and s_h are the fundamental and the harmonic slip respectively.

s_h can be determined by the expression in (5.3)

$$s_h = \frac{hn_1 \mp n}{hn_1} \tag{5.3}$$

Where the negative and positive signs in (5.3) represent the forward and backward rotating harmonics respectively.

Simplifying (5.3), s_h can be expressed for the forward and backward rotating harmonics as given in (5.4) and (5.5) respectively.

$$s_{hf} = \frac{(h-1) + s_1}{h} \tag{5.4}$$

$$s_{hb} = \frac{(h+1) - s_1}{h} \tag{5.5}$$

Note that the rotor resistance R_{rh} varies appreciably with frequency due to skin effect [105] and as shown in (5.2), this variation is separately considered for each harmonic order.

The core loss consisting the sum of the hysteresis and eddy current loss is expressed by (5.6).

$$P_c = k_h \omega_e \varphi^2 + k_e \omega_e^2 \varphi^2 \tag{5.6}$$

Where k_h and k_e are the coefficients of the hysteresis and eddy current loss respectively.

Simplifying (5.6), the stator and rotor core loss can be expressed as:

$$P_{c-s} = (k_h \omega_e + k_e \omega_e^2)\varphi^2 \approx \frac{\omega_e^2 \varphi^2}{R_{fe}} \tag{5.7}$$

$$P_{c-r} = (k_h \omega_{sl} + k_e \omega_{sl}^2)\varphi^2 \approx \frac{{s_k}^2 \omega_e^2 \varphi^2}{R_{fe}} \tag{5.8}$$

Where R_{fe} is the core loss resistance given by $R_{fe} = 1/k_e$

It can be observed that the core loss in (5.7) and (5.8) due to the rotor is quite negligible compared to the stator since $|{s_k}^2\omega_e^2| \ll |\omega_e^2|$. However, for generality, it is recommended to take the rotor core loss into consideration [89]. As shown earlier in chapter 4, the stator and rotor core loss can be represented by series resistances R_{sfe} and R_{rfe} respectively as expressed in (4.10) and (4.11).

While the core loss for the harmonic equivalent circuit was ignored in [86] for simplicity, the formulae, (2.50) – (2.53) suggested in [82] require quite detailed knowledge of the magnetic properties of the machine which can only be obtained through highly intrusive experimental measurements. In [127], the harmonic core loss resistance is calculated using (5.9)

$$R_{c-h} = \frac{E_h^2}{P_{fe-h}/3} \tag{5.9}$$

Where E_h is the h^{th} harmonic back EMF, P_{fe-h} is the total harmonic core loss which is calculated using (5.10).

$$P_{fe-h} = k_h f B^n + k_e f^2 B^2 + k_a f^{1.5} B^{1.5} \tag{5.10}$$

Where k_h, k_e and k_a are the hysteresis, eddy current and anomalous loss coefficients. B is the peak flux density, f is the supply frequency and n is the Steinmetz constant.

Again, this approach requires knowledge of the magnetic properties, hence it cannot be used for nonintrusive efficiency estimation. Although the common assumption in most IM field efficiency estimation is to consider equal core loss resistance for fundamental and harmonic equivalent circuits [65], [84]-[85] (as a trade-off for the intrusive measurements), nonetheless, a more acceptable method for estimating the core loss is required since both the hysteresis and eddy current components of the core loss are dependent on frequency.

Although the variation of the stray-load loss with frequency for non-sinusoidal supply is extremely complex, it can be represented with sufficient accuracy by a series resistance placed on the rotor circuit. This resistance can be calculated by the expression in (5.11) [88].

$$R_{sllh} = h^{0.8} R_{sllf} \tag{5.11}$$

Where R_{sllf} is the fundamental stray-load loss resistance.

As per the friction and windage loss, the value for a non-sinusoidal supply may be slightly higher than that of the sinusoidal supply. This can be attributed to the slight difference in operating speed and the additional vibrations caused by the pulsating torques due to the harmonics in the supply. The test methods in literature for estimating the friction and windage loss are the conventional no-load test and the retardation test. However, both methods are clearly not suitable for field efficiency determination. Therefore, the most common approach is to assign a fixed value to represent the friction and windage loss [59]-[60], [65], [84]-[85]. In this research, it has been demonstrated earlier that the AGT method can give a more acceptable estimate of the friction and windage loss for sinusoidal supply condition. This method is therefore adapted for the non-sinusoidal supply case since the AGT formula not only accounts for the unbalance supply condition but also the harmonics contents in the supply [29].

5.4 Harmonic Equivalent Circuit

The operation of an induction motor under unbalanced non-sinusoidal supply conditions can be represented by three distinct equivalent circuits as shown in Fig. 5.1. The positive and negative sequence equivalent circuits represent the unbalanced condition while the harmonic equivalent circuit represents the non-sinusoidal supply condition. Note that p and n subscripts in Fig. 5.1(a) and 5.1(b) refer to the positive and negative sequence. The harmonic slip $s_h$in Fig. 5.1(c) is as given by (5.3) where the positive and negative signs refer to the forward and backward rotating harmonics respectively. In Fig. 5.1(c), the rotor and core loss resistances are considered to vary

with the harmonics order, therefore, they are estimated separately for each harmonic equivalent circuit.

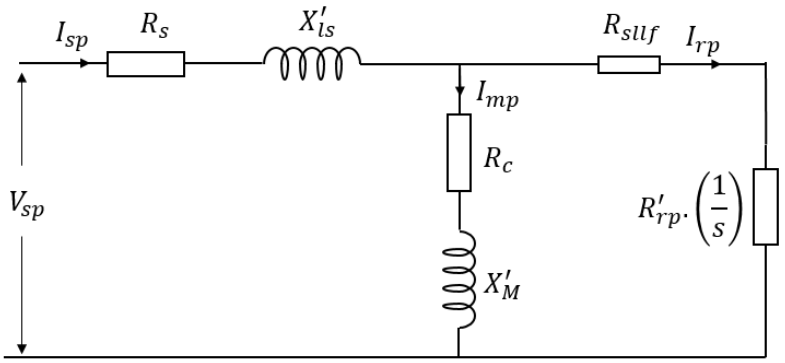

(a)

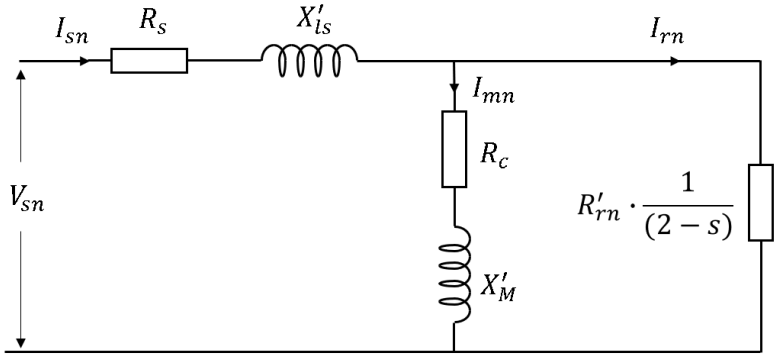

(b)

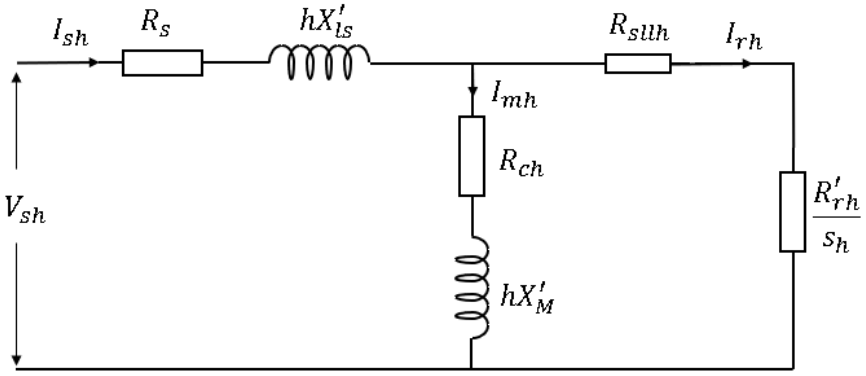

(c)

Fig. 5.1. Induction motor equivalent circuit under unbalanced non-sinusoidal supply voltages (a) Positive sequence equivalent circuit (b) Negative sequence equivalent circuit (c) Harmonic equivalent circuit

5.5 The Proposed Method

The proposed algorithm for induction motor efficiency estimation when operating with non-sinusoidal supply is presented in the flowchart shown in Fig. 5.2. The main steps involved in the proposed method are discussed as follows:

5.5.1 Harmonic and Sequence Component Extraction

From the measured stator line-to-line voltages and line currents signals, the phase sequence voltages (V_{sp} and V_{sn}) and currents components (I_{sp} and I_{sn}) for the positive and negative sequence equivalent circuits are determined according to the procedure presented in chapter 4 (see section 4.5.2).

Under normal operation, the harmonics produced by a 6-pulse inverter are the odd, non-triple harmonics [18]. For an induction motor, the magnitudes of the harmonics diminish above the 17th order [128]. In this study, it was observed that the extracted harmonic voltage magnitudes for the tested motors become negligible by the 13th order, Hence, for simplicity, this study considers the distinct harmonic voltages of order 5^{th}, 7^{th}, 11^{th} and 13^{th} for the non-sinusoidal supply analysis. The harmonic signals imposed on the fundamental are generated using a programmable power supply unit. The waveform signals extracted from the supply unit serve as inputs to the parameter identification algorithm as demonstrated in the next section.

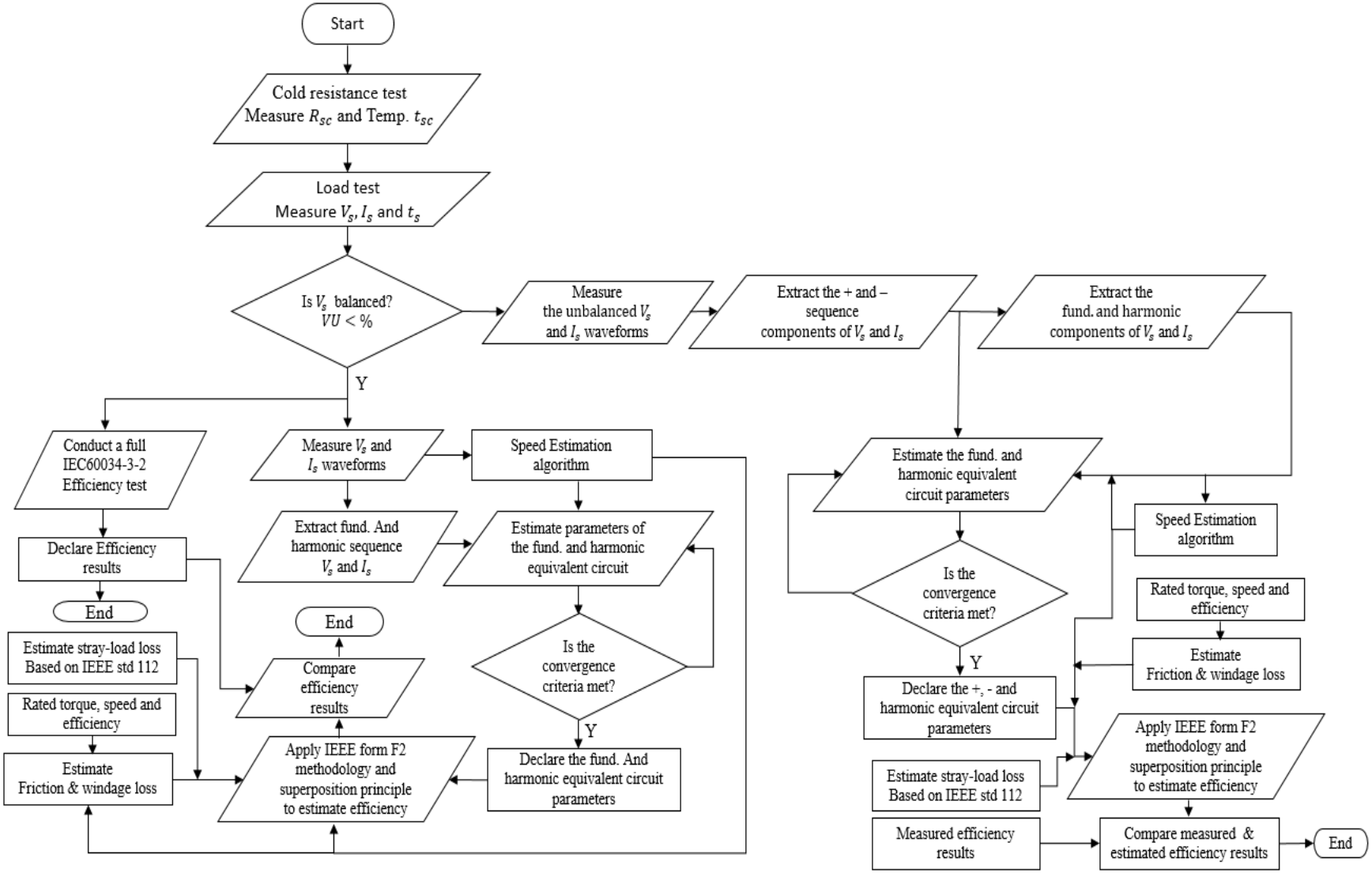

Fig. 5.2. A Complete Flowchart of the Efficiency Estimation Algorithm in the Presence of Unbalance and Harmonics Supply

5.5.2 Parameter Identification

Two steps are followed in estimating the equivalent circuit parameters as demonstrated in Fig. 5.3. The first step involved estimating the parameters of the fundamental equivalent circuit by solving for the optimal parameter vector θ through minimizing the least-square problem defined as follows:

$$\hat{\theta} = \underset{\theta \in [\theta_{min}, \theta_{max}]}{arg\ min}\ F_{err}(\theta) \tag{5.12}$$

Where $F_{err}(\theta)$ is the sum-squared difference between the measured and estimated positive and negative sequence currents (obtained based on Fig. 5.1(a) and 5.1(b)) as defined by (5.13).

$$F_{err}(\theta) = \sum_{j=1}^{N} \left(\left(\tilde{I}_{sp}(j) - \tilde{I}'_{sp}(j) \right)^2 + \left(\tilde{I}_{sn}(j) - \tilde{I}'_{sn}(j) \right)^2 \right) \tag{5.13}$$

Where θ is a vector set of the motor fundamental parameters. $\theta = \left[R'_{rp}, R_c\ X'_{lr}\ X'_m\right]^T$ for a balanced supply and $\theta = \left[R'_{rp}, R'_{rn}, R_c, X'_{lr}\ X'_m\right]^T$ for unbalanced supply, θ_{min} and θ_{max} are the lower and upper boundaries of the constraints respectively, the current sets $\tilde{I}_{sp}$, $\tilde{I}'_{sp}$ and $\tilde{I}_{sn}$, $\tilde{I}'_{sn}$ are the measured and estimated symmetrical component currents in the stator respectively, *j* is the data sample index and *N* is the total number of data samples.

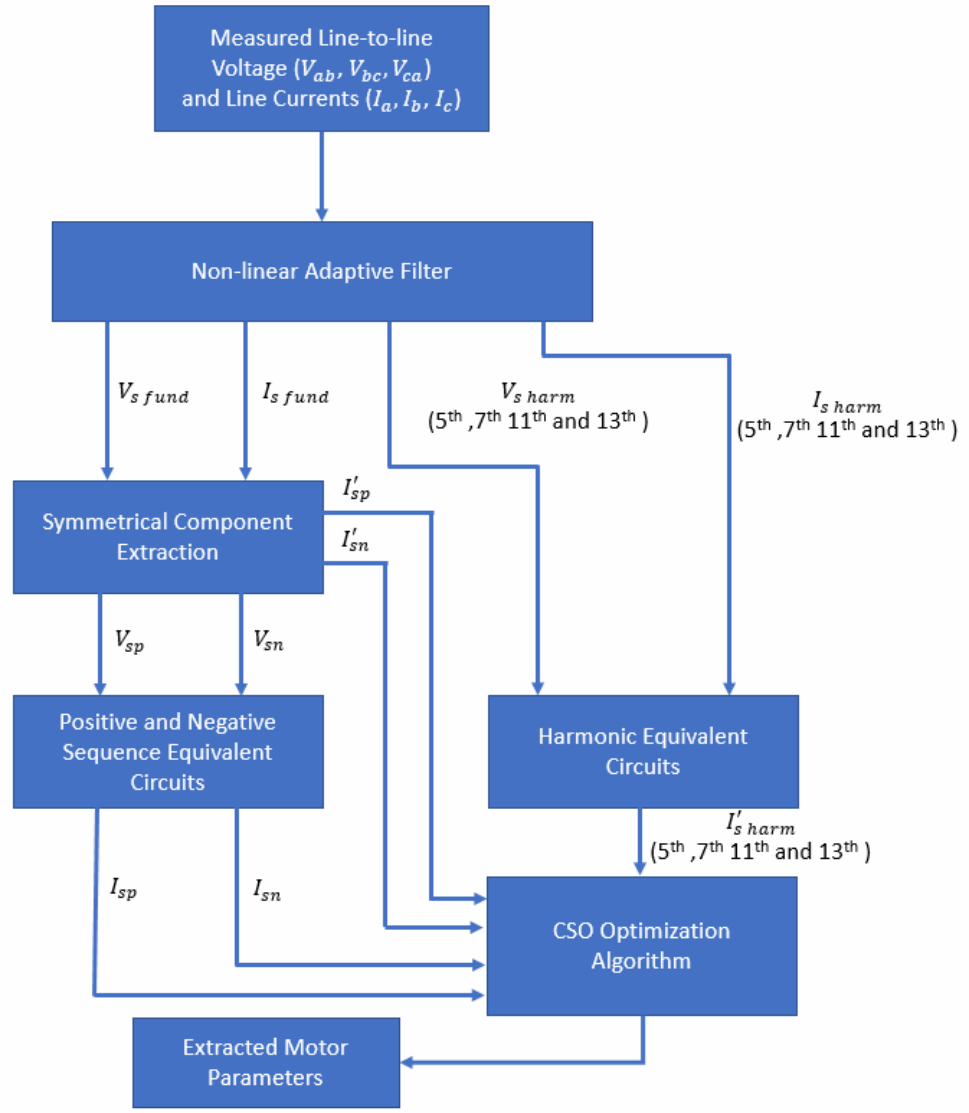

Fig. 5.3 Induction motor parameter estimation scheme under balance/unbalanced non-sinusoidal supply

The second step involves the identification of the harmonic equivalent circuit parameters. Due to their dependence on frequency, the rotor and core loss resistances are set as unknown parameters for each harmonic order. The least-square minimization problem is therefore defined as follows:

$$\hat{\theta} = \underset{\theta \in [\theta_{min}, \theta_{max}]}{arg\,min}\ f_{err}(\theta) \tag{5.14}$$

Where $f_{err}(\theta)$ given in (5.15) is the sum-squared difference between the measured and estimated harmonic currents (based on Fig. 5.1(c)).

$$f(\theta) = \sum_{j=1}^{n} \left(\left(\tilde{I}_{sh}(j) - \tilde{I}'_{sh}(j) \right)^2 \right) \tag{5.15}$$

The parameter vector in this case, is given by $\theta = [R'_{rh}, R_{ch}\,]^T$, where h is the harmonic order. The forward and backward slips are calculated according to (5.4) and (5.5) respectively. The harmonic order associated with the forward and backword fields as shown in Table 5.1.

Note that the speed, friction and windage loss and temperature estimation are all based on the methods proposed in chapter 4 for the sinusoidal supply case.

TABLE 5.1

HARMONICS ORDER ASSOCIATED WITH THE FORWARD AND BACKWARD ROTATING FIELD

k	Forward rotating harmonics order $h = 6k + 1$	Backward rotating harmonics order $h = 6k - 1$
1	7	5
2	13	11

5.5.3 Efficiency Calculation

The superposition principle is applied to calculate the power developed by the positive, negative and harmonics equivalents circuits. The motor efficiency using the proposed equivalent circuit approach is computed as follows:

$$\eta = \frac{P_{out}}{P_{in}} = \frac{\left(P_{dev-p} + P_{dev-n} + \sum_{h=5}^{13} P_{dev-h}\right) - P_{fw}}{P_{in}} \cdot 100\% \tag{5.16}$$

Where:

P_{dev-p} is the power developed by the positive sequence

P_{dev-n} is the power developed by the negative sequence

P_{dev-h} is the power developed by the harmonics

h is nontriplet odd harmonics ranging from the 5th to the 13th harmonic order.

P_{fw} is the friction and windage loss

P_{in} is the input power which is calculated from the instantaneous voltages and current using (5.17)

$$P_{in} = v_a i_a + v_b i_b + v_c i_c = v_{ca}(i_a + i_b) - v_{ab} i_b \tag{5.17}$$

5.6 Experimental Results and Discussions

The 37kW standard and 7.5kW premium efficiency induction motors were tested to validate the proposed NFEE method under different levels of voltage unbalance and harmonics conditions. The nameplate data and experimental test rigs used in testing these motors are as reported in chapter 4 (see Table 4.1 and Fig. 4.19 and 4.20). The experimental tests were performed under two different operating scenarios: Case 1 for a balanced non-sinusoidal supply condition and Case 2 for a combination of different VU and THD levels.

5.6.1 Case 1: Balanced Non-sinusoidal Supply Condition

Firstly, the stator cold resistance test was performed to determine the stator resistance and the ambient temperature prior to starting the test. A rated load test was then performed to heat up the motor to its thermal equilibrium point. As specified by the IEC 60034-2-1 [6], the thermal equilibrium point is attained when the temperature change in 1 hour is less than 2K. The temperature at the thermal equilibrium point was recorded. This test was followed immediately by a load curve test at four different operating points (OP), ie, 100% (rated), 75%, 50% and 25%. It is important to emphasize that the motor parameters for the NFEE method were determined based on a single load point test. Hence, the essence of the load tests at different operating points is to compute the motor reference efficiencies according to the IEC60034-2-3 loss segregation procedure. The tests could also be helpful to verify the consistency of the parameter estimation method under different loading conditions. The tests were performed fast enough to ensure that the temperature variation remains within 5K as

recommended by the IEC60034-2-1. The total voltage harmonic index THD_v in each test point was varied within the range of 10% down to 2% at an interval of 2%. The essence of using high VU level (exceeding the 5% limit set by the IEEE Std. 112 for sinusoidal supply) is to assess more distinctly the impact of the harmonics on the motor efficiency. The programmable power supply (MX60) was used to generate the required voltage harmonics and to ensure a balanced supply condition. The harmonic voltage magnitude associated with each harmonic order was added to the fundamental to give the required THD_v value as shown in Table 5.2. For data acquisition, the *Genesis 7i* Data Acquisition unit from HBM was used. This system has up to 24 DAQ channels and allows the synchronous acquisition of raw data from all the channels.

TABLE 5.2

MEASURED DATA FOR CASE 1 (BALANCED NON-SINUSOIDAL CONDITION)

$THD_v(\%)$	$V_{s-5^{th}}(V)$	$V_{s-7^{th}}(V)$	$V_{s-11^{th}}(V)$	$V_{s-13^{th}}(V)$
9.96	28.94	20.68	14.01	11.34
7.97	23.15	16.54	11.21	9.07
6.04	17.54	12.53	8.49	6.87
3.98	11.58	8.27	5.6	4.54
1.99	5.79	4.14	2.80	2.27

In addition to the measured data for calculating the reference motor efficiency using the loss segregation method, the voltage and current signal waveforms were recorded for each operating point at a sampling rate of 50kHz and a window length of 2s. Fig. 5.4 and 4.5 show zoomed portions of the voltage and current waveforms recorded at the rated operating condition (OP4) with a 10% THD_v value.

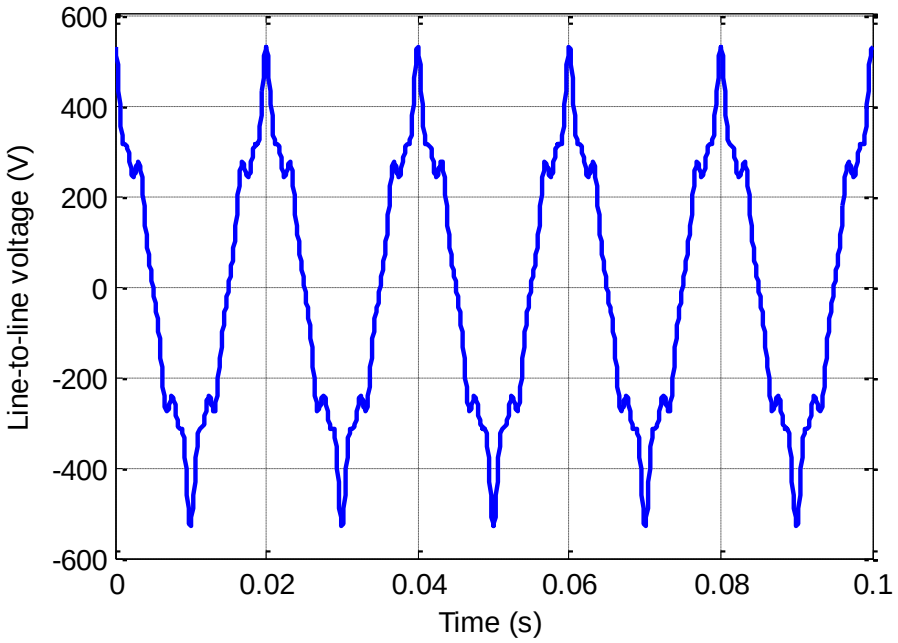

Fig. 5.4 Recorded stator line-to-line voltage signals at OP4 for the 37kW test motor

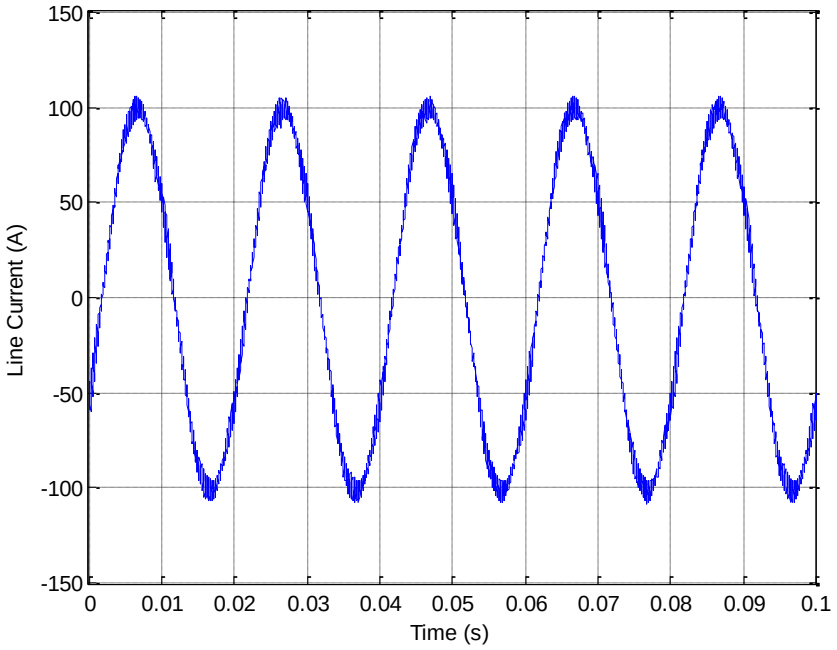

Fig. 5.5 Recorded stator line current signals at OP4 for the 37kW test motor

To estimate the motor equivalent circuit parameters, the recorded voltage and current waveforms were passed through the adaptive non-linear filter to extract the fundamental

and harmonic signal waveforms which serve as inputs to the parameter identification routine using the CSO algorithm.

The estimated parameters at two different operating points as reported in Table 5.3 clearly indicate the consistency of the parameter estimation scheme. Hence, measurements from one single operating point is enough to extract all the motor parameters.

TABLE 5.3

ESTIMATED MOTOR PARAMETERS FOR THE FUNDAMENTAL AND HARMONIC EQUIVALENT CIRCUITS USING CSO ALGORITHM

EC	Parameter	Motor parameters 7.5kW		Motor parameters 37kW	
		OP2 (50%)	OP4 (100%)	OP2 (50%)	OP4 (100%)
Fund.	$R'_{rp}(\Omega)$	0.640	0.642	0.144	0.148
	$X'_{ls}\ (\Omega)$	3.260	3.258	0.791	0.806
	$X'_{m}(\Omega)$	63.294	63.300	26.985	26.962
	$R_{c}(\Omega)$	2.538	2.579	0.302	1.315
Harm.	$R'_{r,\,5^{th}}(\Omega)$	1.346	1.399	0.263	0.265
	$R'_{r,\,7^{th}}(\Omega)$	1.402	1.405	0.271	0.276
	$R'_{r,\,11^{th}}(\Omega)$	1.445	1.448	0.276	0.285
	$R'_{r,\,13^{th}}(\Omega)$	1.529	1.533	0.308	0.321
	$R'_{c,\,5^{th}}(\Omega)$	2.673	2.716	1.375	1.385
	$R'_{c,\,7^{th}}(\Omega)$	2.735	2.779	1.470	1.417
	$R'_{c,\,11^{th}}(\Omega)$	2.810	2.855	1.406	1.456
	$R'_{c,\,13^{th}}(\Omega)$	2.835	2.881	1.454	1.469

Fig. 5.6 and 5.7 show the profiles of the estimated rotor and core loss resistances corresponding to the fundamental and harmonic equivalent circuits. These results confirm the variations of these parameters with the order of the harmonics and therefore

highlight the need to estimate the parameters separately using the harmonic equivalent circuits.

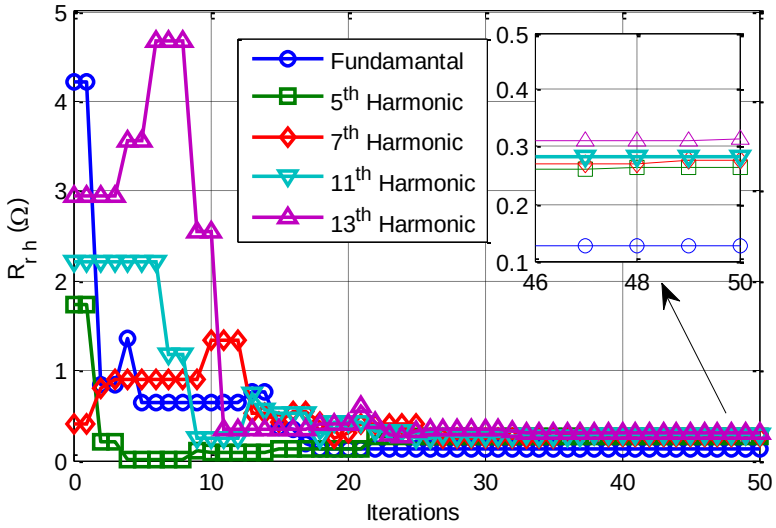

Fig. 5.6. Estimation of the rotor resistance corresponding to each harmonic order at OP4

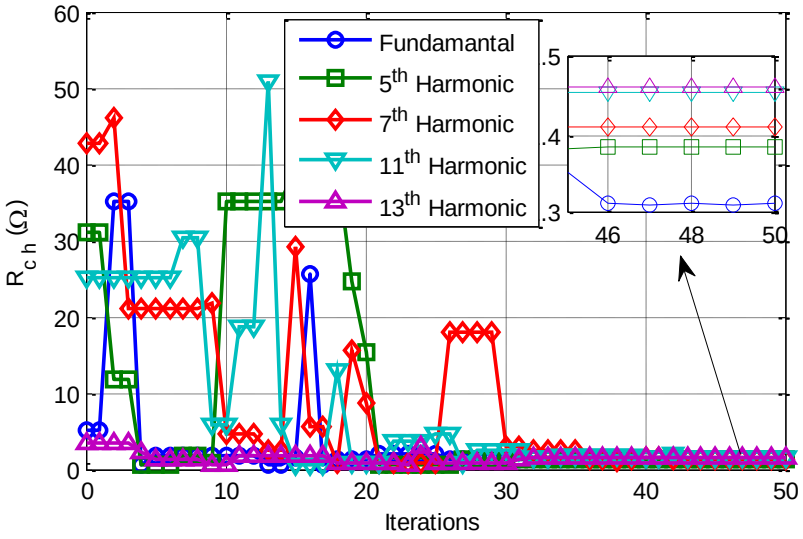

Fig. 5.7. Estimation of the core loss resistance corresponding to each harmonic order at OP4

With the estimated equivalent circuit parameters, the additional losses due to the harmonic supply can be determined based on the segregation of loss method. The results shown in Fig. 5.8 to 5.10 are estimated at the worst THD_v of 10% for the 37kW motor. It is seen that the losses (including the load-dependent copper losses) show fairly constant values for all loading conditions and quite significant dependence on the

harmonics order. While the core loss as seen in Fig. 5.10 is more noticeable for low order harmonics (especially the 5th order harmonic), the trend shows a reduction in the core loss for the higher order harmonics.

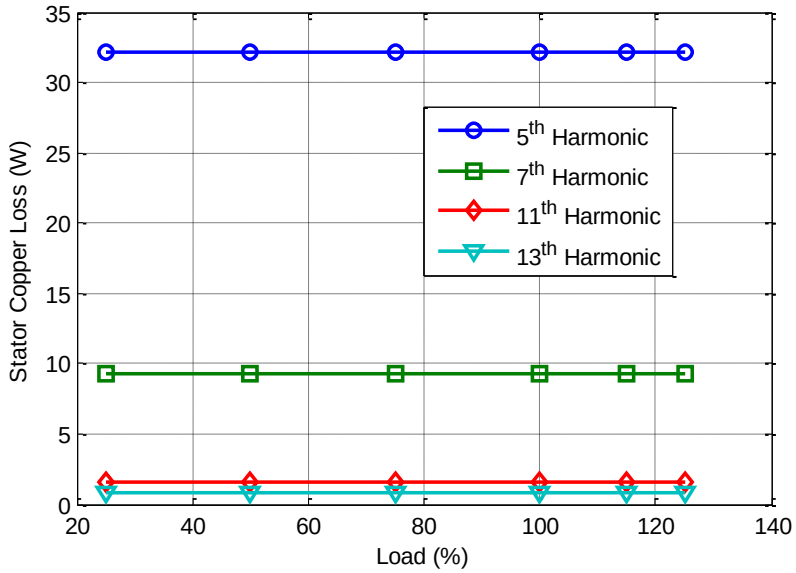

Fig. 5.8. Stator copper loss due to harmonic at 10% THD_v

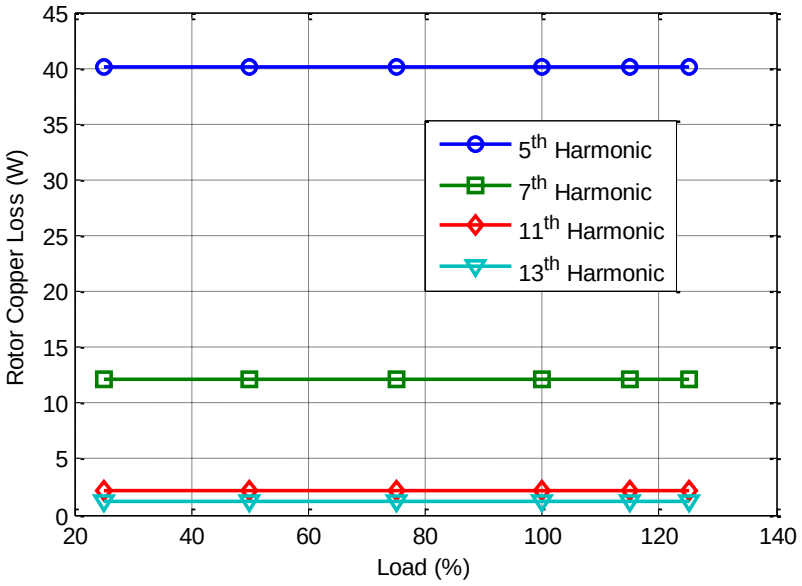

Fig. 5.9. Rotor copper loss due to harmonic at 10% THD_v

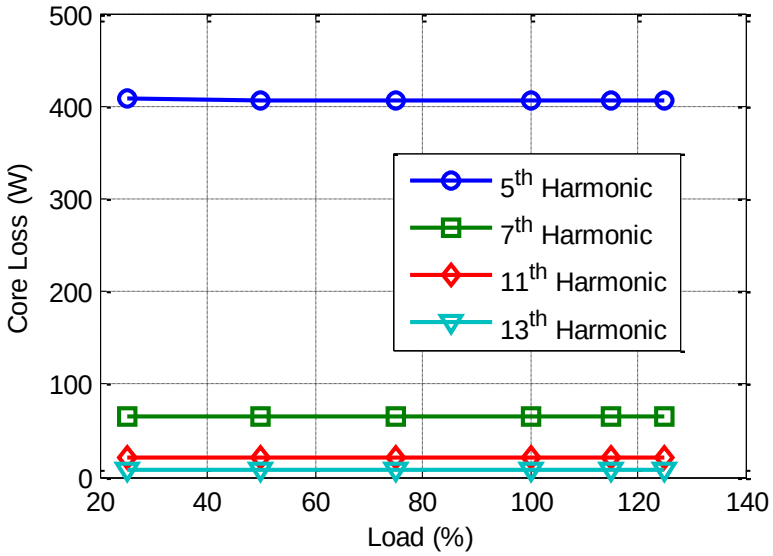

Fig. 5.10. Core loss due to harmonics at 10% THD_v

By comparing the estimated efficiencies of the tested motors at the lowest and highest THD_v for rated condition as shown in Fig. 5.11 and 5.12, it is seen that the 7.5 kW motor efficiency drops significantly by about 1.645% when operated with 9.96% THD_v. This contrasts with the 37kw motor which records only about 0.436% efficiency drop.

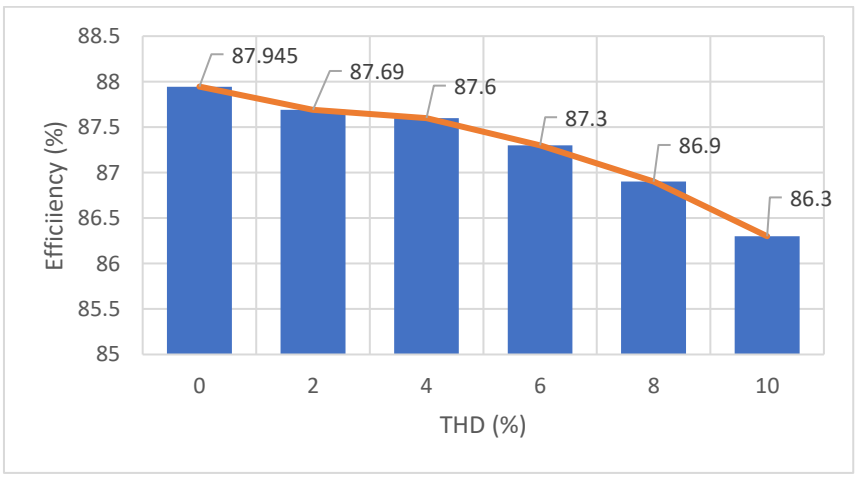

Fig. 5.11. Estimated efficiency values at different THD_v levels for 7.5kW motor

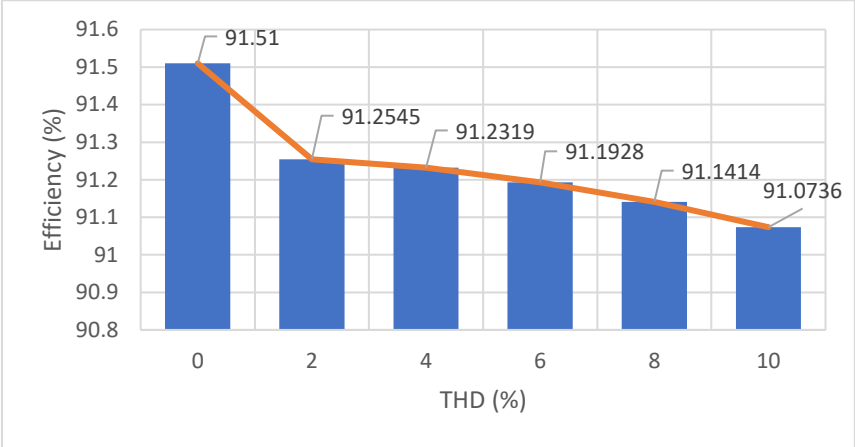

Fig. 5.12. Estimated efficiency values at different THD_v levels for 37kW motor

This disparity could be explained by the difference in how the losses are distributed within the two motors with respect to their design [129]. For the two tested motors, the results as shown in Fig. 5.13 and 5.14 indicate that the predominant disparity in the losses appear to be the core loss, while the stray-load loss remains practically less impacted by the non-sinusoidal supply.

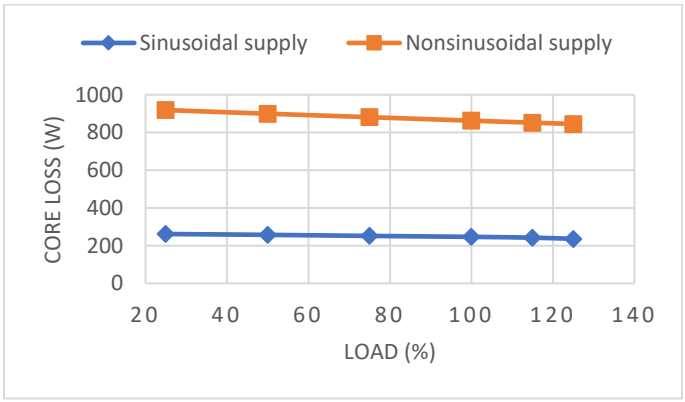

(a)

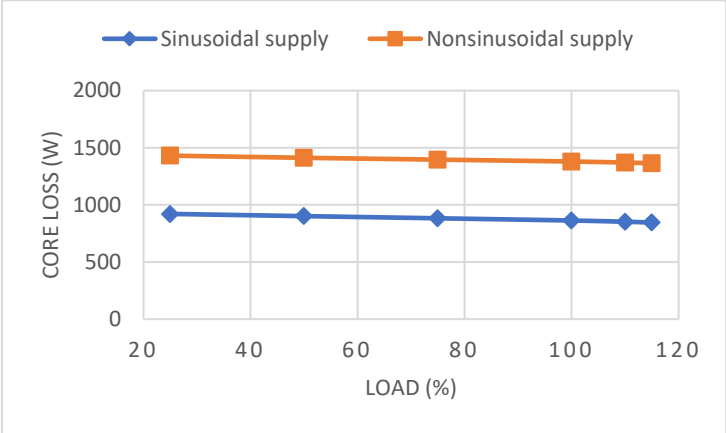

(b)

Fig. 5.13. Core loss estimation for sinusoidal and non-sinusoidal supplies (a) 7.5kW test moor (b) 37kW test motor

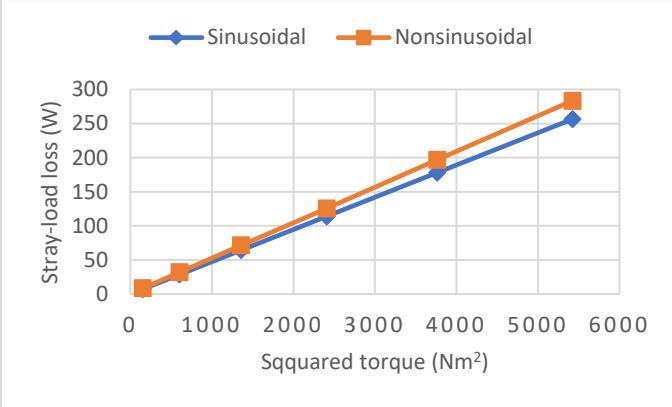

(a)

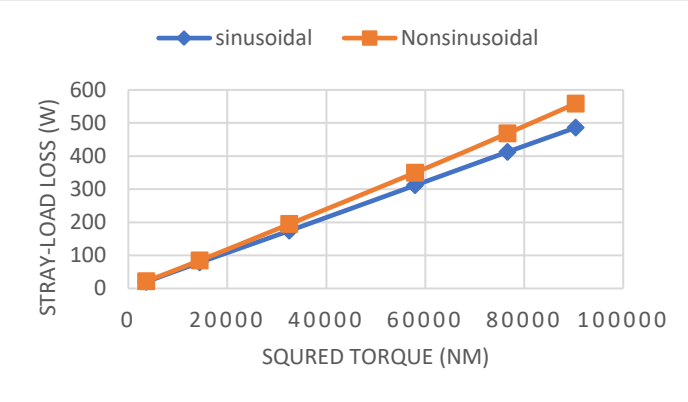

(b)

Fig. 5.14. Stray-load loss estimation for sinusoidal and non-sinusoidal supplies (a) 7.5kW test moor (b) 37kW test motor

The estimated and measured efficiency profiles at different THD_v and load levels for the 37kW motor is shown in Fig. 5.15. The absolute errors between the measured and estimated efficiencies as summarized in Table 5.4 show that the maximum absolute error is 0.248% at 0.5% THD_v. This value indicates an acceptable level of accuracy by the proposed method.

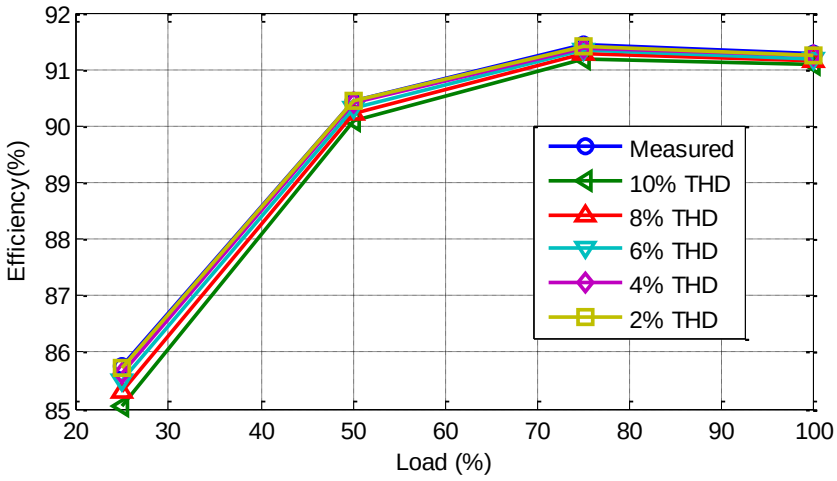

Fig. 5.15. Estimated and measured efficiency profiles at different THD_v and load levels for 37kW motor

TABLE 5.4

MEASURED AND ESTIMATED MOTOR EFFICIENCIES AT DIFFERENT THD_v VALUES UNDER RATED OPERATING CONDITION

	7.5kW			37kW		
THD_v (%)	Measured Efficiency (%)	Estimated Efficiency (%)	Abs. Error (%)	Measured Efficiency (%)	Estimated Efficiency (%)	Abs. Error (%)
0.50	87.698	87.945	0.248	91.420	91.510	0.090
1.99	87.502	87.690	0.187	91.361	91.254	0.106
3.98	87.457	87.600	0.143	91.364	91.232	0.132
6.04	87.202	87.300	0.097	91.398	91.193	0.206
7.97	86.786	86.900	0.114	91.266	91.141	0.125
9.96	86.199	86.300	0.101	91.262	91.074	0.188

5.6.2 Case 2: Unbalanced Non-sinusoidal Supply Condition

The test motors are subjected to different levels of voltage conditions with VU factor ranging from 1% to 5%. For each VU, the THD_v was varied within the range of 2% to 10% at an interval of 2%, and measurements were taken at each test point. The measured and estimated efficiency results corresponding to each test point are compared and the absolute errors are determined as shown in Table 5.5. The proposed method provides results with acceptable accuracies as the maximum absolute errors for the 7.5kW and 37kW motors are 0.3886% and 0.2480% respectively. It can be observed that the efficiencies drop significantly by 3.387% and 2.329% for the 7.5kW and 37kW motor respectively when the motors operate with a combination of both 5% VU and 10% THD_v.

TABLE 5.5

MEASURED AND ESTIMATED MOTOR EFFICIENCIES AT DIFFERENT VU AND THD_v VALUES UNDER RATED OPERATING CONDITION

VU (%)	THD_v (%)	7.5kW			37kW		
		Measured Efficiency (%)	Estimated Efficiency (%)	Absolute Error (%)	Measured Efficiency (%)	Estimated Efficiency (%)	Absolute Error (%)
1	1.99	87.500	87.688	0.188	91.352	91.245	0.107
	3.98	87.450	87.593	0.143	91.356	91.222	0.134
	6.04	87.193	87.291	0.098	91.391	91.185	0.206
	7.97	86.777	86.891	0.114	91.257	91.133	0.124
	9.96	86.190	86.291	0.101	91.253	91.065	0.188
2	1.99	86.206	86.234	0.128	91.244	91.038	0.207
	3.98	86.115	86.182	0.067	91.193	90.986	0.207
	6.04	86.033	86.130	0.096	91.141	90.935	0.206
	7.97	85.892	86.077	0.185	91.090	90.883	0.206
	9.96	85.800	86.025	0.224	91.038	90.832	0.206
3	1.99	85.666	85.924	0.257	90.835	90.634	0.201
	3.98	85.532	85.822	0.290	90.631	90.437	0.194
	6.04	85.398	85.721	0.323	90.427	90.239	0.188
	7.97	85.265	85.620	0.355	90.224	90.042	0.182
	9.96	85.130	85.519	**0.389**	90.021	89.844	0.177
4	1.99	85.093	85.307	0.214	89.719	89.476	0.243
	3.98	84.901	85.096	0.196	89.618	89.394	0.225
	6.04	84.827	84.986	0.159	89.517	89.343	0.174
	7.97	84.745	84.874	0.130	89.416	89.293	0.123
	9.96	84.701	84.637	0.064	89.316	89.243	0.073
5	1.99	84.760	84.511	0.250	89.269	89.162	0.107
	3.98	84.704	84.464	0.240	89.276	89.080	0.196
	6.04	84.648	84.397	0.251	89.176	88.998	0.178
	7.97	84.591	84.312	0.280	89.129	88.916	0.213
	9.96	84.535	84.301	0.234	89.082	88.834	**0.248**

5.7 Conclusions

In this chapter, an acceptable method for efficiency estimation of induction motors operating with non-sinusoidal voltage supply is proposed. The algorithm which is an extension of the method presented in chapter 4 uses the CSO algorithm to estimate the fundamental and harmonics equivalent circuit parameters under field operating

conditions while the motor is still in service. Variations of the motor parameters due to harmonics and skin effects are also considered.

It was observed that the motor parameters remain fairly constant at different operating points, hence, it is enough to extract the parameters using measurements from a single operating point. Furthermore, the parameter estimation results confirm the dependence of the rotor and core loss resistances on the harmonics' order which highlight the need to estimate these parameters separately using the harmonics equivalent circuits.

Although the results based on the segregation of loss method show that the additional harmonic losses are independent of load, the trend in the losses indicate noticeable dependence on the order of the harmonics. An appreciable increase in the harmonic losses has been observed in the case of the 5^{th} order harmonic and the trend tend to reduce for higher order harmonics.

While a significant drop in efficiency of about 1.645% has been observed for the 7.5kW motor when operated at 9.96% THD_v, the 37kw motor records only about 0.436% deterioration in efficiency. This disparity can be explained by the design of these motors and how their losses are distributed. In terms of accuracy, the maximum absolute efficiency error for both motors at 9.96% THD_v was found to be 0.248%. This value confirms the accuracy of the proposed method.

For unbalanced non-sinusoidal supply, it has been observed that the efficiencies of the tested motors drop significantly due to the combined impact of the voltage unbalance and harmonic distortions of the supply. The proposed method provides results with acceptable accuracies as the maximum absolute errors of 0.3886% and 0.2480% were obtained for the 7.5kW and 37kW motors respectively.

Chapter 6

Converter-fed Induction Motor Efficiency Measurement under Variable Frequency/Load Points: An Extension of the IEC/TS 60034-2-3

6.1 Overview

The equivalent circuit method presented in the previous chapter covers the efficiency determination for induction motors driven by variable frequency drives (VFDs) at-rated voltage and frequency. However, in certain applications, induction motors are operated below or above their rated speed and in such applications, determination of the motor losses and its efficiency will entail analysing the converter-fed losses in the constant as well as the field weakening regions.

This chapter, therefore, proposes a new approach to extend the methodology specified by the IEC 60034-2-3 technical specifications at nominal frequency to cover a much

wider speed range. The chapter outlines the procedure to be followed as well as the technical considerations to be established for maintaining repeatable test conditions.

6.2 Introduction

Although VFDs have become popular over the last two decades owing to their energy saving capability and ease of process control, the Pulse-Width Modulated (PWM) voltages and currents introduce additional harmonic losses in the electric motors. Whereas several existing test standards are available for sinusoidal operation, only a handful of draft standards have attempted to standardize the determination of converter-fed induction motor losses [8]-[10]. While the European standard EN 50598-2 [8] and the Canadian Standard CS838-13 [9] generally provide application guidelines for the use of VFDs, with focus on the determination of the complete motor-drive system efficiency, the International Electrotechnical Commission (IEC) 60034-2-3 Technical Specification (IEC/TS) [10] places great emphasis on the methodology for the experimental determination of additional harmonic losses in induction motors. However, as was discussed in chapter 2 (section 2.8), one of the main weakness of the IEC/TS is its limitation to rated voltage and frequency. This is because, in many modern electric drives applications where electric motors are used, different operating speeds are required.

Unlike the IEC/TS, the European Standard EN 50598-2 [8], proposes a method for calculating the motor losses at non-rated operating conditions. The method uses some set of mathematical formulae to relate the motor losses at non-rated operating conditions in terms of its losses at rated condition. As shown in Fig. 6.1, the standard specifies 8 different operating points on the torque-speed plane of a motor for calculating its losses. However, this standard does not provide the loss segregation method; only the direct input-output efficiency method is used. Moreover, the mathematical formulae may not be accurate for non-rated operating points as the distribution of the various loss components in a motor are not fixed but vary depending on its design and classification.

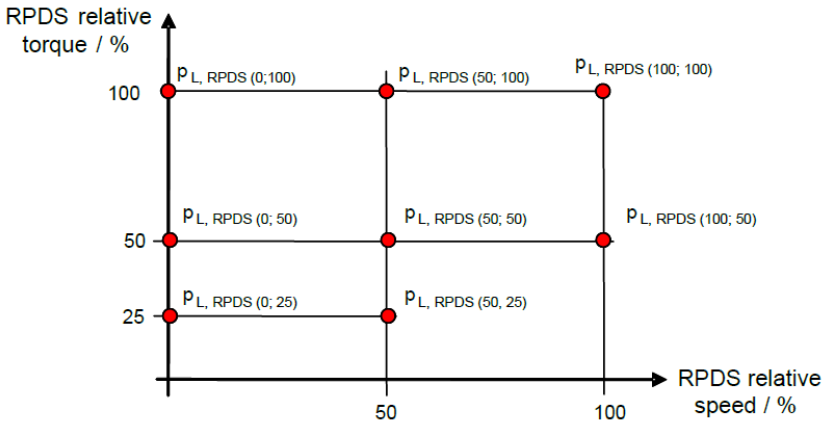

Fig. 6.1. Selected operating point for calculating the relative power losses for converter-fed motors [8]

In [92]-[93] the loss segregation method is used, however, the authors barely reported on the harmonic losses, citing a lack of scientific methods for separating the core and mechanical losses. Therefore, the loss segregation method proposed in this chapter will provide feedback to the relevant IEC standards committee as well as guidance to the research community in general.

6.3 IEC 60034-2-3 Technical Specification

The IEC/TS 60034-2-3 defines test methods for determining the additional harmonic losses and efficiency of voltage-source inverter-fed IMs. These test methods are summarized in Table 6.1. The method of interest in this research is the loss segregation method; referred to as Method 2-3-B. Since these losses are determined by the increase in motor losses between sinusoidal supply and PWM operation, the proposed procedure requires first the determination of fundamental motor losses with a sinusoidal supply according to the already established IEC 60034-2-1 standard and repeating the tests with a PWM supply. The following sections discuss some technical issues that must be considered to ensure an accurate determination of these losses:

TABLE 6.1

THE IEC/TS 60034-2-3 EFFICIENCY TESTING METHODS

Ref	Method	Description	Required facility
2-3-A	Loss segregation: Test converter supply	Losses segregated based on IEC-specified test converter	Variable voltage sinusoidal supply and test coverter supply for rated operation
2-3-B	Loss segregation: Specific converter for final application	Losses segregated using converter for final application	Variable voltage sinusoidal supply and specific coverter supply for rated operation
2-3-C	Input-output	Use direct torque measurement	Dynamometer and specific converter supply
2-3-D	Calorimetric	Losses determined from coolant temp. rise	Specific converter supply

6.3.1 Considerations for Matching Sinusoidal and PWM Supply Tests

To establish repeatable test conditions for the determination of the additional harmonic losses, the IEC/TS defines a set of reference conditions aimed at matching the introduced test converter characteristics to the sinusoidal supply. While some reference conditions require further refinements when extended to method 2-3-B: *Summation of losses with specific converter for final application,* as discussed in [11]-[14], others are straight forward. For instance, the matching of the PWM fundamental voltage to the rated sinusoidal supply value is expected since the sinusoidal supply test is taken as a reference. Two important aspects of the testing process are discussed below:

6.3.1.1 Extraction of Fundamental Quantities:

As is well-known, the true RMS value of PWM voltage is generally much higher than the fundamental value due to the presence of high frequency harmonics. Therefore, to ensure the fundamental voltage component of a PWM supply matches the corresponding sinusoidal supply value, the power analyser to be used for efficiency

tests must be capable of extracting the fundamental voltage component without affecting the active power measurement. While modern analysers like the HBM Genesis 7i used in this study provide Fast Fourier Transform (FFT) algorithms to meet this requirement, the use of digital filters is an acceptable alternative. However, the cut-off frequency must be set at a value that does not lead to over-filtering which impacts active power measurement. Furthermore, care must be taken to ensure the voltage drop across additional components such as output chokes is compensated. In certain instances, this may involve setting a higher fundamental voltage value in the drive parameters than the corresponding sinusoidal supply rated voltage.

6.3.1.2 Matching of Load Torque:

According to the IEC/TS methodology, the induction motor efficiency under a PWM supply is determined using the mechanical power measured during the sinusoidal supply test. Consequently, any mismatch in fundamental frequency and load torque between load test points with the two supplies translates into errors in efficiency. In addition, the determination of stray-load losses (SLL), which constitutes an important aspect of the methodology, is very sensitive to load torque measurements. Thus, a mismatch in load torque between the two tests leads to errors in the additional harmonic loss value obtained. Therefore, the matching of load torque between the two sets of tests cannot be overemphasized.

A description of the loss segregation methodology (Method 2-3-B) is given in the next section.

6.3.2 The IEC/TS Loss Segregation Method (2-3-B)

The loss segregation method 2-3-B is an extension of the IEC 60034-2-1 method 2-1-1B [7] for line-fed induction motors. In this method, the additional harmonic losses due to converter operation are determined through the well-established loss segregation method (2-1-1B) on sinusoidal and converter (PWM) supply as illustrated in Fig. 6.2. The first step in the loss segregation test is the rated load test with sinusoidal supply at

the motor's rated voltage and frequency. The rated load test is performed to allow the motor to attain its rated temperature after which the stator and rotor copper losses are determined. The motor is said to attain thermal equilibrium when the temperature change is not greater than 1K within 30mins [7].

The rated load test is immediately followed by the load curve test. It is important to ensure that the temperature change before this test is within 5K of the motor rated temperature. Measurements are taken at the approximate load values shown in Fig. 6.2. These tests are performed fast enough to minimize temperature changes in the motor.

The final step in the IEC/TS 2-1-1B methodology is the no-load test. This is carried out immediately after the load curve test and measurements are taken in descending order at each of the specified voltages shown in Fig. 6.2. From these tests, the constant no-load losses are determined by subtracting the no-load stator winding loss from the no-load input power.

Finally, as shown in Fig. 6.2, the test with the converter supply is performed at the motor fundamental frequency following the same procedure used in the sinusoidal supply case. However, for the no-load test, only a single test point at the rated voltage is to be considered. The additional harmonic losses caused by the converter supply is calculated as the difference between the motor losses with converter and sinusoidal supply under the no-load test and the load curve test.

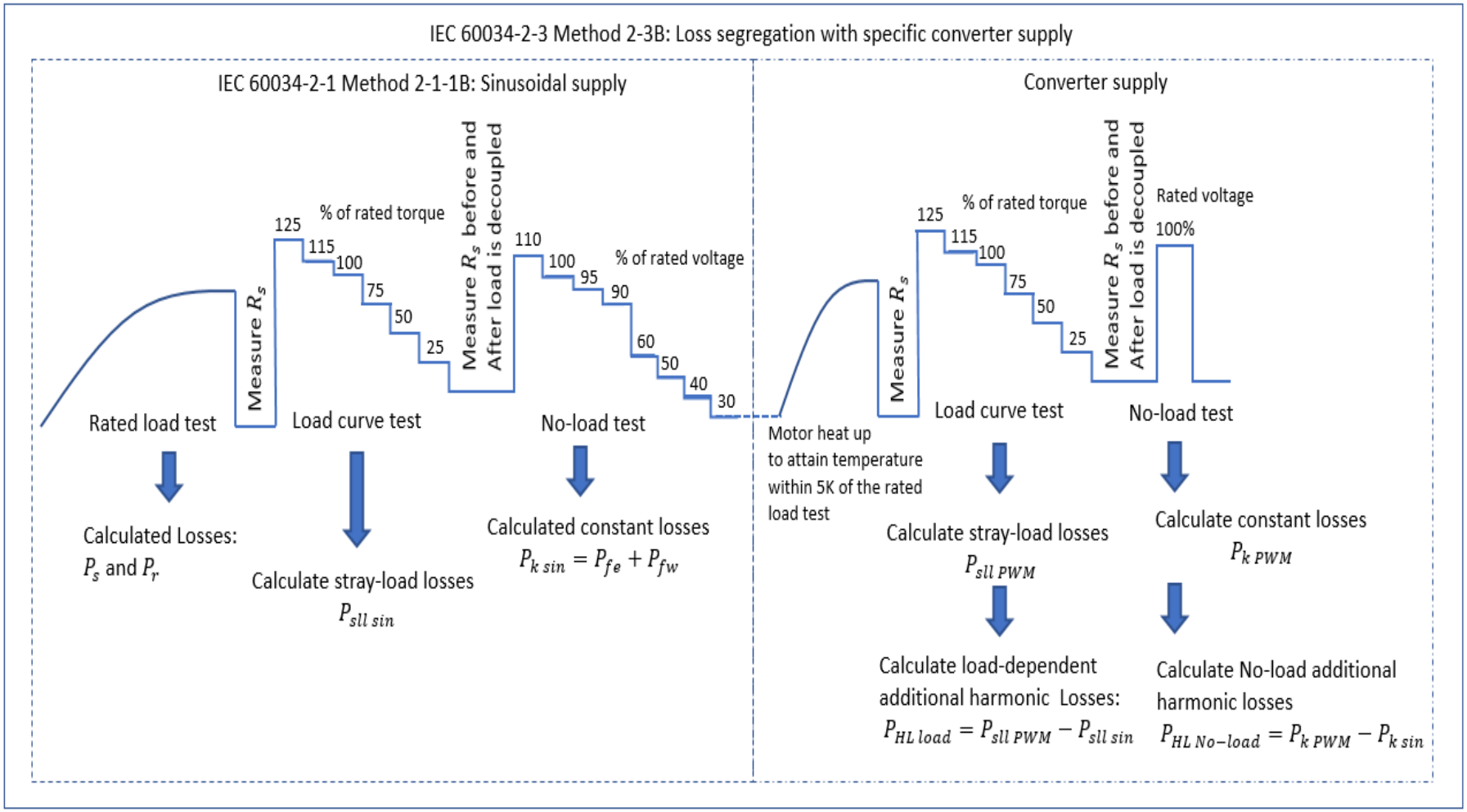

Fig. 6.2. The IEC 60034-2-3 loss segregation methodology

6.4 Methodology for Extending the IEC/TS 60034-2-3 Procedure

Following a call for test facilities to test the practical applicability of the IEC/TS 60034-2-3, its limitation to inverter-fed induction motors operating at rated fundamental voltage and frequency has been identified as its main weakness [11]-[14]. This is expected since induction motor drives are usually operated over a wide range of speed – above and below rated speed.

As shown in [130], [131], the standard loss segregation procedure for IMs under sinusoidal supply at rated frequency can be extended to non-rated frequency. Although the same procedure can also be applied to the PWM supply, certain challenges arise in the seperation of mechanical and core losses. The following sections describe the methodology for determining the additional harmonic losses at variable frequencies according to the IEC/TS procedure. In this study, the open-loop voltage over frequency (V/F) control strategy was adopted and the selected frequencies for the no-load and load tests were in the range 25Hz – 50Hz, in steps of 5Hz, while load torques were applied at 25%, 50%, 75%, 100%, 115%, and 125% of the rated value. The operating points considered in this study are illustrated in Fig. 6.3.

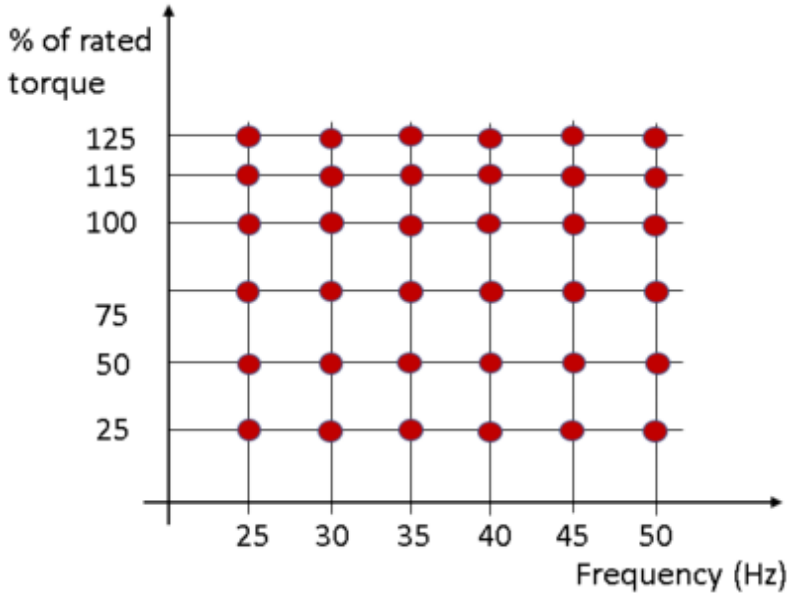

Fig. 6.3. Selected torque-speed operating points for converter-fed motor

6.4.1 No-Load Tests:

At each selected frequency, the no-load tests with sinusoidal and PWM supplies were performed at the end of the load tests according to the IEC 60034-2-1 methodology. The V/F ratio was kept constant for each test (supply) frequency, by adjusting the magnitude of the voltage in proportion to the applied frequency. As the inverter used in this study is designed to operate with a constant DC bus voltage of 700V, a variable modulation index technique was adopted. However, this approach results in a non-linear plot of constant no-load losses (defined by (6.1)) against the square of the fundamental voltage, leading to challenges in the separation of core losses and mechanical losses. Therefore, after several experimental tests and data analysis, it was observed that the best mechanical loss values in the PWM supply tests can be achieved by fitting the last four data points of the no-load test to a third order polynomial curve.

$$P_{k\,sin} = P_{s-nl} - P_{scl-nl} = P_{fw} + P_{fe} \tag{6.1}$$

For the core loss, the primary components are the hysteresis and eddy current loss both of which are frequency dependent. Since the stator magnetic field is at fundamental frequency while the rotor is at slip frequency, the core loss in the stator dominates. For sinusoidal supply, the rotor core loss is quite small and could be neglected without much error. However, for PWM supply, the converse is the case, since harmonic currents through the rotor bars resulting in rotor copper loss even under no-load condition [132]-[133]. Thus, for PWM supply, (6.1) is modified to account for the no-load rotor copper loss as defined by (6.2).

$$P_{k\,PWM} = P_{s-nl} - P_{scl-nl} - P_{rcl-nl} = P_{fw} + P_{fe} \tag{6.2}$$

P_{rcl-nl} is the no-load rotor copper loss which could be calculated using (6.3)

$$P_{rcl-nl} = 1.5R'_r I^2_{harm} = 1.5R'_r\left(I^2_{s-nl} - I^2_{s-fund}\right) \tag{6.3}$$

Where: I_{harm} is the harmonic current, I_{s-nl} is the stator no-load current and I_{s-fund} is the fundamental component of the stator current and R_r' is the equivalent rotor resistance referred to the stator side.

Several methods are employed to estimate the value of R_r'. In this research, the optimization approach as presented in the next section is adapted due to its simplicity and accuracy.

To account for loading effects, the core losses determined by (6.1) and (6.2) for sinusoidal and PWM respectively were corrected to the magnetizing branch voltage according to the IEC 60034-2-1 methodology.

6.4.2 Rotor Resistance Estimation

Since the aim of the parameter estimation is to determine only the rotor resistance, a simplified steady-state equivalent circuit of an induction motor with fewer parameters is used. As shown in Fig. 6.4, the equivalent circuit is based on the inverse Γ-model representation.

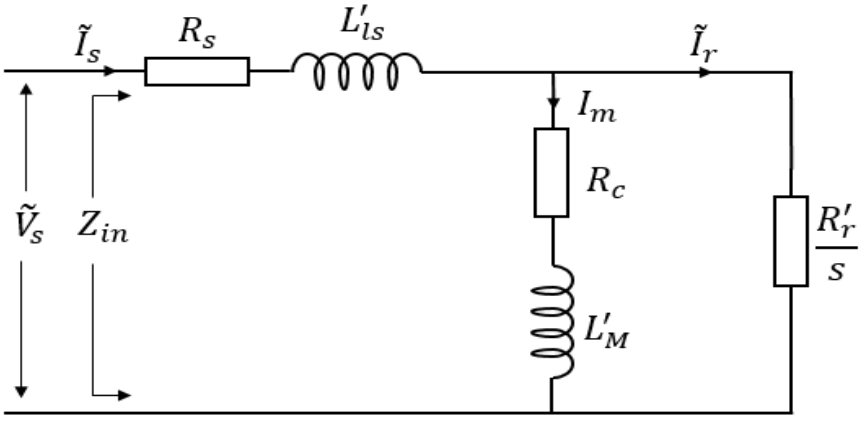

Fig. 6.4. Steady-state Equivalent Circuit of an Induction Motor

When compared to the conventional T-model, this simplified representation has the advantage of not only using fewer parameters (only two inductances are present) but also gives more consistent results when using external measurements [42]. An expression for the total input impedance of the equivalent circuit in Fig. 6.4 is given by:

$$Z_{in} = \frac{\tilde{V}_s}{\tilde{I}_s} = R_s + j\omega_e L_{ls} + \left((R_c + j\omega_e L_m) || \left(\frac{R_r}{s} \right) \right) \tag{6.4}$$

Where: || represents a parallel connection.

Since the value of R_s is known from the dc winding resistance test and R_c can be calculated from the core loss value obtained in the no-load test, the optimization constraints are reduced to only 3 variables, i.e. the stator leakage inductance L_{ls}, the magnetization inductance L_m and the rotor resistance R_r. These parameters are computed by solving the minimization problem formulated as follows:

$$\hat{\theta} = \underset{\theta \in [\theta_{min}, \theta_{max}]}{arg\ min}\ F_{err}(\theta) \tag{6.5}$$

Where $\theta = [\, R_r\ L_{ls}\ L_m]^T$ is a vector set of the unknown motor parameters, , θ_{min} and θ_{max} are the lower and upper boundaries of the parameter constraints respectively.

The cost function $F_{err}(\theta)$, is given by (6.6).

$$F_{err}(\theta) = \frac{1}{n} \sum_{j=1}^{n} \left(\frac{Z_{in-mea}(j) - Z_{in-est}(j)}{Z_{in-mea}(j)} \right)^2 \tag{6.6}$$

Where Z_{in-mea} and Z_{in-est} are the measured and estimated input impedances of the motor respectively, *j* is the data sample index and *n* is the total number of data samples. Z_{in-mea} is calculated using (6.7).

$$Z_{in-mea} = \frac{\tilde{V}_{s-meas}}{\tilde{I}_{s-mea}} \tag{6.7}$$

Where $\tilde{V}_{s-meas}$ and $\tilde{I}_{s-mea}$ are the measured instantaneous stator voltage and current space vectors.

By using the CSO optimization, the algorithm continuously updates the motor parameters for each iteration by minimizing the cost function until a close match is established between the measured and estimated input impedances.

6.4.3 Load Curve Tests:

The load tests were performed at the end of the rated load test, taking into consideration the issues discussed in section 6.3.1 to ensure the sinusoidal and PWM supply tests were well-matched. The component losses were segregated according to the well-known IEC/TS 60034-2-3 procedure. Taking the sinusoidal supply losses as a reference, the additional harmonic losses in the motor due to the PWM supply harmonics were determined according to (6.8) and (6.9) and the converter-fed induction motor efficiency was determined according to (6.10) and (6.11).

$$P_{HL\,No-load} = P_{k\,PWM} - P_{k\,sin} \tag{6.8}$$

$$P_{HL\,load} = P_{sll\,PWM} - P_{sll\,sin} \tag{6.9}$$

$$\eta = \frac{P_2}{P_2 + P_{total\,PWM}} \tag{6.10}$$

with

$$P_{total\,PWM} = P_{total\,sin} + P_{HL} = \left(P_{s,\theta} + P_{r,\theta} + P_{fe} + P_{fw}\right) + \left(P_{HL\,load} + P_{HL\,No-load}\right) \tag{6.11}$$

Where $P_{k\,PWM}$ and $P_{k\,sin}$ are the respective constant no-load losses under PWM and sinusoidal supplies, $P_{SLL\,PWM}$ and $P_{SLL\,sin}$ are the respective stray-load loss under PWM and sinusoidal supplies, P_2 is the mechanical power measured during a sinusoidal supply load test, P_{HL} is the total additional harmonic loss due to the PWM supply, and $P_{total\,sin}$ is the sum of the corrected fundamental core loss, stator and rotor copper loss, stray-load loss and mechanical loss from the sinusoidal supply tests.

6.5 Experimental Activity

The 110kW test rig as preseneted earlier in chapter 4 (Fig. 4.19) was used for the experimental tests. For sinusoidal supply tests, the machine-under-test (MUT) was supplied by a California Instruments MX 60 programmable Power supply to avoid voltage and frequency fluctuations which are unavoidable on the mains supply. The dynamometer is a 110kW induction motor controlled by a bi-directional converter in closed loop vector mode to provide the required load torques. For PWM supply, a 2-level VSI was operated in open-loop (V/F) control mode, with slip compensation turned off, and a switching frequency of 4kHz to meet the IEC/TS requirements. Since the converter model is designed to operate with a DC bus voltage of 700V, all test voltages were obtained from the converter without going into overmodulation mode of operation.

6.6 Experimental Results and Discussions

Two standard efficiency induction motors with power ratings of 37kW and 45kW are tested in line with the IEC/TS 60034-2-3 indirect loss segregation method. The nameplate data of these motors are given in Table 6.2. The measurements are taken after the test motors have attained steady-state thermal equilibrium.

TABLE 6.2

NAMEPLATE DATA OF THE TESTED MOTORS

Parameter	**37kW Motor**	**45kW Motor**
Number of Poles	4	4
Frequency (Hz)	50	50
Voltage (V)	400	400
Current (A)	67.4	81.6
Speed (rpm)	1475	1475
Power factor	0.86	0.86
Insulation Class	F	F
Connection	Δ	Δ

6.6.1 Rotor Resistance Estimation

In solving the optimization problem for the rotor resistance estimation, the CSO algorithm was used. Instantaneous readings of the fundamental stator voltage and current signals at rated operating condition were recorded at a sampling rate of 200μs using Genesis 7i DAQ and serve as inputs to the optimization algorithm. The algorithm was set to run for 10 cycles and the average value was taken for each parameter. This is necessary to confirm the repeatability of the estimation. Fig. 6.5(a) and 6.5(b) show the convergence profiles of the fitness function f_{err} and the estimated rotor resistance respectively. As shown in Fig 6.5(b), the estimated average steady-state value of R_r is 0.131Ω.

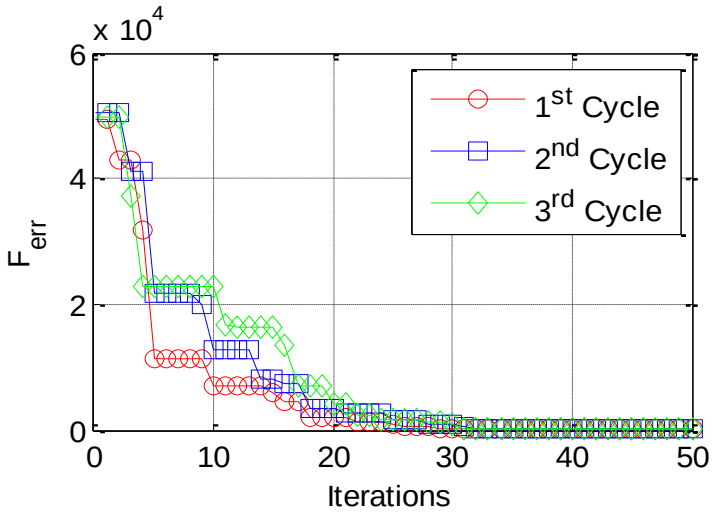

Fig. 6.5(a). Convergence profile of the cost function

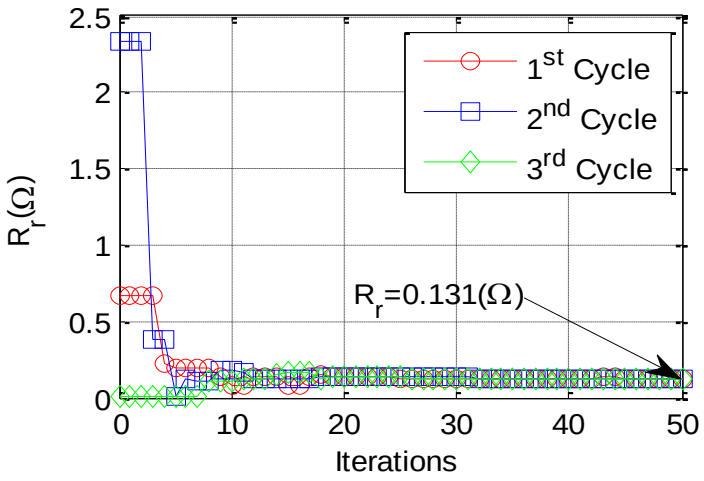

Fig. 6.5(b). Estimated rotor resistance

Fig. 6.5. Rotor resistance estimation using the CSO for the 37kW motor

6.6.2 Additional Harmonic Losses

As discussed in section, 6.3.2, the additional harmonic losses caused by the converter supply is calculated as the difference between the motor losses with converter and sinusoidal supply under the no-load and the load curve test. Taking the sinusoidal supply losses as a reference, the additional harmonic losses in the motor due to the PWM supply were calculated by (6.8) and (6.9).

For the no-load test, the graph of the constant losses versus square of the fundamental voltage for PWM supply when using a constant DC bus and variable modulation index results in a nonlinear curve. This problem as discussed in section 6.4.1 is caused by the increase in core loss due to higher voltage distortions at lower modulation indices. Hence, to separate the friction and windage loss from the constant losses, a third order polynomial was used to correctly fit the nonlinear curve. As shown in Fig. 6.6 and 6.7, the friction and windage results at 50Hz and 25Hz using the PWM and sinusoidal supply are comparable. The slight difference could be attributed to additional heating and vibrations due to the PWM supply. Under loading conditions, the friction and windage losses are corrected at each operating point according to (2.10) to account for variations in the operating speed.

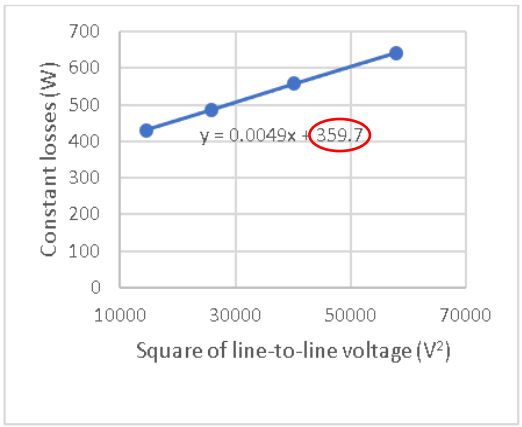

Fig. 6.6(a)

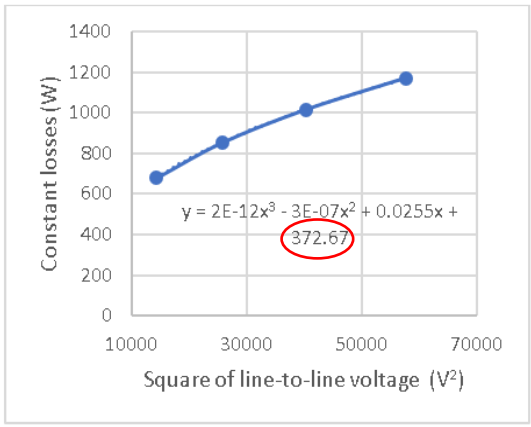

Fig. 6.6(b)

Fig. 6.6. 37kW motor friction and windage loss on sinusoidal and PWM supply at 50Hz

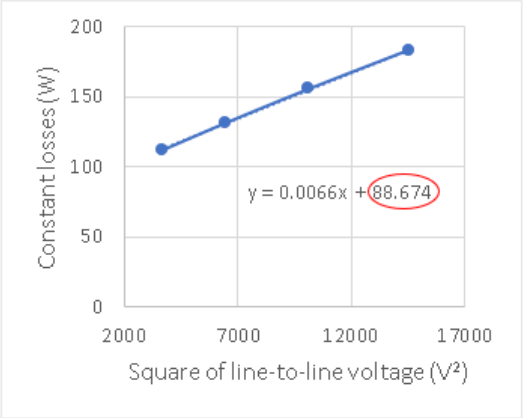

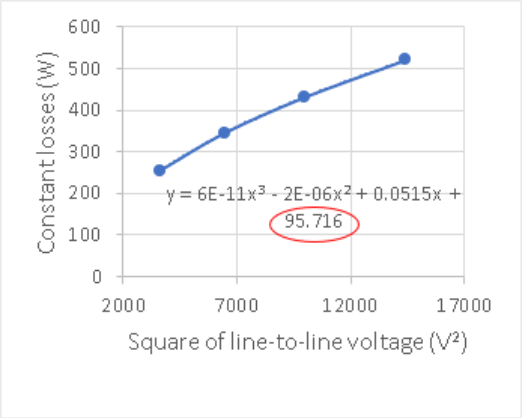

Fig. 6.7(a) Fig. 6.7(b)

Fig. 6.7. 37kW motor friction and windage loss on sinusoidal and PWM supply at 25Hz

By subtracting the friction and windage loss from the constant no-load losses, the core losses are obtained. Fig. 6.8 and 6.9 show the results at 50Hz and 25Hz respectively. From these figures, it can be observed that a substantial part of the additional harmonic losses comes from the increase in the core loss due to PWM supply. It is important to note that the final core loss values are obtained by using the voltage across the magnetization branch instead of the measured terminal voltages as reported in Fig. 6.8 and 6.9. By considering the voltage drop across the stator resistance as specified by the IEC 60034-2-1, slightly lower core loss values are obtained because of the impact of loading on the magnetization voltage.

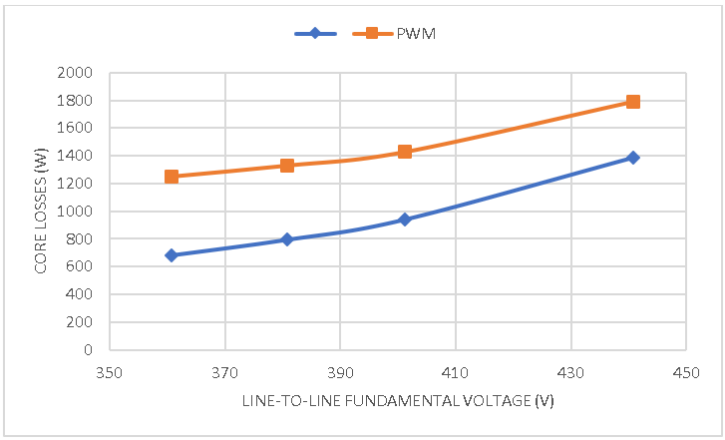

Fig. 6.8. Determination of core losses on sinusoidal and PWM supply at 50Hz for 37kW motor

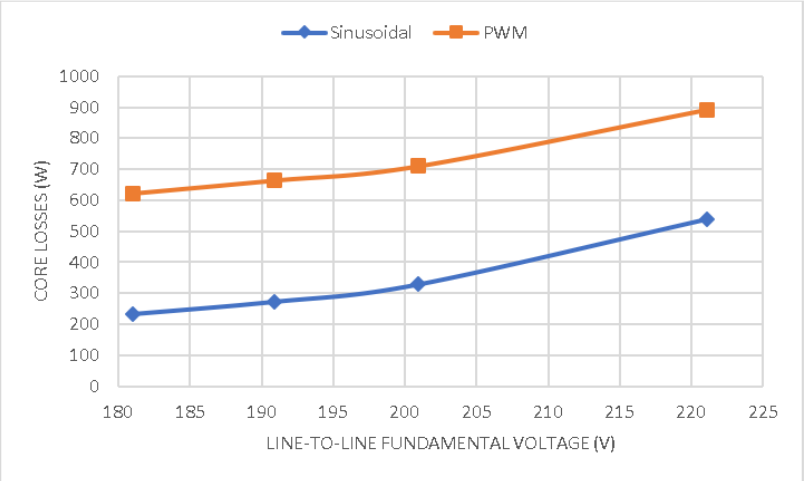

Fig. 6.9. Determination of core losses on sinusoidal and PWM supply at 25Hz

As discussed in section 6.4.1, the PWM supply causes harmonic currents through the rotor bars resulting in no-load rotor copper losses. Using the experimental test data (see Appendix F), the results obtained are as shown in Fig. 6.10 and 5.11. While these losses remain fairly independent of the frequency, their values are small when compared to the measured no-load powers as the maximum value is only about 1.416%. Nonetheless, these losses are considered in the no-load analysis as that will allow for more acceptable assessment of the additional harmonic losses.

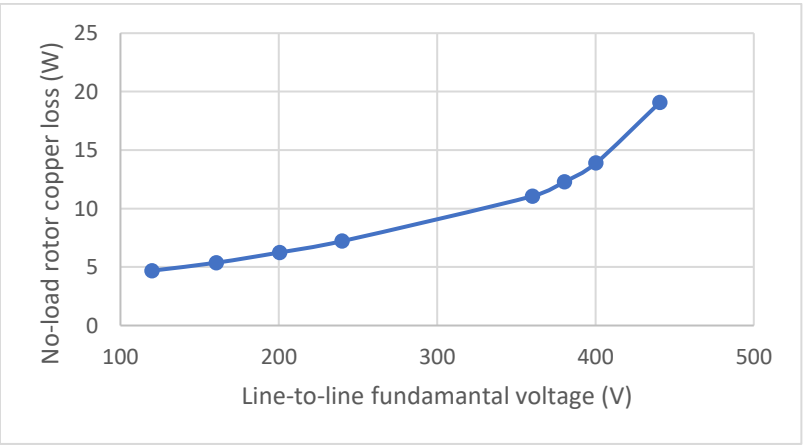

Fig. 6.10. Determination of rotor copper losses on PWM supply at 50Hz for the 37kW test motor

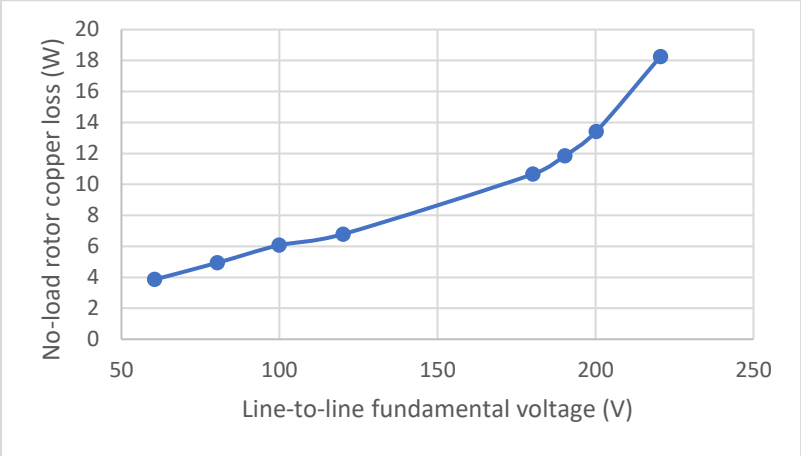

Fig. 6.11. Determination of rotor copper losses on PWM supply at 25Hz for the 37kW test motor

According to the IEC/TS loss segregation procedure, the difference between the stray-load losses on PWM and sinusoidal supply is what constitute the load-dependent additional harmonic losses. The results in Fig. 6.12 and 6.13, clearly indicate that the additional harmonic losses slightly increase with load. However, these losses are small considering the size of the tested motor (37kW). Similar trends were observed in the stray-load losses for all other tested frequencies.

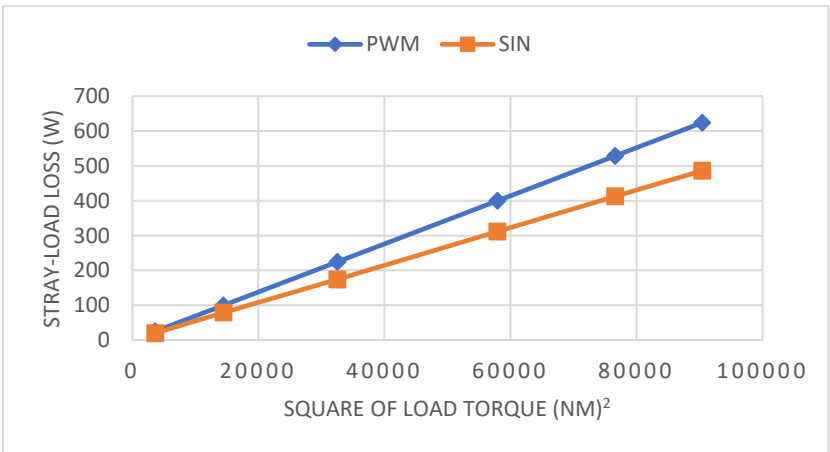

Fig. 6.12. Determination of stray-load loss on sinusoidal and PWM supply at 50Hz for the 37kW test motor

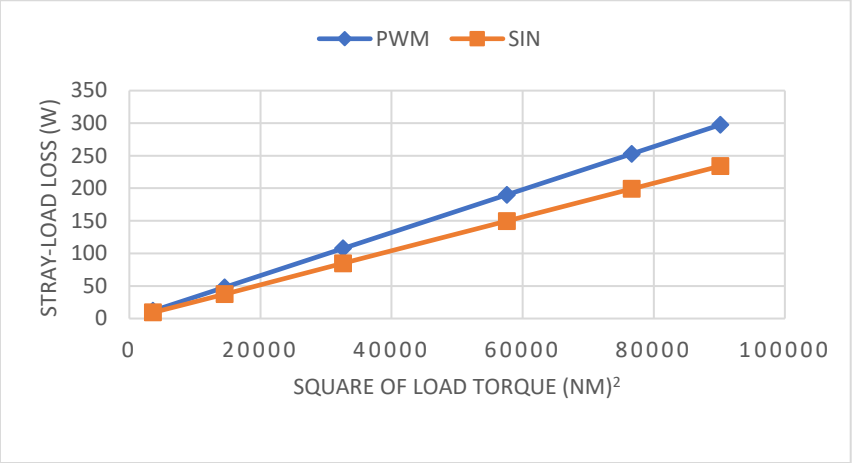

Fig. 6.13. Determination of stray-load loss on sinusoidal and PWM supply at 25Hz for the 37kW test motor

6.6.3 Efficiency and Loss Segregation Results

The efficiency results for the two test motors for sinusoidal and PWM supply are presented by the contour graphs shown in Fig 6.14. The contour representation allows extrapolation of efficiency results at several desired operating points other than the test data points. In addition, different load-speed profiles such as a quadratic or cubic relationship could be superimposed on the contour and the intersections of the curve and the contour plots could give an idea of the achievable efficiency of the motor [4].

As can be observed in Fig. 6.14, the PWM causes changes in the motor efficiency profiles. As expected, higher efficiency values are recorded at higher operating frequencies and loadings. Referring to Fig. 6.14(a), the motor efficiency is highest within a load range of 70% to 90% for the sinusoidal and a wider load range of about 70% to 125% for the PWM as shown in Fig. 6.14(b). This implies a flatter surface for the PWM efficiency profiles at higher frequencies and loadings when compared to the sinusoidal. As shown in Fig. 6.14(c), the reduction in efficiency due to the application of PWM is higher at lower load/frequency operating regions and tend to reduce as the frequency and (or) load is increased.

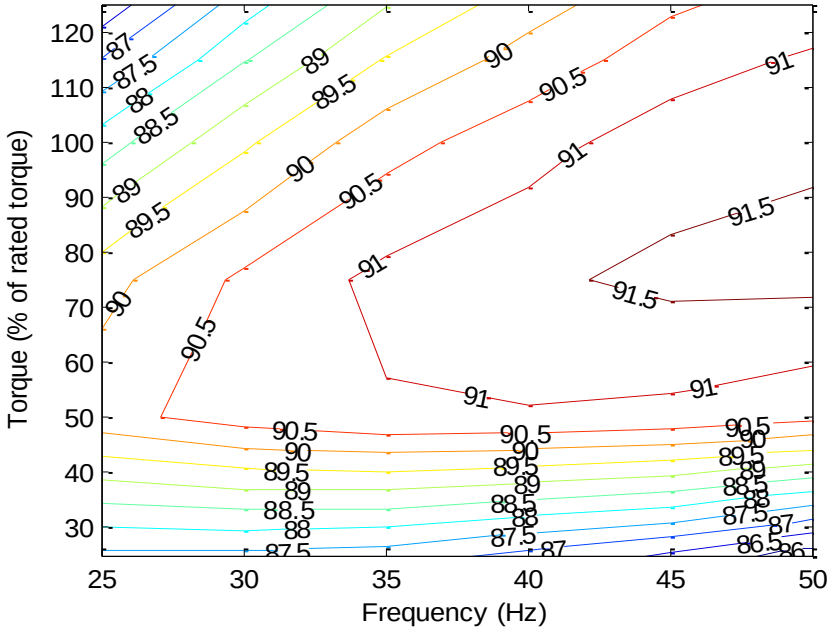

Fig. 6.14(a). Sinusoidal supply efficiency

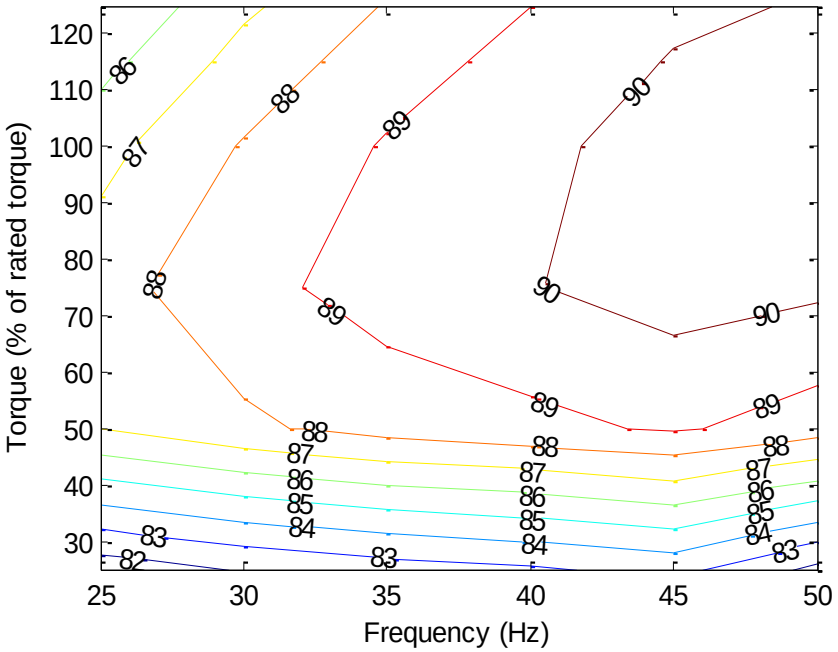

Fig. 6.14(b). PWM supply efficiency

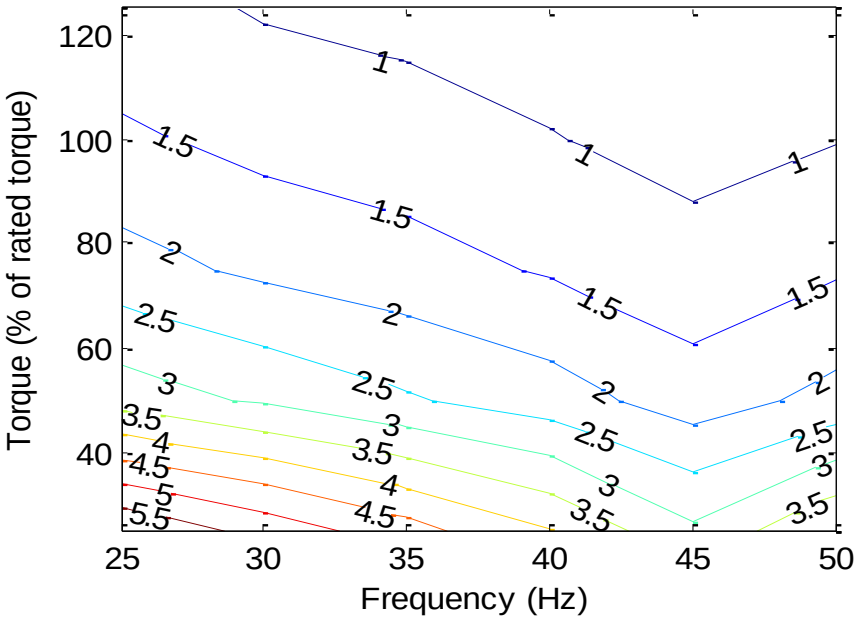

Fig. 6.14(c). Efficiency difference between sinusoidal and PWM supply

Fig. 6.14. Efficiency contour plots for the 37kW motor

Fig. 6.15 shows the efficiency contour plots for the 45kW motor. The results for both sinusoidal and PWM supply shows that the peak efficiency value was recorded over a much wider load range than that of the 37kW motor. However, comparing Fig. 6.14(c) and 6.15(c), a similar trend in the efficiency error between sinusoidal and PWM supply can be observed for the two tested motors.

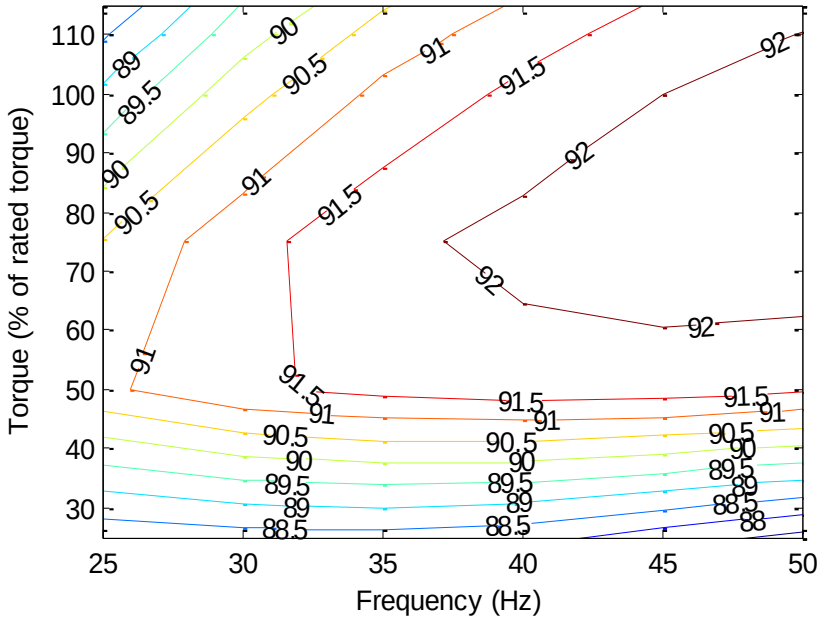

Fig. 6.15(a). Sinusoidal supply efficiency

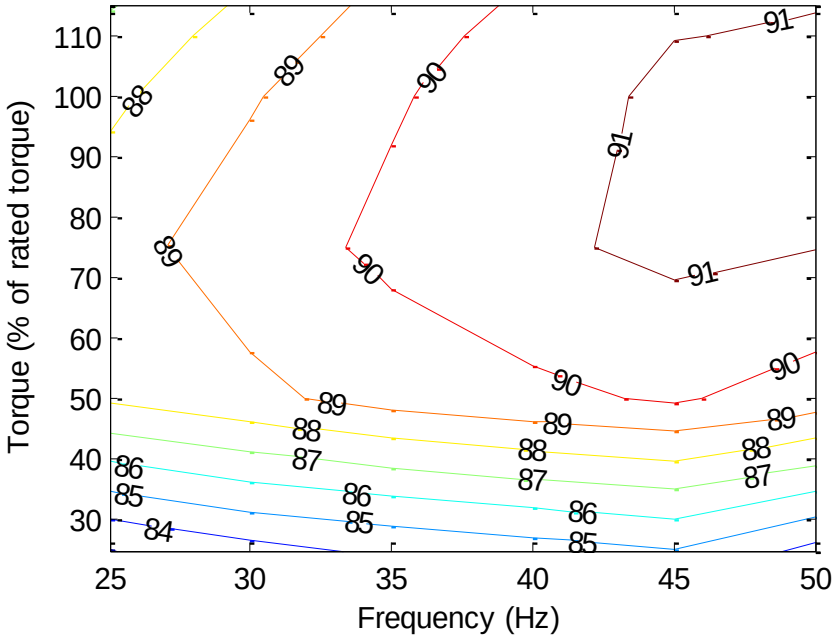

Fig. 6.15(b). PWM supply efficiency

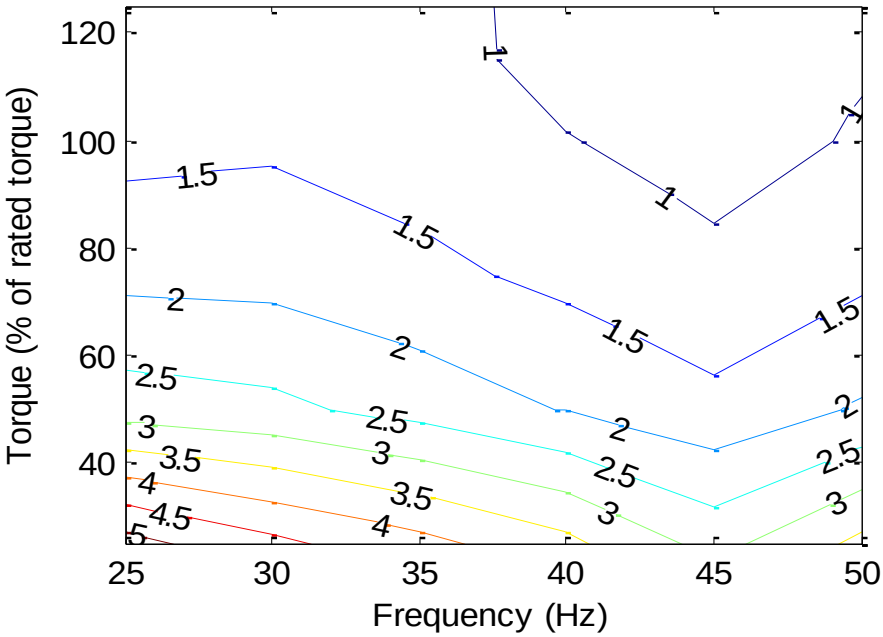

Fig. 6.15(c). Efficiency difference between sinusoidal and PWM supply

Fig. 6.15. Efficiency contour plots for the 45kW motor

The no-load losses comprising of the core loss and the friction and windage loss are shown in Fig. 6.16. As expected, the core loss is reduced during operations below the rated frequency. However, comparing sinusoidal to PWM supply, a substantial increase

in the core loss could be observed based on the results shown in Fig. 6.16(a) and 6.16(b). This could be explained by the presence of low order harmonics in the PWM supply which directly affects both the hysteresis and eddy current components of the core loss. In the context of the IEC/TS, this difference in core losses as shown in Fig. 6.16(a) and 6.16(b) is what constitutes the constant or no-load component of the additional harmonic losses.

The friction and windage loss as seen in Fig. 6.16(c) and 6.16(d) is significantly reduced for operations below the base speed. However, the difference between sinusoidal and PWM supply is quite small mainly due to the slight difference in the operating speeds and the vibrations caused by the PWM supply.

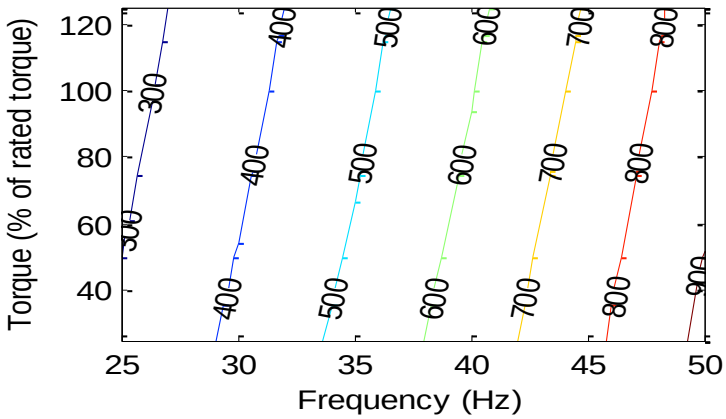

Fig. 6.16(a). Core loss for sinusoidal supply

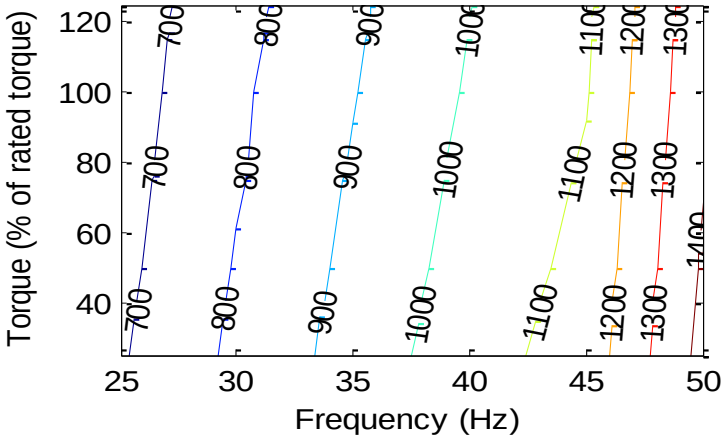

Fig.6.16(b). Core loss for PWM supply

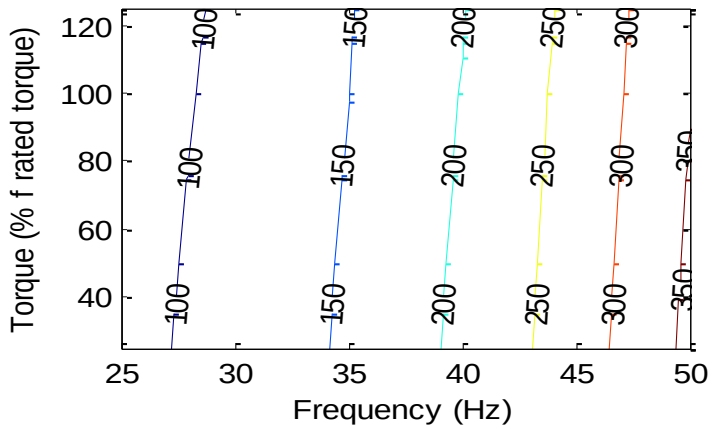

Fig. 6.16(c). Friction and windage for sinusoidal supply

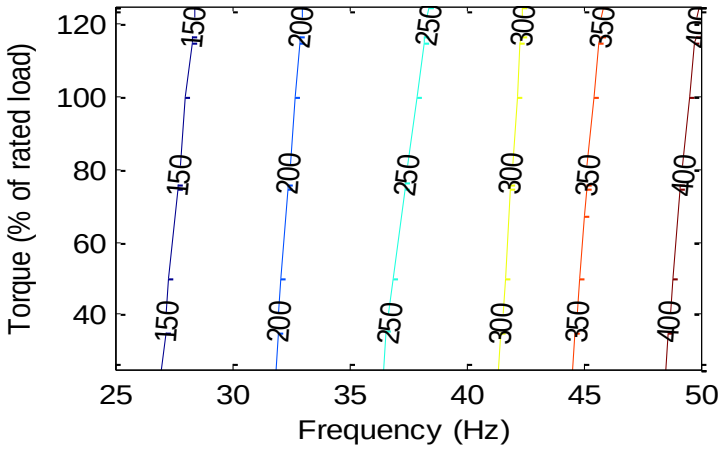

Fig. 6.16(d). Friction and windage for PWM supply

Fig. 6.16. Contour plots of the no-load or constant losses for the 37kW test motor

The stray-load loss represents the components of the losses that are not accounted for in the motor loss mechanism. For the change in stray-load loss due to PWM operation, it is necessary to consider how the other losses in the motor are accounted for. Here, the rotor harmonic currents due to PWM supply are treated as a part of the core loss (load-independent) rather than stray-load loss since they appear during the no-load test. Based on Fig. 6.17, the stray-load loss show more dependence on load than on frequency for both sinusoidal and PWM supplies. According to the IEC/TS 60034-2-3 methodology, the difference in stray load loss between sinusoidal and PWM supply is what constitutes the load-dependent additional harmonic losses.

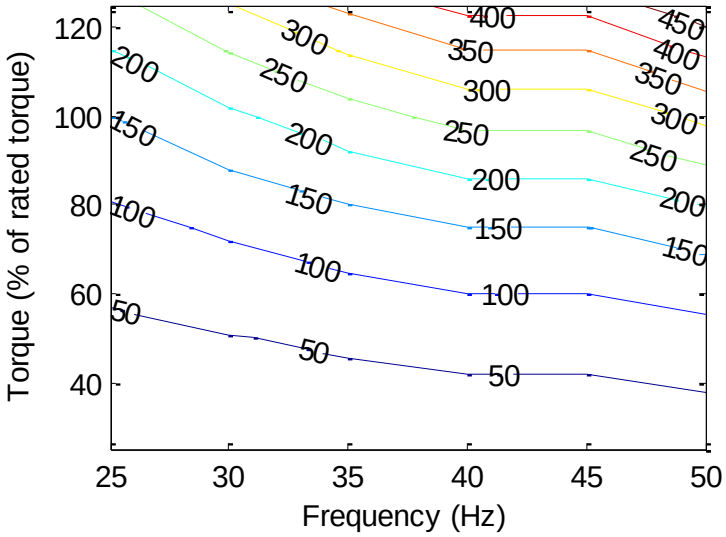

Fig. 6.17(a). Stray-load loss for sinusoidal supply

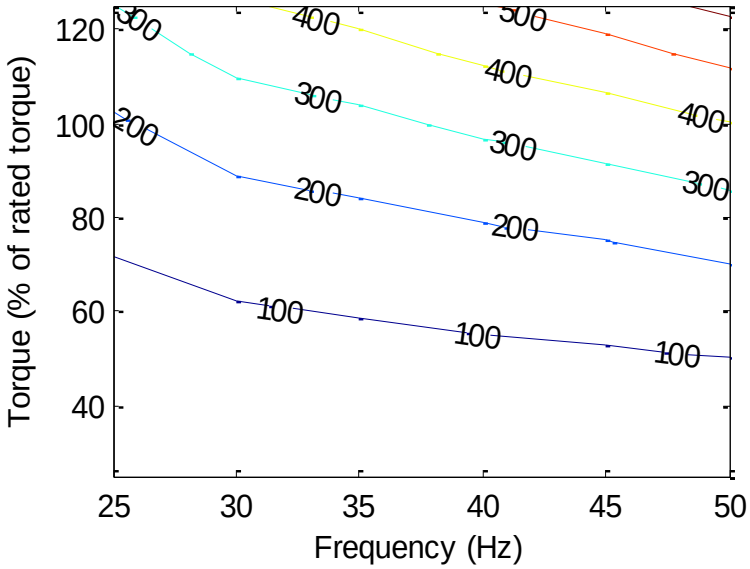

Fig. 6.17(b). Stray-load loss for PWM supply

Fig. 6.17. Stray-load loss contour plots for sinusoidal and PWM supply for the 37kW test motor

6.7 Conclusions

Following the release of the IEC/TS in 2013, several studies have tested its practical applicability and provided feedback to the relevant IEC standards committee. Although the IEC/TS has generally been criticized for providing a testing methodology limited

to induction motor operation at rated frequency and voltage, this research clearly demonstrates how the IEC/TS loss segregation method can be extended to a wide range of operating voltages and frequencies.

The no-load test was performed using variable modulation index at a constant DC bus voltage. This creates problems in separating the mechanical and core losses because of the nonlinearity on the curve of the no-load losses versus the square of the fundamental voltage. To solve this problem, the polynomial curve fitting approach was used. By fitting the last four points of the no-load tests to a third order polynomial, it was shown that results of the separated mechanical losses on PWM supply are comparable to those obtained on sinusoidal supply.

The rotor copper losses under no-load condition were determined for all the test points. It was observed that while these losses remain fairly constant with respect to the frequency, their values are small and cause less impact on the no-load losses. Nevertheless, these losses are considered in this work to allow for more acceptable assessment of the no-load additional harmonic losses.

Although a substantial part of the additional harmonic losses that cause degradation in efficiency due to PWM supply is as a result of the no-load core losses, the load-dependent harmonics loses also contribute to the added losses especially at the higher loading points.

Finally, the analysis of induction motor losses and efficiency on a wide operating range is beneficial as that can guide stakeholders in determining the optimum operating region for variable frequency drives. In addition, the proposed approach provides good feedback to the relevant IEC standards committee which should be taken into consideration during the revision process of the IEC/TS.

Chapter 7

Conclusions and Recommendations

7.1 Conclusions

The main focus of this thesis was to develop methods for estimating the efficiency of induction motors that are capable of dealing with challenges of field operating conditions such as voltage unbalance and (or) harmonics supply conditions. Hence, in order to ensure that the operation of a motor is not hindered, there is need for the testing method to be performed in the least intrusive manner. Hence, the challenging task of ensuring accuracy while maintaining the lowest level of intrusion are important aspects that were considered in this thesis.

In this dissertation, a simplified nonintrusive field efficiency estimation (NFEE) method was proposed using a modified inverse Γ-model equivalent circuit in conjunction with the CSO algorithm. The equivalent circuit parameters, as well as, the efficiencies of four different induction motors were estimated by the developed algorithm using only terminal measurements and some few nameplate data. The tests were conducted for balanced and unbalanced power supplies. Repeatability analysis, sensitivity and error analysis were performed to assess the accuracy of the proposed NFEE method.

The method presented in chapter five proposes an extension to the NFEE method to be able to deal with non-sinusoidal supply conditions. To improve on its accuracy, the method accounts for variations of core loss, rotor bar resistance and leakage inductance due to time harmonics and skin effects in the equivalent circuit modelling. The algorithm was tested on two induction motors (a standard and a premium efficiency IM motors) and the estimated efficiency results were compared to the IEC60034-2-3 standard and the direct input-output method for the case of balanced and unbalanced non-sinusoidal supply conditions respectively.

By using the App designer toolbox in Matlab, a practical efficiency estimation software tool was developed. The software serves as an interactive interface for ease of implementation of the proposed NFEE method. The software will be of great importance (as a practical industrial tool) for end-users.

Chapter six was devoted to the develeopment of a new approach to extend the IEC/TS 60034-2-3 loss segregation methodology for testing the efficiency of converter-fed IM motors at nominal frequency to cover a wider range of frequency-load operating points within the constant-torque region of an induction motor. The technical considerations and procedures to establish repeatable test conditions were presented This methodology was validated on two induction motors using a 2-level voltage source inverter (VSI) opearted in an open-loop v/f control mode.

Based on the findings of this thesis, the following conclusions can be drawn:

7.1.1 CSO Algorithm Assessment

The performance validation using five different tests functions shows that the CSO algorithm outperformed the ABC, DE, GA and PSO algorithms in terms of accuracy, repeatability, robustness and convergence rate. The results show that the CSO strikes a balance between exploration and exploitation of the search space. This is because of its diverse laws of motion while still being able to work as a team by establishing a hierarchical order among the diverse groups.

7.1.2 Efficiency Estimation on Sinusoidal Supply

As shown in this dissertation, the proposed NFEE method requires only few terminal measurements and some nameplate data which makes it suitable for on-site efficiency estimation. When compared to the conventional equivalent circuit method, it was demonstrated that the simplified inverse Γ-model equivalent circuit in conjunction with the range specification for the core loss significantly improved the accuracy of parameter identification and hence the efficiency estimations. The estimated friction and windage loss using the proposed AGT method was found to be more acceptable for nonintrusive efficiency determination than the fixed value as can be seen in most nonintrusive efficiency estimation methods.

To validate the NFEE method, the estimated efficiencies were compared to measured values obtained by the IEEE Std. 112 and the IEC 60034-2-1 loss segregation methods. The maximum absolute error in efficiency recorded at rated load using the NFEE method was found to be 0.79243% for Case 1 (balanced supply). On the other hand, the conventional method gave a maximum absolute error value of 2.4261%. The accuracy of results by the NFEE method can be attributed to the improvements in parameter identifications as well as the friction and windage loss estimation using the proposed AGT method.

Regarding the impact of voltage unbalance on efficiency, the NFEE method was able to predict the efficiency more accurately with a recorded maximum error of 0.48% when compared to the conventional method which gives an error of 1.37%.

The repeatability tests on the 7.5kW motor show that the coefficient of variance for the absolute errors in full-load efficiencies, when compared to the measured values, were calculated as 19.38% and 8.16% for the conventional and NFEE method respectively.

The impact of parameter changes on the performance of the NFEE algorithm was analysed on the 7.5kW motor. The sensitivity analysis shows that the parameter having the most notable influence on efficiency are the stator and rotor resistances. In the case of unbalance voltage supply, it was observed that the impact of the negative sequence

magnetization branch was minimal. However, as shown by the changes in the absolute efficiency errors, it is recommended to keep the magnetization branch for a more acceptable and complete representation of the unbalanced voltage supply condition.

The error analysis results indicate that the proposed NFEE method has about $\pm 0.22\%$ uncertainty level which is an acceptable margin.

7.1.3 Efficiency Estimation on Non-sinusoidal Supply

As shown in chapter five, the estimated parameters of the fundamental and harmonics equivalent circuits were consistent and less dependence on loading. Thus, measurements at a single operating point is sufficient for motor parameter estimation. Also, the results show that the rotor and core loss resistances vary according to harmonics order. Hence, the need to identify these parameters separately using the harmonics equivalent circuit for each harmonic order.

While the trends in the harmonic losses indicate noticeable dependence on the order of the harmonics, it was observed that these losses are less dependent on load. A noticeable increase in the harmonic losses has been observed in the case of the 5^{th} order harmonic and the trends tend to reduce for higher order harmonics.

In the case of a balanced non-sinusoidal supply, the recorded maximum absolute efficiency error for both motors at 9.96% THD_v was 0.248%. This value confirms the accuracy of the proposed method.

For the case of an unbalanced non-sinusoidal supply, the efficiencies of the tested motors drop significantly due to the impact of both voltage unbalance and harmonic distortions. Acceptable results were obtained by the proposed method, as the maximum absolute efficiency errors of 0.3886% and 0.2480% were obtained for the 7.5kW and 37kW motors respectively.

7.1.4 Extension of the IEC/TS 60034-2-3 Methodology For Converter-Fed Motors

Although the IEC/TS has generally been criticized for providing a testing methodology limited to induction motor operation at rated frequency and voltage, this research has shown that with some modifications, it can be extended to a wide range of operating points.

The problems of separating the mechanical and core loss under PWM supply was solved by fitting the last four points of the PWM no-load tests to a third order polynomial. The results obtained using this procedure show that the mechanical losses on PWM supply are comparable to those obtained on using sinusoidal supply.

Although the PWM rotor copper losses under no-load condition were shown to be small, it is recommended that these losses be considered to allow for more acceptable assessment of the no-load additional harmonic losses. Through the loss segregation analysis, it was shown that significant part of the total additional harmonic losses is as a result of the no-load core losses, nonetheless, the load-dependent harmonic loses also contribute to the added harmonic losses especially at higher loading points.

The least recorded correlation coefficient value in the curve fitting for determination of the stray-load loss in all the tested operating points was 0.9791. which confirms the accuracy of the proposed methodology. Hence the proposed mothod will provide good feedback to the relevant IEC standards committee as well as guidance to stakeholders.

7.2 Recommendations

Based on the findings of this thesis, the following recommendations can be made:

While the range specification worked well for estimating the core loss resistance, in further studies, a similar procedure should be used for estimating other EC parameters. This will allow for more faster convergence of the CSO algorithm.

In this research, the stator winding resistances of the tested motors were determined through direct measurement across the terminals of the motors. Although acceptable results were obtained using this procedure, in some applications, it may difficult to access the motor terminals. In such instances, the cable resistance must be taken into consideration during the DC resistance test. In future work, it is recommended to use optimization in estimating the stator winding resistance as that will be more in line with in-service efficiency estimation and also eliminate the need for temperature correction.

Although the CSO algorithm demonstrated superior performance when compared to several other optimization algorithms, different variants of the CSO algorithm have been developed recently. It is recommended to compare these algorithms alongside the conventional CSO in the motor parameter estimation problem.

In this research, only four induction motors have been tested for validating the proposed efficiency estimation methods. In future studies, a greater number of motors should be tested to confirm the applicability of the algorithms to different sizes and different types of induction motors.

In analysing the impact of voltage unbalance on efficiency, only magnitude imbalance was considered. However, in an industrial environment, a combination of both magnitude and phase imbalance are commonly seen. It is therefore essential to also consider the impact of phase imbalance as well as a combination of both magnitude and phase imbalance on the working efficiency of induction motors.

For the converter-fed motor loses and efficiency measurements in a wide operating range, only the constant torque region below the base speed is considered. Thus, it is recommended to also consider the field weakening region for determining the converter-fed motor losses and efficiencies using the loss segregation method.

References

[1] P. Waide and C. U. Brunner., “Energy-Efficiency Policy Opportunities for Electric Motor-Driven Systems,” *Int. Energy Agency, Energy Effic. Ser. Rep.*, pp. 1–132, 2011.

[2] IEC/EN 60034-30-1 Standard "Technical note on efficiency classes for low voltage AC motors,” pp. 1–2, 2014.

[3] R. Saidur, S. Mekhilef, M. B. Ali, A. Safari, and H. A. Mohammed, “Applications of variable speed drive (VSD) in electrical motors energy savings,” *Renew. Sustain. Energy Rev.*, vol. 16, no. 1, pp. 543–550, 2012.

[4] E. B. Agamloh, “Power and efficiency measurement of motor-variable-frequency drive systems,” *IEEE Trans. Ind. Appl.*, vol. 53, no. 1, pp. 766–773, 2017.

[5] I. J. Karassik, J. P. Messina, P. Cooper, and C. C. Heald, Eds., *The Pump Handbook*, 3rd ed. New York, NY, USA: MacGraw-Hill, 2001.

[6] IEEE Standard Test Procedure for Polyphase Induction Motors and Generators, *IEEE Stand. 112-2017*.

[7] IEC 60034-2-1 Standard methods for determining losses and efficiency from tests (excluding machines for traction vehicles), 2014.

[8] EN 50598-2, “Ecodesign for Power Drive Systems, Motor Starters, Power Electronics and Their Driven Applications, Part 2: Energy Efficiency Indicators for Power Drive Systems And Motor Starters,” Dec. 2014.

[9] CSA C838-13, “Energy Efficiency Test Methods For Three-Phase Variable Frequency Drives Systems,” 2013.

[10] IEC-TS 60034-2-3 “Rotating electrical machines - part 2-3: Specific test methods for determining losses and efficiency of converter-fed ac induction motors,” ed. 1.0, Nov. 2013.

[11] A. de Almeida, F. Ferreira, and A. Quintino Duarte, “Technical and economical considerations on super high-efficiency three-phase motors,” IEEE Trans. Ind. Appl., vol. 50, no. 2, pp. 1274–1285, Mar. 2014.

[12] H. Karkkainen, L. Aarniovuori, M. Niemela and J. Pyrhonen, "Converter-Fed Induction Motor Efficiency: Practical Applicability of IEC Methods," in IEEE Industrial Electronics Magazine, vol. 11, no. 2, pp. 45-57, June 2017.

[13] R. Antonello, F. Tinazzi and M. Zigliotto, "Energy efficiency measurements in IM: The non-trivial application of the norm IEC 60034-2-3:2013", in Proc. IEEE-WEMDCD, Torino, Castello del Valentino, Italy, 2015, pp. 248-253.

[14] F. Tinazzi, M. Zigliotto, A. Boglietti and A. Cavagnino, "Energy efficiency assessment for inverter-fed induction motors", in Proc. IET-PEMD, Glasgow, UK, 2016, pp. 1-6.

[15] S. Corino E. Romero L. F. Mantilla, "How the efficiency of induction machine is measured," Proceedings of the International Conference of Renewable Energies and power Quality (ICREPQ '08), 2008.

[16] G. A. McCoy, T. Litman, J. G. Douglass, "Energy-Efficient Electric Motor Selection Handbook", Washington State Energy Office US Dept. of Energy (1993), pp. 3-4.

[17] NDT Resource Centre, Available online at: https://www.nde-ed.org/EducationResources/CommunityCollege/MagParticle/Physics/Hysteresis Loop.htm.

[18] P.C. Sen, "Princple of Electric Machines and Power Electronics" John Wiley and Sons, Second Ed., pp. 270–271, 1997.

[19] M. J. Melfi, "Quantifying the Energy Efficiency of Motors on Inverters," *IEEE Industry Applications Magazine*, pp. 37–43, 2011.

[20] J. Li, Q. Yang, Y. Li, C. Zhang, B. Qu, and L. Cao, "Anomalous Loss Modeling and Validation of Magnetic Materials in Electrical Engineering," IEEE Trans. on Applied Superconductivity, vol. 26, No. 4, 2016.

[21] J. D. Kueck, "Development of a method for Estimating Motor Efficiency and Analyzing Motor Condition" Oak Ridge National Labboratory, Office of Science and Technical information Technical Reports, pp. 67–72, 1998.

[22] J. S. Hsu, J. D. Kueck, M. Olszewski, D. A. Casada, P. J. Otaduy and L. M. Tolbert, "Comparison of Induction Motor Field Efficiency Evaluation Methods," vol. 34, no. 1, pp. 117–125, 1998.

[23] J. Kueck, P. Otaduy, and J. Hsu, "Evaluation of Methods For Estimating Motor Efficiency Without Removing Motor From Service," Oak Ridge National Labboratory, Office of Science and Technical information Technical Reports, pp. 531–540, 1996.

[24] B. Lu, T. G. Habetler, and R. G. Harley, "A Survey of Efficiency-Estimation Methods for In-Service Induction Motors," no. April, 2016.

[25] National Electrical Manufacturers Association (NEMA), NEMA MG 1-2009, for Motors and Gnerators, 2009.

[26] “In-Plant Electric Motor Loading and Efficiency Techniques,’’ Ontario Hydro. Toronto, ON, Canada.

[27] B. Herndler, P. Barendse, and M. A. Khan, “Considerations for improving the non-intrusive efficiency estimation of induction machines using the air gap torque method,” in *Proc. IEEE Elect. Mach. Drives Conf.*, 2011, pp. 1516–1521.

[28] A. G. Siraki, S. and P. Pillay, “Comparison of Two Methods for Full-Load In Situ Induction Motor Efficiency Estimation From Field Testing in the Presence of Over / Undervoltages and Unbalanced Supplies,” *IEEE Trans. Ind. Appl.*, vol. 48, no. 6, pp. 1911–1921, 2012.

[29] J. S. Hsu and B. P. Scoggins, “Field Test of Motor Efficiency and Load Changes through Air-Gap Torque,” *IEEE Trans. Energy Convers.*, vol. 10, no. 3, pp. 477–483, 1995.

[30] B. Lu, T. G. Habetler, and R. G. Harley, “A Nonintrusive and In-Service Motor-Efficiency Estimation Method Using Air-Gap Torque With Considerations of Condition Monitoring,” *IEEE Trans. on Ind. Applications*, vol. 44, no. 6, pp. 1666–1674, 2008.

[31] C. P. Salomon *et al.*, “Induction Motor Efficiency Evaluation Using a New Concept of Stator Resistance,” *IEEE Trans. Instrum. Meas.*, vol. 64, no. 11, pp. 2908–2917, 2015.

[32] H. A. Toliyat, S. Member, E. Levi, S. Member, M. Raina, and S. Member, “A Review of RFO Induction Motor Parameter Estimation Techniques,” *IEEE Trans. on Energy Convers*, vol. 18, no. 2, pp. 271–283, 2003.

[33] D. M. Reed, H. F. Hofmann, S. Member, and J. Sun, “Offline Identification of Induction Machine Parameters With Core Loss Estimation Using the Stator Current Locus,” *IEEE Trans. on Energy Convers*, vol. 31, no. 4, pp. 1549–1558, 2016.

[34] W. M. Lin, T. J. Su, and R. C. Wu, “Parameter identification of induction machine with a starting no-load low-voltage test,” *IEEE Trans. Ind. Electron.*, vol. 59, no. 1, pp. 352–360, 2012.

[35] A. Bechouche, H. Sediki, D. O. Abdeslam, and S. Haddad, “A Novel Method for Identifying Parameters of Induction Motors at Standstill Using ADALINE,” *IEEE Trans. on Energy Convers*, vol. 27, no. 1, pp. 105–116, 2012.

[36] M. Carraro and M. Zigliotto, “Automatic Parameter Identification of Inverter-Fed Induction Motors at Standstill,” *IEEE Trans. on Ind. Elect.*, vol. 61, no. 9, pp. 4605–4613, 2014.

[37] P. Castaldi and A. Tilli, “Parameter Estimation of Induction Motor at Standstill With Magnetic Flux Monitoring” *IEEE Trans. on Cont. Sys. Tech*. vol. 13, no. 3, pp. 386–400, 2005.

[38] A. Marcus and N. Lima, “Nonlinear parameter estimation of steady-state induction machine models,” *IEEE Trans. Ind. Electron.*, vol. 44, no. 3, pp. 390–397, 1997.

[39] B. Abdelhadi, A. Benoudjit, and N. Nait-Said, “Application of genetic algorithm with a novel adaptive scheme for the identification of induction machine parameters,” *IEEE Trans. Energy Convers.*, vol. 20, no. 2, pp. 284–291, 2005.

[40] M. Cirrincione, M. Pucci, G. Cirrincione, and G. A. Capolino, “Constrained minimization for parameter estimation of induction motors in saturated and unsaturated conditions,” *IEEE Trans. Ind. Electron.*, vol. 52, no. 5, pp. 1391–1402, 2005.

[41] M. H. Haque, “Determination of NEMA design induction motor parameters from manufacturer data,” *IEEE Trans. Energy Convers.*, vol. 23, no. 4, pp. 997–1004, 2008.

[42] A. M. Alturas, S. M. Gadoue, B. Zahawi, and M. A. Elgendy, “On the identifiability of steady-state induction machine models using external measurements,” *IEEE Trans. Energy Convers.*, vol. 31, no. 1, pp. 251–259, 2016.

[43] L. Monjo *et al.*, “Squirrel-Cage Induction Motor Parameter Estimation Using a Variable Frequency Test,” *IEEE Trans. Energy Convers.*, vol. 30, no. 2, pp. 550–557, 2015.

[44] E. Laroche and M. Boutayeb, “Identification of the induction motor in sinusoidal mode,” *IEEE Trans. Energy Convers.*, vol. 25, no. 1, pp. 11–19, 2010.

[45] R. . Babau, I. . Boldea, T. J. E. Miller, and N. . Muntean, “Complete Parameter Identification of Large Induction Machines From No-Load Acceleration & Deceleration Tests,” *IEEE Trans. Ind. Electron.*, vol. 54, no. 4, pp. 1962–1972, 2007.

[46] S. R. Shaw and S. B. Leeb, “Identification of induction motor parameters from transient stator current measurements,” *IEEE Trans. Ind. Electron.*, vol. 46, no. 1, pp. 139–149, 1999.

[47] M. Ranta and M. Hinkkanen, “Online identification of parameters defining the saturation characteristics of induction machines,” *IEEE Trans. Ind. Appl.*, vol. 49, no. 5, pp. 2136–2145, 2013.

[48] M. Wlas, Z. Krzeminski, and H. A. Toliyat, “Neural-network-based parameter estimations of induction motors,” *IEEE Trans. Ind. Electron.*, vol. 55, no. 4, pp. 1783–1794, 2008.

[49] J. Rengifo, J. M. Aller, A. Bueno, J. Viola, and J. Restrepo, "Parameter Estimation Method for Induction Machines Using the Instantaneous Impedance During a Dynamic Start-Up," *Andean Reg. Int. Conf. (ANDESCON), 2012 VI*, pp. 11–14, 2012.

[50] J. Benzaquen, J. Rengifo, E. Albanez, and J. M. Aller, "Parameter Estimation for Deep-Bar Induction Machines Using Instantaneous Stator Measurements From a Direct Startup," *IEEE Trans. Energy Convers.*, vol. 32, no. 2, pp. 516–524, 2017.

[51] M. Aminu, P. Barendse and A. Khan (2017), Efficiency Estimation of Induction Machines using Nonintrusive No-load Low Voltage Test, *Proceedings of the IEEE Energy Conversion Congress and Exposition (ECCE), 1 -5 Oct. 2017, Cincinnati Ohio, USA, pp. 3171 – 3178.*

[52] C. Grantham and D. McKinnon, "Rapid parameter determination for induction motor analysis and control," *IEEE Trans. Ind. Appl.*, vol. 39, no. 4, pp. 1014–1020, Jul./Aug. 2003.

[53] J. R. Gomez E. C. Quispe, M. A. De Armas, and P. R. Viego, "Estimation of Induction Motor Efficiency In-Situ under Unbalanced Voltages Using Genetic Algorithms," *In Proc. IEEE Int. Conf. on Electr. Mach.*, pp. 25–28, 2008.

[54] M. G. Bijan, and P. Pillay, "Efficiency Estimation of the Induction Machine by Particle Swarm Optimization Using Rapid Test Data With Range Constraints," *IEEE Trans. Ind. Electron.*, vol. PP, no. IM, p. 1, 2018.

[55] V. Sousa, P. Viego, and J. Gómez, "Bacterial foraging algorithm application for induction motor field efficiency estimation under unbalanced voltages," *Measurement*, vol. 46, no. 7, pp. 2232–2237, 2013.

[56] G. S. Grewal and B. S. Rajpurohit, "Induction Machine Efficiency Estimation Using Population Based Algorithm," *Power Electronics (IICPE), IEEE International Conf. on Power Electronics (IICPE)*, India, 2014.

[57] M. S. Aspalli and S. B. Shetagar, "Estimation of Induction Motor Field Efficiency for Energy Audit and Management Using Genetic Algorithm," *3rd International Conference on Sensing Technology, Taiwan*, No. 4, pp. 1–6, 2008.

[58] P. Pillay, V. Levin, P. Otaduy and J. Kueck, "In-Situ Induction Motor Efficiency Determination using the Genetic Algorithm," *IEEE Trans. Energy Convers*, vol. 13, no. 4, pp. 326-333, 1998.

[59] V. S. Santos P. R. Viego, J. R. Gomez, N. A. Lemozy A. Jurado and E. C. Quispe, "Procedure for Determining Induction Motor Efficiency Working Under Distorted Grid Voltages" ," *IEEE Trans. Energy Convers,* vol. 30, no. 1, pp. 331–339, 2015.

[60] V. Sousa, P. R. Viego , J. R. Gomez, E. C. Quispe and M. Balbis “Shaft Power Estimation in Induction Motor Operating Under Unbalanced and Harmonics Voltages”, IEEE Latin America Trans., vol. 14, no. 5, pp. 2309–2315, 2016.

[61] J. Rengifo, J. Benzaquen, A. Bueno, and J. M. Aller, “Full-Load Range In-Situ Efficiency Estimation Method for Induction Motors using only a Direct Start-up,”, 2018 XIII Inter. Conf. on Electrical Machines (ICEM) pp. 1213–1219, 2018.

[62] C. S. Gajjar, J. M. Kinyua, M. A. Khan, and P. S. Barendse, “Analysis of a Nonintrusive Efficiency Estimation Technique for Induction Machines Compared to the IEEE 112B and IEC 34-2-1 Standards,” *IEEE Trans. Ind. Appl.*, vol. 51, no. 6, pp. 4541–4553, 2015.

[63] A. G. Siraki, C. Gajjar, M. A. Khan, P. Barendse, and P. Pillay, “An Algorithm for Nonintrusive In Situ Efficiency Estimation of Induction Machines Operating With Unbalanced Supply Conditions,” *IEEE Trans. Ind. Appl.*, vol. 48, no. 6, pp. 1890–1900, 2012.

[64] M. Al-Badri, P. Pillay, and P. Angers, “A Novel In Situ Efficiency Estimation Algorithm for Three-Phase IM Using GA, IEEE Method F1 Calculations, and Pretested Motor Data,” *IEEE Trans. Energy Convers.*, vol. 30, no. 3, pp. 1092–1102, 2015.

[65] M. Al-Badri, P. Pillay, and P. Angers, “A Novel in Situ Efficiency Estimation Algorithm for Three-Phase Induction Motors Operating with Distorted Unbalanced Voltages,” *IEEE Trans. Ind. Appl.*, vol. 53, no. 6, pp. 5338–5347, 2017.

[66] V. P. Sakthivel R. Bhuvaneswari S. Subramanian, “Non-intrusive efficiency estimation method for energy auditing and management of in-service induction motor using bacterial foraging algorithm,” vol. 4, no. March, pp. 579–590, 2010.

[67] M. Çunkaş and T. Sağ, “Efficiency determination of induction motors using multi-objective evolutionary algorithms,” *Adv. Eng. Softw.*, vol. 41, no. 2, pp. 255–261, 2010.

[68] B. Lu, W. Cao, I. French, K. J. Bradley, and T. G. Habetler, “Non-intrusive efficiency determination of in-service induction motors using genetic algorithm and air-gap torque methods,” *Conf. Rec. - IAS Annu. Meet. (IEEE Ind. Appl. Soc.*, pp. 1186–1192, 2007.

[69] X. Meng, Y. Liu, X. Gao et al., “A new bio-inspired algorithm: chicken swarm optimization,” in *Advances in Swarm Intelligence*, vol. 8794 of *Lecture Notes in Computer Science*, pp. 86–94, Springer, 2014.

[70] D. Wu, F. Kong, W. Gao, Y. Shen, and Z. Ji, “Improved chicken swarm optimization,” *2015 IEEE Int. Conf. Cyber Technol. Autom. Control Intell. Syst. IEEE-CYBER 2015*, pp. 681–686, 2015.

[71] L. Ching-Yin, "Effects of unbalanced voltage on the operation performance of a three-phase induction motor," *IEEE Transactions on Energy Conversion*, vol. 14, no. 2, pp. 202,208, Jun 1999.

[72] American National Standard for Electrical Power Systems and Equipment – Voltage Ratings (60 Hertz), ANSI C84.1-1995

[73] R. F. Woll, "Effect of unbalanced voltage on the operation of polyphase induction motors," IEEE Trans. Industry Applications, vol. IA-11, no. 1, pp. 38–42, Jan./Feb. 1975.

[74] P. Pillay and P. Hofmann, "Derating of induction motors operating with a combination of unbalanced voltages and over or undervoltages," IEEE *Trans. Energy Convers*, vol. 17, no. 4, pp. 485,491, December 2002.

[75] J. E. Williams, "Operation of Three-Phase Induction Motors on Unbalanced Voltages," *A/EE Transactions*, pt. IDA, *Power Apparatus* and *Systems*, Vol. 73, pp. 125-33, Apr., 1954.

[76] Gafford, W. C. Duesterhoeft and C. C. Mosher, "Heating of Induction Motors on Unbalanced Voltages," *AIEE Transactions***,** pt. ID-A, *Power Apparatus and Systems,* Vol. PAS-78, pp. 282-297, June, 1959.

[77] C. Y. Lee, B. K Chen, W. J. Lee, and Y. F. Hsu, "Effects of various unbalanced voltages on the operation performance of an induction motor under the same voltage unbalance factor conditions," *Electric Power Syst. Res.*, vol. 47, pp. 153–163, Nov. 1998.

[78] W. H. Kersting and W. H. Phillips, "Phase frame analysis of the effects of voltage unbalance on induction machines," IEEE Trans. Industry Applications, vol. 33, no. 2, pp. 415–420, Mar./Apr. 1997.

[79] P. Gnacinski, "Windings temperature and loss of life of an induction machine under voltage unbalance combined with over- or undervoltages," *IEEE Trans. Energy Convers*., vol. 23, pp. 363–371, 2008.

[80] X. Liang and Y. Luy, " Harmonic Analysis for Induction Motors" *Canadian Conference on Electrical and Computer Engineering*, 2006.

[81] K. Vasudevan, G. Shidhara and P. S. Rao, "Harmonics in Induction Machines,", Notes on Elec. Mach. II vol. 42, Indian Inst. of Tech. Madras, no. 28, pp. 42–48.

[82] K. Venkatesan and J. F. Lindsay, "Comparative Study of the Losses in Voltage and Current Source Inverter Fed Induction Motors," *IEEE. Trans. on Inds. Appl*., vol. I, no. 3, pp. 240–246, 1982.

[83] IEEE Guide for Harmonic Control and Reactive Compensation of Static Power Converters, ANSI/IEEE Standard 519, Apr. 1981.

[84] P. Phumiphak, “Nonintrusive method for estimating field efficiency of inverter-fed induction motor using measured values,” *2008 IEEE Int. Conf. Sustain. Energy Technol.*, pp. 580–583, 2008.

[85] M. Chirindo, M. A. Khan, S. Member, and P. S. Barendse, “Considerations for Nonintrusive Efficiency Estimation of Inverter-Fed Induction Motors,” *IEEE Trans. Ind. Electron.*, vol. 63, no. 2, pp. 741–749, 2016.

[86] A. Eugene and H. E. Jordan, “Polyphase Induction Motor Performance and Losses on Non-sinusoidal Voltage Sources,” *IEEE Trans. on power apparatus and sys.* no. 3, pp. 624–631, 1968.

[87] P. K. Sen and H. A. Landa, “Derating of Induction Motors Due to Waveform Distortion,” *IEEE. Trans. on Inds. Appl.*, vol. 26, no. 6, pp. 1102–1107, 1990.

[88] P. G. Cummings, “Estimating Effect of System Harmonics on Losses and Temperature Rise of Squirrel-Cage Motors,” *Int. Conf. on Power Elec. and Drives*, vol. 1, no. 6, pp. 1121–1126, 1986.

[89] J. Jung, S. Member, and K. Nam, “A Vector Control Scheme for EV Induction Motors with a Series Iron Loss Model,” *Ieee Trans. Ind. Electron.*, vol. 45, no. 4, pp. 617–624, 1998.

[90] C. Burt, X. Piao, F. Gaudi, B. Busch, and N. Taufik, “Electric motor efficiency under variable frequencies and loads,” in Journal of irrigation and drainage engineering, 134(2), pp.129-136, 2008.

[91] M. Benhaddadi, F. Landry, R. Houde and G. Olivier, "Energy efficiency electric Premium motor-driven systems," International Symposium on Power Electronics Power Electronics, Electrical Drives, Automation and Motion, Sorrento, 2012, pp. 1235-1239.

[92] H. Kärkkäinen, L. Aarniovuori, M. Niemelä and J. Pyrhönen, "Converter-fed induction motor losses in different operating points," 2016 18th European Conference on Power Electronics and Applications (EPE'16 ECCE Europe), Karlsruhe, 2016, pp. 1-8.

[93] L. Aarniovuori, A. Kosonen, M. Niemelä and J. Pyrhönen, "Frequency converter driven induction motor losses," IECON 2013 - 39th Annual Conference of the IEEE Industrial Electronics Society, Vienna, 2013, pp. 2881-2886.

[94] X. S. Yang, Nature-Inspired Metaheuristic Algorithms, Luniver Press, 2008.

[95] L. Wang, “Swarm Intelligence Optimization Algorithms and Their Application,” , Wuhan International Conference on e-bussiness, 2015.

[96] X. S. Yang, Firefly algorithms for multimodal optimization, Proc. 5th Symposium Stochastic Algorithms, Foundations and Applications, SAGA 2009, Eds. 5792, 169-178(2009).

[97] C. ZhaoHui and T. HaiYan, “Cockroach swarm optimization,” in Proceedings of the 2nd International Conference on Computer Engineering and Technology (ICCET '10), vol. 6, pp. 652–655, 2010.

[98] X. S. Yang and S. Deb, “Cuckoo search via Levy fights”, in: Proc. of World Congress on Nature & Biologically Inspired Computing, IEEE Publications, USA, pp. 210-214, 2009.

[99] D. Karaboga, “An idea based on honey bee swarm for numerical optimization”. Technical Report-TR06, Erciyes University, Engineering Faculty, Computer Engineering Department, 2005.

[100] X. S. Yang, “A new metaheuristic bat-inspired algorithm”, in: Nature Inspired Cooperative Strategies for Optimization, Springer, 65-74, 2010.

[101] S. Surjanovic and D. Bingham, “Virtual Library of Simulation Experiments: Test Functions and Datasets”, 2013, https://www.sfu.ca/~ssurjano/index.html.

[102] A. M. Alturas and S. Gadoue, “Structural Identifiability Analysis of Steady-State Induction Machine Models Structural Identifiability Analysis of Steady-State Induction Machine Models,” 4th International Conference on Electric Power and Energy Conversion Systems (EPECS), 2015.

[103] P. Vaclavek, P. Blaha, and I. Herman, “AC drive observability analysis,” *IEEE Trans. Ind. Electron.*, vol. 60, no. 8, pp. 3047–3059, 2013.

[104] D. W. Novotny and T. A. Lipo, “Vector Control and Dynamics of AC Drives”, Oxford University Press Inc. NY, USA, 1996.

[105] R. S. Gordon, “Modelling of induction machines for electric drives”, *IEEE Trans. Ind. Appl., vol. 25, no. 6, pp. 1126-1131, 1989.*

[106] I. Boldea and S. A. Nasar, “The Induction Machine Handbook, CRC Press, 2002.

[107] P. J. Gawthrop, and G. P. Bevan, "Bond-graph modeling," IEEE Control. Systems. Magazine., vol. 27, no. 2, pp. 24-45, 2007.

[108] J. F. Broenink, " Introduction to physical systems modelling with bond graphs, “Report on Simulation methodologies. University of Twente,1999.

[109] M. S. Zaky, M. Khater, H. Yasin, and S. S. Shokralla, *Review of Different Speed Estimation schemes for Sensorless Induction Motor Drive"*, Journal of Electrical Engineering, 2008.

[110] K. D. Hurst and T. G. Habetler, “Sensorless speed measurement using current harmonic spectral estimation in induction machine drives,” *IEEE Trans. Power Electron.*, vol. 11, no. 1, pp. 66–73, 1996.

[111] N. Bianchi and M. Dai Pre, “Active power filter control using neural network technologies,” *IEE Proceedings-Electric Power Appl.*, vol. 150, no. 2, pp. 139–145, 2003.

[112] M. Aiello, a. Cataliotti, and S. Nuccio, “An induction motor speed measurement method based on current harmonic analysis with the chirp-Z transform,” *IEEE Trans. Instrum. Meas.*, vol. 54, no. 5, pp. 1811–1819, 2005.

[113] V. Dlamini, R. Naidoo, and M. Manyage, “A non-intrusive compensated slip method for motor efficiency estimation using vibration signature analysis,” *IEEE AFRICON Conf.*, no. September, pp. 13–15, 2011.

[114] *G.* Bottiglieri, *G.* Scelba, *G.* Scarcella, A. Testa and A. Consoli, “Sensorless Speed Estimation in Induction Motor Drives**,”** IEEE International Conf. on *Electric Machines and Drives (IEMDC'03),* pp. 624–630, 2003.

[115] W. Kong, J. Huang, M. Kang, and B. Li, “Research of sensorless control for multiphase induction motor based on high frequency injection signal technique,” *2011 Int. Conf. Electr. Mach. Syst. ICEMS 2011*, 2011.

[116] A. Chibah, M. Menaa, K. Yazid, I. Electrical, and H. Boumediene, “Rotor Speed Estimation of Doubly Fed Induction Motor Using High Frequency Carrier Signal Injection,” no. 3, pp. 751–756, 2014.

[117] L. Baghli, I. Al-Rouh, and A. Rezzoug, “Signal analysis and identification for induction motor sensorless control,” *Control Eng. Pract.*, vol. 14, no. 11, pp. 1313–1324, 2006.

[118] J. Holtz, “Sensorless control of induction motor drives,” *Proc. IEEE*, vol. 90, no. 8, pp. 1359–1394, 2002.

[119] A. Consoli, G. Scarcella, and A. Testa, “A new zero-frequency flux-position detection approach for direct-field-oriented-control drives,” *IEEE Trans. Ind. Appl.*, vol. 36, no. 3, pp. 797–804, 2000.

[120] C. Lascu, I. Boldea, and F. Blaabjerg, “Very-low-speed variable-structure control of sensorless induction machine drives without signal injection,” *IEEE Trans. Ind. Appl.*, vol. 41, no. 2, pp. 591–598, 2005.

[121] T. C. Green, C. A. Hernandez-Aramburo, and A. C. Smith, “Losses in grid and inverter supplied induction machine drives,” *Proc. Inst. Elect. Eng Elect. Power Appl.*, vol. 150, no. 6, pp. 712–724, Nov. 2003.

[122] A. K. Ziarani, “Extraction of non-stationary sinusoids,” Ph.D. dissertation, Univ. Toronto, Toronto, ON, Canada, 2002.

[123] H. Zhang, P. Zanchetta, K. J. Bradley, and C. Gerada, “A low-intrusion load and efficiency evaluation method for in-service motors using vibration tests with an accelerometer,” *IEEE Trans. Ind. Appl.*, vol. 46, no. 4, pp. 1341–1349, 2010.

[124] B. Lu, W. Cao, and T. G. Habetler, “Error Analysis of Motor-Efficiency Estimation and Measurement,” IEEE Power Specialists Conf. pp. 612–618, 2007.

[125] B. Herndler, P. Barendse, and M. A. Khan, “Error Analysis of Efficiency Estimation Methods for Induction Motors,” *IEEE International Electric Machines and Drives Conf*. pp. 1498–1503, 2011.

[126] M. J. Melfi, “Quantifying the Energy Efficiency of Motors on Inverters,” *IEEE Industry Applications Magazine*, pp. 37–43, 2011.

[127] S. Lee, J. Kim, D. An, and J. Hong, “Equivalent Circuit Considering the Harmonics of Core Loss in the Squirrel-Cage Induction Motor for Electrical Power Steering Application,” *IEEE Trans. Magn.*, vol. 50, no. 11, pp. 1–4, 2014.

[128] S. J. Lee, S. I. Kim, and J. P. Hong, “A study on characteristics of PM synchronous motors according to pole slot combinations for EPS application,” in *Proceedings, Compumag*, 2011.

[129] E. B. Agamloh, S. Member, S. Peele, and J. Grappe, “Operation of Variable-Frequency Drive Motor Systems With Source Voltage Unbalance,” vol. 53, no. 6, pp. 6038–6046, 2017.

[130] A. Boglietti, R. Bojoi, A. Cavagnino and S. Vaschetto, "Influence of the sinusoidal supply frequency on the induction motor stray load losses," IECON 2012 - 38th Annual Conference on IEEE Industrial Electronics Society, Montreal, QC, 2012, pp. 1847-1851.

[131] M. Bašić, D. Vukadinović and M. Polić, "Stray Load and Iron Losses in Small Induction Machines Under Variable Operating Frequency and Flux: A Simple Estimation Method," in IEEE Transactions on Energy Conversion, vol. 33, no. 2, pp. 869-876, June 2018.

[132] A. Boglietti, P. Ferraris, M. Lazzari, and M. Pastorelli, “Influence of the inverter characteristics on the iron losses in PWM inverter-fed induction motors,” *IEEE Trans. Ind. Appl.*, vol. 32, no. 5, pp. 1190–1194, 1996.

[133] A. Boglietti, R. Bojoi, A. Cavagnino, and M. Lazzari, “Core loss estimation for PWM inverter-fed induction motors, "IECON 2010- 36th Annual Conference on IEEE Industrial Electronics Society, Glendale, AZ, 2010, pp. 811-816.

Appendix A: Author's Publications

A.1 Conferences

A.1.1 **M. Aminu**, P. Barendse and A. Khan (2017), Efficiency Estimation of Induction Machines using Nonintrusive No-load Low Voltage Test, *Proceedings of the IEEE Energy Conversion Congress and Exposition (ECCE), 1 -5 Oct. 2017, Cincinnati Ohio, USA, pp. 3171 – 3178.* https://ieeexplore.ieee.org/document/8096577/

A.1.2 **M. Aminu**, P. Barendse and A. Khan (2017), Nonintrusive Efficiency Estimation of Induction Machines Using Parameter Identification Based on Steady-state Stator Current Curve, *Proceedings of the IEEE AFRICON, 18 – 20 September 2017, Cape Town, South Africa, pp. 1364 – 1369.* https://ieeexplore.ieee.org/document/8095680/

A.1.3 **Muhammad Aminu**, John Mushenya, Paul Barendse, Mohammed Azeem Khan, "Converter-fed induction motor efficiency measurement under variable frequency/load points: An extension of the IEC/TS 60034-2-3" *IEEE energy conversion congress and expo (ECCE), September 2019, Baltimore, USA, pp. 3046 – 3052.* https://ieeexplore.ieee.org/stamp/stamp.jsp?tp=&arnumber=8912619

A.2 Journals

A.2.1 Muhammad Aminu, Paul Barendse and Mohammed Azeem Khan "A Simplified Equivalent Circuit Method for Induction Machine Nonintrusive Field Efficiency Estimation" DOI 10.1109/TIE.2019.2945269, IEEE Transactions on Industrial Electronics. https://ieeexplore.ieee.org/stamp/stamp.jsp?tp=&arnumber=8863119

Appendix B: No-load and Load Curve Tests Data on Sinusoidal Supply

B.1 No-Load Tests Data

Table B.1.1 7.5kW Premium Efficiency motor (No-Load Test Data)

% of Rated Voltage	Voltage (V)	Current (A)	Power (W)	Temp. (℃)
125	475.08	8.80	687.63	51.32
110	418.63	5.84	401.72	51.72
100	380.05	4.91	336.90	52.09
75	285.46	3.66	255.88	51.57
50	190.20	1.78	171.97	51.22
25	95.150	1.51	152.73	50.12

Table B.1.2 11kW Premium Efficiency motor (No-Load Test Data)

% of Rated Voltage	Voltage (V)	Current (A)	Power (W)	Temp. (℃)
125	474.07	18.19	1357.13	73.75
110	418.63	12.76	693.25	74.98
100	380.38	10.14	5.03.32	74.44
75	285.40	7.55	365.28	73.53
50	191.45	3.53	251.57	71.96
25	95.99	2.76	225.59	70.83

Table B.1.3 37kW Premium Efficiency motor No-Load Test Data

Voltage (V)	Current (A)	Power (W)	Temp. (℃)
440.84	34.26	2044.49	84.98
401.15	25.21	1459.77	84.91
380.84	22.10	1277.32	84.53
360.74	19.80	1140.14	84.29
240.61	12.11	678.77	83.91
200.55	10.10	582.28	83.51
160.49	8.19	501.78	83.23
120.38	6.44	440.83	82.94

Table B.1.4 45kW Premium Efficiency motor (No-Load Test Data)

Voltage (V)	Current (A)	Power (W)	Temp. (℃)
440.80	43.59	2253.96	85.86
401.11	32.07	1571.25	85.89
380.81	28.12	1363.50	85.76
360.70	25.22	1212.23	85.61
240.59	15.29	688.19	85.39
200.54	12.73	583.09	85.14
160.48	10.22	497.49	84.89
120.37	7.90	429.91	84.64

B.2 Load Curve Tests

Table B.2.1 7.5kW Premium Efficiency motor (Variable Load Test Data)

Load (%)	Voltage (V)	Current (A)	Power (W)	Torque (Nm)	Speed (rpm)	Freq. (Hz)	Temp. (℃)
150	376.28	22.71	13538.72	73.74	1430.13	49.99	115.33
125	381.50	18.52	11057.20	61.25	1445.80	50.00	120.54
100	382.41	14.96	8838.16	49.10	1457.76	50.00	120.95
75	381.62	11.71	6659.48	36.91	1471.10	50.01	118.20
50	382.71	8.74	4562.09	24.49	1481.88	50.02	114.71
25	382.87	6.28	2516.28	12.32	1491.78	50.01	108.56

Table B.2.2 11kW Premium Efficiency motor (Variable Load Test Data)

Load (%)	Voltage (V)	Current (A)	Power (W)	Torque (Nm)	Speed (rpm)	Freq. (Hz)	Temp. (℃)
150	381.28	35.82	19250.42	106.58	1430.50	49.99	99.51
125	382.55	29.71	15913.01	88.09	1446.76	49.99	102.24
100	382.79	23.19	12719.67	70.88	1460.01	50.00	102.42
75	385.53	19.32	96252.71	52.49	1471.16	50.01	100.19
50	386.02	15.61	6607.16	34.39	1482.42	50.01	97.12
25	387.17	11.79	3651.00	17.60	1491.78	50.02	93.13

Table B.2.3 37kW Premium Efficiency motor Variable Load Test Data

Load (%)	Voltage (V)	Current (A)	Power (W)	Torque (Nm)	Speed (rpm)	Freq. (Hz)	Temp. (℃)
125	400.38	84.17	51080.00	300.70	1467.00	50.00	104.18
115	400.39	77.77	46980.00	276.80	1470.00	50.00	105.03
100	400.48	68.42	40810.00	240.70	1474.40	50.00	104.75
75	400.64	53.77	30660.00	180.30	1481.40	50.00	103.03
50	400.77	40.77	20790.00	120.20	1487.80	50.00	101.16
25	400.93	30.50	11110.00	60.10	1493.90	50.00	98.80

Table B.2.4 45kW Premium Efficiency motor (Variable Load Test Data)

Load (%)	Voltage (V)	Current (A)	Power (W)	Torque (Nm)	Speed (rpm)	Freq. (Hz)	Temp. (℃)
115	400.00	93.50	56600.00	335.00	1472.70	50.00	100.98
110	400.49	89.73	54090.00	320.20	1474.00	50.00	101.89
100	400.58	82.56	49250.00	291.60	1476.60	50.00	101.92
75	400.74	65.27	37050.00	218.40	1482.90	50.00	100.79
50	400.88	50.12	25270.00	146.30	1488.70	50.00	98.71
25	401.04	38.04	13530.00	73.30	1494.30	50.00	96.93

Appendix C: Parameter Identification Results using the CSO Algorithm

C.1 Conventional T-Model

Table C.1.1 Conventional T-Model Parameters (7.5kW Motor)

Cycle	T-Model (7.5kW Motor)				
	$R_r(\Omega)$	$X_{ls}(\Omega)$	$X_{lr}(\Omega)$	$X_m(\Omega)$	$R_{fe}(\Omega)$
1	0.652	3.646	4.465	59.310	1723.390
2	0.628	3.626	4.449	65.178	1889.620
3	0.650	3.267	4.857	62.817	1843.700
4	0.614	4.685	3.239	61.533	1753.350
5	0.657	2.992	5.218	61.662	1458.380
6	0.644	2.818	5.467	65.993	1632.170
7	0.664	2.394	5.889	62.887	1845.950
8	0.621	4.514	3.536	62.027	1512.190
9	0.664	2.920	5.281	59.172	1679.440
10	0.626	3.893	4.194	64.405	1844.040
σ^a	0.642	3.475	4.659	62.498	1718.220
μ^b	0.017	0.704	0.805	2.154	140.500
cv	2.686	20.255	17.279	3.446	8.177

Table C.1.2 Conventional T-Model Parameters (11kW Motor)

Cycle	T-Model (11kW Motor)				
	$R_r(\Omega)$	$X_{ls}(\Omega)$	$X_{lr}(\Omega)$	$X_m(\Omega)$	$R_{fe}(\Omega)$
1	0.615	4.105	3.924	67.590	1837.920
2	0.637	3.828	4.264	61.043	1678.020
3	0.659	2.348	5.940	64.850	1785.300
4	0.609	4.662	3.384	63.647	2000.000
5	0.622	3.837	4.249	67.198	2000.000
6	0.615	4.091	3.968	65.768	1787.280
7	0.617	4.536	3.454	62.307	1836.180
8	0.627	3.996	4.064	63.138	1777.970
9	0.640	3.064	5.128	65.558	1774.080
10	0.653	2.290	6.000	68.829	1788.030
σ^a	0.630	3.676	4.437	64.993	1826.480
μ^b	0.016	0.792	0.891	2.353	96.070
cv	2.561	21.558	20.082	3.620	5.260

Table C.1.3 Conventional T-Model Parameters (37kW Motor)

Cycle	T-Model (37kW Motor)				
	$R_r(\Omega)$	$X_{ls}(\Omega)$	$X_{lr}(\Omega)$	$X_m(\Omega)$	$R_{fe}(\Omega)$
1	0.127	1.599	0.339	31.480	1368.030
2	0.135	1.467	0.466	23.564	1071.720
3	0.132	1.342	0.596	29.080	845.803
4	0.138	1.477	0.468	20.000	724.437
5	0.131	1.443	0.503	28.269	1135.590
6	0.134	0.931	1.052	36.795	1272.260
7	0.131	1.362	0.607	30.058	1573.720
8	0.139	0.143	1.886	38.645	1358.480
9	0.132	1.060	0.905	37.788	1642.750
10	0.136	1.150	0.784	26.791	821.900
σ^a	0.134	1.198	0.761	30.247	1181.470
μ^b	0.004	0.403	0.429	5.820	301.000
cv	2.621	33.659	56.388	19.240	25.477

Table C.1.4 Conventional T-Model Parameters (45kW Motor)

Cycle	T-Model (45kW Motor)				
	$R_r(\Omega)$	$X_{ls}(\Omega)$	$X_{lr}(\Omega)$	$X_m(\Omega)$	$R_{fe}(\Omega)$
1	0.125	0.738	0.551	24.000	798.390
2	0.132	0.431	0.873	20.895	1274.380
3	0.125	0.701	0.598	21.604	1052.150
4	0.131	0.373	0.943	22.347	1119.630
5	0.125	1.064	0.206	20.319	913.235
6	0.124	1.070	0.207	20.491	898.923
7	0.132	0.411	0.899	20.253	1435.250
8	0.131	0.193	1.126	23.045	1030.120
9	0.122	0.824	0.465	27.264	869.926
10	0.129	0.693	0.588	20.000	1054.350
σ^a	0.128	0.650	0.646	22.021	1044.640
μ^b	0.004	0.280	0.295	2.155	184.664
cv	2.852	43.037	45.643	9.785	17.677

C.2 Inverse Γ-Model

Table C.2.1 Inverse Γ-Model Parameters (7.5kW Motor)

Inverse Γ-Model (7.5kW Motor)				
Cycle	$R_r(\Omega)$	$X_{ls}(\Omega)$	$X_m(\Omega)$	$R_c(\Omega)$
1	0.639	3.259	63.182	2.345
2	0.640	3.258	63.757	2.368
3	0.640	3.258	63.597	2.282
4	0.640	3.259	63.438	2.338
5	0.641	3.253	62.972	2.368
6	0.640	3.259	63.576	2.316
7	0.640	3.256	62.945	2.332
8	0.640	3.254	63.028	2.385
9	0.640	3.256	63.209	2.352
10	0.640	3.258	63.206	2.353
σ^a	0.640	3.257	63.291	2.344
μ^b	0.001	0.002	0.270	0.028
cv	0.093	0.061	0.427	1.190

Table C.2.2 Inverse Γ-Model Parameters (11kW Motor)

Inverse Γ-Model (11kW Motor)				
Cycle	$R_r(\Omega)$	$X_{ls}(\Omega)$	$X_m(\Omega)$	$R_c(\Omega)$
1	0.650	2.479	69.200	2.639
2	0.650	2.479	69.141	2.632
3	0.650	2.480	69.167	2.629
4	0.650	2.479	69.163	2.622
5	0.650	2.479	69.175	2.628
6	0.650	2.479	69.130	2.628
7	0.650	2.479	69.143	2.638
8	0.650	2.479	69.074	2.604
9	0.650	2.479	69.138	2.636
10	0.650	2.479	69.133	2.632
σ^a	0.650	2.479	69.146	2.629
μ^b	0.000	0.000	0.032	0.010
cv	0.007	0.013	0.046	0.364

Table C.2.3 Inverse Γ-Model Parameters (37kW Motor)

Inverse Γ-Model (37kW Motor)				
Cycle	$R_r(\Omega)$	$X_{ls}(\Omega)$	$X_m(\Omega)$	$R_c(\Omega)$
1	0.140	0.796	26.948	0.870
2	0.140	0.796	26.991	0.875
3	0.140	0.796	26.844	0.868
4	0.140	0.796	27.107	0.874
5	0.140	0.796	26.975	0.867
6	0.140	0.796	26.973	0.878
7	0.140	0.796	26.896	0.865
8	0.140	0.796	27.015	0.876
9	0.140	0.796	26.999	0.866
10	0.140	0.796	26.933	0.862
σ^a	0.140	0.796	26.968	0.870
μ^b	0.000	0.000	0.067	0.005
cv	0.024	0.031	0.249	0.588

Table C.2.4 Inverse Γ-Model Parameters (45kW Motor)

Inverse Γ-Model (45kW Motor)				
Cycle	$R_r(\Omega)$	$X_{ls}(\Omega)$	$X_m(\Omega)$	$R_c(\Omega)$
1	0.130	0.519	21.094	0.598
2	0.130	0.519	21.180	0.607
3	0.130	0.519	21.060	0.590
4	0.130	0.519	21.070	0.599
5	0.130	0.519	21.174	0.608
6	0.130	0.519	21.169	0.604
7	0.130	0.519	21.158	0.611
8	0.130	0.519	21.155	0.615
9	0.130	0.519	21.107	0.602
10	0.130	0.519	21.056	0.595
σ^a	0.130	0.519	21.122	0.603
μ^b	0.000	0.000	0.048	0.007
cv	0.034	0.021	0.225	1.181

Appendix D: Sensitivity Analysis Results on the 7.5kW Premium Efficiency Motor

D.1 Case A – F: A $\pm 10\%$ change in parameter value

Table D.1.1 T-Model- Change in R_s

Load points	Efficiency at $+10\%\ of\ R_s$	Efficiency at $-10\%\ of\ R_s$	Measured Efficiency	Absolute Error 1	Absolute Error 2
150%	84.009	85.418	83.757	0.252	1.661
125%	86.519	87.702	86.105	0.414	1.597
100%	88.326	89.321	87.699	0.628	**1.622**
75%	89.473	90.311	88.702	0.771	1.608
50%	89.473	90.202	88.606	0.867	1.596
25%	86.014	86.780	84.898	1.117	1.882

Table D.1.2 Inverse Γ-Model- Change in R_s

Load points	Efficiency at $+10\%\ of\ R_s$	Efficiency at $-10\%\ of\ R_s$	Measured Efficiency	Absolute Error 1	Absolute Error 2
150%	82.761	84.381	83.757	0.996	0.624
125%	85.412	86.806	86.105	0.693	0.701
100%	87.359	88.535	87.699	0.340	**0.836**
75%	88.588	89.601	88.702	0.115	0.899
50%	88.590	89.508	88.606	0.016	0.902
25%	84.899	85.917	84.898	0.001	1.020

Table D.1.3 T-Model- Change in X_{ls}

Load points	Efficiency at $+10\%\ of\ R_s$	Efficiency at $-10\%\ of\ R_s$	Measured Efficiency	Absolute Error 1	Absolute Error 2
150%	84.713	84.702	83.757	0.956	0.945
125%	87.113	87.100	86.105	1.008	0.994
100%	88.830	88.812	87.699	**1.131**	1.113
75%	89.902	89.878	88.702	1.200	1.175
50%	89.855	89.818	88.606	1.249	1.212
25%	86.430	86.361	84.898	1.532	1.463

Table D.1.4 Inverse Γ-Model- Change in X_{ls}

Load points	Efficiency at $+10\%\ of\ R_s$	Efficiency at $-10\%\ of\ R_s$	Measured Efficiency	Absolute Error 1	Absolute Error 2
150%	83.564	83.562	83.757	0.193	0.195
125%	86.116	86.109	86.105	0.010	0.004
100%	87.949	87.937	87.699	**0.250**	0.238
75%	89.101	89.082	88.702	0.398	0.380
50%	89.062	89.031	88.606	0.456	0.426
25%	85.435	85.375	84.898	0.537	0.478

Table D.1.5 T-Model- Change in X_{lr}

Load points	Efficiency at $+10\%\ of\ R_s$	Efficiency at $-10\%\ of\ R_s$	Measured Efficiency	Absolute Error 1	Absolute Error 2
150%	84.619	84.795	83.757	0.862	1.038
125%	87.035	87.177	86.105	0.930	1.071
100%	88.765	88.876	87.699	1.066	**1.177**
75%	89.849	89.931	88.702	1.146	1.228
50%	89.809	89.863	88.606	1.204	1.257
25%	86.383	86.408	84.898	1.485	1.511

Table D.1.6 T-Model- Change in X_m

Load points	Efficiency at $+10\%\ of\ R_s$	Efficiency at $-10\%\ of\ R_s$	Measured Efficiency	Absolute Error 1	Absolute Error 2
150%	84.842	84.535	83.757	1.085	0.778
125%	87.249	86.921	86.105	1.144	0.816
100%	88.981	88.610	87.699	**1.282**	0.911
75%	90.084	89.632	88.702	1.382	0.929
50%	90.103	89.478	88.606	1.498	0.872
25%	86.847	85.790	84.898	1.949	0.893

Table D.1.7 Inverse Γ-Model- Change in X_m

Load points	Efficiency at $+10\%\ of\ X_m$	Efficiency at $-10\%\ of\ X_m$	Measured Eff (%)	Absolute Error 1 (%)	Absolute Error 2 (%)
150%	83.653	83.442	83.757	0.104	0.315
125%	86.234	85.948	86.105	0.129	0.158
100%	88.109	87.720	87.699	**0.410**	0.021
75%	89.324	88.778	88.702	0.622	0.076
50%	89.402	88.569	88.606	0.796	0.037
25%	86.042	84.556	84.898	1.144	0.342

Table D.1.8 T-Model- Change in R_{fe}

Load points	Efficiency at $+10\%\ of\ R_{fe}$	Efficiency at $-10\%\ of\ R_{fe}$	Measured Efficiency	Absolute Error 1	Absolute Error 2
150%	84.785	84.614	83.757	1.028	0.857
125%	87.206	86.985	86.105	1.101	0.880
100%	88.950	88.663	87.699	**1.251**	0.965
75%	90.066	89.677	88.702	1.363	0.974
50%	90.097	89.519	88.606	1.491	0.914
25%	86.855	85.841	84.898	1.957	0.943

Table D.1.9 Inverse Γ-Model- Change in R_c

Load points	Efficiency at $+10\%\ of\ R_c$	Efficiency at $-10\%\ of\ R_s$	Measured Efficiency	Absolute Error 1	Absolute Error 2
150%	83.630	83.481	83.757	0.127	0.276
125%	86.200	86.006	86.105	0.095	0.100
100%	88.058	87.803	87.699	**0.359**	0.104
75%	89.249	88.901	88.702	0.546	0.198
50%	89.280	88.763	88.606	0.674	0.157
25%	85.813	84.912	84.898	0.915	0.014

D.2 Case G: Magnetization branch omitted on negative sequence EC

Table D.2.1 T-Model: Magnetization branch omitted

Load points	Estimated Eff (%)	Measured Eff (%)	Absolute Error
150.00%	83.446	81.343	2.103
125.00%	85.900	84.109	1.791
100.00%	87.615	86.079	**1.536**
75.00%	88.600	87.290	1.310
50.00%	88.269	87.098	1.171
25.00%	83.983	82.723	1.260

Table D.2.2 Inverse Γ-Model: Magnetization branch omitted

Load points	Estimated Eff (%)	Measured Eff (%)	Absolute Error
150.00%	83.057	81.343	1.714
125.00%	85.560	84.109	1.451
100.00%	87.332	86.079	**1.253**
75.00%	88.326	87.290	1.036
50.00%	88.004	87.098	0.905
25.00%	83.674	82.723	0.951

D.3 Case H: Changes in rotor leakage reactance omitted

Table D.3.1 T-Model – Change in rotor leakage reactance

Load points	Estimated Eff (%)	Measured Eff (%)	Absolute Error
150.00%	83.777	81.343	2.434
125.00%	86.159	84.109	2.050
100.00%	87.808	86.079	**1.729**
75.00%	88.726	87.290	1.437
50.00%	88.323	87.098	1.225
25.00%	83.949	82.723	1.226

D.4 Case I: Changes in both rotor resistance and leakage reactance omitted

Table D.4.1 T-Model – Change in both rotor resistance and leakage reactance omitted

Load points	Estimated Eff (%)	Measured Eff (%)	Absolute Error
150.00%	83.432	81.343	2.089
125.00%	85.807	84.109	1.698
100.00%	87.431	86.079	**1.751**
75.00%	88.292	87.290	1.002
50.00%	87.761	87.098	0.662
25.00%	83.058	82.723	0.335

Table D.4.2 Inverse Γ-Model – Change in the rotor resistance and leakage reactance omitted

Load points	Estimated Eff (%)	Measured Eff (%)	Absolute Error
150.00%	84.114	81.343	2.771
125.00%	86.376	84.109	2.267
100.00%	87.904	86.079	**1.824**
75.00%	88.681	87.290	1.391
50.00%	88.080	87.098	0.982
25.00%	83.349	82.723	0.626

Appendix E: Error Analysis

E.1 Direct Method

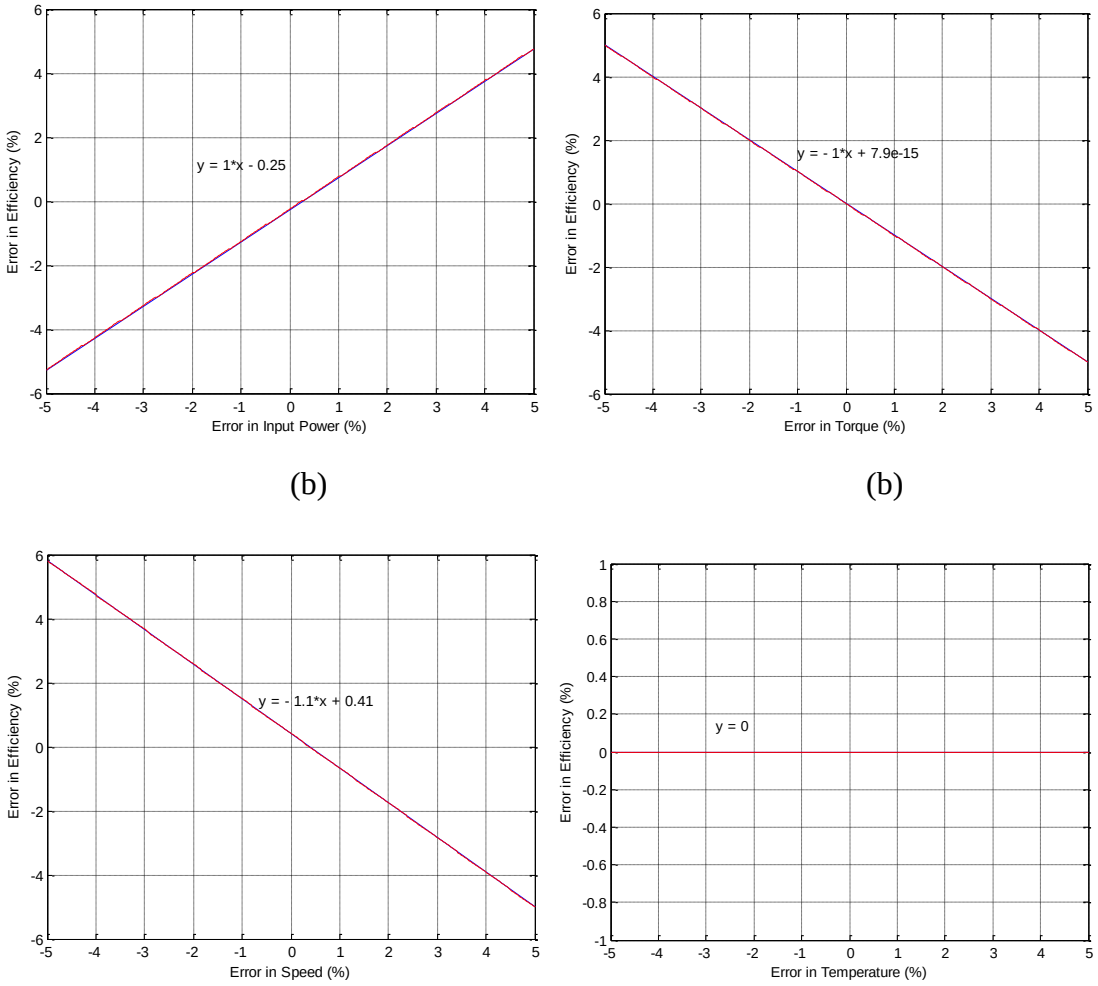

(b) (b)

(c) (d)

Fig. E.1.1. Direct method influence coefficients for the 7.5kW premium efficiency motor (a) Input power (b) Torque (c) Speed (d) Temperature

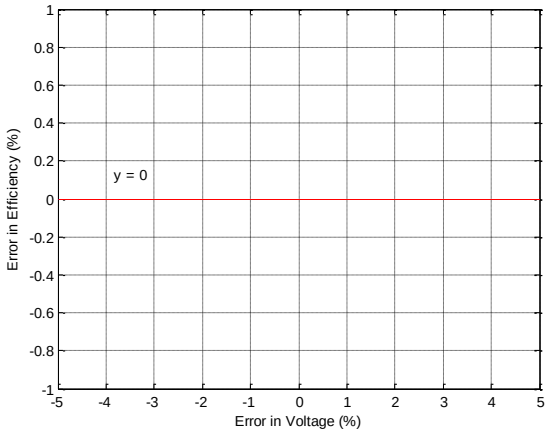

(a)

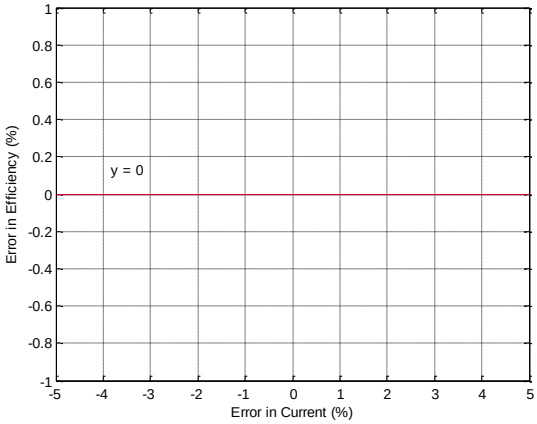

(b)

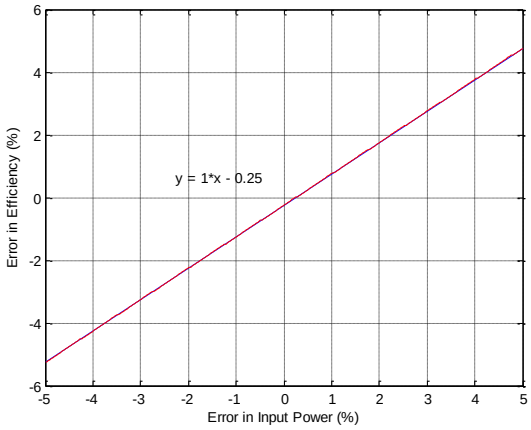

(c)

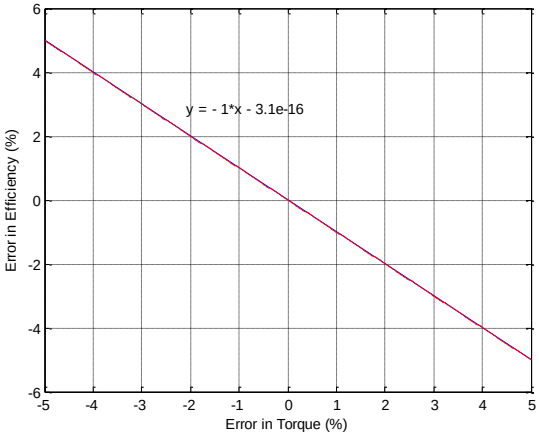

(d)

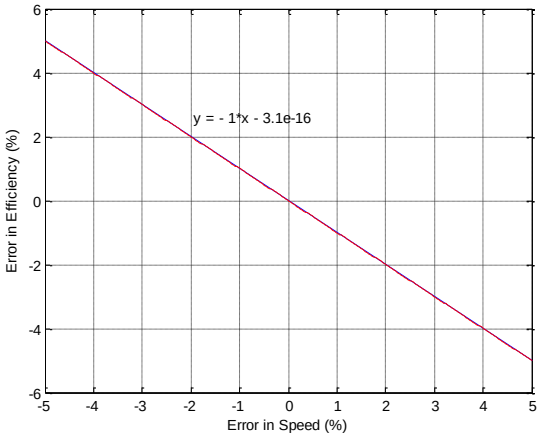

(e)

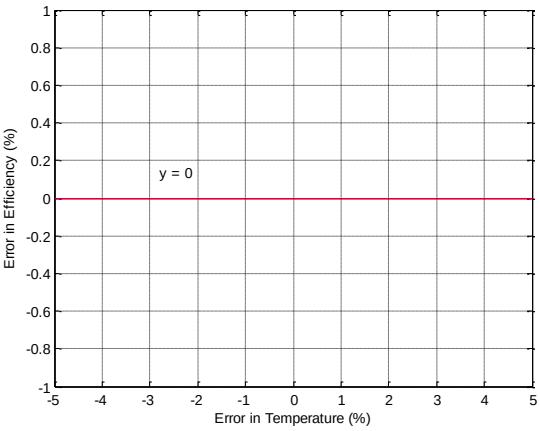

(e)

Fig. E.1.2. Direct method influence coefficients for the 37kW standard efficiency motor (a) Voltage (b) Current (c) Input power (d) Torque (e) Speed (f) Temperature

E.2 Proposed NFEE Method

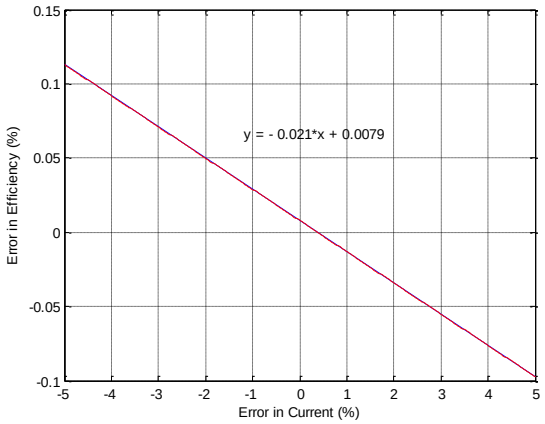

(a)

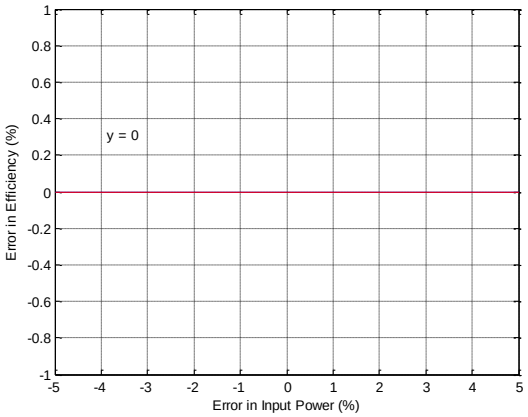

(b)

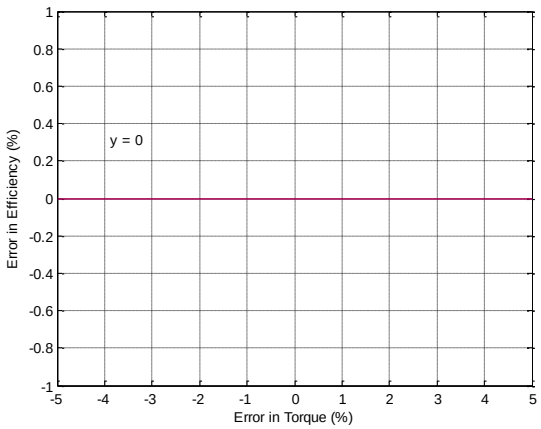

(c)

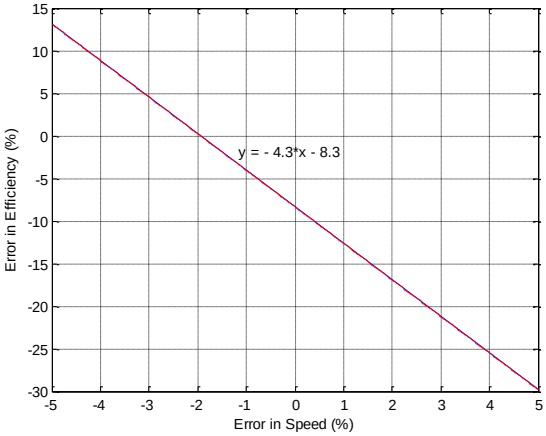

(d)

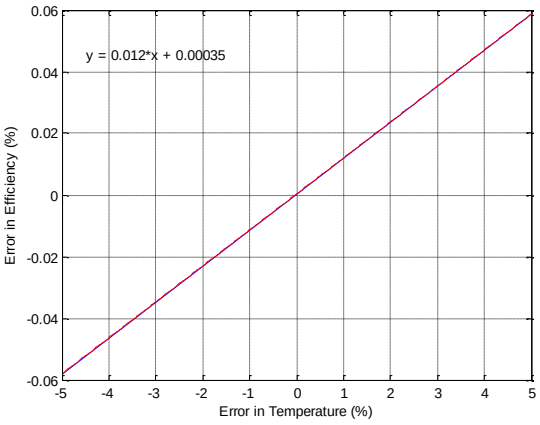

(e)

Fig. E.2.1. Proposed NFEE method influence coefficients for the 7.5kW premium efficiency motor (a) Current (b) Input power (c) Torque (d) Speed (e) Temperature

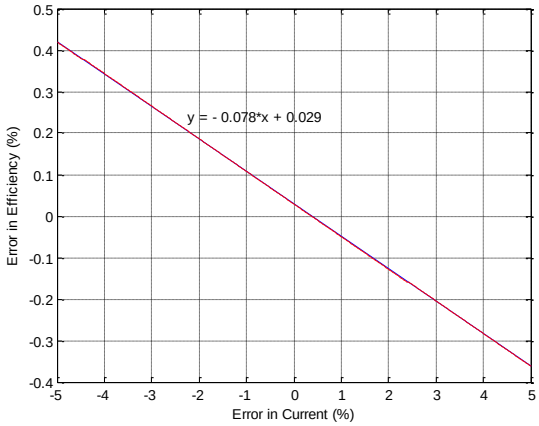

(a)

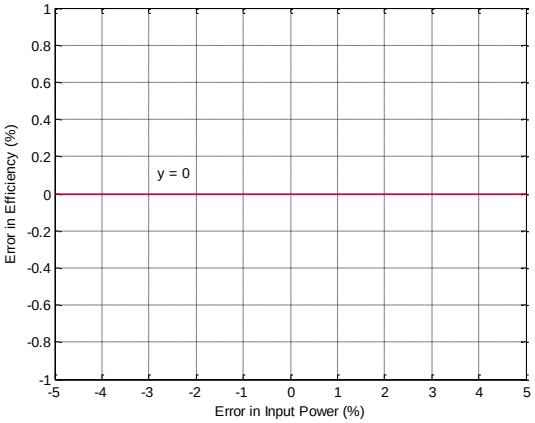

(b)

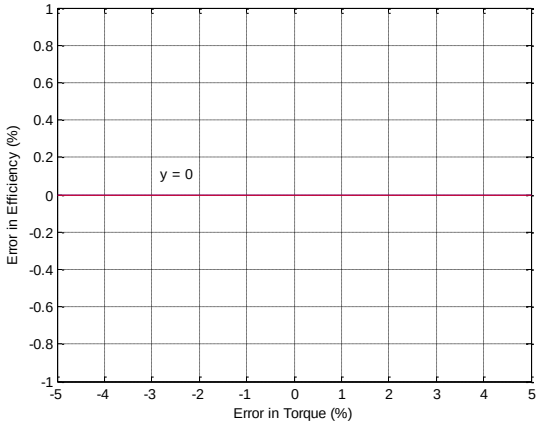

(c)

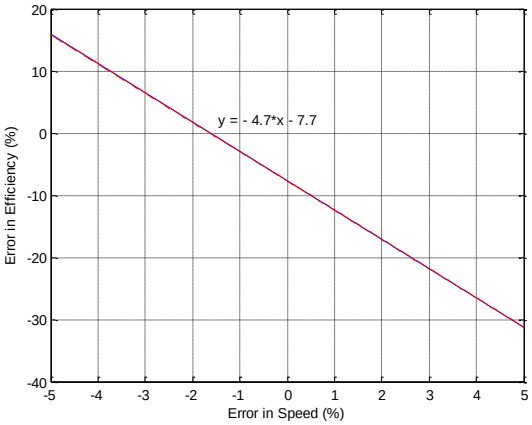

(d)

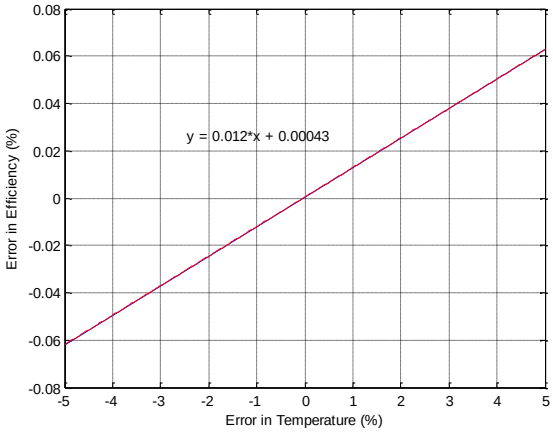

(e)

Fig. E.2.1. Proposed NFEE method influence coefficients for the 37kW standard efficiency motor (a) Current (b) Input power (c) Torque (d) Speed (e) Temperature

Appendix F: No-Load Rotor Copper Loss on PWM Supply

Table F.1.1 No-Load Test Data on PWM Supply at 50Hz

Stator Voltage (V)	Stator Current (A)	Stator Fund. Current (A)	Input Power (W)	Rotor Copper Loss (W)	Rotor Copper Loss (%)
440.685	35.632	34.476	2044.494	19.077	0.933
400.363	26.445	25.304	1459.770	13.899	0.952
380.585	23.485	22.345	1277.316	12.306	0.963
360.281	21.205	20.067	1140.141	11.062	0.970
240.118	13.522	12.337	678.767	7.219	1.063
200.644	11.516	10.300	582.285	6.250	1.073
160.599	9.606	8.335	501.776	5.372	1.071
119.904	7.898	6.517	440.832	4.690	1.064

Table F.1.2 No-Load Test Data on PWM Supply at 25Hz

Stator Voltage (V)	Stator Current (A)	Stator Fund. Current (A)	Input Power (W)	Rotor Copper Loss (W)	Rotor Copper Loss (%)
440.685	35.632	34.476	2044.494	19.077	0.933
400.363	26.445	25.304	1459.770	13.899	0.952
380.585	23.485	22.345	1277.316	12.306	0.963
360.281	21.205	20.067	1140.141	11.062	0.970
240.118	13.522	12.337	678.767	7.219	1.063
200.644	11.516	10.300	582.285	6.250	1.073
160.599	9.606	8.335	501.776	5.372	1.071
119.904	7.898	6.517	440.832	4.690	1.064